HUNGARIAN UNIVERSITY OF
AGRICULTURE AND LIFE SCIENCES
(SZENT ISTVÁN UNIVERSITY formerly)

The Effect of Integrating an Earth-Air Heat Exchanger on Photovoltaic Module Efficiency in Combination with a Solar Chimney

DOI: 10.54598/004280

PhD Dissertation

by

Mohammed Hussein Ali

Gödöllő
2024

Doctoral school

Denomination: Doctoral School of Mechanical Engineering

Science: Mechanical Engineering

Leader: Prof. Dr. Gábor Kalácska, DSc

Institute of Technology

Hungarian University of Agriculture and Life Sciences, Szent István Campus, Gödöllő, Hungary

Supervisor: Prof. Dr. János Beke, DSc

Institute of Technology

Hungarian University of Agriculture and Life Sciences, Szent István Campus, Gödöllő, Hungary

Co-supervisor: Associate Prof. Dr. Zoltán Kurják, PhD

Institute of Technology

Hungarian University of Agriculture and Life Sciences, Szent István Campus, Gödöllő, Hungary

……..…… ….....……

Affirmation of supervisor Affirmation of head of school

CONTENTS

NOMENCLATURE AND ABBREVIATIONS

Abbreviations

AIR	Air
AMB	Ambient
ASHRAE	American Society of Heating, Refrigeration and Air-conditioning Engineers
BS	Back Surface of PV module
CELL	Solar Cell
Coll	Collector
CP	Cooling Potential
EAHE	Earth-Air Heat Exchanger
FR	Heat removal factor
G	Glass
I	Insulating Sheet
PCM	Phase Change Material
PV	Photovoltaic
PV/T	Photovoltaic/Thermal collector
REF	Reference condition
SAC	Solar Air Collector
SC	Solar Chimney
SCPP	Solar Chimney Power Plant
SOIL	Soil
SR	Solar Radiation
T	Tedlar
TH	Thermal
W	Wind

Symbols

A	Area (m^2)
AFP	The air fan power (W)
A_o	Annual amplitude of the ambient temperature, (^oC)
A_{surf}	Pipe's internal surface area (m^2)
C_{loss}	The bend loss coefficient (-)
C_p	Specific heat capacity (kJ/kg K)
C_{pd}	Soil dry specific heat capacity (840 J/kg K)
C_{pw}	Specific heat capacity of water (4180 J/kg K)
C_v	Volumetric heat capacity (J/ m^3 K)
d	Damping depth of annual fluctuation (m)
$Dpipe$	Burial pipe inner diameter (m)
E_{g0}	The band gap for silicon = 1.1 eV
f	Friction factor (-)
g	Acceleration due to gravity (m/s)
h	Convective heat transfer coefficient (W/m^2 K)

H	Chimney height (m)
h_{CONV_UND}	Convective heat transfer coefficient on a lower surface of insulating module (W/m^2 K)
h_{CONV_UPP}	Convective heat transfer coefficient on upper surface of PV module (W/m^2 K)
h_f	Convective heat transfer coefficient inside the air duct (W/m^2 K)
h_{RAD}	Radiative heat transfer coefficient from solar cells to ambient (W/m^2 K)
h_{RAD_DUCT}	Radiative heat transfer coefficient inside the duct (W/m^2 K)
I	Incident solar intensity (W/m^2)
I_0	Module saturation current (A)
I_{ph}	The light generated current in a PV module (A)
I_{pv}	Output current of a PV module (A)
I_{rs}	The PV module reverse saturation current (A)
I_{SCr}	The PV module short-circuit current at 25 ^{o}C and 1000 W/m^2 = 2.55 A
k	Thermal conductivity (W/m K)
K_i	The short-circuit current temperature co-efficient at I_{SCr} = 0.0017 A/^{o}C
k_{soil}	Soil thermal conductivity (W/m K)
L	Thickness (m)
L_{pipe}	Total burial pipe length (m)
L_{pv}	Length of PV module (m)
M	Mass (kg)
N_p	The number of cells connected in parallel
N_s	The number of cells connected in series
Nu	Nusselt number (-)
P	Pressure (Pa)
p	Packing factor
P_{PV}	The extracted PV power (W)
Pr	Prandtl number (-)
Q	Amount of heat (W)
q	Electron charge = 1.6×10^{-19} C
Q	Heat gain (W)
Q_U	Rate of useful energy transfer (W)
Ra	Rayleigh number
Re	Reynolds number (-)
R_s	The series resistance of a PV module (Ω)
T	Temperature (°C)
T_a	Ambient air temperature (°C)
T_{ch}	Mean chimney air temperature (°C)
$T_{in\text{-}EAHE}$	EAHE air inlet temperature (°C)
$T_{in\text{-}SC}$	SC air inlet temperature (°C)
t_o	Time lag between an arbitrary starting date (considered as Jan. 1) (days)
T_o	Outdoor air temperature (°C)
$T_{out\text{-}EAHE}$	EAHE air outlet temperature (°C)
$T_{out\text{-}SC,L}$	SC air outlet temperature (°C)
T_{PV}	The module operating temperature (°C)
T_{ref}	The reference temperature = 25 (°C)

T_{soil}	Undisturbed ground temperature (°C)
U_0	Overall heat loss coefficient (W/m^2 K)
U_{b0}	Overall back loss coefficient from upper surface of insulation to ambient (W/m^2 K)
U_t	Overall heat transfer coefficient from solar cell to ambient (W/m^2 K)
U_T	Conductive heat transfer coefficient through solar cell and Tedlar (W/m^2 K)
U_{tT}	Overall heat transfer coefficient from glass to tedlar through solar cell (W/m^2 K)
v_a	Airflow velocity (m/s)
V_{pv}	Output voltage of a PV module (V)
V_w	Wind velocity (m/s)
W	Width of PV module (m)
w	Water content (%)
z	Depth under the ground (m)
α	Thermal diffusivity (m^2/day)
Δp	Pressure drop (N/m^2)
Δp_{stack}	Pressure drop due to buoyancy (N/m^2)
ΔT_{ch}	Mean chimney temperature elevation above ambient temperature (^{o}C)
ΔT_{lm}	The logarithmic average temperature difference (-)
Δx	Layer thickness (m)
$\dot{m}$	Mass flow rate (kg/s)

Greek

$(\alpha\tau)_{EFF}$	Product of effective absorptivity and transmissivity
μ	Dynamic viscosity (kg/m s)
α	Absorptance of the collector absorber plate
$\acute{\alpha}$	Thermal diffusivity (m^2/s)
β	Efficiency reduction coefficient
δ	Declination angle (°)
ε	Emissivity
η	Efficiency (%)
θ_z	Zenith angle (°)
λ	The PV module illumination= 1000 W/m^2
μ	Dynamic viscosity (kg/m s)
ν	Kinematic viscosity (m^2/s)
ρ	Density (kg/m^3)
ρ_a	Ambient air density (kg/m^3)
ρ_{ch}	Mean chimney air density (kg/m^3)
ρ_d	Dry soil density (kg/m^3)
ρ_{soil}	Soil density (kg/m^3)
ρ_w	Density of water (kg/m^3)
σ	Boltzman constant = 1.3805 × 10^{-23} J/K

σ	Stefan-Boltzmann constant W/(m^2 K^4)
τ	Transmissivity of the glass cover

Subscripts/superscripts

a	Ambient, air
ch	Solar chimney
coll	Collector
g	Glass
in	Inlet, initial
o	Outlet, overall
s	Sky
u	Useful
w	Wind, water content

1. INTRODUCTION, OBJECTIVES

This chapter describes the background and objectives of the current research.

1.1. Introduction

Solar energy is fundamentally an inexhaustible source and potentially capable of meeting a significant portion of the world's future energy desires. It is the most promising unconventional energy source, particularly for contributing to low-temperature applications like Photovoltaic (PV) modules, solar thermal, and solar chimneys. The cost of solar energy has decreased fast in recent years (Zarezade and Mostafaeipour, 2016). Solar energy can be generated in solar thermal power plants and PV modules. Moreover, there is another method, namely, the solar chimney (SC) (Ahmed and Hussein, 2018).

The efficiency of the PV module is affected by the rise of the operating cell temperature, particularly in hot climates. It's causing a reduction in their electricity generation. Solar Chimneys or solar towers are forms of passive solar design that can produce electricity. SC (often referred to as a thermal chimney) is a way of improving the natural ventilation of buildings by using convection of air heated by passive solar energy. A simple description of a SC is a vertical shaft utilizing solar energy to enhance the natural stack ventilation through a building (Al-Dabbas, 2011). The diligent development of the concept has included the investigation of new methods to increase the parallel solar chimney efficiency and capacity to reduce the cost of this type of power plant.

The high temperature of the air had a negative impact on the PV module's efficiency and its lifetime. This requires cooling the PV module to improve its efficiency and thus obtain better energy. One of the methods used to cool the PV module is passing water on its surface. The hybrid solar chimney was also used to increase the velocity of the air surrounding the PV module, thereby increasing the heat exchange between it and the surrounding air. In some seasons such as summer and in tropical and subtropical regions, the air temperature is very high, which leads to a heat exchange between the PV module and the ambient air. A heat exchange is insignificant and, thus, energy loss even in the case of increased air velocity. This requires a supply of relatively cold air to pass on the surface of the PV module and thus increases the resulting energy (increasing its efficiency).

This present work aims to enhance the efficiency of PV modules. The Earth-Air Heat Exchanger system (EAHE) will supply relatively cold air for the cooling PV module to increase the system's total useful power with the solar chimney's assistance. The purpose of using a SC is to increase air velocity (Kinetic power) without energy consumption. As a result, it enhances the efficiency of PV modules by using a hybrid system. Thus, this work aims to investigate the effect of integrating an EAHE on the efficiency of the PV modules in combination with SC.

PV modules, SC, and EAHE have merits and drawbacks. A hybrid solar-geothermal system may outperform the stand-alone energy system by taking over some advantages and overcoming some problems of the two energy resources because of the mutual compensation in energy properties and structures. Realizing the above outperformance requires that solar assets are abundant at the locations.

As is known, the PV module generates electrical energy by a certain amount, which depends on the size of the PV system itself and its efficiency, which depends on the type of the PV module, radiation intensity, ambient temperature, and other factors. The role of combining the PV system with other systems is coming to make a new hybrid system that aims to improve the efficiency of the PV module in particular and the entire system in general. One type of this combination is the PV modules system with a geothermal system and a solar chimney. This type of combination has not been applied practically yet, and researchers have not taken it up extensively. One researcher

suggested a system similar to this type and intended to improve the efficiency of the solar chimney by using PV modules and a geothermal system. The researcher proposed Hybrid Geothermal/SCPP (Solar Chimney Power Plant) and Hybrid Geothermal/PV/SCPP for prospective SCPP in the south region of Libya. Geothermal hot water is pumped and circulated through pipes embedded on the soil surface under the collector roof, thus hating up the adjacent air to generate artificial wind (hot air stream) that turns the turbine. The Hybrid Geothermal/PV/ SCPP is similar to the Hybrid Geothermal/Solar Chimney Power Plant but includes PV as auxiliary energy converted and an inverter that converts the DC power generated by the PV to AC power to enhance the power generation (Hussain, 2007).

1.2. Objectives

A limited number of studies have examined the topic of PV-EAHE integration or SC-EAHE integration, according to the literature study. There has also been a lack of research into how SC-PV-EAHE affects ventilation and cooling in structures and rooms during hot, moderate, and cold climates. To address this gap, this research will simulate and conduct experiments to develop a new system that integrates SC, PV, and EAHE; the goal is to determine how integrating SC and EAHE affects the efficiency of photovoltaic modules. Two cities with contrasting climates, one with hot and dry weather and the other with cold weather will serve as the sites of this investigation. This study's thorough analysis of renewable energy source integration is crucial to decreasing energy consumption and addressing the issue of solar modules' high temperature and short lifespan. In addition, the results of this study demonstrate that prior research has not given this issue sufficient attention. It should be noted that EAHE design, soil temperature distribution estimation, and SC-PV-EAHE system design have not used MATLAB much despite its reputation for accurately resolving design difficulties. Therefore, this study adds to our knowledge of how SC, EAHE, and PV system integration can improve PV module efficiency and reduce energy usage in various climates. It enhances research in this area by presenting a novel MATLAB/Simulink model for efficiently designing such systems. To achieve these objectives, the research endeavours to address the following key aims:

- To examine the effect of thermo-physical properties of the multilayer soil on the earth-air heat exchanger efficiency.
- To develop a novel MATLAB simulation model to examine and construct the hybrid system using EAHE, SC, and PV modules. The model estimates global temperature gradients and thermo-physical features to aid future studies and save time, money, and effort.
- To study the effect of the geometric configuration on natural airflow generation in the integrated system consisting of PV module, SC, and EAHE. This airflow is used for cooling the PV modules.
- To determine how the forced airflow and earth-air heat exchanger affect the efficiency of the PV modules.
- To explore the effect of the solar air collector integrated with the hybrid system (PV, SC, EAHE) on the efficiency of the PV modules.
- To investigate how the efficiency of an earth-air heat exchanger system is affected by the geometric configuration of the system.

2. LITERATURE REVIEW

This chapter aims to furnish a comprehensive overview of various components, including the EAHE, PV modules, SC, Soil characteristics and heat transfer, MATLAB simulation models for renewable energy systems, and the integration of EAHE, PV modules, and SC. It delves into their key attributes and potential applications in diverse thermal contexts. Additionally, the chapter emphasizes a meticulous examination of the integration techniques presented in the previous literature studies. This extensive analysis aligns with the dissertation's overarching theme.

2.1. Earth-Air Heat Exchanger System

2.1.1. Fundamentals, components, and working principle of earth-air heat exchanger

Geothermal energy has a long history of use as a sustainable source of power. It is well-known for its capacity to store vast quantities of energy and deliver reliable system operations, which in turn reduces building energy usage (Ascione et al., 2016; Zhang et al., 2018, 2019; Cuny Lapertot et al., 2020; Tang et al., 2020). The weather and environmental factors impact geothermal energy systems less than other renewable energy sources like wind and solar power (Qin Z. Liu et al., 2021). Because the soil temperature is relatively stable at specific depths, typically below 2-4 m, the geothermal energy system is also very efficient for both heating and cooling spaces (Mehdid et al., 2018; Zeng et al., 2019). Because of its straightforward design and inexpensive running costs, EAHE have become a popular and practical method of using geothermal energy in buildings. In the past few decades, it has garnered a lot of interest (Li et al., 2019; Cuny Lin et al., 2020).

Fig. 2.1 depicts an EAHE system consisting of horizontal pipes buried in the ground. Its purpose is to supply cooling and heating systems in buildings with outside air for ventilation and to reduce or replace part of the energy required to run the system (Tzaferis et al., 1992; Magraner et al., 2010; Barakat et al., 2019; Romanska-Zapala et al., 2019; Zhou et al., 2020). Because of its low maintenance needs and tremendous potential for energy savings, EAHE are a great option to consider. The phenomenon can only be explained by changes in soil temperature relative to the air around it. When it's hot outside, the soil dips lower than the air temperature. In addition, there is a rather constant soil temperature at a given depth below ground level all year round (Bisoniya et al., 2013; Kumar Singh and Sharma, 2017; Faridi et al., 2019, 2021). Heat exchange between the air and the ground via the tube walls (air-ground) systems, which are frequently employed to transmit soil heat, warms the cold air as it enters the exchanger (Kaushik et al., 2013). The depth of the soil temperature profile is also affected by the soil's physical characteristics and the weather conditions (Zhongbing Liu et al., 2019; Ali et al., 2021; Qin Z. Liu et al., 2021).

2.1.2. Variations and installation methods of earth-air heat exchanger

Diaphragm-less heat exchangers, such as plate-type, comb-type, and gravel-type exchangers, can enhance EAHE (Chmielewski, 2017; Zukowski and Topolanska, 2018; Amanowicz and Wojtkowiak, 2021). Both (Zukowski and Topolanska, 2018) and (Besler et al., 2022) verified the experimental efficiency. A gravel-type exchanger is a kind of heat exchanger that uses a layer of gravel about 1 m below ground to alter the humidity and temperature of the air passing through it, hence eliminating the need for a membrane. Comb-type exchangers use two combs to distribute and discharge air through corrugated ducts and gravel layers, sprinkler systems installed for improved regeneration and humidification, and insulation covering the system to a suggested depth of 1 m (Zukowski and Topolanska, 2018). Plate-type exchangers use a 50 mm gravel bed and polystyrene insulation to simulate an 8 m depth without a membrane.

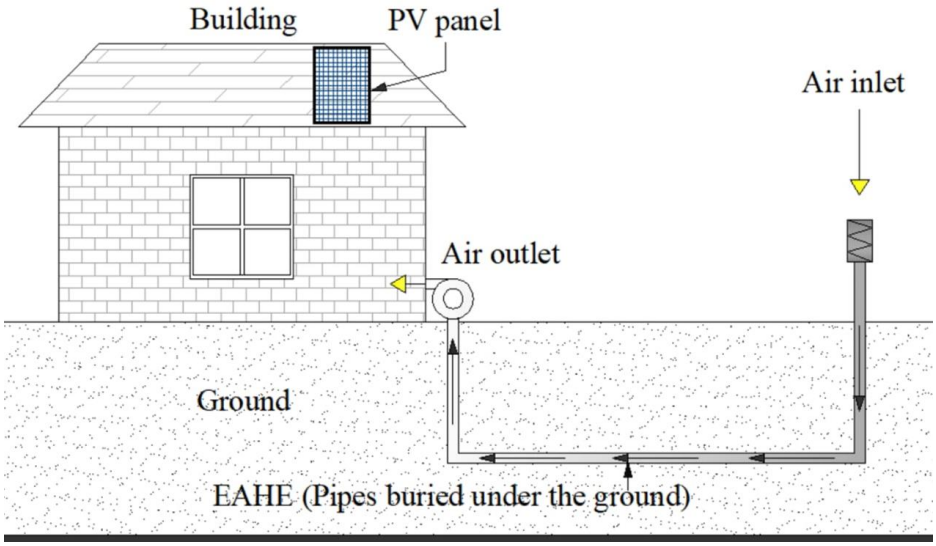

Fig. 2.1. Portrays a conceptual diagram of EAHE passive air-conditioning (Ali et al., 2023).

Underground pipes, either rectangular (Wei and Yang, 2019) or circular (Sinacka and Szczechowiak, 2017; Agrawal et al., 2020, 2021) in shape, are one method of construction for an EAHE. Exchangers of the pipe type can have either one or several pipes. Configurations using a single pipe are more flexible and can be coiled to fit into smaller areas. Parallel pipes linked by manifolds form multipipe systems. Fig. 2.2 shows the two kinds of systems. Separate types of EAHE exist based on the type of pipe arrangement (vertical, horizontal, helical, or slinky) and the type of loop (closed, open, or hybrid) (Soares et al., 2021). Tables containing data from analytical and experimental studies of EAHE are included in this review (Bordoloi et al., 2018; Amanowicz and Wojtkowiak, 2020b).

The EAHE can be installed horizontally or vertically. Although vertical installation is an option, it involves digging to a greater depth, resulting in higher digging and piping expenses. The vertical configuration is not ideal in many locations, particularly those with geological layers, making it unsuitable for widespread use. The tube installation location can be next to or under the greenhouse, and drilling costs account for about 70% of the total EAHE installation costs (G. N. Tiwari et al., 2006; Bordoloi et al., 2018).

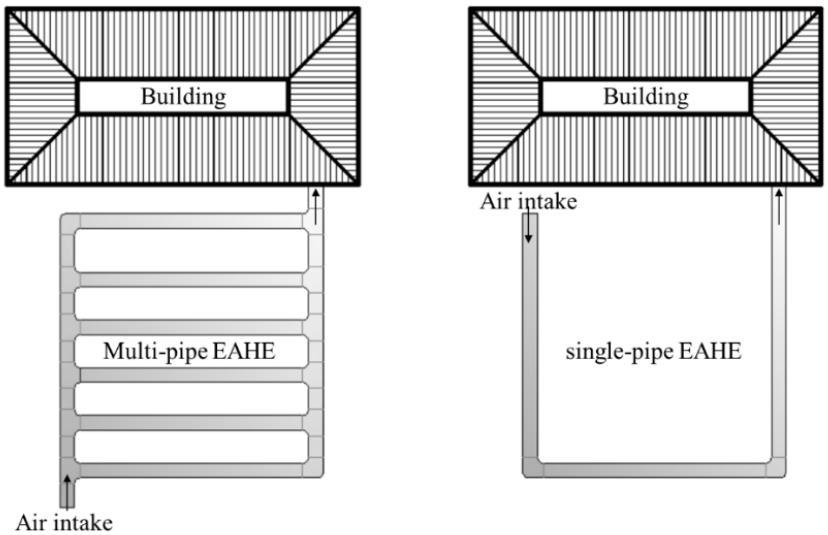

Fig. 2.2. Presents the top perspective of exemplary multi-pipe and single-pipe exchangers (Ali et al., 2023).

2.1.3. Operating modes and design considerations for earth-air heat exchanger

EAHE can function continuously or intermittently (Florides and Kalogirou, 2007; Ozgener, 2011; Peretti et al., 2013; Yu et al., 2014; Soni et al., 2015; Mathur Srivastava Agrawal et al., 2015; Mathur Srivastava Mathur et al., 2015; Mathur Surana et al., 2015; Bordoloi et al., 2018; Rouag et al., 2018; Liu et al., 2018; Zhongbing Liu et al., 2019; Maytorena et al., 2021; Minaei et al., 2021). In a transient investigation, Niu et al. (Niu et al., 2015) revealed that intermittent operation saves energy by reducing ground temperature restoration time. Mahdavi et al. (Mahdavi et al., 2019; Maytorena et al., 2021) examined EAHE's summer and winter greenhouse air temperature regulation. Transient analysis is essential for long-term EAHE efficiency, especially when phase-change materials are utilized to improve energy efficiency (Zhengxuan Liu et al., 2019; Zhou et al., 2020; Qin J. Liu et al., 2021; Z. Liu et al., 2021). System temperature drop during continuous operation decreases significantly with low soil thermal conductivity (Bansal et al., 2013b). Increased flow velocity lowers the system's thermal performance (Misra Bansal Agrawal Mathur and T. K. Aseri, 2013), while continuous operating duration and soil thermal conductivity affect transient thermal performance. Intermittently operated systems improve air temperature and cooling capacity because soil temperature and capacity recover during non-working periods (Niu et al., 2015). Pipe length increases mean daily efficiency, but pipe cross-sectional area and air velocity decrease it (Benhammou and Draoui, 2015). High soil-specific heat and low moisture promote thermal saturation, reducing EAHE efficacy (Mathur et al., 2016). Subsoil thermal characteristics and moisture can be improved (Agrawal et al., 2019). Longer pipes reduce continuous operating system thermal saturation. Heat diffusion in a pipe increases at 5 m/s, reaching 10 cm after 6 hours and 50 cm after 120 hours (Minaei and Safikhani, 2021).

Designed for high-demand structures, multi-pipe EAHE reduces overall pressure losses in ventilation systems compared to single-pipe systems (Górka et al., 2013; Zukowski and Topolanska, 2018). However, new experimental and computational fluid dynamics (CFD) studies (Górka et al., 2013; Brum et al., 2019) have demonstrated that airflow varies considerably across pipes in typical multi-pipe EAHE, although this is not observed in single-pipe EAHE studied using CFD (Brum et al., 2019). The maximum airflow in a single branch pipe of an exchanger might significantly surpass the minimum airflow due to the static pressure differential between the input and exit of the final pipes (Amanowicz, 2018), as stated in (Amanowicz and Wojtkowiak, 2020a). Neither the U-type nor the Z-type is without flaws, but the former does a better job of distributing airflow.

According to both experimental and CFD research, U-type structures outperform Z-type equivalent exchangers in terms of thermal performance (Wojtkowiak, 2012; Amanowicz, 2018; Amanowicz and Wojtkowiak, 2018). This is because U-type structures distribute airflow more uniformly and experience lower pressure losses. However, due to temperature fluctuations at the exchanger's output, CFD simulations have shown that U-type designs are less efficient than Z-type ones (Badescu and Isvoranu, 2011). In contrast to the findings in (Amanowicz and Wojtkowiak, 2020b), a basic CFD model of a five-branch-pipe EAHE predicted that Z-type structures would have cooler outlet temperatures than U-type structures, assuming an input temperature of -20°C and ground/pipe wall temperatures of 8°C.

Compared to similarly complicated U-type structures, Z-type structures show more variation in the distribution of airflow between parallel branch-pipes. According to reference (Amanowicz and Wojtkowiak, 2020a), the total pressure losses are higher at 90-degree connection angles than at 45-degree angles, and Z-type structures generate more pressure losses than U-type structures. Significant losses in thermal efficiency (up to 20%) can occur in multi-pipe EAHE due to non-uniform airflow distribution between parallel branch pipes, as stated in (Amanowicz and Wojtkowiak, 2020a). This highlights the need to include the actual airflow distribution in thermal calculations and to account for transient conditions according to the operating parameters of the system (Bansal et al., 2013a; Misra Bansal Agrawal Mathur and T. Aseri, 2013a, 2013b).

2.1.4. Mathematical models and simulation studies of earth-air heat exchanger

Several mathematical models, techniques, and computer tools have been established and applied in the open literature to understand EAHE thermal performance better. Based on this data, Krarti and colleagues (Krarti and Kreider, 1996) developed an analytical model for the EAHE. For a tubular air/soil heat exchanger with isothermal boundary conditions, Hollmuller produced a thorough analytical solution (Hollmuller, 2003). (De Paepe and Janssens, 2003) conducted a study on the impact of EAHE design factors on thermal-hydraulic performance using a 1-D model. A 2-D numerical transient technique, devised by (Badescu, 2007), enables the estimation of soil temperature at different depths using an EAHE model. EAHE was evaluated in Rhineland-Palatinate, Germany, to determine their suitability for providing cooling and heating in residential buildings. Bansal et al. (Bansal et al., 2013a)evaluated the thermal efficiency of an EAHE (Earth Air Heat Exchanger) using an experimental technique and CFD modeling. The assessment was conducted in a transient regime, taking into account the meteorological variables in Ajmer, India.

The equations suggested by researchers (Mihalakakou et al., 1997), (Mihalakakou, 2002), and (Ozgener et al., 2013) may predict the ground temperature profile based on meteorological data, exchanger depth, and ground thermal characteristics. The study conducted by (Rodrigues et al., 2015) focused on numerical analysis of a multi-pipe EAHE system. Specifically, it investigated the influence of pipe depth on thermal performance. The analysis assumed equal airflow in each branch pipe to assess the pipe arrangement's effects. A numerical analysis was conducted by (Akbarpoor et al., 2021) with a domed roof, but neither pressure losses nor multipipe structures were examined. (Lapertot et al., 2021) Employed a multi-criteria decision-making methodology to enhance the efficiency of a single-pipe EAHE system in conjunction with a residential structure. Nevertheless, the study did not investigate the possible application of multi-pipe EAHE in thermal terms. The numerical simulations of a 65.5 m 3-pipe heat exchanger in the study by (Khabbaz et al., 2016) assumed that the air-flow distribution was uniform. However, the study did not consider the total pressure losses and airflow dispersion (Rosa et al., 2020). The analysis focused on the thermal efficiency and assumed a constant airflow across the exchanger.

Researchers (Zhao et al., 2019) conducted CFD simulations to investigate how pipe depth, pipe length, and air input velocity affect the thermal performance of a 1:20 scale model of a four-pipe EAHE. However, they made the assumption of consistent airflow in each branch pipe, hence neglecting its potential impact on many factors. Researchers (Ahmed et al., 2016) ran a CFD simulation on a 20-pipe EAHE to evaluate its cooling efficiency. An investigation was conducted to analyze the influence of pipe length, pipe diameter, exchanger depth, and air velocity on the cooling effectiveness of the exchanger.

2.2. Photovoltaic Module Efficiency

2.2.1. Fundamentals of photovoltaic modules

A PV module is a device that converts sunlight into electricity. It consists of multiple interconnected solar cells made of semiconducting materials, typically silicon. When sunlight hits the PV cell, photons in the sunlight transfer their energy to electrons in the semiconductor material (Widhiyanuriyawan et al., 2022). This excitation of electrons creates a flow of electric current, which can be harnessed and used as electricity. The electric current generated by the PV module can be used to power various electrical devices and systems, such as lights, appliances, and even entire buildings. The PV module captures sunlight and converts it into usable electricity through the photovoltaic effect. The PV module is typically made up of several layers, including a front glass cover to protect the solar cells, an anti-reflective coating to enhance light absorption, a layer of semiconductor material where the photovoltaic effect occurs, and a back sheet layer for insulation and protection. The PV module is designed to be durable and weather-resistant, as it needs to withstand various environmental conditions, such as rain, snow, wind, and UV radiation.

Overall, a PV module is a key component of a photovoltaic system and plays a crucial role in harnessing solar energy to generate electricity (Vélez-Sánchez et al., 2019).

A PV module is an individual device, but a PV panel consists of a minimum of two PV modules connected in series. Integrating solar panels results in the creation of an array or string, as depicted in Fig. 2.3 (Zsiboracs et al., 2021).

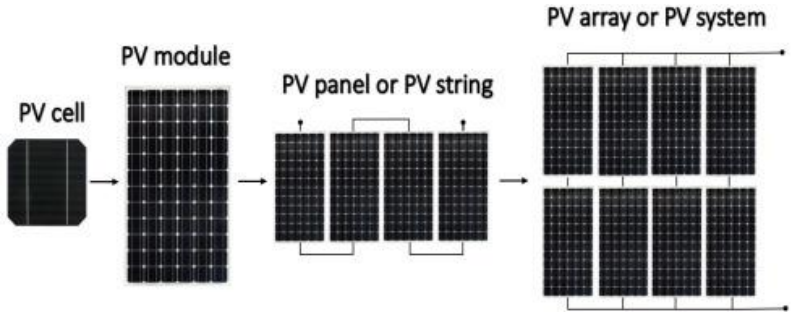

Fig. 2.3. The constituent parts of the photovoltaic system (Zsiboracs et al., 2021).

Several different types of PV cells are commonly used in photovoltaic systems. Some common types of PV modules include monocrystalline silicon, polycrystalline silicon, thin-film, and multi-junction cells. Monocrystalline silicon PV cells are made from a single crystal structure, which gives them a high efficiency and makes them more expensive to produce. Polycrystalline silicon PV cells are made from multiple crystals, resulting in a lower efficiency but a lower production cost. Thin-film PV cells are made by depositing thin layers of semiconductor materials onto a substrate. This makes them more flexible and lightweight but also less efficient. Multi-junction cells comprise multiple layers of different semiconductor materials, allowing them to capture a broader range of solar wavelengths and achieve higher efficiencies (Zhang et al., 2020).

The use of different types of PV cells allows for various options in designing photovoltaic systems, depending on factors such as cost, space availability, and desired efficiency (Abd Malek et al., 2018). PV cell types play a crucial role in the design and efficiency of PV systems. PV cell types determine photovoltaic systems' efficiency, cost, and design options. Different types of PV cells have different characteristics and efficiencies, making them suitable for different applications (Vélez-Sánchez et al., 2019). For example, monocrystalline silicon PV cells are known for their high efficiency and are commonly used in residential and commercial installations where space is limited and efficiency is a priority.

In previous years, polycrystalline silicon PV cells were more cost-effective and often used in larger installations where space is not a constraint. However, the Photovoltaics Report 2023 published by the Fraunhofer Institute for Solar Energy Systems, ISE, confirmed that monocrystalline silicon technology dominates the vast majority of the current photovoltaic market (Fraunhofer Institute for Solar Energy Systems, 2023). With their flexibility and lightweight nature, thin-film PV cells are often used in applications where aesthetics and versatility are important, such as building-integrated photovoltaics. Overall, the choice of PV cell type depends on various factors such as cost, efficiency, space availability, and specific application requirements (Zhu et al., 2016).

2.2.2. Factors influencing the efficiency of photovoltaic modules

The efficiency of PV modules is influenced by several factors, including:

- The PV cells' quality and performance impact their conversion efficiency.
- The orientation and positioning of the PV panels, as proper alignment, can optimize sunlight absorption (Som et al., 2020).
- The use of anti-reflection coatings on the surface of the PV cells reduces losses due to reflection and increases overall efficiency (Chen et al., 2019).

- Photonic band gap materials can enhance light absorption and improve the efficiency of PV cells (Asokan et al., 2010).
- The efficiency of power converters, which are responsible for converting the DC electricity generated by the PV cells into usable AC electricity (Ogoulola et al., 2020).
- The efficiency of maximum power point tracking techniques optimizes the PV system's operation and ensures maximum power output (Yoomak and Ngaopitakkul, 2020).

These factors play a crucial role in determining the overall efficiency and performance of PV modules. Still, the operating temperature of the PV modules has the most significant impact on PV module efficiency (Thulasiyammal and Sutha, 2014).

The temperature rise adversely impacts photovoltaic cells. The increase in module temperature causes a loss of around 10% in the output power and efficiency of solar cells (KR et al., 2023). Due to the heat-absorbing properties of the dark-colored surfaces of the solar cells, the surface temperature of the modules can reach a maximum of 80 °C. As the temperature of the module rises, the tension in the P-characteristic drops. Due to the negative impact of temperature on PV modules, the module's output voltage and power decrease as the temperature rises. With the escalation of solar radiation, both the voltage and current of the module experience an increase. Aside from temperature, the effectiveness of PV systems is also diminished by other factors, including shadowing, dust accumulation, and reflection (Amran et al., 2023). The global production of electricity using PV technology is experiencing a steady rise. In 2017, PV technology accounted for 2.1% of total energy production. However, in 2018, it experienced a growth and reached 2.58%. Experts contend that PV power generation is projected to account for 30-50% of the overall world energy production by the year 2050. The elements that impact the efficiency of PV technology, which is progressively playing a larger role in overall energy generation, are crucial factors that require attention and enhancement.

The primary energy source for PV modules is radiation intensity. Hence, the production of power is exactly proportional to the level of radiation that reaches the surface of the module. Solar cells produce electrical energy, however, this causes the temperature of the modules to rise. An essential contributor to reduced efficiency in modules is the elevated surface temperature resulting from the combination of ambient temperature and solar radiation (KR et al., 2023). According to the study, a rise in cell temperature by one degree might lead to a decrease in efficiency ranging from 0.04% to 0.065%. The efficiency of the modules is influenced by parameters such as the material composition of the modules, radiation intensity, environmental temperature, and module temperature. A decline in surface temperatures results in an enhancement of PV performance. Gedik et al. assert that an increase of 14.9 °C in the surface temperature of the PV module results in a fall in module efficiency from 12.07% to 10.7% (Sultan et al., 2022)(Benato et al., 2021).

2.2.3. Previous work on enhancing the efficiency of photovoltaic modules

Various cooling methods are available for PV modules to prevent temperature rise, including active cooling with forced air or water, passive cooling using phase change materials (PCM), photovoltaic/thermal (PV/T) collector, and passive cooling with porous media. PCM can be applied to the surface of the PV module to maintain a temperature of 25°C. The melting point of PCM must exceed the ambient temperature (Anderson et al., 2008). PV/T is the combination of photovoltaic panels and solar thermal collectors to generate electricity and simultaneously utilize heat energy from the sun. To implement the heat pipe concept, one can install copper pipes and aluminum fins on the rear side of PV modules. According to reports, these applications are capable of maintaining the surface temperature of the PV cells exposed to solar radiation at a rate of (20-100) W/cm² at 40 °C. Utilizing the active cooling system results in a 10% enhancement in module efficiency (Jakhrani et al., 2017). In order to get greater efficiency in PV modules, it is necessary to cool the surface of the modules. Effective cooling enhances electrical efficiency, diminishes cell degradation, and prolongs the lifespan of PV modules (Siecker et al., 2017). These methods play

a crucial role in maintaining the optimal temperature of PV modules, ensuring their long-term performance, and maximizing power output. Fig. 2.4 shows the flat plat PV/T collector classification and Fig. 2.5 shows the structures of different PV/T collectors.

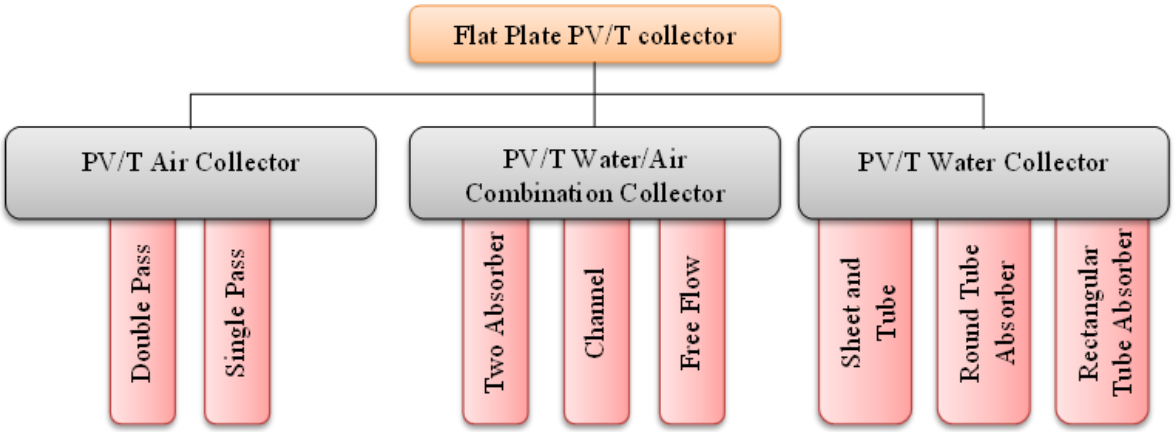

Fig. 2.4. Classification of PV/T collectors (Ibrahim et al., 2011).

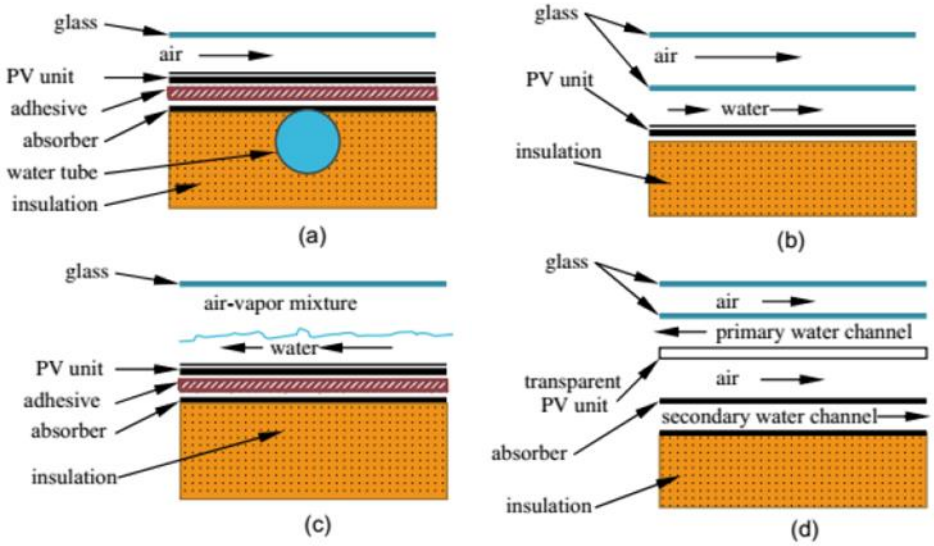

Fig. 2.5. Structure of different types of PV/T collectors (a) sheet-and-tube PV/T, (b) channel PV/T, (c) free-flow PV/T, and (d) two-absorber PV/T (Oner, 2016).

By utilizing PCM, the passive cooling method maximizes heat transfer and enhances the efficiency of PV panels. Furthermore, the use of PV/T systems allows for dual-purpose heating and cooling, making them a more sustainable and efficient option (Kothari et al., 2021)(Palomba et al., 2021)(Kim et al., 2011).

The internal energy of PCMs begins to rise when they are heated. The temperature of the substance approaches the phase transition temperature if its internal energy keeps growing. A consistent temperature is required for phase transition to occur in PCM when heat is continually delivered to it. During a phase transition, latent heat is stored while the material's temperature stays the same. The temperature of the liquid PCM begins to rise upon exposure to heat. Everything stays the same until the temperature at which water evaporates is attained.

Fins are used to lower the average temperature of air-cooled photovoltaic modules. Increasing the air flow rate enhances cooling and PV performance when the ambient temperature is (20-33.4) °C and solar radiation is (895-900) W/m² (Chabane et al., 2014). Passive cooling can be achieved by attaching finned, corrugated, or tubular surfaces to the reverse of PV modules. The efficiency of

the module can be enhanced by connecting PCMs to finned coolers (Singh et al., 2020). The efficiency of the module rises from 5.33 percent to 9.82 percent on finned surfaces, and its performance goes up from 0.63 percent to 0.66 percent, or 4.88 percent, according to (Singh et al., 2020). The system's anticipated heat storage capacity can be achieved with the PCM selected for the PV modules (Hishikawa et al., 2017). The three main types of PCMs are eutectic, organic, and inorganic. The heat storage capacity of inorganic substances is reportedly over double that of biological substances per unit volume (Eslamnezhad and Rahimi, 2017). Photovoltaic and hybrid systems can make use of PCMs. Minimizing efficiency loss is achieved by maintaining the PV system in close proximity to the test conditions. Using PCM in PV allows Mohamet et al. to state that modules can be held at 30 °C (Mohamed et al., 2017).

Research conducted in China's HSCW climate zone focused on the use of PV/T-GCHPs (Photovoltaic/photothermal - Ground-coupled heat pump system) to solve the problem of thermal accumulation in underground soil, which affects the heat pump system's performance (H. Wang et al., 2023). In West Africa, PV/T modules were studied to improve the efficiency of solar PV systems and promote their use in rural areas for electricity and hot water production (TOSSA et al., 2023). Solar drying techniques, including PV/T solar dryers, were explored as a clean and effective method for drying agricultural and industrial products, focusing on energy consumption and efficiency (Agrawal et al., 2023). A numerical analysis of a water-ethylene glycol-based PV/T collector was conducted to understand its dynamic behavior and performance (Soytürk et al., 2022). Another study investigated the energy performance of PV/T systems with and without PCM, showing improved electrical efficiency and thermal performance compared to uncooled PV systems (KB, 2023).

Another study by Gharzi et al. developed a hybrid concentrated photovoltaic/thermal (CPV/T) system using compound parabolic concentrators (CPC) and a combined cooling mechanism involving Nano-PCM and water pipes (Gharzi et al., 2023). Another study by Abdulmouti aimed to develop a passive cooling system for PV panels using air channels and chimneys, which proved to be efficient and cost-effective (Gharzi et al., 2023). Alwesabi et al. researched the performance of PV modules under different water temperatures and dust levels, finding that cooling the modules increased efficiency and reduced dust accumulation (Abdulmouti and EMIRATES, 2022). Aguilar and Celis compared three cooling methods, including water cooling, and found that temperature reductions of up to 7.7% and system efficiencies of up to 17.2% were observed (Alwesabi et al., 2022). These studies highlight the importance of cooling PV modules to enhance their efficiency and extend their lifetime.

As the temperature rises, PV cells become less efficient. Because of the positive effect that temperature variation has on generator conversion efficiency. According to reports, the most efficient technique to boost the system's efficiency is to combine PV with a TEG (Thermoelectric Generator) (Kwan and Wu, 2016). One key component that drastically impacts system efficiency is the amount of solar energy used in hybrid systems.

2.2.4. Design methods and simulation tools for optimizing PV system performance

There are several design methods available for designing PV systems. These methods consider various parameters such as load requirements, PV module size and orientation, availability of sunlight intensity and temperature at the installation site. One commonly used design method is to analyze the relationship between architectural design specifications and PV characteristics.

Another important consideration is the aesthetic integration of PV systems with the building and its surroundings. This aspect is often overlooked but can significantly impact the visual appeal of the PV system.

The Analytical Hierarchy Process is a proven decision-making process that can be used to evaluate and compare different PV module alternatives. It allows for a thorough evaluation of the different

criteria and helps determine the best-suited PV module for a specific installation. In addition to these design methods, numerical design and simulation software are crucial in the PV system design process. With the calculating and parametric tools of numerical design and simulation software, it is possible to analyze energy consumption, daylight intake, solar activities and shade relationships, radiation gain, wind usage, and natural ventilation (Alagöz and Beyhan, 2020). These design methods, along with the use of numerical design and simulation software, allow for an effective and accurate analysis of PV system performance and energy output.

When designing a PV system, it is important to consider several factors such as load requirements, PV module size and orientation, and the availability of sunlight intensity and temperature at the installation site. To optimize the design and performance of PV systems, it is essential to utilize accurate mathematical and simulation modeling (Song et al., 2021). These modeling techniques enable designers to accurately predict the performance of the PV system and determine the most optimal design parameters. In addition, there are various commercially available PV analysis and planning software packages that can aid in predicting the performance of grid-connected PV systems. These software packages, such as PVSYST, RET Screen, TRNSYS, and PVSOL, provide calculative accuracy for simulating and optimizing the performance of a PV system. These software packages allow installers and architects to analyze the energy generation, evaluate the system's economic viability, and optimize the design parameters for maximum efficiency and energy output. PV system design methods involve considering factors such as load requirements, PV module size and orientation, and the availability of sunlight intensity and temperature at the installation site. By utilizing numerical design and simulation software, designers can accurately predict the performance of the PV system and assess its energy output (Ishaque et al., 2011).

2.3. Solar Chimneys

Solar chimneys have been a subject of interest in renewable energy systems for several decades. The concept of a solar chimney dates back to the late 19th century when Spanish engineer Isidoro Cabanyes proposed the idea of using solar heat to generate electricity. However, significant advancements in solar chimney technology only emerged in the late 20th century. A pioneering project in this field was the construction of the Manzanares solar chimney in Spain during the early 1980s. This solar chimney, standing at a height of 195 meters, served as a milestone in the development of solar chimney technology, demonstrating the potential of utilizing solar heat for power generation (Zuo et al., 2012).

2.3.1. Fundamentals, components, and working principle of solar chimney

A solar chimney is a renewable energy system that harnesses solar radiation to create air movement and ventilation within a building or structure (Ahmed et al., 2021). A solar chimney, also known as a solar thermal chimney or solar updraft tower, is a passive ventilation system that harnesses solar energy to create airflow within a building or structure (Ahmed et al., 2021). Solar chimneys operate on the principles of thermodynamics. The basic principle behind a solar chimney is using solar energy to heat air, creating a pressure difference that drives air movement. This pressure difference is created by the temperature difference between the air inside the solar chimney and the ambient air outside (Khan and Singh, 2017). While the efficiency of solar chimneys is approximately 2%, which may initially seem low (Hussain et al., 2021), this technology holds great promise for converting solar energy into electricity and improving energy efficiency in renewable energy systems. The solar chimney consists of three main components: a solar collector, a chimney, and an air outlet vent. The solar collector is usually a transparent glazing or roof that allows sunlight to pass through and heat the air inside. The heated air rises and creates an upward flow, which is directed into the chimney. Inside the chimney, the heated air continues to rise and creates a natural draft. As the heated air exits through the top of the chimney, cooler air is drawn in through the bottom opening, creating a continuous air circulation. This continuous air circulation helps ventilate the building, removing hot air and replacing it with cooler air from

outside. The solar chimney operates on the principle of natural convection, utilizing the temperature difference between the solar-heated air inside the chimney and the cooler ambient air outside to create airflow. The airflow created by the solar chimney can be used for various purposes, such as cooling the building, reducing the need for mechanical ventilation or air conditioning systems, and improving indoor air quality. In addition, the airflow generated by a solar chimney can also be harnessed to generate electricity. Their applications extend beyond power generation and include uses in solar energy drying of crops, fruits, wood, and grains and building ventilation. Researchers and engineers have explored integrating solar chimneys into various contexts, such as low-carbon buildings, to optimize energy usage and reduce reliance on traditional power sources (H. Liu et al., 2021).

2.3.2. Factors influencing the efficiency of solar chimney

The efficiency of solar stacks can be improved by various factors such as collector design, metal pipe geometry, solar radiation intensity, the heat flux density of internal heat sources, external wind speed, and relative location of internal heat sources. The use of metal tubes as solar radiation absorbers in the collector design can increase the temperature and velocity distribution, resulting in higher collector efficiency (Rezaei et al., 2023). The intensity of solar radiation, outdoor wind speed, and heat flux density of indoor heat sources all positively affect the ventilation performance of solar chimneys, and their effects reinforce each other (Yue et al., 2023). Hybrid solar stacks, which combine solar stacks with other renewable or conventional energy systems, have been shown to improve efficiency and offer the potential for further development (Ahmed et al., 2022). The dimensions of the heated cavity and chimney gap also play an important role in the performance of solar chimneys for heating applications (Nguyen and Nguyen, 2021). In addition, the shape and location of obstacles placed on the heated surface of the air duct can affect the local flow and heat transfer characteristics, as well as the solar chimney's rise in temperature and thermal efficiency (Nguyen et al., 2021).

Solar chimneys made of pipes can come in different colors. One study mentions that the solar heating tube can be made into either black, blue, or deep blue without plating it with film (Okada et al., 2015). Another study describes a solar chimney power generation system where the heating pipes are composed of a solar vacuum pipe, and the layers include a steel pipe. However, the color of these pipes is not specified in this study (Okada et al., 2015). Therefore, based on the information provided, the colors of solar chimneys made of pipes can include black, blue, and deep blue.

Previous studies have not explicitly mentioned the colors of solar chimneys made from PVC pipes. However, one study indicates that the top of the synthetic resin tube is colorless and transparent, while the bottom is black (Okada et al., 2015). Another summary indicates that the tubes used to absorb heat can be made of glass or plastic and be darkly colored to improve heat absorption (Okada et al., 2015). Therefore, it can be inferred that the color of the plastic pipes used in solar chimneys can vary, but they may be transparent or dark depending on the system's design and purpose.

Different types and shapes of solar chimneys have also been studied and developed. Chungloo and Limmeechokchai demonstrated the advantages of a house set up with a solar chimney installed on the south roof and a cool metal ceiling installed on the north roof (Lei et al., 2016). Wei et al studied a series of solar chimneys comprising a slanted section on the roof and a vertical section near the south wall in a typical two-story house (Belhadj et al., 2021). They examined the effect of various parameters such as the length and total width of the chimney, inclination angle of the second-floor entrance, length ratio of vertical section to inclined section, and inclination angle of the chimney on ventilation performance. Similarly, Saifi et al. developed an experimental and numerical study for a tilted solar chimney, investigating the influence of chimney width and angle of inclination on airspeeds (Laurini et al., 2018). Different geometries of solar chimneys have been

studied to optimize their thermal efficiency and flow rate (Belhadj et al., 2021). In recent years, scholars have conducted studies on the architectural design of solar chimneys (Lin and Lei, 2022).

Some researchers have explored modifications of the basic 2D geometry of solar chimneys to improve their functionality at different times of the day (Mehranfar et al., 2022). These studies aimed to exploit the design features of solar chimneys that operate more efficiently in the morning and afternoon, with a lesser performance at noon in June. The studies mentioned above have shown that different types and shapes of solar chimneys can have varying performance and efficiency depending on factors such as inclination angle, width and length of the chimney, placement on the roof, and other design parameters (Belhadj et al., 2021). This research indicates that solar chimneys come in various types and shapes, including inclined chimneys, chimneys with slanted sections on the roof, and chimneys with vertical sections near the walls (Davidsson et al., 2013). These variations allow for customization and optimization of solar chimneys according to specific climate conditions, latitude, and desired ventilation performance.

Therefore, it can be concluded that solar chimneys have different types and shapes that can be adjusted to optimize their performance for specific conditions and desired ventilation outcomes and the width and inclination angle of solar chimneys affect factors such as airflow rate, airspeeds within the chimney, and overall ventilation effectiveness. The length ratio of the vertical section to the inclined section and the inclination angle of the chimney also plays a role in determining ventilation performance. Additionally, the height and width of the solar chimney are also found to impact the induced air volume (Chen et al., 2021).

Tan and Wong (Tan and Wong, 2013) explained the effect of the solar chimney's stack height, depth, width and inlet position on the interior performance and proposes an optimal tropical solar chimney design. According to the four parameters (height, depth, width, and inlet position), as input parameters and physical and computational models have been developed, 300 cases of employing the solar chimney in the tropics are generated, of which 139 cases are simulated. All simulations showed that the output air temperature of the chimney remains constant. Also, the results showed that the solar chimney's width was the most significant factor influencing the output air speed. The solar chimney's length to hydraulic diameter should be greater than 15 to ensure developed flow, and the solar chimney's stack height to width should be less than seven if airflow within the solar chimney is to be two-dimensional. The chimney position had limited influence on the output airspeed. However, the region near the solar chimney's inlet shows an increase in airspeed but is damped when the airspeed is averaged across the plane. Ghaffari and Mehdipour (Ghaffari and Mehdipour, 2015) are improved and modeled solar dryer integrated with a solar chimney using computational fluid dynamics. The chimney model was a part of this study, and based on the kinetic energy balance for a chimney element with a length of (dy) and the distance of (y) from the chimney's inlet, the outlet air temperature of the chimney equation was obtained as follows:

$$T_{out-SC,L} = T_a + (T_{in-SC} - T_a)\, exp\hat{}(((-\pi\, D_{SC}\, L_{SC}\ h) / (\dot{m}\, C_p))) \qquad (2.1)$$

Where $T_{in\text{-}sc,L}$ and $T_{out\text{-}sc,L}$ are the chimney inlet and outlet air temperatures respectively, D_{sc} and L_{sc} is the chimney's diameter and length respectively, h is the chimney's convective heat transfer coefficient of air inside the solar chimney, T_a is the ambient temperature, $\dot{m}$ is the air mass flow rate.

2.3.3. The design methods of solar chimney systems

Solar chimney design, mathematical modeling and simulation methods have been examined in several studies. Hmood and Amori performed a numerical analysis using CFD to predict a solar chimney's thermal performance and airflow (Amori and Hmood, 2013). Ravanfar developed a thermal model implemented in SIMULINK to simulate the thermal response of a solar chimney-

integrated solarium (Ravanfar, 2013). Proposed by Tlatelpa-Becerro et al. A strategy for building a reference model for solar chimney design using dynamic simulation and artificial neural networks (Ravanfar, 2013). Use Sharbaf et al. Numerical simulation by using MATLAB to study four physical models of solar chimneys and choose the best model for a specific location (Tlatelpa-Becerro et al., 2022). These studies provide insights into the design and optimization of solar chimneys, considering factors such as geometry, materials and performance specifications.

Layeni et al. discuss the computational analysis and sensitivity analysis of a solar chimney system for buildings using ANSYS Fluent CFD package and Design Expert statistical package (Layeni et al., 2021). W. Li et al review five energy evaluation methods for solar chimneys, including mathematical modeling and simulation (W. Li et al., 2021). Huynh & Nguyen discuss the use of numerical simulation, specifically CFD, to investigate the effects of different computational domains on the performance of a solar chimney for the natural ventilation of buildings (Huynh and Nguyen, 2021). According to Kong's research, a two-dimensional model of an inclined solar chimney was developed and numerically simulated for various inclination angles (Lin and Lei, 2022). The optimal inclination angle of the solar chimney was found to vary from 45° to 60° depending on the latitude and season of operation. The processes of heat transfer and efficiency of natural ventilation driven by a solar chimney have been extensively studied (Lahcene et al., 2020). Researchers have developed mathematical models and conducted simulations to estimate and optimize the design of solar chimneys (Sakhri et al., 2021).

These models consider various parameters such as the size of the solar chimney, air flow rate and temperature, air gap between glazing and absorber surface, air inlet and exit elevation, and the effect of insolation rate and ambient air temperature. Furthermore, researchers have investigated the impact of geometric and operational parameters such as incident solar radiation, wind speed, and ambient temperature on the performance of solar chimneys. Mathematical and simulation modeling have been used to analyze the performance of solar chimneys in terms of natural ventilation and heat transfer. These studies have shown that solar chimneys can increase air mass flow rate by up to 50% in conditions of high solar intensity and low wind speed. Furthermore, the design of solar chimneys for natural ventilation is still an area of uncertainty, as there is limited knowledge on determining the optimal parameters for efficient and effective solar chimney design (Li et al., 2004). To address this, researchers have conducted theoretical and experimental studies to evaluate the size and design parameters of solar chimneys.

They have also conducted numerical investigations to determine the best inclination angle, which has been found to be between 45° and 60°. In summary, designing solar chimneys for natural ventilation involves mathematical and simulation modeling to analyze heat transfer, efficiency, and airflow. These modeling methods consider parameters such as chimney size, airflow and temperature, insulation rate, and ambient air temperature. By using these modeling methods, researchers have optimized the design of solar chimneys and improved their performance in terms of natural ventilation and heat transfer.

2.4. Solar Air Collector

2.4.1. Fundamentals of solar air collector

Solar air collector (SAC) is equipment that make use of solar energy to heat the air. It is made up of a number of different components, including solar collectors, the heat collecting sheets, ducts for air, fans, and components that release heat. The solar collector is responsible for heating the air, which is then converted into heat energy. This is the operating principle behind the solar collector. The hot air is then supplied with air through air supply ports or hot air outlets, and it is then circulated through air ducts before being released into the intended space. Through the design of flow channels, such as concentric square form channels for flow or S-shaped air ducts, which allow for better contact between air and heat absorption plates, the efficiency of heat exchange can

be improved. The effectiveness of SAC in terms of heat collection is further improved by the utilization of selective absorption layers, discharge cavities, and heat accumulation layers (Rahl, 2015)(Dutkowski et al., 2023).

In the field of air heating, SAC is an indispensable instrument, solidifying its place as a well-liked solar collector across a wide range of applications. The bags typically comprise of a box made of wood or metal that has been insulated with appropriate materials, a cover that is flat and transparent so that sunlight may pass through it, and heat-absorbing surfaces that are designed to gather solar energy. The efficiency of the solar absorbing capacitor (SAC) is contingent on its capacity to transfer as much heat as feasible from the solar radiation that it has absorbed to the working fluid (Debnath et al., 2018)(Salih et al., 2019). On the other hand, conventional SAC typically encounters challenges as a result of the limited efficiency of the heat exchange process that occurs between the absorption surface and the air that is circulating there. Because of this, the temperature of the absorber plate increased, which led to an increase in the amount of heat that was lost and, eventually, a decrease in the total thermal efficiency. SAC has an intrinsic limitation since air has a very low specific heat, which is approximately one-fourth of the capacity of water. it is the reason why SAC are not as effective as water. The thermal efficiency of these systems is directly impacted by this disparity, as evidenced by references (Mund et al., 2021)(Razak et al., 2016).

2.4.1. Factors influencing the efficiency of solar air collectors

There are a number of factors that can influence the efficiency of SAC. These include the type of fluid that is utilized, the arrangement and orientation of the collector itself, the presence of fixed fins or artificial roughness on the absorber plate, and the design of the collector itself (Dutkowski et al., 2023). The collector is classified as either a liquid or an air collector, depending on the type of fluid that is implemented. The arrangement and orientation of the collector can have an effect on its efficiency, whereas a vertical configuration does not necessarily ensure the highest possible efficiency (GÜLÇİMEN et al., 2023). When used in a flow setting, fixed fins have the ability to expand the flow channel and promote heat transfer. Additionally, the efficiency of the system improves as the fin angles decrease (Dhaundiyal, 2023). It is possible for the installation of wooden barriers below absorption panels to have an impact on the rates of entropy creation and energy destruction (Sharma and Chauhan, 2023). It is also possible for other artificial roughness geometries, such as arc ribs and V-shaped ribs, to have an impact on the effective efficiency of the collector. Variations in their performance can be detected across a variety of Reynolds number ranges (Alomar et al., 2022). In addition, it has been demonstrated that the utilization of a modified V-shaped corrugated absorber panel can improve the thermal efficiency of SAC with regard to their performance.

It is vital to improve thermal energy transfer in solar air collectors to improve their thermal performance and overall efficiency by increasing their efficiency. Researchers have been rigorously exploring ways to increase the thermal performance of these collectors, with a particular focus on novel design adjustments to the absorption surface, which is an essential component of the system. The goal of these modifications is to improve the thermal efficiency of collection systems. It is possible for this plate to have a surface that is smooth, wavy, or finned.

Akpinar et al. (Akpinar and Koçyiğit, 2010) carried out exhaustive experimental research on a specific SAC, during which they investigated three distinct obstacle configurations in addition to a situation in which there were no obstacles. Following the meticulous evaluation of the heat leakage coefficients, thermal gain factors, and efficiency of these various configurations, they proceeded to conduct an in-depth comparison analysis. According to their findings, the solar radiation density, absorber plate construction, and air path length all have a major impact on the efficiency of the collector. In addition, they found that the efficiency of the system improved when the airflow velocities and temperature gradients were increased. This finding suggests that greater temperature differences result in a reduction in the overall losses.

2.4.1. The design methods of solar air collectors

There are both practical and software approaches that can be utilized in the design of SAC systems. It is necessary to conduct process characterization studies and experimental tests in order to validate the design while using the practical design approach. As an illustration, Tiendrebeogo et al. developed a SAC that utilized forced convection and validated it through the use of simulations and experimental tests (Tiendrebeogo et al., 2022). The multiple input multiple output design is yet another useful design technique that takes into consideration unknown factors and thermal balancing calculations. The multiple input multiple output design was utilized by Nnamchi et al. in order to construct a SAC and enhance its performance (Nnamchi et al., 2020). Alternatively, software approaches include simulations and numerical analysis as part of their methodology. A corrugated SAC was designed and tested by Mehta et al. using simulations, and the performance of the corrugated collector was compared to that of a flat plate collector (Mehta et al., 2020). The performance of a finned single-pass air-type photovoltaic/thermal solar collector was investigated by Khalili et al. (Khalili et al., 2020) through the use of both theoretical analysis and experimental research. As established by Nassab (Gandjalikhan Nassab, 2024), CFD analysis and numerical simulations are two methods that can be utilized to enhance the performance of SAC mechanisms.

An investigation into SAC designs was carried out by Parag et al. (Bezbaruah et al., 2020) through the completion of analytical research using Ansys Fluent 18.0. They concentrated on developing a one-of-a-kind design that had a finned absorption plate that encouraged spiral airflow. The research concluded that the formation of localized vortices and vortices in this spiral flow pattern results in an increase in the rate of heat transfer. Having said that, it also raises the frictional resistance, which ultimately leads to a decrease in pressure.

2.5. Soil Properties and Heat Transfer

2.5.1. Thermo-Physical properties of soil

Soil thermo-physical properties are crucial in understanding heat transfer mechanisms within the soil. These properties encompass thermal conductivity, heat capacity, and density. Thermal conductivity measures a material's ability to conduct heat and influences the heat transfer rate in soil. Heat capacity, conversely, dictates the soil's capacity to store and release heat. Density, the third thermo-physical property, refers to mass per unit volume.

The influence of various soil properties, including moisture content, porosity, and composition, on thermal conductivity and heat capacity has been well-documented (Liu et al., 2003). Accurate measurement and estimation of these properties are essential for a wide range of energy applications and agricultural practices. Researchers have developed analytical and numerical models to predict heat transfer through geomaterials, with a focus on estimating soil thermo-physical properties (Abuel-Naga et al., 2015). Additionally, obtaining site-specific values for soil thermal conductivity is emphasized to ensure precise heat transfer predictions (Aguilar et al., 2018). Soil moisture's impact on thermo-physical properties has been studied across different soil types, including pure sand, clay, and bentonite-sand mixtures (Cuny et al., 2018). For instance, Yin and Arp calculated soil thermal conductivity based on bulk density and volumetric water content (Liu et al., 2003). In conclusion, comprehending and accurately measuring soil thermo-physical properties are vital for energy applications and agriculture. Researchers continue to explore these properties to enhance our understanding of heat transfer in soils (Abuel-Naga et al., 2015).

2.5.2. Soil temperature gradients

Soil temperature gradients are significant for ecological processes and have implications for ecosystem functioning. Various factors, such as soil moisture, climate conditions, land use, and topography, affect these gradients.

In mountainous forest ecosystems, topography and elevation differences result in variations in soil temperature gradients (Kukreti et al., 2023). The slope aspect and gradient also influence solar radiation and subsequently affect soil temperature. Research often combines terrain factors, such as aspect, slope, and elevation, to characterize complex terrain (Qi and Li, 2022).

Understanding soil temperature gradients is crucial for ground-source heat exchange, a sustainable method for heating and cooling buildings using the stable ground temperature. Researchers have examined soil temperature variations across different climate conditions to gauge their implications. For example, they found that south-facing slopes receive more solar radiation and have higher soil temperatures compared to north-facing slopes. Climate conditions, including temperature and precipitation, significantly impact soil temperature variations. In regions with higher temperatures and lower precipitation, soil temperatures tend to be higher due to increased solar radiation and reduced soil moisture (Höfle et al., 2000).

Slope position also plays a role, with higher positions on slopes having lower soil temperatures due to reduced solar radiation exposure and increased water movement (Valley et al., 2020). Factors influencing soil temperature gradients are multifaceted, including topography, climate conditions, and human-induced factors like land use and management practices. Considering these factors is essential when studying soil temperature variations and their implications for ground-source heat exchange (D. Wang et al., 2023).

2.5.3. Effect of soil thermo-physical properties on the performance of EAHE system

The thermal performance of an EAHE prominently depends on the thermo-physical properties of the soil. Among all thermo-physical properties, the performance of EAHE is profoundly influenced by soil thermal conductivity, specific heat capacity, and density. These three soil properties can be expressed in terms of thermal diffusivity as:

$$\alpha = k_{soil} / (C_{p,soil}\, \rho_{soil}) \qquad (2.2)$$

A soil's thermal diffusivity is, thus, crucial when considering EAHE. Soil thermal diffusivity should be very high since heat builds up in the layers closest to the pipe and doesn't move quickly enough to the next layers, leading to thermal saturation and a decline in EAHE performance.

In their study, Mathur et al. (Mathur Srivastava Mathur et al., 2015) took three soil thermal diffusivities into account while evaluating EAHE's thermal performance: 1.37×10-7 m^2/s, 4.37×10-7 m^2/s, and 9.69×10-7 m^2/s. Research shows that soils with higher thermal diffusivity can move heat more rapidly from the surrounding soil to the outer subsoil.

Soil thermal conductivity is a vital attribute for EAHE because it mostly determines the heat transfer in these types of systems. Dry density, saturation level, particle size, packing geometry, and mineralogy of the soil are the primary determinants of its thermal conductivity (Gow and Langston, 1977). (i) Compositional factors and (ii) Environmental factors are the two main categories into which these elements fall. Soil mineral components, particle size, grading, and form are all aspects of soil composition. The arrangement of soil particles is determined by their shape and size. This, in turn, influences the soil heat conductivity and determines the soil structure or packing. Quartz, among soil minerals, has a better thermal conductivity, coming in at about 7.9 W/m K. Consequently, for optimal heat transfer rates, soils with a higher quartz concentration are preferred (Zhang and Wang, 2017).

Temperature, moisture, and density are some of the environmental variables that affect soil thermal conductivity. Wet soil has a greater heat conductivity than dry soil (Misra et al., 1995). As the density of the soil rises, the physical contact area between its particles grows, making it more thermally conductive (Abu-Hamdeh and Reeder, 2000). Soil thermal conductivity also rises as soil temperature raises (Smits et al., 2013). The impact of soil and pipe heat conductivity on EAHE performance was studied by Song et al. (Song et al., 2006). Findings showed a 100.8%

improvement in heat transfer capacity at a soil thermal conductivity level of 2.5 W/m K, up from 1.1 W/m K.

2.5.3.1.Soil moisture contents

The soil's thermal conductivity is largely affected by its moisture level. Soil heat flow and thermal conductivity are both improved when thin water films fill in the spaces between soil particles, increasing the contact area. Soil thermal conductivity stops increasing after a specific moisture content because all the pores in the soil have been filled. It is the crucial moisture content that determines the maximal thermal conductivity. Packs of the same sand saturated with water had a thermal conductivity six to eight times higher than packs of the same sand saturated with air (Misra et al., 1995).

Soil thermal conductivity with respect to moisture content fluctuation can be predicted using a number of different models. Taking into account the impacts of water content, saturation level, porosity, pressure, and temperature, Tong et al. (Tong et al., 2009) established a model for computing the thermal conductivity of soil. Which is expressed as:

$$k = \eta_1(1-\phi)k_s + (1-\eta_2)[1-\eta_1(1-\phi)]^2 \times \left[\frac{(1-\phi)(1-\eta_1)}{k_s} + \frac{\phi S_r}{k_w} + \frac{\phi(1-S_r)}{k_g}\right]^{-1} + \eta_2\left[(1-\phi)(1-\eta_1)k_s + \phi S_r k_w + \phi(1-S_r)k_g\right] \quad (2.2)$$

Eq. (2.2) presented the relationship between the thermal conductivities of solids (k_s), water (k_w), and gas (k_g), soil porosity (ϕ), and the pore structure of a solid/gas mixture (η_1): [0<$\eta_1(\phi)$<1], and η_2 is the function of saturation degree (Sr) and temperature ([0<$\eta_2(\phi,Sr,T)$<1].

Similarly, Haigh (Haigh, 2012)(Wang et al., 2020) developed a theoretical model for the thermal conductivity of sands. He considered heat conduction among the soil, solid, water, and air. The model is given as:

$$k = \eta_1(1-\phi)k_s + (1-\eta_2)[1-\eta_1(1-\phi)]^2 \times \left[\frac{(1-\phi)(1-\eta_1)}{k_s} + \frac{\phi S_r}{k_w} + \frac{\phi(1-S_r)}{k_g}\right]^{-1} + \eta_2\left[(1-\phi)(1-\eta_1)k_s + \phi S_r k_w + \phi(1-S_r)k_g\right] \quad (2.3)$$

(2.2

Where k and k_s are the thermal conductivity of soil and solid, respectively, and x are the coefficients for the thickness of water film and degree of saturation, α_w= k_w/k_s and α_a= k_a/k_s.

Kersten (Williams, 1991) introduced an empirical relation to determining the thermal conductivity of soils by considering nineteen different soil types. The mathematical expressions of the model are:

$$k = 0.1442[0.9\log\ w - 0.2] \times 10^{0.6243}\gamma_d \text{ (for slits or clay)} \quad (2.4) \quad (2.2)$$

$$k = 0.1442[0.7\log w + 0.4] \times 10^{0.6243\gamma_d} \text{ (for sandy soils)} \quad (2.5)$$

Where k is the thermal conductivity of soils, *w* is the soil moisture content, %; Y_d is the density of dry soil (kg/m^3).

Johansen (Johansen, 1977) also presented an empirical relation for the thermal conductivity of soil, which can be expressed as:

$$k = \left(k_w^n\, k_s^{1-n} - \frac{0.137\rho_d + 64.7}{2650 - 0.947\rho_d}\right)k_r + \frac{0.137\rho_d + 64.7}{2650 - 0.947\rho_d} \quad (2.6)$$

Where k_w and k_s are the thermal conductivities of water and solid, respectively, *n* is the porosity and ρ_a is the density of dry soil, *k*, is the normalized thermal conductivity called "Kersten number".

$$k_r = 0.7 \log (S_r) + 1 \text{ (For median and fine sands)} \quad (2.7)$$

$$k_r = \log (S_r) + 1 \text{ (For fine soils)} \quad (2.8)$$

$$k_r = S_r + 1 \text{ (For frozen fine sand and fine soils)} \quad (2.9)$$

Where: the S_r is the degree of saturation.

Chen (Chen, 2008) presented a model based on a laboratory test to determine the thermal conductivity of quartz sand, and it is expressed as:

$$k = k_{\mathrm{w}}^{n} k_{\mathrm{s}}^{1-n} [(1-b)S_r + b]^{cn} \quad (2.10)$$

Where b and c are empirical coefficients, and for quartz sand, they are values 0.0022 and 0.78, respectively.

Because of heat and moisture flow phenomenon in soil, the earth surrounding the EAHE pipe dries out as the pipe cools (Mei, 1987). An increase in thermal resistance and a subsequent decrease in thermal capacitance are the outcomes of soil drying out near the EAHE pipe. For the composite climate of Delhi (India), Sodha et al. (Sodha et al., 1990) studied the pipe length requirements in cooling mode with different surface treatments. They found that a lengthy tunnel was necessary to satisfy the cooling load needs of a dry sunny surface, but a short one was sufficient for a wet shaded surface. Just a 150-meter-long pipe buried 4 meters below a dry, sunny surface (the usual surface condition) was enough to achieve the cooling load, which supplied air at a speed of 3 meters per second. For dry, shady, and moist shaded ground surfaces, the pipe length might be 105 m, 78 m, and 70 m, respectively.

The thermal and moisture behaviors of dry and wet soils heated by buried capillary plaits were investigated experimentally by Balghouthi et al. (Balghouthi et al., 2005). The thermal diffusivity of moist soil was determined to be greater than that of dry soil. Based on their model, Mihalakakou et al. (Mihalakakou et al., 1994) determined that in an EAHE system, moisture and heat transport gradients along axial and radial directions promote energy transfer inside the soil. The performance of dry soil EAHE was compared to that of wet soil EAHE using two similar experimental settings created by Agrawal et al. (Agrawal Misra et al., 2018). The researchers found that the wet system had a 24.1% increase in average heat transfer rate and a 24.0% improvement in COP over the dry system.

2.5.3.2.Soil density

Soil thermal conductivity grows as soil density rises. The thermal conductivity of soil can be improved by increasing its mass density, which is the weight of soil per unit volume. This is because, as the volume of soil particles increases, their contact area grows, creating a larger pathway for heat to travel through the soil (Abu-Hamdeh and Reeder, 2000). For a modest laboratory-scale EAHE system consisting of 1.5 m of copper pipe with an inner diameter of 1.5 cm, Elminshawy et al. (Elminshawy et al., 2017) examined three separate soil compaction levels, each with its own relative density, void ratio, and porosity. Results showed that when soil compaction level increases, air temperature drops and EAHE system performance improves, according to the controlled conditions of the trials.

2.5.3.3. Soil mineral composition

There is a correlation between the mineral makeup of soil and its thermal conductivity; for example, sand with a high quartz content is more thermally conductive than sands with high pyroxene, plagioclase, or feldspar contents (Vieira et al., 2017). Soil heat conductivity is poor in

organically rich soils, according to research by Abu-Hamdeh and Reederb (Abu-Hamdeh and Reeder, 2000).

2.5.3.4.Soil texture and particle shapes

The form and texture of soil particles also affect the soil's heat conductivity. Soils with angular grains and coarse textures have a higher heat conductivity than those with fine grains and fine textures, for the same soil moisture content and unit weight (Abu-Hamdeh, 2003). Because silt has a higher thermal conductivity than loam and clay, Shojaee and Malek (Shojaee and Malek, 2017) found that silt soil resulted in the largest energy savings when compared to the other two types of soil. Round (spherical) and angular sand particles were contrasted by Jackson (Yu et al., 2022). He made the interesting observation that interparticle heat conduction is enhanced in sand composed of angular particles with a higher contact area.

2.6. Combination of Earth-Air Heat Exchanger and Solar chimney for PV Efficiency

Integrating an EAHE with a PV module in combination with a SC can improve the efficiency of the PV module. The integration of the EAHE provides a heat sink and allows for better harvesting of solar radiation, resulting in increased energy production (Alkaragoly et al., 2022). The solar chimney and EAHE system combination also provides fresh air and cooling capacity without any electricity consumption (Alkaragoly et al., 2022).

There has been a lot of interest about SC and EAHE's passive heating and cooling systems recently. One natural passive approach to controlling the indoor climate is a SC system, which converts solar energy into buoyancy effects that push airflow via an air duct (Liu and Li, 2015)(Li et al., 2017). An EAHE is a subterranean conduit that carries air into a building. The ground can be utilized as either a heat source in the winter or a heat sink in the summer due to its practically constant temperature at a particular depth throughout the year (Samuel et al., 2013).

The efficiency of a hybrid system that incorporates both a SC and an EAHE has been the subject of numerous analyses. An experimental investigation on a novel passive air conditioning system that combined SC with an EAHE was conducted by Li et al. (Li et al., 2014) at the University of Nebraska in the US. By combining the EAHE and SC systems, this technology can reduce peak summer electricity consumption and conserve energy in the building industry. At a test facility, trials were conducted over the summer to evaluate the system's functionality. Findings showed that the integrated system can keep interior thermal environmental comfort within the range needed to satisfy ASHRAE thermal comfort standards. For their study, Li et al. (Y. Li et al., 2021) utilized a full-scale experimental test rig to examine how well a SC-EAHE ventilated and cooled on a normal sunny summer day. The research took place in the hot and cold climate of Tongling City, Anhui Province, China. Evidence from experiments suggests that the buoyant driving force generated by the SC system can facilitate the air flow in the EAHE system during the day. Experimental findings indicate that a building's thermal mass in conjunction with its SC provides a continual natural ventilation system. According to the results, the air quality at the entrance of the EAHE system was unaffected by the fluctuating ambient air quality.

In order to improve the passive cooling and natural ventilation in a solar house, Maerefat and Haghighi (Maerefat and Haghighi, 2010) investigated numerically and analytically low energy consumption methods that combine an earth-air heat exchanger (SC-EAHE) with a solar chimney. The findings of this study suggest that this technology can be used to achieve the necessary thermal comfort conditions in hot weather, in addition to the potential for energy savings and environmental friendliness. Another study by Haghighi and Maerefat (Haghighi and Maerefat, 2015) used numerical analysis to determine building heating needs with adaptive thermal comfort parameters by creating a hybrid system that incorporates both a SC and an EAHE. This study's thermal comfort research demonstrated that the solar chimney can run the subsurface heating system for a few hours on bright days, even when the ambient temperature is low and the heating

demand is high. Former coworkers of Li's in the first study, Yu et al. (Yu et al., 2014), also performed experiments on the identical system in the second study (Study (Li et al., 2014)). An American testing center in Nebraska monitored the system's active and passive cooling capabilities throughout the summer. When operating regularly, the results show that the test facility may be sufficiently cooled by the geothermal system, which includes a SC and an EAHE. In terms of thermal comfort, the results demonstrate that the natural airflow stage's interior air conditions are more bearable than the forced airflow stage's, based on the average expected rating and the projected percentage of unsatisfied people. Experimental and numerical investigations were conducted into a hybrid system that Serageldin et al. (Serageldin et al., 2018)(Serageldin et al., 2020) developed, which comprised of an EAHE and a SC. The study's experimental work involved installing the SC and the EAHE in a tiny wooden room at the Egyptian-Japanese University of Science and Technology in Alexandria, Egypt. The results demonstrated a high degree of concordance between the experimental and simulated outcomes. The study demonstrated (Serageldin et al., 2018) that alterations to the system components' dimensions of design parameters have a substantial effect on the outcomes. During the summer, the air temperature within a building is often lower than the air temperature outside, according to a study (Serageldin et al., 2020).

One study has analyzed the performance of a hybrid system that combines a PV and an EAHE. The study by Yildiz et al. (Yildiz et al., 2011) presented the experimental results of a PV-assisted EAHE by equipping it with the necessary electricity to operate the equipment needed to circulate the air inside the EAHE used for greenhouse cooling in Turkey. The system was successfully operated during the 2010 summer cooling season, and the practical performance of the system was examined. The paper discussed the results and their implications for various performance metrics, such as the impact of climatic and operational conditions on system performance. The results indicate that the system can be effectively used for greenhouse cooling in Turkey's Mediterranean and Aegean regions. Therefore, this study did not study the cooling of PV when integrated with the EAHE, but the panels generated electricity to operate the exchanger.

Fig. 2.6 shows some research results on the cooling and ventilation of buildings using SC, PV panels, and EAHE (SC-PV-EAHE). A building in Borge Alarb, Alexandria, Egypt, was cooled and ventilated experimentally by Elghamry and Hassan (Elghamry and Hassan, 2020) using a mix of SC and EAHE. Power generation is achieved by installing a photovoltaic (PV) module behind the chimney and comparing its efficiency to that of a comparable module located outside the room. This study evaluated the effects of both natural and artificial airflow within the geothermal system's tube, as well as chimneys and PV panels oriented south at 30° and 45° horizontal angles. The data shows that the system can reduce the room temperature below the ambient air temperature and has a high daily air change rate. At a 30° angle, the chimney system's natural geothermal air pipe releases the least quantity of air for ventilation, while at a 45° angle, a room releases the most heat for the day. To achieve natural ventilation, thermal comfort, and electricity generation in buildings, Alkaragoly et al. quantitatively devised a hybrid system that integrates SC, PV panels, and EAHE. This research did not use an EAHE to cool the PV panels. In spite of this, the suggested system provided thermal comfort while meeting the building's cooling need of 116 W-1500 W and producing enough power to cover the majority of electrical demands (Alkaragoly et al., 2022).

Based on previous studies, it has been shown that few studies have been conducted on the combination of SC and EAHE (SC-EAHE) (Maerefat and Haghighi, 2010)(Haghighi and Maerefat, 2015)(Yu et al., 2014)(Serageldin et al., 2020)(Serageldin et al., 2018)(Li et al., 2014)(Y. Li et al., 2021) or PV and EAHE (Yildiz et al., 2011), and only two studies have been conducted on cooling and ventilation of buildings with three systems, it consists of SC, PV panels, and EAHE (SC-PV-EAHE), one of them is experimentally (Elghamry and Hassan, 2020) and the second numerically (Alkaragoly et al., 2022).

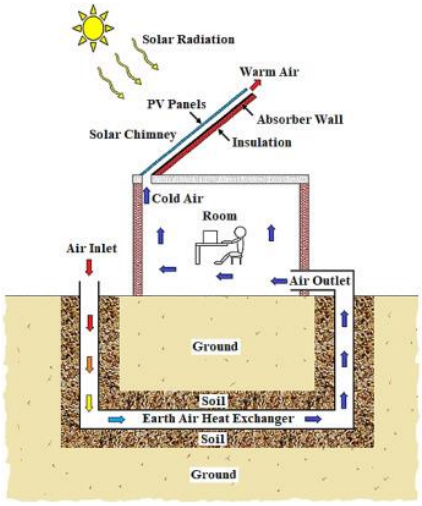

Fig. 2.6. Schematic diagram of the proposed system by Alkaragoly et al. (Alkaragoly et al., 2022).

2.7. MATLAB Simulation in Renewable Energy Research

2.7.1. Matlab simulation models for renewable energy systems

Simulation modeling is a cornerstone of renewable energy research, enabling researchers to predict and optimize the performance of various renewable energy systems and components. In this section, we delve into the prominent role of MATLAB as a versatile and powerful tool for designing and simulating renewable energy technologies. MATLAB, short for MATrix LABoratory, is a widely embraced platform in renewable energy research. Its rich toolkit facilitates the development of accurate simulation models that mirror the behavior and efficiency of renewable energy systems. Furthermore, MATLAB provides a suite of robust tools and functions that prove instrumental in analyzing and optimizing renewable energy systems.

Applications of MATLAB:

1. Earth-Air Heat Exchangers: MATLAB is a favored choice for modeling EAHE, a technology that taps into the earth's stable temperature to provide heating and cooling. Researchers employ MATLAB to simulate the intricate heat transfer processes within these systems. The result is the ability to predict and enhance their performance under various environmental conditions (Bihari and Sadhu, 2022).
2. Solar Chimneys: Solar chimneys, which harness solar energy to induce air circulation, are another domain where MATLAB finds its utility. Researchers use MATLAB to model heat transfer and fluid flow phenomena within solar chimneys, gaining insights into their efficiency and performance (Farooq et al., 2015).
3. PV Modules: Photovoltaic (PV) modules are pivotal in renewable energy systems. MATLAB simulation models account for crucial factors like solar radiation, temperature, and electrical characteristics. This approach enables precise predictions of PV module energy output, thereby supporting system optimization (Bihari and Sadhu, 2022).

Advantages of MATLAB:

MATLAB simulations offer a plethora of advantages:

- Versatility: MATLAB's flexibility allows for tailoring simulation models to represent the behavior of renewable energy systems accurately. This adaptability is invaluable for exploring diverse operating conditions and optimizing system performance.
- Integration of variables and parameters: Researchers can integrate multiple variables and parameters, facilitating investigations into the influence of various factors on system

performance. This capability empowers informed decision-making concerning system design and operation.
- Resource efficiency: MATLAB simulations eliminate the need for extensive physical testing, thus conserving time and resources.

Limitations of MATLAB:

Despite its merits, MATLAB simulations do have limitations, notably:

- Accuracy Dependency: The accuracy of MATLAB simulations hinges on the precision of underlying mathematical models and assumptions. Deviations from real-world complexities and uncertainties may occur.
- Computational Resources: Resource-intensive computational demands arise with complex MATLAB models, particularly when simulating large-scale renewable energy systems or conducting extensive parameter sensitivity analyses.
- Data Challenges: The availability and quality of data, such as solar radiation, wind velocities, and electricity costs, can pose challenges in achieving realistic simulations.

In sum, MATLAB emerges as a formidable modeling tool in the domain of renewable energy research. Its applications span from EAHE and SC to PV modules. The versatility, parameter integration capabilities, and resource efficiency offered by MATLAB simulations make it an indispensable asset for researchers seeking to understand, optimize, and innovate in the field of renewable energy systems.

2.7.2. Validation and sensitivity analysis

In the context of rapidly evolving renewable energy technologies, precise weather forecasts are imperative for effective energy production. This section delves into the pivotal roles of model validation and sensitivity analysis in ensuring accurate renewable energy forecasts.

Model validation is the linchpin in renewable energy research, guaranteeing the credibility and reliability of forecasting models. This critical process involves comparing model predictions with observed data to assess accuracy and dependability. Accurate forecasts are fundamental for the successful integration of renewable energy sources into the grid (Ren et al., 2015)(Ren et al., 2014). Sensitivity analysis is another indispensable tool for evaluating forecasting models in renewable energy research. This method explores how changes in input variables affect model outputs. By conducting sensitivity analysis, researchers can identify the key factors influencing forecasting model accuracy and understand the model's overall behavior concerning inputs. The practical implications of model validation and sensitivity analysis cannot be overstated. Inaccurate forecasts can lead to suboptimal energy utilization and inefficient resource allocation. Real-world examples, like the study by Smith et al. that validated a solar power forecasting model, underscore the significance of these processes (Smith et al., 2019).

In summary, model validation and sensitivity analysis are indispensable in the realm of renewable energy research. These processes guarantee the accuracy and reliability of forecasts, ensuring the optimal integration of renewable energy sources into our ever-evolving energy landscape.

2.8. Summary of Literature Review

An extensive literature analysis was provided in the aforementioned works, which examined the effects on performance and energy efficiency of integrating EAHE, PV modules, and SC systems. Multiple primary sections, each addressing a different facet of the research, made up the literature review.

It was done to Identify the basics, components, and working principles of the EAHE. The differences and methods of installing EAHE were then delved into, highlighting the various

approaches to implementing this technology. In addition, it addressed the operating modes and design considerations of EAHE and explored the mathematical models and simulation studies that have contributed to understanding their performance. The basics of PV modules and the factors affecting their efficiency were also discussed. Previous research efforts aimed at enhancing the efficiency of PV modules were also reviewed, focusing on design methods and simulation tools that played a crucial role in improving the performance of the PV system. The basics, components, and working principles of SC have been explained. The factors affecting SC efficiency were further analyzed, and the different design approaches used in SC systems were explored. Emphasis was placed on soil properties and heat transfer, and soil temperature gradients and the influence of soil thermo-physical properties on the performance of the EAHE were discussed. The synergistic combination between EAHE and SC systems was investigated to enhance PV energy efficiency and production. MATLAB simulation model for renewable energy research was presented, focusing on their role in simulating and analyzing different aspects of renewable energy systems. Validation and sensitivity analysis methods were also discussed to ensure the accuracy of the simulation results.

Based on previous research, it has been found that few studies have addressed the integration between the SC system and EAHE or between the PV module system and EAHE (PV-EAHE) system. In addition, few studies have been conducted to analyze the effect of these three systems (SC-PV-EAHE) on space cooling and ventilation under multiple climatic conditions, including hot, temperate, and cold weather conditions.

This research aims to fill this knowledge gap through an experimental and simulation study of a new system that combines these three systems (SC, PV, and EAHE), intending to estimate the effect of the integration between SC and EAHE on the efficiency of PV modules. This study was conducted in two cities with different climates, Al-Najaf in Iraq (which has a hot and dry environment) and Gödöllő in Hungary (which has cold weather).

The importance of this study lies in providing a comprehensive overview of the integration of renewable energy sources, thus reducing energy consumption and solving the problem of overheating PV modules and reducing their lifespan. This study also shows that this topic has not been extensively addressed in previous research.

It is worth noting that although MATLAB is known for its accuracy in addressing design problems, it has not been widely used in EAHE design, soil temperature distribution estimation, and SC-PV-EAHE system design. This study presents a MATLAB/Simulink model that can efficiently predict soil temperature distribution and design an EAHE and SC-PV-EAHE system. This model provides great flexibility in the design process and can be used to achieve optimal design effectively. In addition, this study provides a comprehensive comparison between four different types of EAHE systems, providing essential data that researchers and engineers can use to choose the system best suited to their needs.

In summary, this study contributes to enhancing our understanding of the benefits of integration between SC, EAHE, and PV systems in improving the performance of PV modules and reducing energy consumption under multiple climate conditions. It presents an innovative MATLAB/Simulink model to design these systems effectively, thus enhancing research in this field.

3. MATERIALS AND METHODS

Pursuing sustainable energy solutions is central to addressing global challenges associated with climate change and the growing demand for clean energy sources. Within this context, this chapter outlines the materials and methods employed in this comprehensive research study. This study investigates the intricate interplay between renewable energy technologies, specifically EAHE and SC systems, climatic conditions, and environmental factors to enhance the efficiency of photovoltaic modules and improve their performance.

3.1. Research methodology

In this research, the thermal gradient of the soil was measured and analyzed, measurements of the thermo-physical properties of the soil were performed, performance measurements of EAHE, measurements of enhancing the efficiency of PV modules, and the performance of SC. Moreover, an innovative MATLAB simulation model was developed capable of performing all simulations of the proposed hybrid system (SC-PV-EAHE), through which extensive simulation studies were conducted for the same study locations, capable of performing calculations of soil thermo-physical properties, performance calculations of EAHE, efficiency enhancement calculations of PV modules, and performance calculations of EAHE and SC. Fig. 3.1 presents the procedures and sequence of experiments conducted in this study.

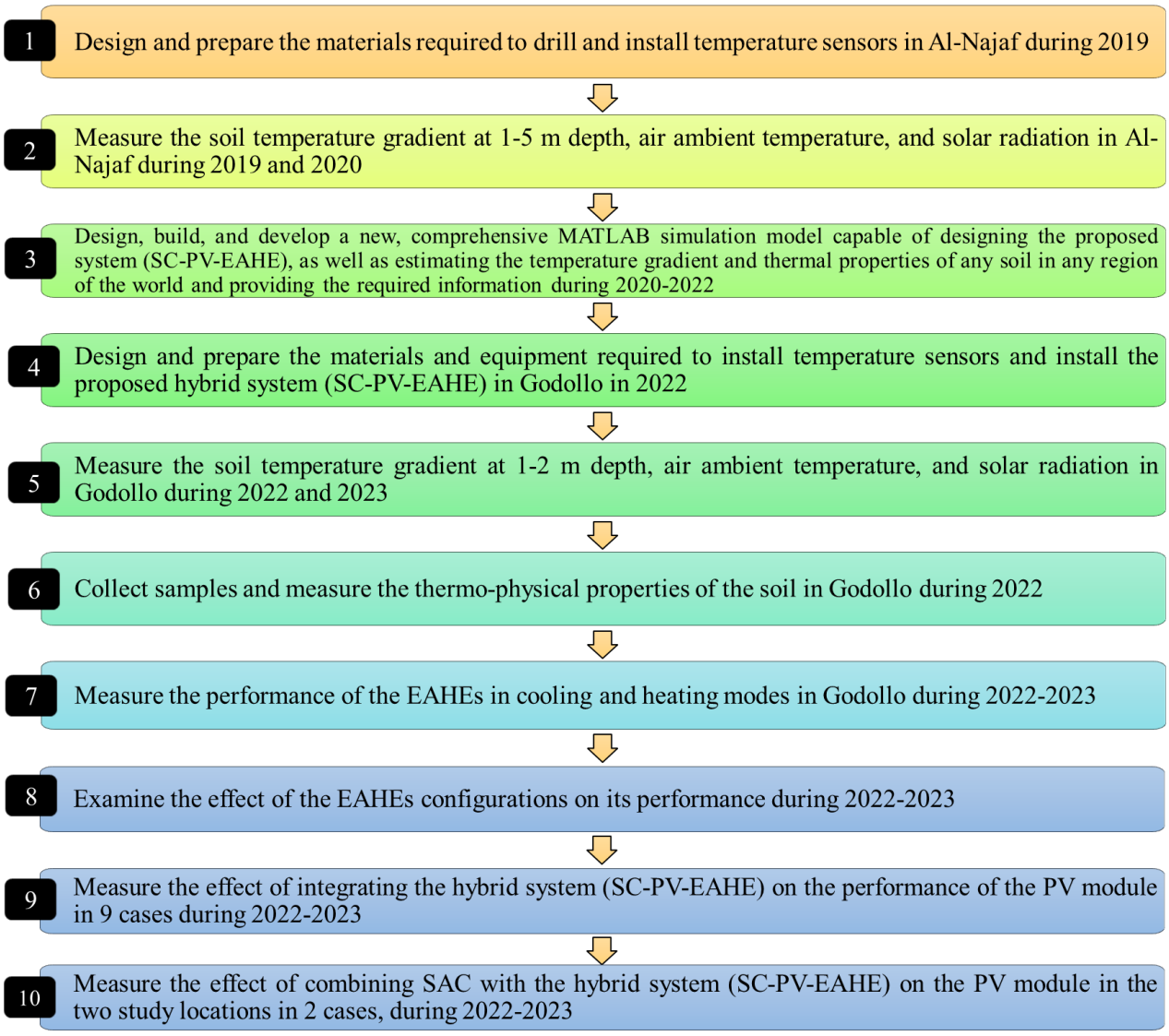

Fig. 3.1. Flowchart for the research methodology

3.2. Study location

The city of Al-Najaf, geographically defined at 32.026231 N latitude and 44.354390 E longitude, is one of the primary study sites. The choice of this location depends on its climate, which is characterized by very hot summers and mild winters, especially in recent years. Al-Najaf provides an ideal representation of areas with scorching summers, which provides valuable data to evaluate the performance of the proposed hybrid system, especially the (PV modules, SC, and EAHE) under extreme heat (*Köppen climate classification*, 2022).

In stark contrast to the warmth of Al-Najaf, Gödöllő, located at 47.593434 N latitude and 19.364198 E longitude at the MATE University Szeint Istvan campus, presents a unique set of climatic challenges. Located in the heart of Hungary, Gödöllő experiences colder winters and milder summers in comparison with Al-Najaf's climate. Incorporating Gödöllő as a major study location brings a rich diversity to the research. It allows for a comprehensive assessment of the robustness of the proposed hybrid system (SC-PV-EAHE), especially in conditions that are diametrically opposed to those in Al-Najaf. Fig. 3.2. shows the two study sites in Iraq and Hungary.

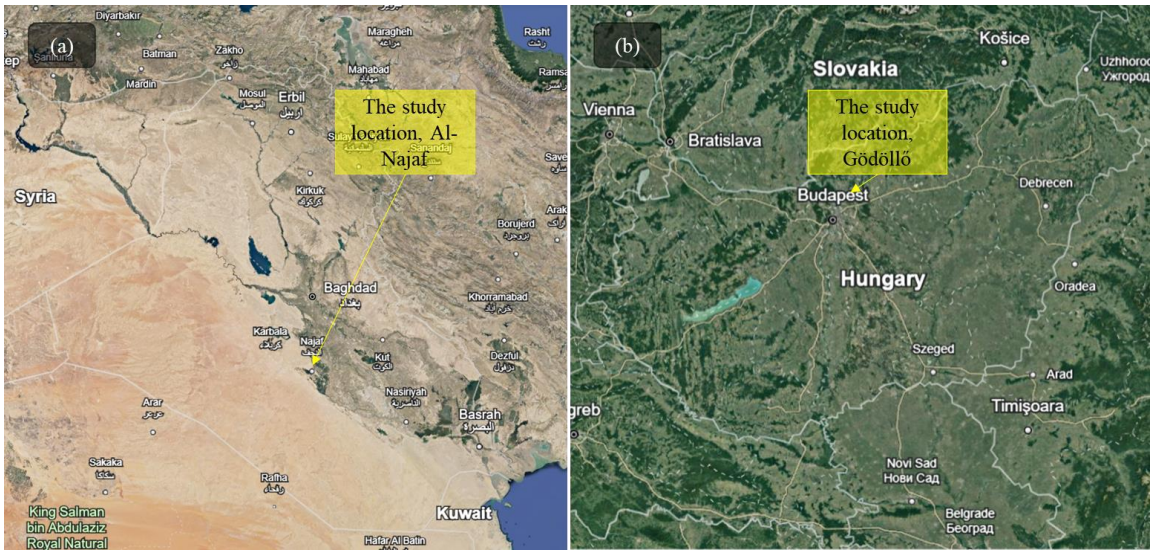

Fig. 3.2. Geographical map with highlighted study locations (a) Al-Najaf, Iraq and (b) Gödöllő, Hungary.

3.2.1. Diverse climatic conditions

The inclusion of these two distinct study sites, each representing contrasting climate regimes, reinforces the importance of the research. By examining the performance of the proposed hybrid system across temperature ranges, incident solar radiation, and seasonal variations, this study seeks to provide valuable insights into the adaptability and efficiency of renewable energy technologies under real-world conditions.

Fig. 3.3 (a) shows the clear variation in temperature between the two study sites. As for Iraq and Hungary, the climatic differences between them are clear and noticeable. Iraq, as a hot country, is characterized by extreme temperatures during the summer, while Hungary has a continental climate where temperatures are more moderate during the summer and colder during the winter. Fig. 3.3 (b) shows the clear variation in incident solar radiation between the two study sites. As for Iraq and Hungary, the differences in solar radiation falling between them are clear and noticeable. Iraq, as a country with clear skies for most months of the year, is characterized by high rates of solar radiation, especially during the summer, while Hungary enjoys a cloudier climate at many times of the year, where the incident solar radiation is the lowest monthly rate during the summer and winter.

The weather in Al-Najaf is harsh during the summer and is characterized by high ambient temperatures during the day (some days reaching 50 ^{o}C) and night (some days reaching 30 ^{o}C),

which requires high-performance attention throughout the day. July is usually the hottest summer month which usually features long hours of sunshine (exceeding 1000 W/m^2 in June) and high ambient temperatures. In contrast, October represents a transitional month characterized by relatively high daytime temperatures and cool nights. The weather in Gödöllő is cold most seasons of the year when compared to the city of Al-Najaf, the difference between the ambient temperature in Al-Najaf and Gödöllő is between 15 and 20 ^{o}C. The weather is milder and hotter during the summer (but compared to the city of Najaf, it is relatively cooler). August is usually the hottest summer month in Gödöllő, with longer hours of sunshine (namely from 10:00 to 16:00, exceeding 900 W/m^2 in August) and higher ambient temperatures.

The experimental days were carefully selected with respect to clear sky and relatively similar weather conditions to ensure effective use of the proposed system under different weather conditions. Moreover, most of the experiments were conducted during July, August, and September, which are suitable hot summer months in both countries. Summer days in Gödöllő, where all the experiments of the proposed hybrid system were conducted, are generally sunny (more than 19 days/month), with clear sky and high solar radiation. As for the city of Al-Najaf (the city in which the soil temperature gradient experiments were conducted), summer days are generally sunnier and hotter (more than 29 days/month), with clear sky and high solar radiation.

The following sections detail the materials and methods used to conduct this multifaceted study, including data collection, experimental procedures, and MATLAB simulation model development and validation. These methodologies are crucial in achieving research objectives and enhancing our understanding of sustainable energy integration in different climates.

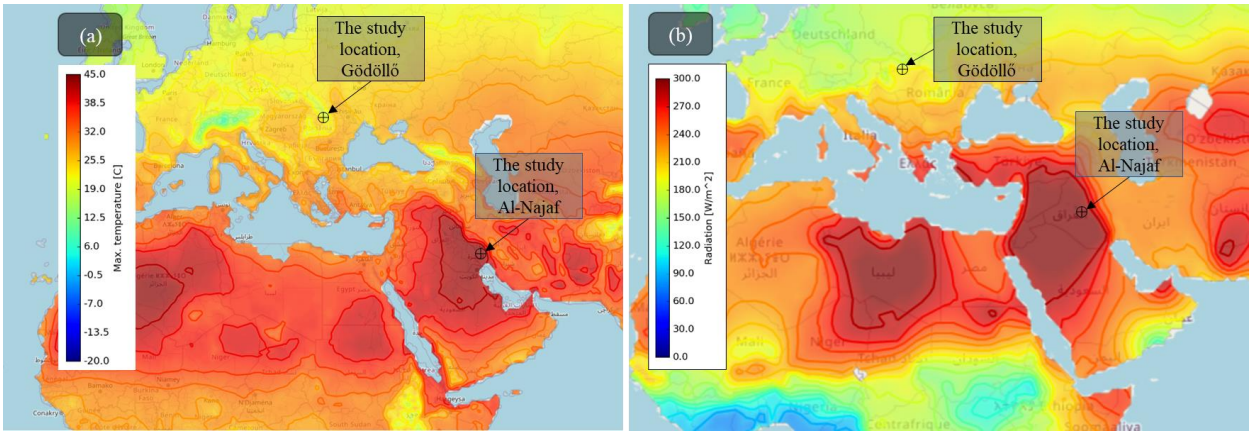

Fig. 3.3. The variation in temperatures and radiation between the two study locations (a) Ambient temperature and (b) Solar radiation (Bart Römgens, 2021).

3.2.2. Locations for practical experiments

In order to accomplish the overall goals of this study, practical tests were carried out in two specified locations, namely Al-Najaf and Gödöllő. This component of the research will include details on the practical experiments and their respective sites. Each process will be briefly explained, as indicated in Table 3.1.

The soil temperature distribution in Al-Najaf and Gödöllő was measured at two different depths as shown in Table 3.1. The difference in depth of soil temperature gradient testing at the two study locations is due to financial and practical considerations. The cost of temperature testing up to a depth of 5 m in Al-Najaf is lower than its cost in Gödöllő due to the easy access to the site and the availability of sufficient space to conduct the tests. The study location at Gödöllő was surrounded by structures and sewer pipes, making it difficult or impossible to conduct tests at great depth. These considerations were taken into account when designing the study, as a depth of 5 m was chosen in Al-Najaf and 2 m in the city of Gödöllő, which is a sufficient depth to study the temperature gradient in the surface layers of the soil and achieve the objectives of this study.

However, all comparisons between the two study sites were made for each depth at its corresponding depth at the other study site.

Table 3.1. The practical experiments were conducted at the study locations with clarifications.

The measurements	Clarification	Location
Temperature gradient analysis measurements	Measuring and analyzing thermal gradients within the soil at different depths. Analysis of thermal gradients is a crucial element in understanding heat transfer mechanisms.	Al-Najaf (1-5 m depth) and Gödöllő (1-2 m depth)
Measurements of soil thermo-physical properties	Conduct a comprehensive examination and documentation of the thermal and physical properties of the soil. These properties include thermal conductivity, heat capacity, and density. Understanding these properties is essential for accurately modeling and predicting heat transfer within soils.	Gödöllő
Performance measurements of EAHE	Evaluation of the performance of EAHE at a depth of 2 m.	Gödöllő
Measure the effect of integrating the hybrid system (SC-PV-EAHE) on the performance of the PV module	Evaluation of the effect of combining EAHE and SC on the efficiency of PV modules.	Gödöllő
Measure the effect of combining SAC with the hybrid system (SC-PV-EAHE) on the PV module in the two study locations in 2 cases	Evaluating the performance of solar chimneys in different shapes and colors.	Gödöllő
Ambient and solar radiation measurements	Measuring temperatures and incident solar radiation is necessary to achieve the objectives of the study.	Al-Najaf and Gödöllő

3.3. Experimentation

The experimental procedures conducted in this research were carefully designed and implemented to verify the efficiency of the proposed new hybrid system (SC-PV-EAHE), performing temperature gradient measurements, soil thermal and physical properties, performance measurements of EAHE, efficiency enhancement PV modules, and performance measurements of solar stacks under different climatic conditions. This section describes the specific procedures used to collect planned experimental data at the study sites.

3.3.1. Soil Temperature Gradient Measurement

Measuring soil temperature gradients at different depths is fundamental to understanding heat transfer mechanisms within the Earth and evaluating EAHE performance. Therefore, temperature sensors were installed at multiple depths inside the soil, ranging between 1, 2, 3, 4, and 5 m at Al-Najaf and 1 and 2 m deep at the Gödöllő. Sensor placement follows standardized guidelines to ensure accurate temperature measurements and the procedure followed by the previous studies (ASTM, 2008)(Rubio, 2013)(Al-Maliky, 2011)(Mengistu et al., 2017). Sensors are configured to record soil temperatures at regular intervals. Data were collected throughout the study period, covering all seasons and ambient temperature changes. The collected temperature data were analyzed to determine temperature gradients, evaluate seasonal changes, and identify trends in soil temperature profiles.

A hole was dug at Al-Najaf to a depth of 5 meters to measure the soil temperature during all months of the year. Five thermocouples (K-type) were inserted into the hole at different depths (1, 2, 3, 4,

and 5 m) in order to be used to measure the actual soil temperatures, and the sixth thermocouple was used to measure the ambient air. To document and compare daily temperatures at different intervals (every ten minutes) in 2019, with the aim of more accurately identifying and evaluating the possibilities for underground use. Data were collected using a "Temperature Recorder, Model: TM500" daily 144 times a day.

As for conducting the experiment in the city of Gödöllő, the same methodology was applied that was applied when conducting the experiment in Al-Najaf, and the same measuring device was used. The soil temperature was examined at a depth of 1 and 2 m during all study periods and months of the year. Two thermocouples (K-type) were inserted into the hole at different depths (1 and 2 m depth) in order to measure the actual soil temperatures, and the third thermocouple was used to measure ambient temperatures to document and compare daily temperatures. Temperature at different intervals (every ten minutes) in 2022-2023, with the aim of more accurately identifying and evaluating underground use possibilities. Data were collected using a "Temperature Recorder, Model: TM500" daily 144 times a day. The schematic diagram shows the experimental models and experimental setup for soil temperature at the two experimental sites.

A PVC pipe was used and inserted into the two holes dug as a solid wall to avoid demolition and dirt falling into the test pit and its collapse, and then the sensors were inserted through it. Fig. 3.4 shows the schematic diagram of the experimental models and experimental setup for soil temperature at the two experimental locations.

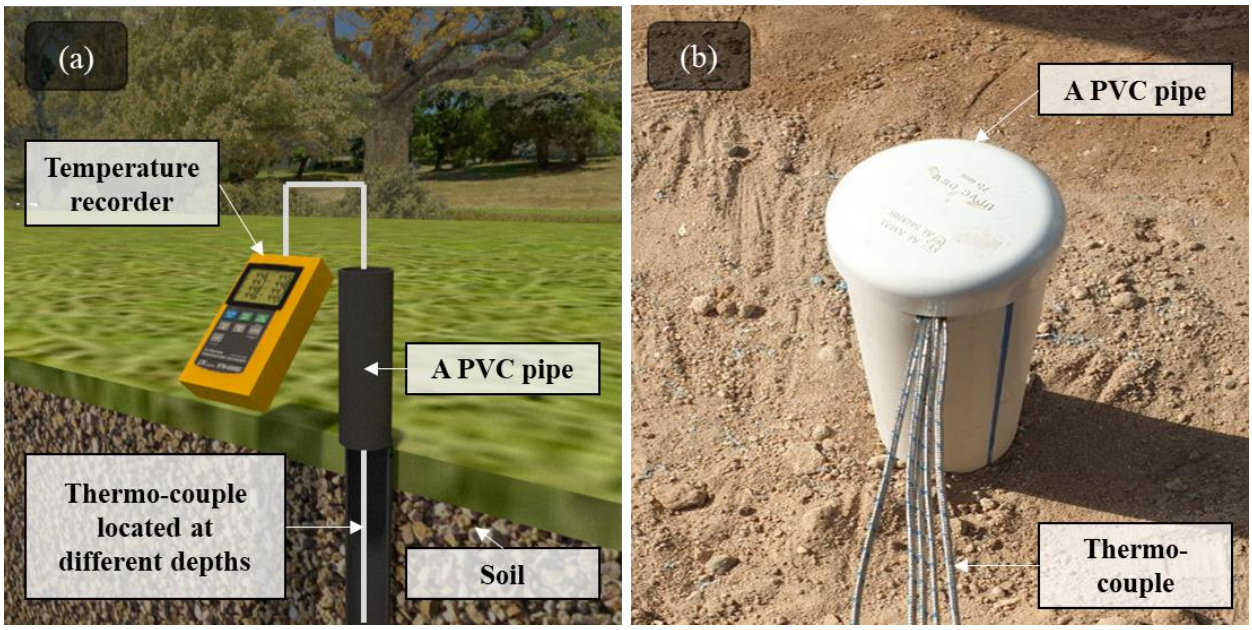

Fig. 3.4. The schematic diagram shows the experimental models and experimental setup for soil temperature at the two experimental locations (a) Schematic drawing and (b) Experimental setting.

3.3.2. Soil Thermo-physical Properties Measurement

One of the objectives of this study is to develop an experimental approach to measure and calculate the thermo-physical properties of soil in the study location as well as the equivalent thermo-physical properties of multilayer soils and to study their effect on the performance of EAHE. Accurate determination of soil thermo-physical properties, including moisture content, thermal conductivity, specific heat capacity, and thermal diffusivity. The proposed experimental approach involves measuring soil properties using an inverse analysis technique to determine which soil properties best fit the measured data.

In order to accomplish this, the study area (Gödöllő) was excavated to a depth of 2 meters, and it was found that the excavated area consists of five different layers of soil in terms of type and thickness (as illustrated in Fig. 3.5). Soil samples of each layer were collected and preserved in a

way that preserved their properties in situ and preparate for the examination, Fig. 3.6 shows the soil samples. Table 3.2 shows the thickness of each soil layer and the percentage of each layer relative to the total depth. The collected soil samples were subjected to careful laboratory analysis to determine their thermo-physical properties. To measure the thermo-physical properties of the soil, the experimental device, which is the Mettler-Toledo HE53 dryer, was used. The HE53 has a capacity of 54 grams and a readability of 1 milligram or 0.01% moisture content.

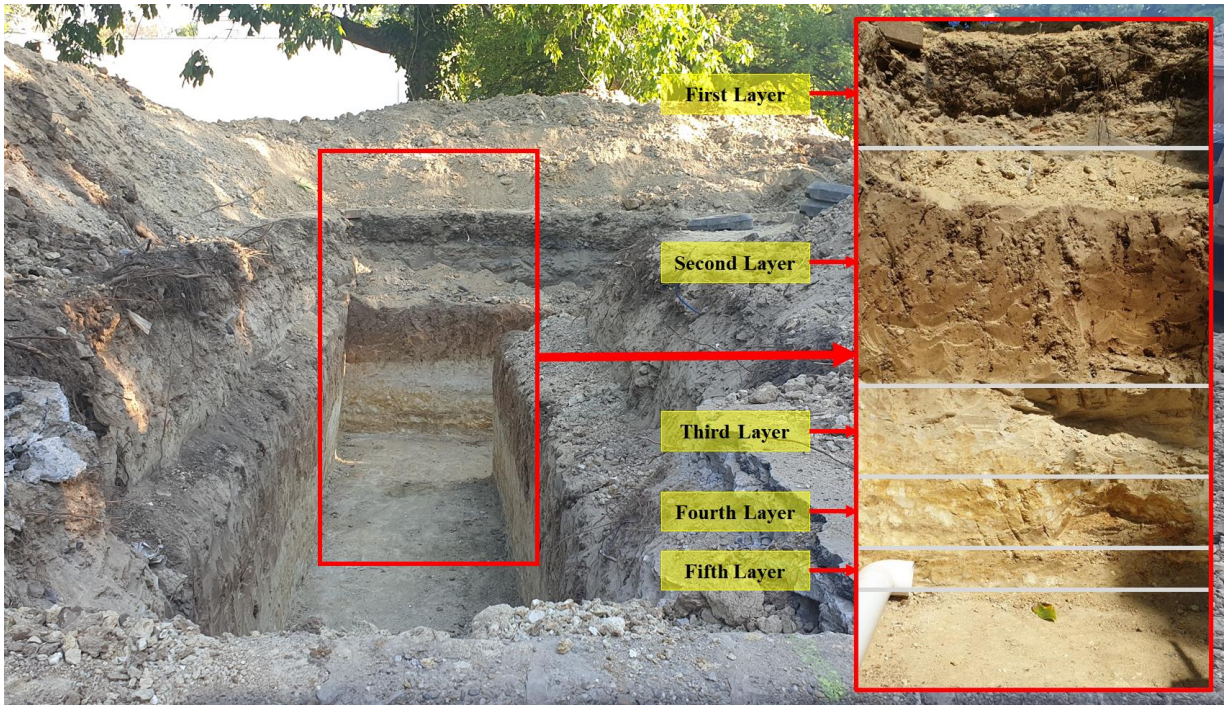

Fig. 3.5. Different soil layers of the excavated trench.

Fig. 3.6. The five soil samples.

Table 3.2. The thickness of the soil layers, along with the percentage of each one relative to the total depth.

	Fifth Layer	Fourth Layer	Third Layer	Second Layer	First Layer	Total depth
Layer Thickness, m	0.10	0.27	0.35	0.88	0.40	2
Layer thickness ratio, %	5	13.5	17.5	44	20	100

3.3.2.1.Single-layer Soil Thermo-physical Properties Measurement

The method for measuring the thermo-physical properties of each sample individually will be described in this section. Samples were prepared as described (Fig. 3.6), before starting the process of measuring properties, the initial volume of each sample was measured before it was inserted

into the experiment device (the volume was measured using a graduated glass tube (see Fig. 3.7)), and the initial mass was also measured using the experiment device itself.

After that, each sample was inserted into the experimental device (Moisture Analyzer). Fig. 3.7 shows the examination device. Each sample was treated according to the operating instructions of the Moisture Analyzer HE53. The final mass was then measured after the end of the experiment using the same measuring device, and the final sample volume was measured using the same graduated glass tube. Thus, the properties obtained up to this step are moisture content, wet density, and dry density. Through them, the density of each sample, thermal conductivity, specific heat capacity, and thermal diffusivity for each of them will be obtained using the equations mentioned in section 3.5.1.1.

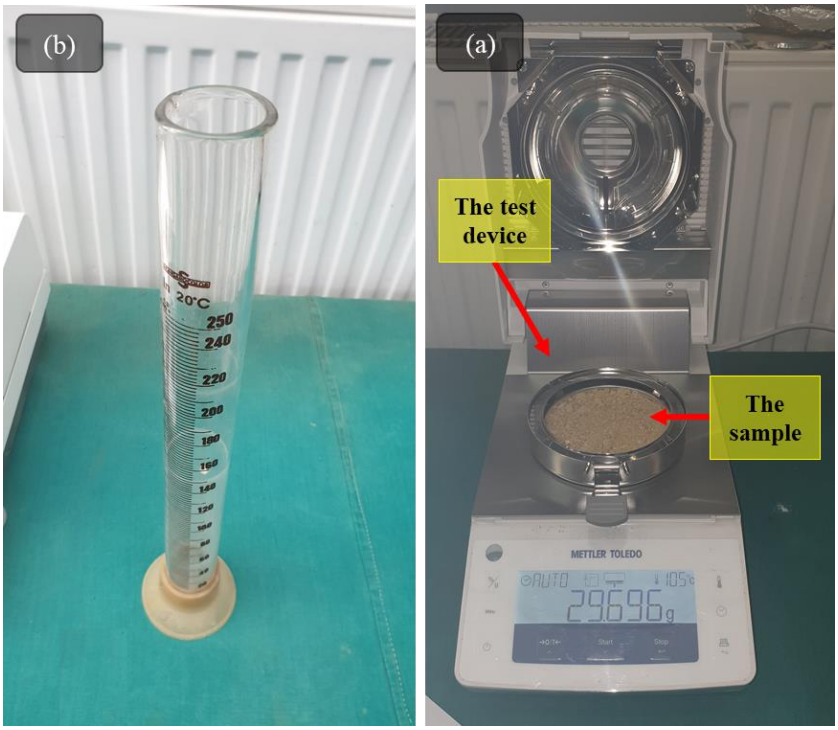

Fig. 3.7. Instruments used to measure soil thermo-physical properties (a) The graduated glass tube and (b) the test device.

3.3.2.2. Multi-layered Soil Thermo-Physical Properties Measurement

Often, when excavation operations are carried out to install the EAHE deep in the ground, the extracted soil is collected randomly. When the hole is reburied after the installation of the EAHE is completed, the burial process will take place by returning the extracted soil itself, which in this case is a mixture of several types of soil, which means that the current mixture does not reflect the reality of the surrounding soil, which is composed of layers. Also, for calculating and estimating the temperature gradient of any soil using any approved method, it will be essential to provide the thermal-physical properties of the soil (Agrawal Agrawal et al., 2018). When the soil is composed of a single layer, it can be dealt with in a fairly simple way. The values of its properties are entered within the procedures of the established calculation method. Still, when the soil is composed of several layers, there is no specific method up to now that regulates the management of this type of soil. Therefore, it is necessary to develop a new method to calculate and estimate the thermo-thermal properties required for multi-layer soil. Thus, this study presents two new approaches.

1- The new laboratory approaches

To measure the equivalent thermo-physical properties of multilayer soil, all samples were mixed, and the mixing ratios were based on the ratio of the thickness of each sample to the total thickness (total depth of the trench), as shown in Table 3.2 and Fig. 3.8. The resulting sample was collected

and preserved in such a way as to preserve its in situ properties (soil samples are shown in Fig. 3.9). The collected soil samples underwent careful laboratory analysis to determine their thermal and physical properties. The same experiment device was used to measure its thermo-physical properties.

Before starting the properties measurement process, the initial volume of the sample was measured before inserting it into the experiment apparatus (the volume was measured using a graduated glass tube (Fig. 3.7)), and the initial mass was measured using the experiment apparatus itself. The sample was then inserted into the experimental device, processed individually inside the device, and dried at a temperature of 105 ^{o}C. The final mass was then measured after the experiment ended using the same measuring device, and the final sample volume was measured using the same graduated glass tube. Therefore, the properties obtained up to this step are moisture content, wet density, and dry density. Through them, the sample density, thermal conductivity, specific heat capacity, and thermal diffusivity were obtained using the equations mentioned in section 3.5.1.1.

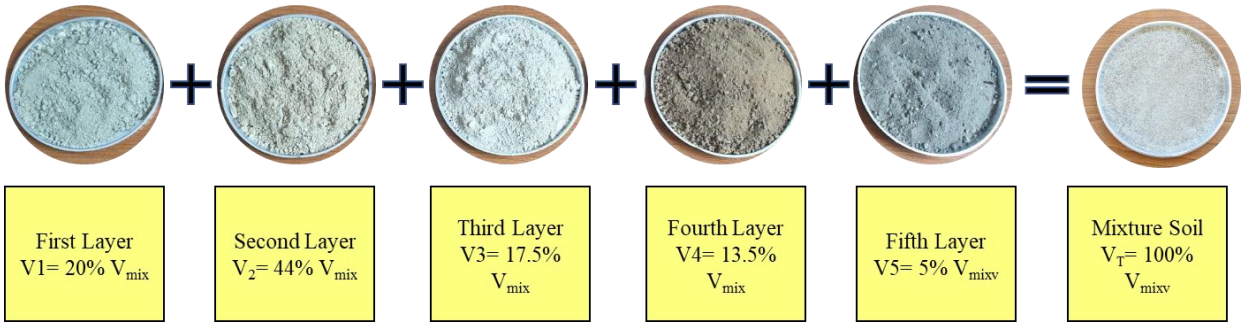

Fig. 3.8. The types of mixed soil layers according to the indicated percentages.

Fig. 3.9. The mixed soil sample.

2- The new estimation approaches

Moisture content and dry and wet densities are the basic properties on which the other soil's thermo-physical properties depend, such as density, thermal conductivity, and specific heat capacity (Agrawal Agrawal et al., 2018). Therefore, if these two properties are available, whether

experimentally or theoretically, it is possible to calculate the other soil properties. So, this study presents the new appropriate methods to estimate these required thermo-physical properties.

If the sample size of each extracted soil layer is available and the amount of moisture content for each sample is also available, the following equation is used to estimate the equivalent moisture content.

$$w_{eq} = w_1 \times \frac{V_1}{V_T} + w_2 \times \frac{V_2}{V_T} + w_3 \times \frac{V_3}{V_T} + w_4 \times \frac{V_4}{V_T} + w_5 \times \frac{V_5}{V_T} + \ldots\ldots + w_n \times \frac{V_n}{V_T} \tag{3.1}$$

In typical trench excavation operations, the length and width of the excavation are usually known and approximately equal for all trench layers. Therefore, the thickness of each layer is used to calculate the total thickness of the hole instead of using the size of each layer to the total size, so the equation is as follows:

$$\begin{aligned} w_{eq} = {} & w_1 \times \frac{L_1 \times W_1 \times t_1}{L_T \times W_T \times t_T} + w_2 \times \frac{L_2 \times W_2 \times t_2}{L_T \times W_T \times t_T} + w_3 \times \frac{L_3 \times W_3 \times t_3}{L_T \times W_T \times t_T} \\ & + w_4 \times \frac{L_4 \times W_4 \times t_4}{L_T \times W_T \times t_T} \\ & + w_5 \times \frac{L_5 \times W_5 \times t_5}{L_T \times W_T \times t_T} + \ldots\ldots + w_n \times \frac{L_n \times W_n \times t_n}{L_T \times W_T \times t_T} \end{aligned} \tag{3.2}$$

As we mentioned, in usual excavation operations, the length and width or diameter of the excavation is usually known and is the same for all layers, so:

$$L_1 = L_2 = L_3 = L_4 = L_5 = L_n = L_T$$

$$W_1 = W_2 = W_3 = W_4 = W_5 = W_n = W_T$$

It is possible to delete the length and width of the holes from all terms of the equation to simplify the equation so that the equation becomes as follows:

$$w_{eq} = w_1 \times \frac{t_1}{t_T} + w_2 \times \frac{t_2}{t_T} + w_3 \times \frac{t_3}{t_T} + w_4 \times \frac{t_4}{t_T} + w_5 \times \frac{t_5}{t_T} + \ldots\ldots + w_n \times \frac{t_n}{t_T} \tag{3.3}$$

If the moisture content of each layer is unavailable, the following equation is used.

$$\begin{aligned} w_{eq} = {} & \left(\frac{M_{1_{be}} - M_{1_{af}}}{M_{1_{be}}} \times 100\right) \times \frac{t_1}{t_T} + \left(\frac{M_{2_{be}} - M_{2_{af}}}{M_{2_{be}}} \times 100\right) \times \frac{t_2}{t_T} \\ & + \left(\frac{M_{3_{be}} - M_{3_{af}}}{M_{3_{be}}} \times 100\right) \times \frac{t_3}{t_T} + \left(\frac{M_{4_{be}} - M_{4_{af}}}{M_{4_{be}}} \times 100\right) \times \frac{t_4}{t_T} \\ & + \left(\frac{M_{5_{be}} - M_{5_{af}}}{M_{5_{be}}} \times 100\right) \times \frac{t_5}{t_T} + \ldots\ldots + \left(\frac{M_{n_{be}} - M_{n_{af}}}{M_{n_{be}}} \times 100\right) \times \frac{t_n}{t_T} \end{aligned} \tag{3.4}$$

To simplify further:

$$w_{eq} = \frac{\left(\begin{array}{l} \left(\frac{M_{1_{be}} - M_{1_{af}}}{M_{1_{be}}}\right) \times t_1 + \left(\frac{M_{2_{be}} - M_{2_{af}}}{M_{2_{be}}}\right) \times t_2 + \left(\frac{M_{3_{be}} - M_{3_{af}}}{M_{3_{be}}}\right) \times t_3 + \\ \left(\frac{M_{4_{be}} - M_{4_{af}}}{M_{4_{be}}}\right) \times t_4 + \left(\frac{M_{5_{be}} - M_{5_{af}}}{M_{5_{be}}}\right) \times t_5 + \ldots\ldots + \left(\frac{M_{n_{be}} - M_{n_{af}}}{M_{n_{be}}}\right) \times t_n \end{array}\right)}{\frac{t_T}{100}} \tag{3.5}$$

In this context, *M* is the mass of the sample, *1*, *2*, *3*, *4*, *5*, and *n* are the name of the sample, *be* and *af* are the time samples (the samples taken before and after processing in the testing device), and *t* is the soil thickness of the sample.

It is required to make a mixture consisting of layered soil types and measure and calculate their properties, and the samples must be mixed according to the ratio quantity of each sample to the total quantity, as in the following equation:

$$V_1 = \frac{t_1}{t_T} \times V_T \, , V_2 = \frac{t_2}{t_T} \times V_T \, , V_3 = \frac{t_3}{t_T} \times V_T \, , V_4 = \frac{t_4}{t_T} \times V_T \, , V_5 = \frac{t_5}{t_T} \times V_T \, , V_n = \frac{t_n}{t_T} \times V_T \tag{3.6}$$

Then, the soil samples are mixed, and the total mass of the entire mixture, which consists of a set of masses for all samples, as the mass percentage of any sample differs from the other, is as follows:

$$M_1 = \frac{t_1}{t_T} \times \frac{\rho_1}{\rho_T} \times M_T \, , M_2 = \frac{t_2}{t_T} \times \frac{\rho_2}{\rho_T} \times M_T \, , M_3 = \frac{t_3}{t_T} \times \frac{\rho_3}{\rho_T} \times M_T \, ,$$
$$M_4 = \frac{t_4}{t_T} \times \frac{\rho_4}{\rho_T} \times M_T \, , M_5 = \frac{t_5}{t_T} \times \frac{\rho_5}{\rho_T} \times M_T \, , M_n = \frac{t_n}{t_T} \times \frac{\rho_n}{\rho_T} \times M_T \tag{3.7}$$

Therefore, the final equation for estimating moisture content will be as follows:

$$w_{eq} = \left(\frac{(M_1 + M_2 + M_3 + M_4 + M_5 + \ldots\ldots + M_n)_{be} - (M_1 + M_2 + M_3 + M_4 + M_5 + \ldots\ldots}{(M_1 + M_2 + M_3 + M_4 + M_5 + \ldots\ldots + M_n)_{be}} \times 100 \right) \tag{3.8}$$

To simplify further:

$$w_{eq} = \left(\frac{(M_T)_{be} - (M_T)_{af}}{(M_T)_{be}} \times 100 \right) \tag{3.9}$$

Likewise, the final equation for estimating wet density will be as follows:

$$\rho_{eq,wet} = \left(\frac{(M_1 + M_2 + M_3 + M_4 + M_5 + \ldots\ldots + M_n)_{be}}{(V_1 + V_2 + V_3 + V_4 + V_5 + \ldots\ldots + V_n)_{be}} \right) \tag{3.10}$$

To simplify further:

$$\rho_{eq,wet} = \left(\frac{(M_T)_{be}}{(V_T)_{be}} \right) \tag{3.11}$$

Likewise, the final equation for estimating dry density will be as follows:

$$\rho_{eq,dry} = \left(\frac{(M_1 + M_2 + M_3 + M_4 + M_5 + \ldots\ldots + M_n)_{af}}{(V_1 + V_2 + V_3 + V_4 + V_5 + \ldots\ldots + V_n)_{af}} \right) \tag{3.12}$$

To simplify even more:

$$\rho_{eq,dry} = \left(\frac{(M_T)_{af}}{(V_T)_{af}} \right) \tag{3.13}$$

By measuring and estimating these properties, it is possible to calculate and predict the density, thermal conductivity, and specific heat capacity of the soil, such as specific heat, thermal conductivity, soil density, and diffusivity, on which the efficiency of the heat exchanger system directly depends.

3.3.3. Earth-Air Heat Exchanger Performance Evaluation

The performance of EAHE has been evaluated for their effectiveness in facilitating heat exchange between soil and air, especially in cold and temperate climates.

1. Installation: EAHE was installed at a depth of 2 m in Gödöllő, Hungary, as specified in the study design section. A trench was dug, 1 m wide, 2 m deep, and 14 m long. Two EAHE systems were installed, one called EAHE-a and the other called EAHE-b, which are PVC pipes with a diameter of 0.1 m and a horizontal length of 10 m each. The two ends of each are connected to an inclined pipe at an angle of 45^{o} and a length of 3 m, with 2.8 m of it inside the soil and 0.2 m of it outside it to achieve the required level. Each of these two systems contains another branch from its middle to divide each system into two halves to provide the possibility of using this system with a length of 10 m and 5 m for purposes of comparison and study. This branch is vertical, 2 m long inside the soil and 0.2 m outside the soil. Thus, each system has two ends for air entry when the length of the system is 10 m and when it is 5 m according to the requirements of the study case, and its third end is linked to the space required to be cooled or heated according to the season and weather condition. In this study, it was connected to PV/T to cool PV modules. To circulate the air through the pipes, an axial AC fan with a 0.1 m diameter (Model: 100 VKO1) was installed and controlled by a controller to determine the required speed.
2. Temperature measurements: Seven temperature sensors were used, one sensor was installed to measure the ambient temperature and six temperature sensors were placed at the inlet and outlet of each of the EAHE to monitor the temperature of the air entering and exiting the system to know and understand the performance of the EAHE.
3. Airflow velocity measurements: Two anemometers (anemometer, airflow meter with thermometer, USB connection, and Voltcraft PL-135HAN) were used to measure airflow velocity at both ports of the EAHE (EAHE-a and EAHE-b), providing insight into the heat transfer rate.
4. Continuous monitoring: Data loggers were used to continuously record temperature and airflow velocity data. SmartDEN Logger - A web-based temperature data logger with analog/digital inputs was used to record temperatures (set to record at 1 minute), and anemometer software was used to record airflow velocity (set to record at 1 minute).
5. Seasonal variation analysis: Data collected over multiple seasons allowed the performance of EAHE to be evaluated under different thermal conditions. Temperatures and airflow speed were recorded every minute. Then, the average was calculated for the readings measured over 10 minutes, and these averages were used in the studies and analyses targeted by this research.

The first step begins with starting the digging process and completing the system's installation. Fig. 3.10 shows the three-dimensional schematic of the proposed new hybrid system, which shows the full details of the system.

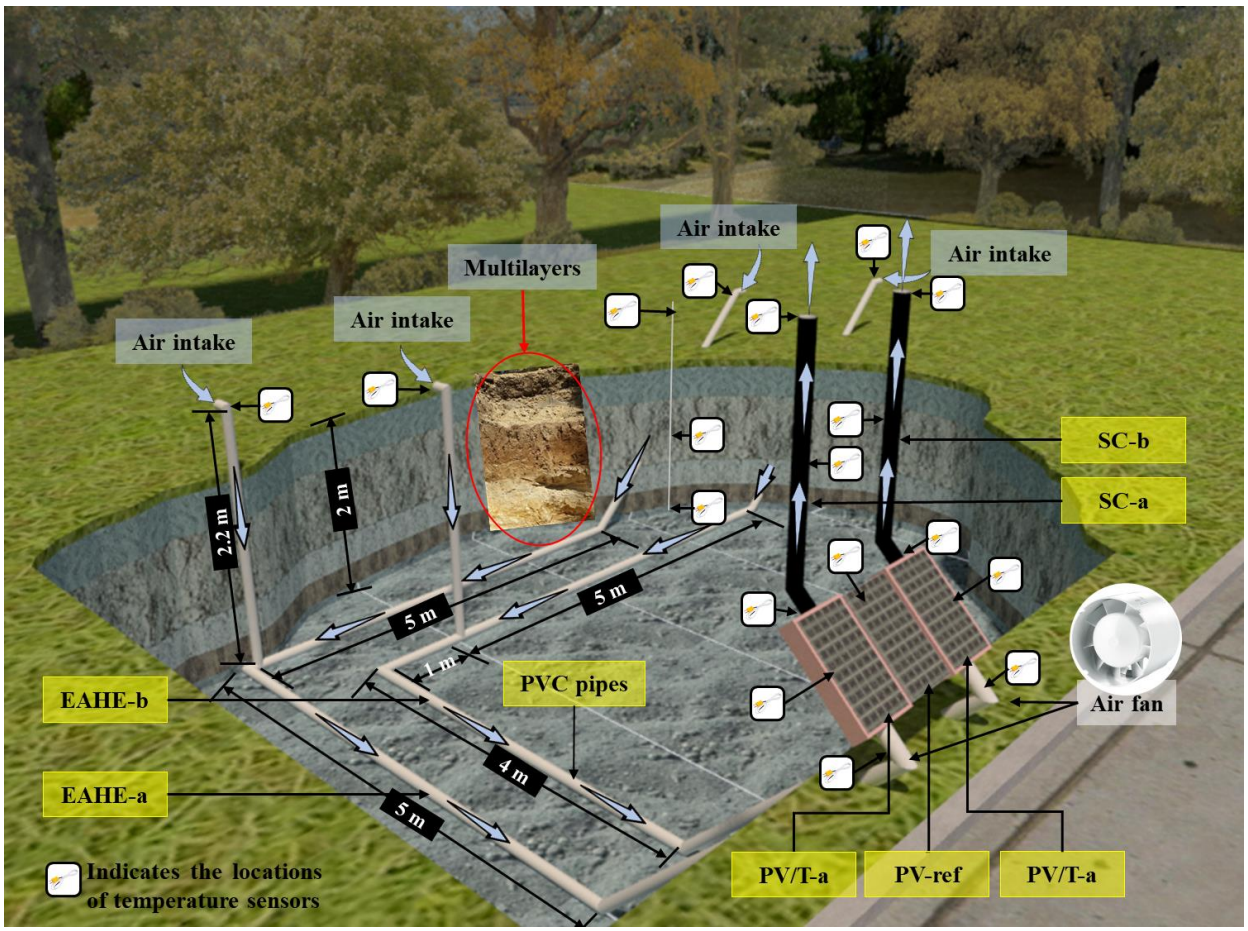

Fig. 3.10. The three-dimensional schematic of the proposed new hybrid system.

3.3.4. Integrated PV Module Performance Evaluation

To evaluate the impact of integrating PV modules with the EAHE and SC systems on overall efficiency and electricity generation.

1. Installation: Three monocrystalline PV modules (87TH424) were used in this study to make a comparison between their efficiency and output power. It had a module area of 0.268 m^2 and a nominal power of 50 W.
2. Two of these three PV modules were used to construct a simple PV/T model. A polystyrene sheet with a thickness of 0.02 m was used as a thermal insulation wall with a 0.025 W/m.K thermal conductivity in the manufacturing process of the PV/T. It was cut into sizes and areas that suited the manufacturing process of the PV/T and formed the channel that surrounded the back of the PV module to form a duct through which the air needed to cool the PV module passed. Adhesive materials with high tolerance to heat and weather conditions were used and tested in this study for the purpose of using them in the process of connecting the polystyrene sheet and forming the PV/T duct.
3. This duct is connected to the bottom to EAHE and the top is connected to SC. For naming and differentiation purposes, one of these two PV/T is called in this research PV/T-a, and the second is called PV/T-b. PV/T-a is connected to the bottom to EAHE-a and the top is connected to SC-a, PV/T-b is connected to the bottom to EAHE-b and the top is connected to SC-b.
4. As for the third PV module, it is a reference PV module. It was not integrated with PV/T, it was not linked at all with EAHE and SC. Through this PV module, the output power is measured based on the incident solar radiation and the temperature of the surroundings without its cooling. In this study, it is called PV-ref.
5. All three PV modules (PV/T-a, PV/T-b, and PV-ref) were constructed and installed with a tilt angle of 45^o and an azimuth angle of -20^o.

6. Temperature measurements: Eight temperature sensors were used. One temperature sensor was installed to measure the ambient temperature, four temperature sensors were placed at the inlet and outlet of both the PV/T-a and PV/T-b to monitor the temperature of the air entering and exiting the systems to know and understand the performance of the PV/T-a and PV/T-b respectively, and three temperature sensors were placed at the back of the PV-a, PV-ref, and PV-b to monitor the temperature of the PV-a, PV-ref, and PV-b modules to know and understand the performance of the PV-a, PV-ref, and PV-b modules respectively.
7. Solar radiation and electrical parameters measurements: Photoelectric solar radiation sensor was used to measure the solar radiation and the electric wires were used to connect the PV modules to the smart Arduino Denkovi-smart-32.
8. Continuous monitoring: Smart Arduino Denkovi-smart-32 was a data-acquisition logger has been used to record solar radiation, current, voltage, and temperatures. Additionally, a desktop computer was used to run the display moods to monitor the sensor values. It was set to record at every 1 minute.

As for the SC integrated with the system, it comes in several sizes and configurations according to the case study. It is a circular and rectangular tube with a hydraulic diameter of 0.1 m and a length of 1.5 m. It comes in two colors (white and black).

Fig. 3.11 illustrates the actual picture of the fabrication process of the PV/T models and their final form. Fig. 3.12 shows the PV/T models and PV modules installed on a supporting iron structure. Fig. 3.13 shows the final realistic image of PV modules integrated with SC and EAHE at the study location. The operating and design parameters of the PV/T model air system used in the model simulations are described in Table 3.3.

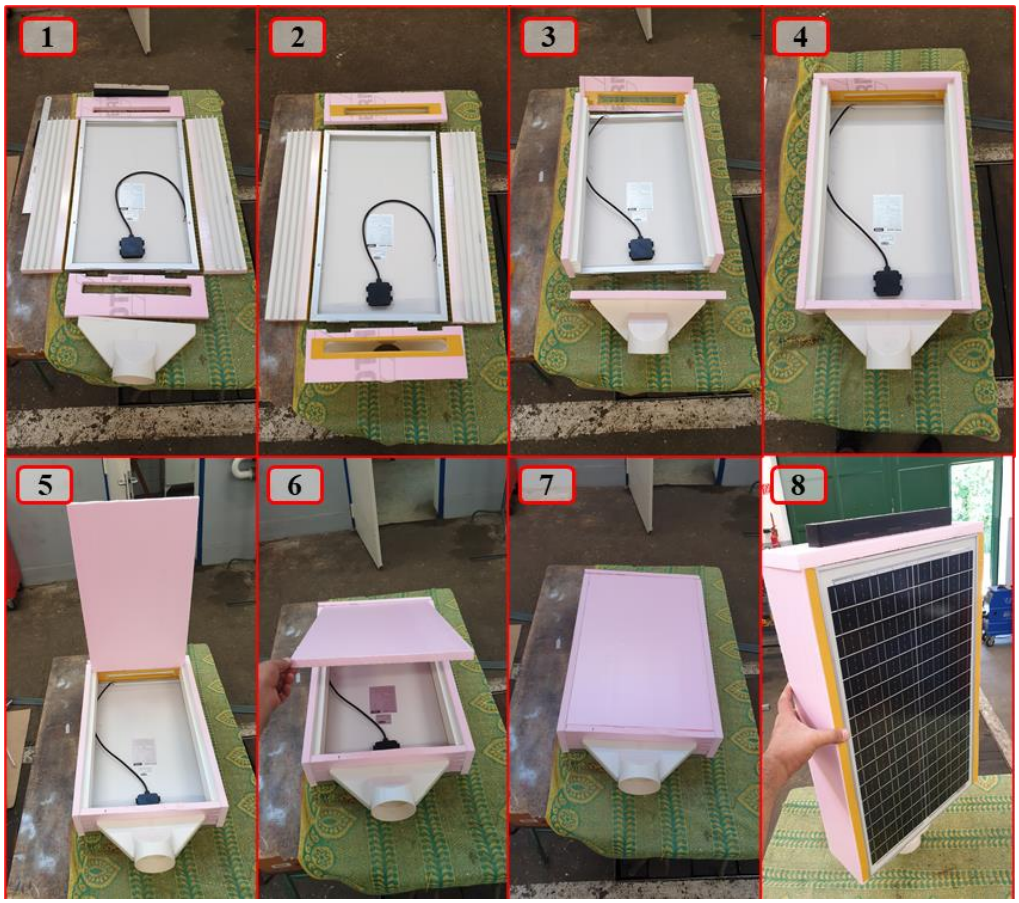

Fig. 3.11. The practical installation and manufacturing steps of the PV/T duct and PV modules.

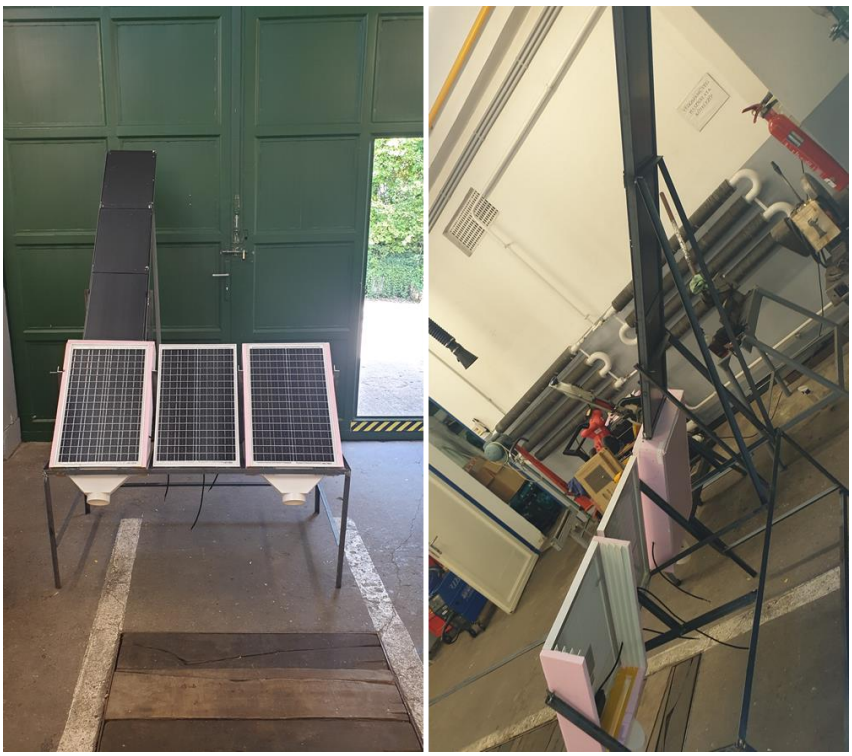

Fig. 3.12. The PV/T duct and PV modules are installed on the supporting iron structure.

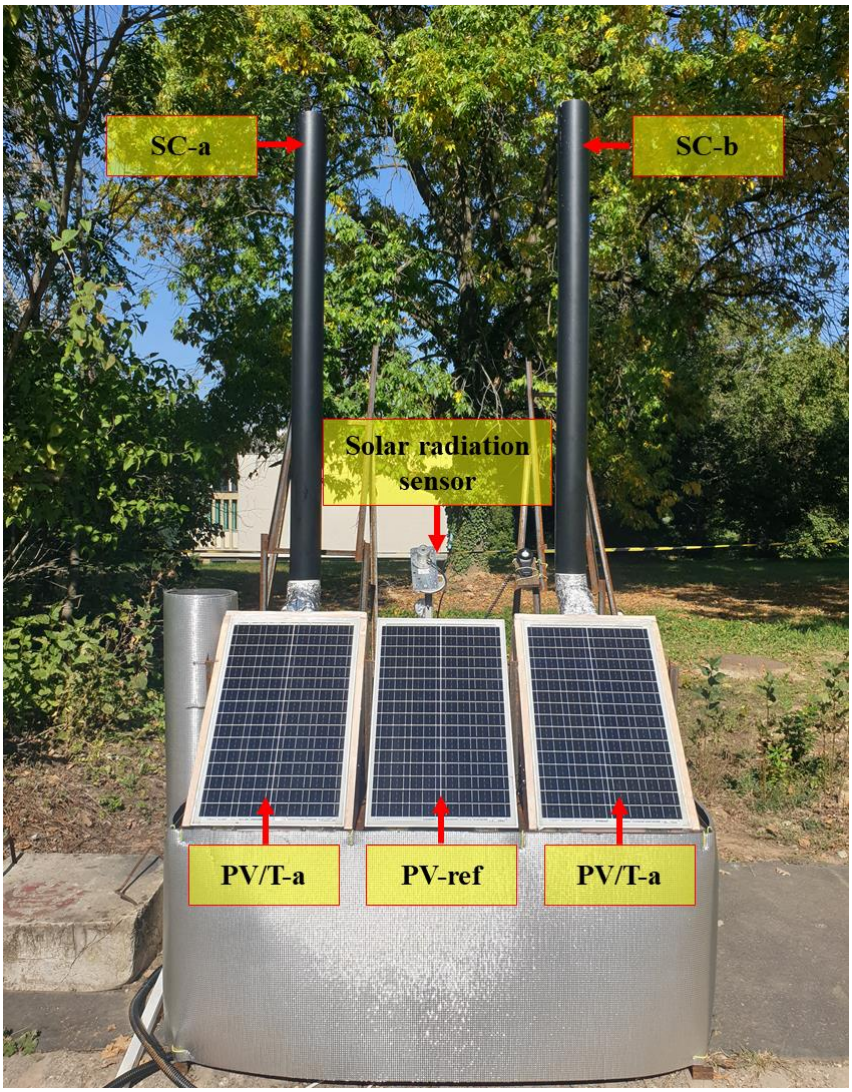

Fig. 3.13. The final realistic image of PV modules integrated with SC and EAHE.

Table 3.3. Design parameters of the PV/T air system.

PV/T air hybrid system parameters	Value
Length of PV module and air duct, L_D	0.67 m
Width of PV module, W_D	0.40 m
Thickness of glass cover, L_G	0.003 m
Conductivity of glass cover, K_G	1 W/(m K)
Transmissivity of the glass cover, τ_G	0.95
Emissivity of the glass cover, ε_G	0.88
Absorptivity of solar cell, α_{CELL}	0.85
Thickness of solar cells, L_{CELL}	300×10^{-6} m
Conductivity of solar cells, K_{CELL}	0.036 W/(m K)
Absorptivity of tedlar, α_T	0.5
Thickness of tedlar, L_T	0.5×10^{-3} m
Conductivity of tedlar, K_T	0.033 W/(m K)
Emissivity of tedlar, ε_T	0.87
Emissivity of insulation upper surface, ε_I	0.1
Thickness of insulation, L_I	0.02 m
Conductivity of insulating sheet, K_I	0.025 W/(m K)
Equivalent duct depth	0.04 m and 0.06 m
Packing factor of solar cells, p	0.83
Electrical efficiency at Standard Conditions, η_{REF}	0.1866
Solar cells temperature at Standard Conditions, T_{REF}	298 K
Solar radiation intensity at Standard Conditions, I_{REF}	1000 W/m^2

3.3.5. Integrated Solar Chimney Performance Evaluation

To evaluate the impact of integrating SC with the EAHE and PV systems on overall efficiency and PV's electricity generation.

1. Installation: The SC integrated with the proposed system was available in several sizes, lengths, and colors, according to the case study in this research.
2. In this research, three types of solar chimneys were used. Two of them are cylindrical, with a length of 1.5 m and a diameter of 0.1 m, one of which is white and the other is black. The third SC was a rectangular channel with a cross-section of dimensions (0.31 x 0.06) m with a length of 1.5 m and black (its hydraulic diameter of 0.1 m). These types were used for comparison purposes, as well as studying the effect of color and shape on the efficiency of the SC.
3. These solar chimneys were connected to the PV/T-a and PV/T-b according to the case study in this research and accordingly, the solar chimneys were named SC-a SC-b respectively.
4. All previous solar chimneys (SC-a and SC-b) were installed vertically on a supporting iron structure as shown in Fig. 3.14.
5. Temperature Measurements: five temperature sensors were used. One temperature sensor was installed to measure the ambient temperature, four temperature sensors were placed at the inlet and outlet of both the SC-a and SC-b to monitor the temperature of the air entering and during the systems to know and understand the performance of the SC-a and SC-b respectively.
6. Continuous Monitoring: Smart Arduino Denkovi-smart-32 was a data-acquisition logger has been used to record temperatures. Additionally, a desktop computer was used to run the display moods to monitor the sensor values. It is set to record every 1 minute.

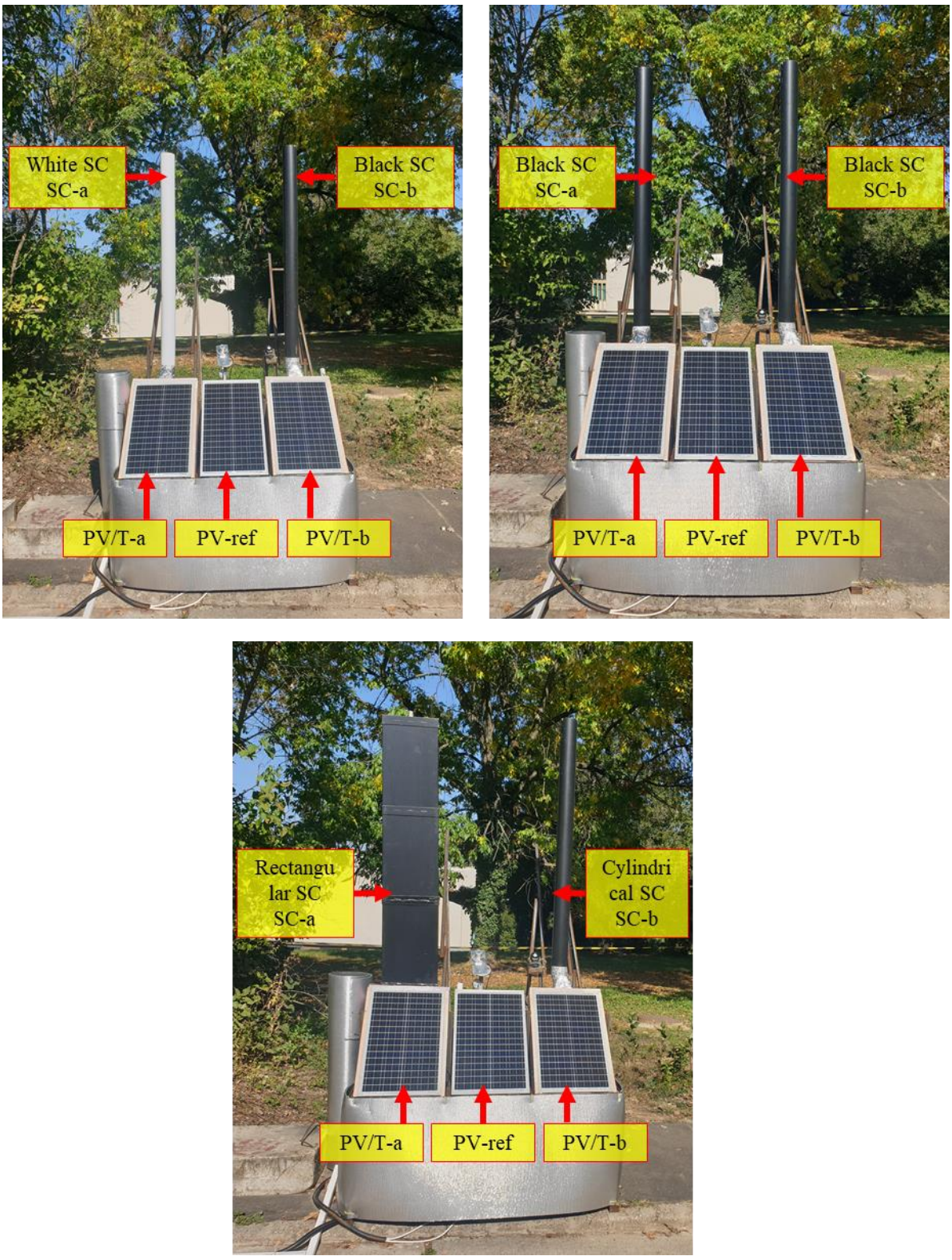

Fig. 3.14. The types of the examined solar chimneys.

3.4. Data Collection Methods

Accurate and comprehensive data collection forms the bedrock of this research study. The following section outlines the meticulous methods employed to gather a diverse range of data, essential for evaluating the performance and efficiency of the integrated renewable energy systems in the study locations, Al-Najaf City, Iraq, and Gödöllő City, Hungary.

3.4.1. Measured Parameters and Instrumentation

The study encompassed many parameters, necessitating specialized instrumentation capable of precise measurements. Table 3.4 illustrated parameters and details of the specific sensors and devices employed were measured. Fig. 3.15 shows the sensors and devices used in the experiments.

Table 3.4. The measured parameters and details of the specific sensors and devices employed.

Measured Parameters	**Sensor Used**		**Device Used**
	Type	**Uncertainty**	
Temperature	Temperature sensor (K-type)	±0.4%	12-channel thermometer LUTRON BTM-4208SD
Temperature	Temperature sensor B57500M103A005 (-55 to +155°C, NTC-type)	±0.5%	SmartDEN Logger - Web-enabled temperature datalogger with analog/digital inputs
Solar radiation	Photoelectric solar radiation sensor	±3%	
Instant current and voltage	Analogue inputs within the SmartDEN-Denkovi data logger	±0.2%	
Airflow velocity	Anemometer, air flow meter with thermometer, USB connection, Voltcraft PL-135HAN	±0.5%	Computer software
Power consumption	Voltmeter maxwell 25304	±0.2%	Display Screen
Thermo-physical properties of soil	Moisture analyzer model HE53 METTLER TOLEDO	±0.5%	Moisture Analyzer
Soil volume	Glass graduated measuring cylinder	±0.5%	-

These sensors and devices were meticulously selected to ensure the accuracy and reliability of data collected during the study. Regular calibration and validation procedures were implemented to maintain measurement precision.

Fig. 3.15. The sensors and devices used in the experiments performed (a) SmartDEN logger, (b) Voltmeter maxwell 25304, (c) 12-channel thermometer, (d) Airflow velocity anemometer, (e) Solar radiation sensor, and (f) Moisture analyzer.

3.4.2. Data Collection Procedure

The data collection procedure involved the following key steps:

1. **Sensor Placement:** Sensors were strategically placed within the study locations, including soil depths, EAHE, PV/T models inlets and outlets, and other relevant positions.
2. **Continuous Monitoring:** Data loggers and sensors were configured to continuously monitor temperature, airflow velocity, solar radiation, and other relevant parameters. Data acquisition intervals were carefully adjusted to capture both short-term variations and long-term trends.
3. **Data Storage and Retrieval:** Collected data were stored in digital format within the data loggers and periodically retrieved for analysis. The storage system ensured data integrity and accessibility throughout the study period.
4. **Quality Control:** Rigorous quality control measures were implemented to identify and rectify any anomalies in the collected data. Sensor calibration checks and periodic maintenance were conducted to minimize measurement errors.
5. **Data Synchronization:** Data from multiple sensors were synchronized to ensure accurate analysis of system performance and environmental conditions.

3.4.3. Data Analysis

The data obtained through the abovementioned methods were comprehensively analyzed using advanced statistical techniques and software tools by using Microsoft Excel spread sheet (Version 2201 Build 16.0.14827.20198) and MATLAB R2017b programming. The analysis aimed to:

- Assess the impact of temperature gradients on the efficiency of the integrated renewable energy systems.
- Evaluate the performance of the EAHE under varying climatic conditions.
- Determine the influence of weather patterns on power generation and system efficiency.
- Validate the accuracy of the developed MATLAB simulation model through comparison with experimental data.

The resulting data and analysis form the basis for drawing meaningful conclusions and insights into the behavior of the hybrid system under real-world conditions.

3.5. Simulation Model Development

The development of a robust and comprehensive MATLAB simulation model is a cornerstone of this research. This section delineates the intricacies of model development, including key equations, parameters, and validation procedures. The model is a powerful tool for assessing the behavior and performance of integrated renewable energy systems (EAHE, SC, and PV modules) under varying climatic conditions.

The primary objective of the MATLAB simulation model is to replicate the behavior of the integrated systems in a virtual environment. The model is constructed based on principles of heat transfer, fluid dynamics, and electrical performance. The model incorporates the following fundamental equations and algorithms:

1. **Heat Transfer Equations**: Heat transfer within the soil, air, and PV modules is governed by the heat conduction equation, accounting for thermal conductivity, heat capacity, and temperature gradients.
2. **Fluid Flow Equations**: Fluid flow within the PV/T module, SC, and EAHE is modeled using fluid dynamics equations, considering airflow velocity, cross-sectional areas, and pressure differentials.
3. **Photovoltaic Power Generation**: The electrical performance of PV modules was designed and calculated using the equations for calculating PV cell productivity, taking into account solar radiation, temperature, and electrical characteristics of the modules.

4. **System Integration**: The model integrates these equations to simulate the performance of the entire hybrid system, including the influence of soil temperature gradients on heat exchange.

Accurate parameter estimation and validation are essential for ensuring the model's accuracy in replicating real-world conditions. The following steps were undertaken:

1. **Parameter Estimation**: Parameters such as soil thermo-physical properties, system efficiencies, meteorological data, and electrical characteristics of PV modules were estimated based on empirical measurements and literature values.
2. **Validation Against Empirical Data**: The model was rigorously validated by comparing its predictions with empirical data obtained from field experiments. Temperature profiles, airflow velocities, and electrical outputs were analyzed for congruence between model predictions and actual measurements.
3. **Calibration and Adjustment**: Any disparities between model predictions and empirical data were addressed through calibration and adjustment of model parameters. The iterative process ensured alignment with real-world observations.

The developed MATLAB simulation model is a versatile tool with the following capabilities:

1. **System Evaluation**: The model can simulate the performance of the integrated renewable energy systems, allowing for the assessment of individual components and their interplay.
2. **Climate Variability**: It accommodates climate variability by accepting meteorological data as input, enabling simulations under various weather conditions.
3. **Global Applicability**: The model can be applied to different geographic locations by inputting location-specific data, making it a versatile tool for future studies.

Model validation and verification procedures were conducted to ascertain its accuracy and reliability.

1. **Validation**: Validation was performed by comparing model predictions with empirical data from field experiments, ensuring that the model accurately replicates real-world behavior.
2. **Verification**: Model verification was carried out through rigorous testing against established analytical solutions and benchmark cases to confirm its computational accuracy and stability.

The MATLAB simulation model, once validated, can be a valuable resource for future studies and research endeavors.

1. **Accessibility**: The model will be made available for use by the scientific community, reducing the time, cost, and effort required for similar investigations.
2. **Further Analysis**: It can be employed for in-depth analyses, exploring additional scenarios and configurations of integrated renewable energy systems.
3. **Parameter Studies**: The model allows for sensitivity studies to assess the influence of different parameters on system performance.

The following sections will present a comprehensive overview of the mathematical equations and models used to develop the MATLAB simulation model and draw conclusions.

3.5.1. Mathematical modeling for Soil gradient and Earth-Air Heat Exchanger

Polyvinyl chloride (PVC) is the main ingredient of an EAHE. The buried pipe's length and diameter are employed in the thermal analysis. To use an EAHE, you'll need a powerful blower to move hot exterior air down into the pipe, where it will be cooled. Heat is transferred to the ground at a lower temperature, thus lowering the air temperature. Afterward, the cooled air is pumped into the building or any other space, such as via a PV module system, etc. Table 3.5 depicts air and

pipe's physical and thermal characteristics, whereas Table 3.6 summarizes the EAHE parameters utilized in this simulation.

Table 3.5. This study utilized the physical and thermal properties of pipe and air (Bansal et al., 2009).

Material	Air	PVC
Density (kg/m^3)	1.225	1380
Thermal conductivity (W/m.K)	0.0242	0.16
Heat capacity (J/kg.K)	1006	900

Table 3.6. The EAHE parameters utilized in the simulation.

Parameter	Reference value (m)
Pipe length	10
Pipe diameter	0.1
Pipe depth	2

A consistent airflow within the pipe may further simplify the configuration mentioned. The surrounding soil's thermal qualities are assumed to be homogeneous and constant, as are the pipe's size and physical attributes. Monthly maximum and lowest temperatures were recorded experimentally to simulate the place under investigation.

The model is based on energy balance equations when the ground temperature remains constant. EAHE air temperature fluctuates throughout the pipe's length, considering ambient air temperature, soil temperature at a particular depth, geometries and types of the pipes, and air velocity.

3.5.1.1. Soil temperature modeling

Soil properties that determine its response to temperature changes at the surface are volumetric heat capacity, C_v, soil thermal conductivity, k_{soil}, and water content (moisture), w (Abbas and Al-Naseri, 2008). The method for sizing the EAHE requires knowledge of the minimum and maximum ground temperature at the EAHE depth. The undisturbed ground temperature, T_{soil}, expressed in °C, can be calculated using (Han et al., 2021):

$$T_{soil}(z,t) = T_{mean} + A_o \exp(-z/d)\,[\sin((2\pi(t - t_o)/365) - (z/d) - (\pi/2))] \quad (3.14)$$

In which T_{soil} (z,t) denotes the temperature of the soil at time t (day) and depth z (m), T_{mean} defines the average ambient temperature (^{o}C), A_o connotes the annual amplitude of the ambient temperature (^{o}C), which is given by Eq. (3.15), d is the damping depth (m) of annual fluctuation and t_o is the time lag (days) between an arbitrary starting date (considered as Jan. 1) and the Eq. (3.16) calculates the damping depth as follows (Han et al., 2021):

$$A_o = (T_{max} - T_{min})/2 \quad (3.15)$$

$$d = (2\alpha/\gamma)^{1/2} \quad (3.16)$$

Where α is the thermal diffusivity (m^2/day), the heat transfer coefficient (thermal diffusivity) is a parameter that indicates how well the ground conducts heat in proportion to its thermal capacity. It may be computed using Eq. (3.17). In which $\gamma = 2\pi / 365$ (1/day) (Mortaza et al., 2005).

$$\alpha = k_{soil} / (C_{p,soil}\, \rho_{soil}) \quad (3.17)$$

Where $C_{p,soil}$ is the specific heat capacity of the soil (J/kg.K) and ρ_{soil} is the soil density (kg/m^3). Due to the fact that heat conducts more quickly as compared to thermal mass, a high thermal diffusivity value is desired (Le Feuvre, 2007). In order to determine these thermal characteristics, Eqs. ((3.18)-(3.21)) have been utilized to develop analytical equations:

$$k_{soil} = 0.14423\,(0.9 \log(w) - 0.2)\, 10^{\,0.000642\,\rho_d} \quad \text{(For silt and clay soils)} \quad (3.18)$$

$$k_{soil} = 0.14423\,(0.7 \log(w) + 0.4)\, 10^{\,0.000642\,\rho_d} \quad \text{(For sand soil)} \quad (3.19)$$

In this equation, ρ_d is the dry soil density. The adjusted specific heat capacity of soil may be calculated as follows:

$$C_{p,soil} = \frac{[w\, C_{pw} + (100 - w)\, C_{pd}]}{100} \quad (3.20)$$

C_{pw} is water's specific heat capacity (4180 J/kg.K), and C_{pd} is the soil's dry specific heat capacity (840 J/kg.K). The corrected density of soil may be given by:

$$\rho_{soil} = \frac{[w\, \rho_w + (100 - w)\, \rho_d]}{100} \quad (3.21)$$

Where: ρ_w is the density of water.

3.5.1.2. Earth-air heat exchanger modeling

The PVC pipe is buried to a certain depth, determined using the data and sources provided. Temperature is defined as "relatively constant" in Eq. (3.14) to pick the buried depth in this study. It is possible to estimate the length of the tube and the amount of land needed to bury the pipe by utilizing the design scheme based on the desired performance. The most significant equations and techniques for obtaining the required data to complete the EAHE design are summarized (Ali et al., 2021).

Definition of limits: Relative pressure was zero atm at the EAHE pipe's exit (Subsonic flow regime). The static air inlet temperature $T_{in\text{-}EAHE}$ (°C), and airflow velocity v_a (m/s) must be specified at the EAHE pipe's inlet or outlet. At a static inlet air temperature, the thermodynamic and transport parameters of air, such as its specific heat capacity C_p (J/kg K), density ρ (kg/m^3), thermal conductivity K (W/m K), and dynamic viscosity μ (kg/m s), may be determined (Muehleisen, 2012; Bisoniya, 2015). Temperatures on the pipe surface (wall) were specified to equal the earth's temperature at a certain depth and distributed equally in the longitudinal direction. The depth of the buried pipe is particular to the design goal based on the distribution of the earth's temperature.

The convective heat transfer coefficient (CHTC) during the pipe is characterized by:

$$h = \frac{Nu\, K}{D} \quad (3.22)$$

A PVC EAHE with a total burial length of L_{pipe} and an inner diameter of D_{pipe} was examined in this research. The Nu correlations described in (De Paepe and Janssens, 2003) may be utilized to simulate the performance of the EAHE if the inside surface of PVC pipes used in the EAHE is smooth.

$$Nu = \frac{\left(\frac{f}{8}\right)(Re - 1000)Pr}{1 + 12.7\sqrt{\frac{f}{8}}\,(Pr^{\frac{2}{3}} - 1)} \tag{3.23}$$

$$f = (1.82\ logRe - 1.64)^{-2} \tag{3.24}$$

If $5 \times 10^6 > Re \geq 2300$ and $10^6 > Pr > 0.5$

The Reynolds number is related to the average air velocity and diameter:

$$Re\ = \frac{D_{pipe}\ \rho v_a}{\mu} \tag{3.25}$$

The Prandtl number is given by:

$$Pr = \frac{\mu\ C_p}{k} \tag{3.26}$$

- Effectiveness of the EAHE and construction.

The air passing through a buried pipe loses or absorbs the following amount of heat:

$$Q = \dot{m}\ C_p\ (T_{in} - T_{out}) \tag{3.27}$$

The mass flow rate of air.

$$\dot{m} = N_p\ \frac{\pi}{4}\ {D_{pipe}}^2\ \rho\ v_a \tag{3.28}$$

The following equation may also provide the transferred heat due to convection between the airflow and the wall pipe:

$$Q = h\ A_{surf.}\ \Delta T_{lm} \tag{3.29}$$

The diameter and the length of the EAHE affect the pipe's internal surface area (A_{surf}).

$$A_{surf} = \pi\ D_{pipe}\ L_{pipe} \tag{3.30}$$

$$\Delta T_{lm} = \frac{T_{in-EAHE} - T_{out-EAHE}}{ln\frac{T_{in-EAHE} - T_{wall}}{T_{out-EAHE} - T_{wall}}} \tag{3.31}$$

The following is the temperature of the air outlet at x=L:

$$T_{out-EAHE,L} = T_{soil} + (T_{in-EAHE} - T_{soil})\ exp\text{^}(((-\pi\ D_{pipe}\ L_{pipe}\ h)\ /\ (\dot{m}\ C_p))) \tag{3.32}$$

The EAHE efficiency, η_{EAHE}, as:

$$\eta_{EAHE} = 1 - exp^{-(\frac{hA}{\dot{m}\ C_p})} = \frac{T_{out} - T_{in}}{T_{soil} - T_{in}} \tag{3.33}$$

The pressure drop in a smooth pipe is given by:

$$\Delta p = f \frac{L}{D} \rho \frac{{v_a}^2}{2} \quad (3.34)$$

To calculate the pressure drop in the pipe as a result of bends in the pipe:

$$\Delta p_{loss} = C_{loss} \rho \frac{v_a^2}{2} \quad (3.35)$$

Where C_{loss} is the bend loss coefficient can be gotten from fitting the measured data introduced in the ASHRAE Handbook (ASHRAE, 2009) to a quadratic condition. The results got are:

$$C_{loss} = 0.09057 - 0.001439 D_{pipe} + 0.001294 D_{pipe}^2 \quad (3.36)$$

Then, the total drop pressure in EAHE (Δp_T) given by:

$$\Delta p_T = \Delta p + \Delta p_{loss} \quad (3.37)$$

The air fan power (AFP) required to move the volume of air (m^3/s) over the total pressure drop Δp_T is then computed as:

$$AFP = V_{air} \ \Delta p_T \quad (3.38)$$

Where: N_p is the number of parallel pipes (-), $T_{out\text{-}EAHE}$: is the temperature of air at outlet of EAHE pipe (°C), ΔT_{lm}: The logarithmic average temperature difference (-), T_{wall}=T_{soil} at a certain depth, Nu: is Nusselt number, V_{air} is the airflow volume, and f: is the friction factor for smooth pipes.

3.5.1.3. Earth-air heat exchanger configurations

This research presents a comparison between four types of configurations that make up the EAHE as shown in Fig. 3.16 All these types consist of the same pipe material, which is PVC, with a total length of 65 m for each type and a diameter of 0.148 m, so that each type transmits the total airflow of each type, which is also the same with an amount of 0.034 m^3/s. All The information included in the comparison process are shown in Table 3.7. The first type consists of a single tube extending horizontally in one direction only and is called a single pipe. The second type consists of a group of pipes (five branches) connected to each other by main pipes of the same diameter to form a U-type multi-pipe EAHE with a connection angle of 90 degrees, and it is called multiple pipes. The third type consists of a different type of tubes configuration, where this type of heat exchanger consists of multiple tubes (five pipes) but separated from each other, unlike the third type in which the tubes are connected to each other and can be called Multiple-Single pipes (MS-EAHE), The airflow in each pipe of the MS-pipe EAHE type is uniform and equivalent to the total airflow divided by the number of branches (five). The fourth type consists of only one tube, but it differs from the first type in that it is twisted to save space, as in a multi-pipe, but it is a single twisted tube, and it can be called Twisted-Single pipes (TS-EAHE).

In order to evaluate the efficiency of a multi-pipe type EAHE, it is crucial to accurately measure and understand the variations in flow ratios between individual tubes. To this end, this study will use the flow ratio data presented by (Amanowicz and Wojtkowiak, 2020a) in its results, which includes detailed tables and figures. This data will be incorporated into the simulation process to ensure an accurate assessment of EAHE performance.

In this comparison, ambient air temperatures that were experimentally measured during the year 2021 in Iraq (Al-Najaf) were adopted (Ali et al., 2023).

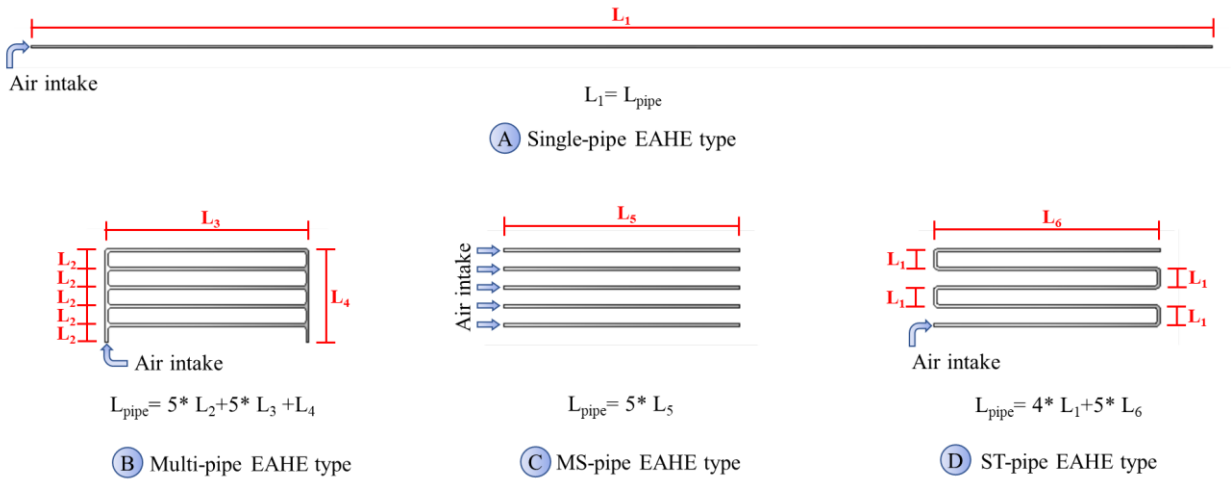

Fig. 3.16. The four heat exchanger configurations utilized compare (L_{pipe}= 65 m, d_{pipe}= 0.148 m, L_1= L_{pipe}= 65 m, L_2=6*d_{pipe}= 0.886 m, L_3= 76*d_{pipe}= 11.227 m, L_4= 5*L_2= 4.432 m, L_5=13 m, and L_6= 12.29 m).

Table 3.7. EAHE parameters for the four heat exchanger configurations utilized to compare.

Type of EAHE	Single pipe EAHE (Pipes in one direction)	Multiple pipe EAHE (Parallel Pipes)	MS-EAHE pipe (Separated Pipes)	TS-EAHE (Pipes in twisted direction)
Total pipe length, (m)	65	65	65	65
Pipes diameter, (m)	0.148	0.148	0.148	0.148
Pipe depth, (m)	6	6	6	6
Total airflow, V (m^3/s)	0.0343	0.0343	0.0343	0.0343
Number of elbows	4	14	20	12
Number of branches	1	5	5	1
Configuration type	Pipes connected in series and one direction (Fig. 3.16 (A))	Connected parallel pipes (Fig. 3.16 (B))	Separate parallel pipes (Fig. 3.16 (C))	Twisted and connected parallel pipes (Fig. 3.16 (D))

3.5.2. Solar chimney system

It is clear from the literature study that airflow behavior is the main factor affecting the overall efficiency of the SC system. Predicting this behavior helps to optimize the system as a whole. To achieve that, it is necessary to have a good knowledge of the laws of heat and mass transfer. The study of chimney behavior in passive solar application is then crucial as it enhances the airflow inside the system.

3.5.2.1. Solar chimney system modeling

The effect of the thermal conductivity in heat transfer is considered significant when dealing with a heat transfer process between the outside and inside chimneys. Still, the physical and mechanical properties of the chimney material will not be accounted in this study. The chimney should be

designed so that the rate of heat losses should be considered in determining the optimum height so as not to exceed the height at which the chimney air cools to the same temperature as ambient. The design will maintain mean chimney temperatures above ambient temperature, which produce a pressure difference or stack effect and given in the equation as (Ekechukwu and Norton, 1997):

$$\Delta P_{stack} = gH\Delta\rho = gH(\rho_a - \bar{\rho}_{ch}) = \rho gH(T_{ch} - T_a) \tag{3.39}$$

Assuming that the flow is turbulent flow with the average density of the air through the cylindrical duct, the velocity can be given as a function of temperature change across the chimney:

$$v = 0.453\left[\frac{Dg\Delta T_{ch}}{\dot{\rho}}\right]^{1/2} \tag{3.40}$$

From experimental data, the mean airflow temperature inside the chimney and the ambient air temperature can easily be found, and the average density was calculated from the equation:

$$\dot{\rho} = 1.11363 - 0.00308\,T \tag{3.41}$$

Where: g: Acceleration due to gravity (m/s), H: Chimney height (m), ΔP_{stack}: Pressure drop due to buoyancy (N/m^2), T_a: Ambient air temperature (K), T_{ch}: Mean chimney air temperature (k), ρ: Air density (kg/m^3), ρ_a: Ambient air density (kg/m^3), ρ_{ch}: Mean chimney air density (kg/m^3), v: Velocity of the air (m/s), D: Duct diameter (i.e. chimney diameter) (m), ΔT_{ch}: Mean chimney temperature elevation above ambient temperature (K), $\bar{\rho}$: Mean air density (kg/m^3) and T: is air temperature (K).

3.5.3. Photovoltaic solar system

It is clear from the literature study that the weather conditions are the main factors affecting the overall efficiency of the PV module. Predicting this behavior helps to optimize the system as a whole. In order to achieve this, it is necessary to have a good knowledge of the laws of heat and mass transfer.

3.5.3.1. Mathematical model for photovoltaic module

A PV cell is a p-n junction fabricated in a thin semiconductor wafer. The electromagnetic radiation of solar energy can be directly converted to electricity through the photovoltaic effect. Being exposed to sunlight, photons with energy greater than the band gap energy of the semiconductor creates some electron-hole pairs proportional to the incident irradiation (Dhinesh et al., 2020).

PV cells are grouped in larger units called PV modules, which are further interconnected to form PV arrays in a parallel series configuration. The PV module can be modeled mathematically as given in Eqs. ((3.42)-(3.45)) (Chowdhury et al., 2008; Nema et al., 2010; Pandiarajan and Muthu, 2011).

$$I_{ph} = [I_{SCr} + K_i(T - 298)] * \lambda/1000. \tag{3.42}$$

$$I_{rs} = I_{SCr}/[\exp\left(\frac{qV_{OC}}{N_s kAT}\right) - 1] \tag{3.43}$$

$$I_o = I_{rs}[\frac{T}{T_r}]^3 \exp[\frac{q*E_{g0}}{Bk}\left\{\frac{1}{T_r} - \frac{1}{T}\right\}] \tag{3.44}$$

$$I_{PV} = N_P * I_{ph} - N_P * I_o[exp\left\{\frac{q * (V_{PV} + I_{PV}R_S)}{N_S AkT}\right\} - 1] \quad (3.45)$$

Where: I_{ph}: The light generated current in a PV module (A), I_{SCr}: The PV module short-circuit current at 25 °C and 1000W/m^2 = 2.55A, K_i: The short-circuit current temperature co-efficient at I_{SCr} = 0.0017A /°C, T: The module operating temperature in Kelvin, λ: The PV module illumination (W/m2) = 1000W/m^2, I_{rs}: The PV Module reverse saturation current (A), q: Electron charge = 1.6 × 10-19 C, N_s: The number of cells connected in series, σ: Boltzman constant = 1.3805 × 10-23 J/K, $A = B$: an ideality factor = 1.6, I_0: Module saturation current (A), T_r: the reference temperature = 298 K, E_{g0}: the band gap for silicon = 1.1 eV, I_{pv}: Output current of a PV module (A), V_{pv}: Output voltage of a PV module (V), R_s: The series resistance of a PV module, N_p: The number of cells connected in parallel, and P_{PV} is the extracted PV power (W).

3.5.4. Mathematical modeling PV/T hybrid system

3.5.4.1. Configuration of a simple PV/T hybrid system

The specific configuration of the hybrid PV/T system studied consists of a PV module combined with a SC and an EAHE. A typical structure of the system is shown in Fig. 3.17. For such a system, a one-dimensional thermal model is formulated based on models reported in the literature (A. Tiwari et al., 2006; Dubey and Tiwari, 2008; Dubey et al., 2009; Joshi et al., 2009; Sarhaddi et al., 2010). The energy balance equations were modified considering the radiation between the back surface of the PV module and the opposite wall of the channel. Fig. 3.18 shows a simplified cross-section view of a PV/T air collector consisting of three layers. Moreover, the equivalent thermal resistance circuit of the system discussed in this section is also shown in Fig. 3.18.

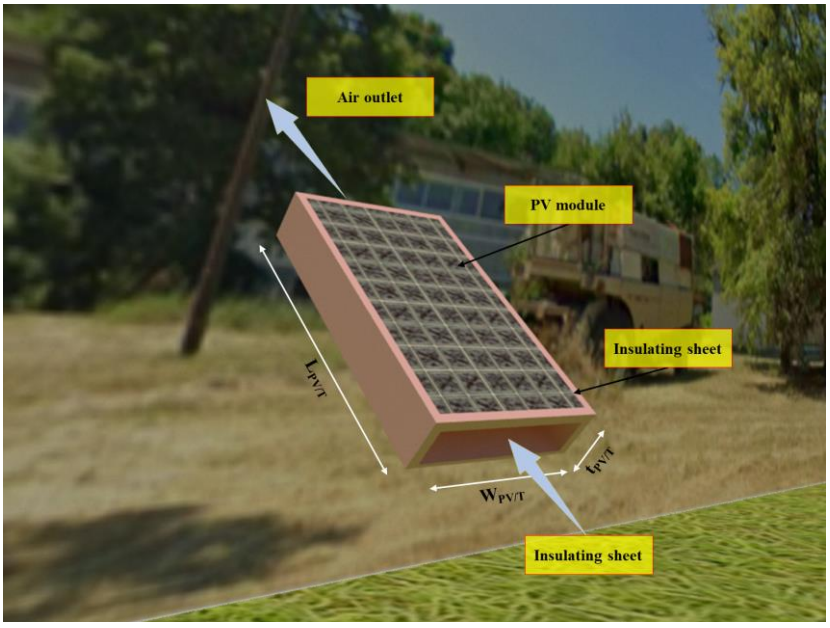

Fig. 3.17. Perspective view of the hybrid PV/T system studied.

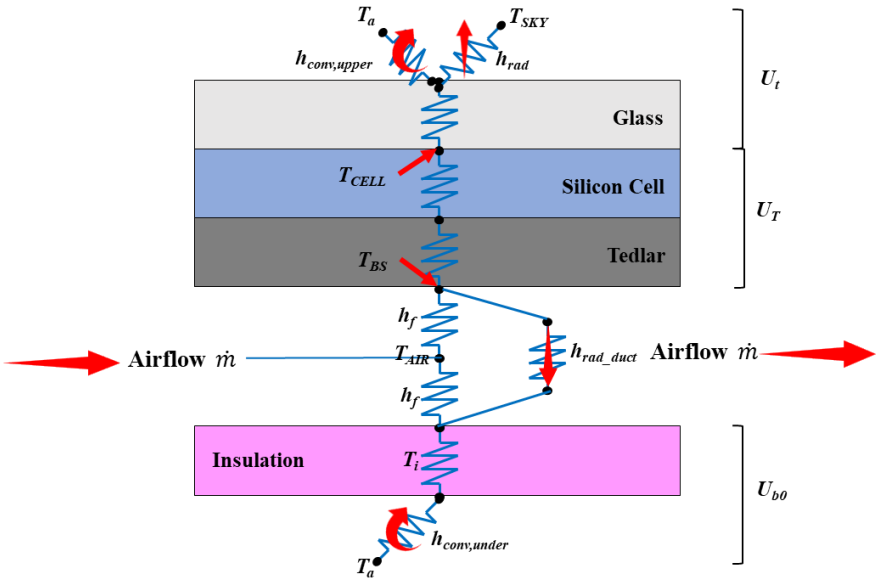

Fig. 3.18 Thermal resistance circuit diagram for PV/T collector.

- Energy balance for PV/T hybrid system

To formulate the energy balance equations for each component of the PV/T hybrid system, the following assumptions have been made:

▪ The heat conduction is one-dimensional (only along the height of the module).

▪ The temperature of the model layers is uniform.

▪ The system is in a quasi-steady state.

▪ The ohmic losses in the solar cell are negligible.

▪ Air flow in the duct between a Tedlar layer and an insulating structure is one-dimensional.

Four energy balance equations must be written to determine solar cell temperatures and the system's efficiency. According to Fig. 3.18, the total heat transfer equation from the upper side of the module to the ambient under the insulation can be written as follows:

$$\tau_G \cdot [\alpha_{CELL} \cdot p \cdot I + (1-p) \cdot \alpha_T \cdot I] \cdot b \cdot dx = [U_t \cdot (T_{CELL} - T_{AMB}) + U_T \cdot (T_{CELL} - T_{BS})] \cdot b \cdot dx + \alpha_{CELL} \cdot \eta_{CELL} \cdot p \cdot \tau_G \cdot I \cdot b \cdot dx \quad (3.46)$$

Where the terms in Eq. (3.46) are the following:

1- The rate of solar energy available on PV. = 2- An overall heat loss from the top surface of PV to the ambient. + 3- An overall heat transfer from PV to the back surface of Tedlar. + 4- The rate of electrical energy produced.

The second energy balance equation describes the heat transfer for back surface of tedlar:

$$U_T \cdot (T_{CELL} - T_{BS}) \cdot b \cdot dx = h_f \cdot (T_{BS} - T_{AIR}) \cdot b \cdot dx + h_{RAD\_DUCT} \cdot (T_{BS} - T_I) \cdot b \cdot dx \quad (3.47)$$

Where the terms in Eq. (3.47) are the following:

3- An overall heat transfer from PV to the back surface of Tedlar. = 5 - The rate of heat transfer from back surface of the tedlar to flowing fluid. + 6- The rate of heat transfer from the back surface of Tedlar to the insulation's upper surface.

The following equation is the overall duct energy balance:

$$h_f \cdot (T_{BS} - T_{AIR}) \cdot b \cdot dx + h_{RAD\_DUCT} \cdot (T_{BS} - T_I) \cdot b \cdot dx = \dot{m_{AIR}} \cdot C_{AIR} \cdot \frac{dT_{AIR}}{dx} \cdot dx + U_{b0} \cdot (T_I - T_{AMB}) \cdot b \cdot dx \quad (3.48)$$

Where the terms in Eq. (3.48) are the following:

5 - The rate of heat transfer from back surface of the tedlar to flowing fluid. + 6- The rate of heat transfer from the back surface of Tedlar to the insulation's upper surface. = 7- The mass flowrate of flowing fluid + 8- An overall heat transfer from the upper surface of insulation to the ambient.

Finally, the fourth energy balance equation for the upper surface of insulation can be written as:

$$h_{RAD\_DUCT} \cdot (T_{BS} - T_I) \cdot b \cdot dx = U_{b0} \cdot (T_I - T_{AMB}) \cdot b \cdot dx + h_f \cdot (T_I - T_{AIR}) \cdot b \cdot dx \quad (3.49)$$

Where the terms in Eq. (3.48) are the following:

6- The rate of heat transfer from the back surface of Tedlar to the insulation's upper surface. = 8- An overall heat transfer from the upper surface of insulation to the ambient. + 9- The rate of heat transfer from the upper surface of insulation to flowing fluid.

The mathematical transformations to obtain the explicit formula for all temperatures, as well as the relationships used in equations ((3.46)-(3.49)) for the heat transfer coefficients and the assumptions adopted for calculating radiant heat and the transfer coefficient are described in the Appendix(A3).

To calculate the temperature-dependent electrical efficiency of the PV module, the following expression has been used (Evans, 1981; Schott, 1985; Rahman et al., 2017):

$$\eta_{CELL} = \eta_{REF} \cdot [1 - \beta \cdot (T_{CELL} - T_{REF})] \quad (3.50)$$

The rate of thermal energy obtained from the hybrid system is:

$$\dot{Q}_U = \dot{m}_{AIR} \cdot C_{AIR} \cdot \left(T_{AIR}(L_D) - T_{AIR\_IN}\right) \quad (3.51)$$

The thermal efficiency of the PV/T system has been calculated using the following equation:

$$\eta_{TH} = \frac{\dot{Q}_U}{b \cdot L_D \cdot I} \quad (3.52)$$

3.5.4.2.Temperature of the back surface of the PV module

The heat transfer between the back surface of the PV module and the air flowing in the duct should be optimized to achieve the most significant temperature reduction of PV cells.

The convective heat transfer coefficient (h_f), which identifies the amount of heat exchanged between the module and the air flow rate, the Nusselt number, and the friction factor has been calculated and then uses these values to evaluate the pressure drop along the duct and the mentioned convective heat transfer coefficient. The input parameters of that function are the size of the duct (width, height, length), the average airflow temperature, pressure, and the air mass flow rate.

3.5.5. Hybrid (PV, EAHE and SC) system

For EAHE to work, they must be designed to determine the preferred length, diameter, and material of the pipe, as well as how much heat is transferred to it, what velocity of supplied airflow is appropriate for the space to be conditioned, and how much energy is required to circulate it. These variables are determined by calculating the expected inlet air temperature, mass flow rate, and outlet air temperature. Everything is subject to change depending on the soil temperature at a certain depth.

For PV modules to perform well, their systems must be designed so that they can make the most of the solar radiation falling on them under the surrounding weather conditions, including the temperature of the surrounding air and the speed of the wind, and therefore the amount of power generated from them, especially when integrated with other systems such as the EAHE. These variables are determined by calculating the expected inlet air temperature coming from the EAHE, the mass flow rate, the outlet air temperature, and the temperature of the PV module after it has cooled. Everything is subject to change depending on the temperature of the PV module at a particular location.

The same applies to the SC, as its design requires specifying its dimensions and components and comparing the temperature of the air entering it with the temperature of the surrounding air for the purpose of obtaining the required difference for the purpose of generating a suitable airflow to cool the PV module integrated with it. As a result, everything can be changed depending on the temperature of the PV module at a specific location.

Eqs (2.1), ((3.1)-(3.52)), and Eqs. in Appendix (A3) were used. The mathematical and programming connection was made between them all to build the MATLAB/Simulink model (as shown in Fig. 3.19). Anywhere in the world, using this model, designers can know the temperature distribution at different depths in the soil. It also calculates the physical and thermal properties of the desired soil location. The temperature of the PV module, the power generated, and its efficiency. Determine the appropriate dimensions of the SC through which sufficient airflow can be developed to move the air and pull it from the surrounding atmosphere through the EAHE passing through the PV and then to the SAC that was specially integrated to raise the temperature of the air entering the SC, which in turn pushes the air into the surrounding atmosphere at the end course.

It is observed in this simulation, using equations, that simple underground pipes connected to a building or space can essentially manage the internal temperature comfort of the structure and thus help save energy in hot and dry climates such as AL-Najaf, Iraq and cold and temperate such as Gödöllő, Hungary. The airflow ratios given in (Amanowicz and Wojtkowiak, 2020a) were used to simulate multi-pipe exchangers, and the simulation results are presented in this study.

By using this model, designers can design and estimate the performance of the SC-PV-EAHE system in different locations in the world, as it has a good ability to estimate the length of the tube and the land area required to bury the pipe sufficient to cool the air needed to cool the PV module integrated with the SC.

The final form of the model is illustrated in Fig. 3.19. It takes ambient temperature, solar radiation, and soil temperature and assumed the pipe diameter of EAHE, PV system dimension, the aimed mass flow rate, and the dimension of cross-section area of SC. When running this model, we need 5 seconds to get all the needed data, such as the length of EAHE, the height of SC and current, voltage, and power resulting from this suggested hybrid system.

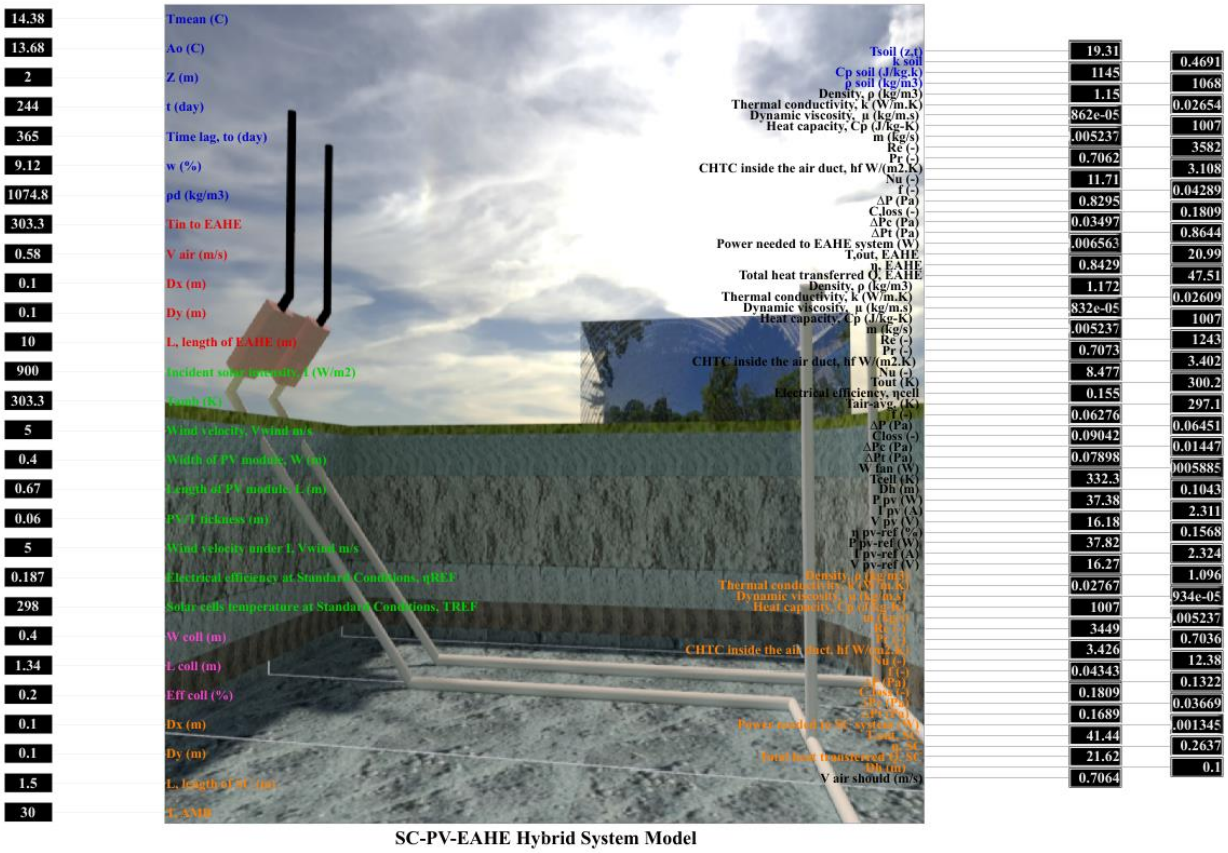

Fig. 3.19 Simulink model of the hybrid system.

3.6. Experiments and tests conducted by this study

Many practical experiments, tests, and simulations were conducted using the developed MATLAB model. This chapter listed the work methodology adopted to achieve it as best as possible. All the materials and installation methods and the devices and techniques used to use them were listed. The hypotheses that were taken into consideration were listed. We summarize here all the experiments and tests that were conducted during this research, which are as follows:

1. Verification of the new MATLAB simulation model by comparing the simulated MATLAB results with the results of practical experiments in Gödöllő.
2. Measurement of the temperature gradient at the two study locations in Al-Najaf, Iraq and Gödöllő, Hungary.
3. Measurement of the thermo-physical properties of soil at the study location in Gödöllő. And developing a new methodology to measure the thermal properties of multi-layered soil practically, theoretically, and programming.
4. Evaluating the effect of soil thermo-physical properties on air temperature inside EAHE.
5. Evaluating the performance of the EAHE practically for a platform system at the study location in Gödöllő. In two modes (cooling and heating).
6. Studying the effect of different configurations on the performance of the EAHE by testing four types of EAHE.
7. Evaluation of the performance of the PV module integrated with the EAHE and the SC. This Evaluation was done through the following case studies.

- Investigating the effect of natural ventilation using a SC on the performance of the PV module.
  1) The effect of the solar chimney on the PV module efficiency.
  2) The impact of solar chimney color on the PV module efficiency.
  3) The effect of solar chimney shape on the PV module efficiency.
  4) The effect of the EAHE length on the PV module efficiency.

5) The effect of duct depth of PV/T on the efficiency of the PV module.
6) The effect of the EAHE on the PV module efficiency.

- Investigating the effect of forced ventilation on the performance of the PV module.
  1) The effect of forced air (0.5 m/s) and EAHE on the PV module efficiency.
  2) The effect of forced air (1 m/s) and EAHE on the PV module efficiency.
  3) The effect of forced air (1.5 m/s) and EAHE on the PV module efficiency.
- Investigating the effect of SAC integration on the performance of the PV module.
  1) The effect of SAC on the efficiency of PV modules.
  2) The effect of solar air collectors on the efficiency of the PV module in different climates.

Figs. 3.20, 3.21, and 3.22 illustrate the three-dimensional schematic of experiments evaluating natural ventilation experiments by SC, forced ventilation experiments, and the effect of incorporating SAC on the performance of PV modules when combined with EAHE and SC.

This chapter detailed the data collection methods and instrumentation used to gather critical information for the study. It underscores the precision and rigor employed to ensure the reliability of the data collected, which is essential for the scientific validity of the research findings.

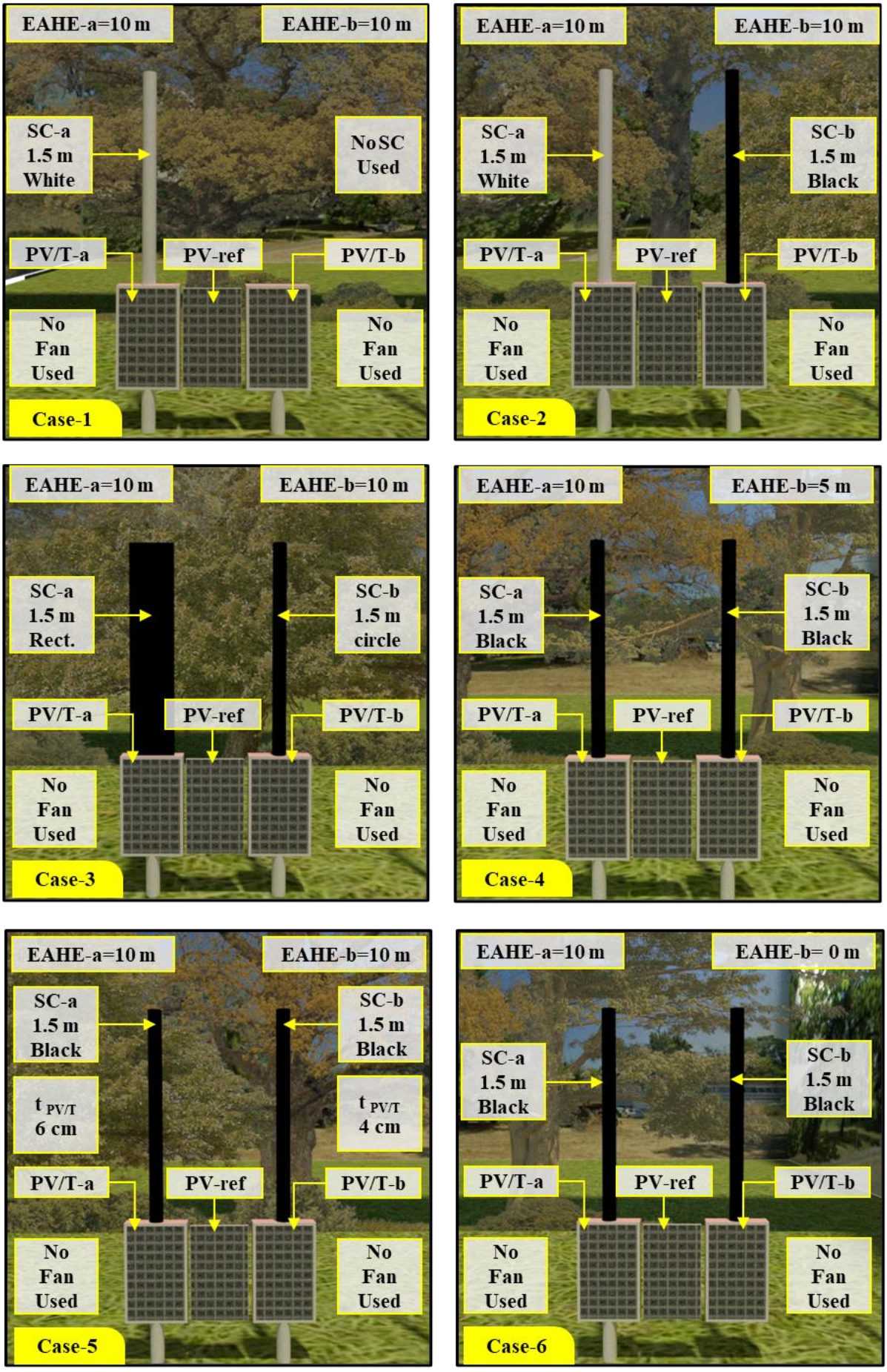

Fig. 3.20. The three-dimensional schematic of natural ventilation experiments by SC to evaluate the performance of PV modules when combined with EAHE.

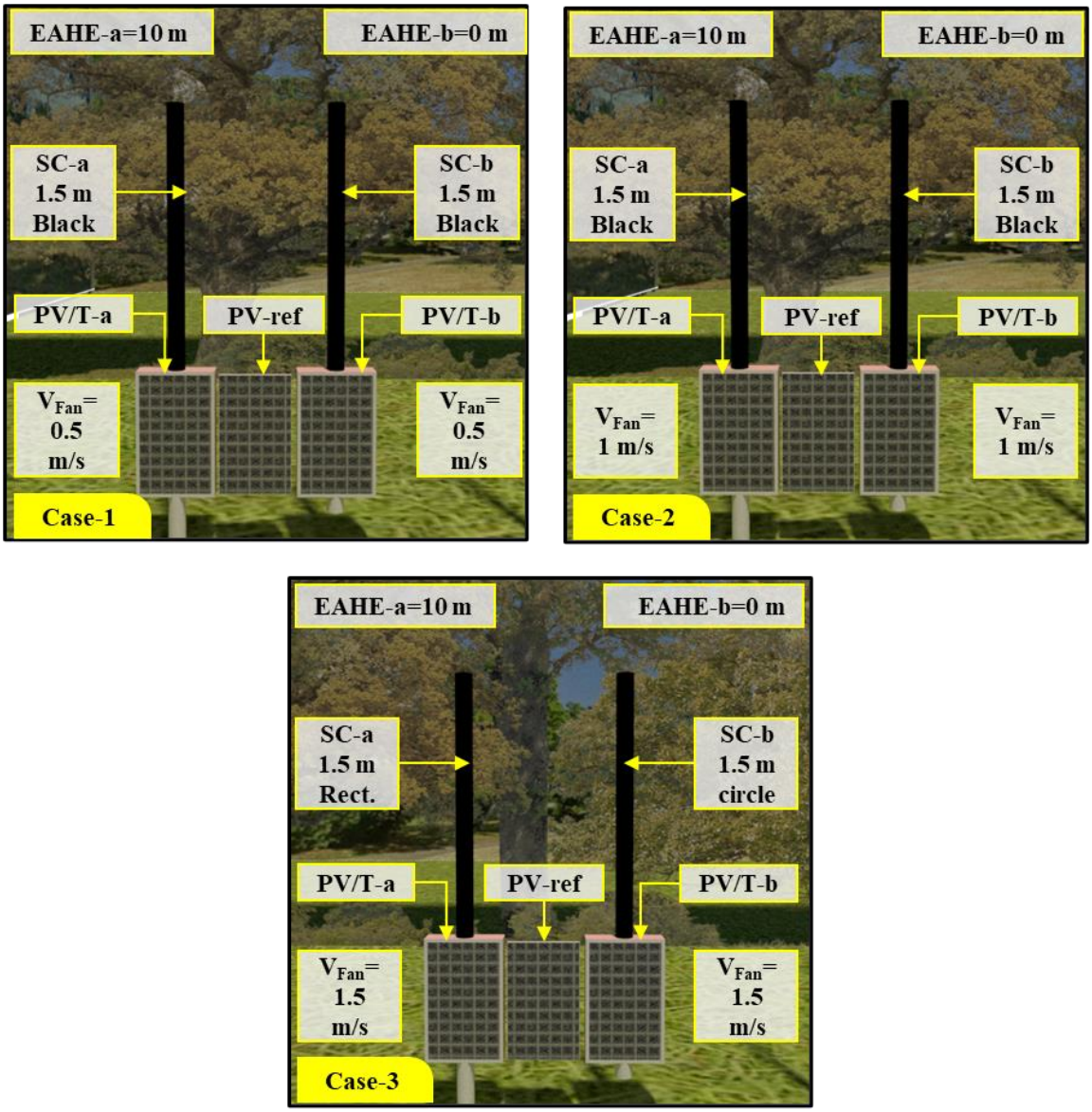

Fig. 3.21. The three-dimensional schematic of forced ventilation experiments to evaluate the performance of PV modules when combined with EAHE.

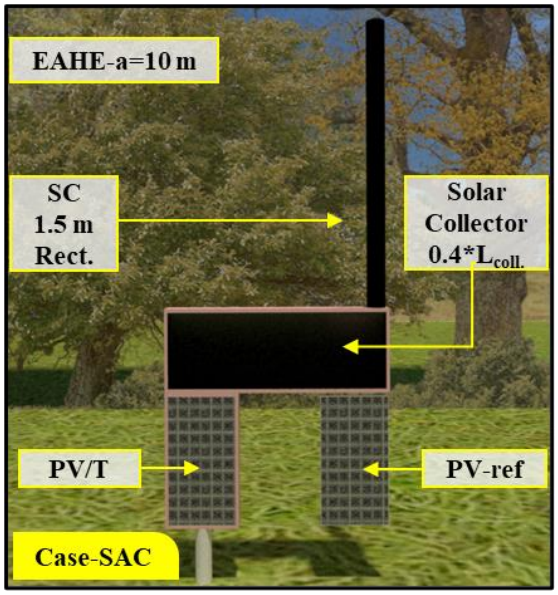

Fig. 3.22. The three-dimensional schematic of experiments evaluating the effect of incorporating SAC on the performance of PV modules when combined with EAHE and SC.

4. RESULTS AND DISCUSSION

The experiments' results are presented in this chapter, along with discussions, suggestions, and new findings. The chapter includes the experimental studies conducted to specify the temperature gradient analysis for Gödöllő and Al-Najaf soils, thermo-physical properties of soil experimentally and suggest a new methodology for measuring and calculating them, the performance of EAHE installed in Gödöllő in heating and cooling modes, the efficiency of the PV modules; PV modules alone versus PV modules integrated with a new hybrid system (PV-SC-EAHE). Moreover, the chapter also involved the extended MATLAB simulations verified on the installed PV-SC-EAHE system in Gödöllő. In the end, the new findings drawn from the studies are listed.

4.1. Model Validation and Analysis

Verification helps ensure that the simulated model accurately reflects the behavior of the real system. This means you have an accurate and robust system analysis and design tool. It also helps reduce the risks associated with implementing the system in actual work. If it is verified that the model corresponds well with reality, you increase the chances of project success and reduce the possibility of unexpected problems. By better understanding the model's performance and how well it fits the actual data, you can use this knowledge to optimize and design the hybrid system and adapt parameters and components to ensure better performance. When you know precisely how a change in a particular parameter affects performance, you can direct your efforts and resources to improve that parameter. In addition, the verification results can help guide future research and development of the hybrid system. Evidence gathered from the validation process can be used to suggest modifications or improvements or recommend future research directions.

In general, verification significantly impacts the design of the hybrid system and understanding how different components and parameters interact. It can help in achieving better performance and optimum utilization of available resources.

Therefore, one of the priorities of this study is to verify the new MATLAB simulation model developed to test its accuracy while taking all required measures to achieve the necessary precision (described in section 3.5). Accordingly, the model was verified using experimental data obtained through experiments and tests completed at the study location in Gödöllő.

Many interim verification tests were applied during the stages of its construction and after the construction process's completion. It was modified based on the recorded results to reach the current necessary accuracy. Through this section of this research, one of the tests was conducted by measuring and simulating the necessary parameters after the completion of its construction, as well as after the completion of installing the entire hybrid system at the study location. Due to the large number of data and its complexity, it will display only the main parameters of each component system of the hybrid system in an integrated state of connection between all its components. Due to the large amount and complexity of data, the main parameters that impact the performance of the parts of the entire hybrid system and each system individually will be presented.

Fig. 4.1 shows measured soil temperature data compared to simulated predictions over time. Based on the data provided, it has been observed that there is a difference between the measured data and MATLAB model predictions. During the middle of the examination period, it appeared that the difference between the measured data and the model predictions began to split, as the measured data began to increase while the simulated predictions continued to stabilize. After that, the measured data and the simulated predictions started to come closer together.

There could be several reasons for the difference between the measured soil temperature and the simulated predictions. Actual conditions may not be adequately captured within the simulation

model, and changing climate conditions may have directly affected soil temperature. Soil temperature may vary over time depending on ambient and climatic factors.

But in general, the percentage of difference was very appropriate. There is excellent agreement between the measured data and the simulated predictions, as the percentage of difference did not exceed 7.2%, which supports the possibility of trusting this new simulation model.

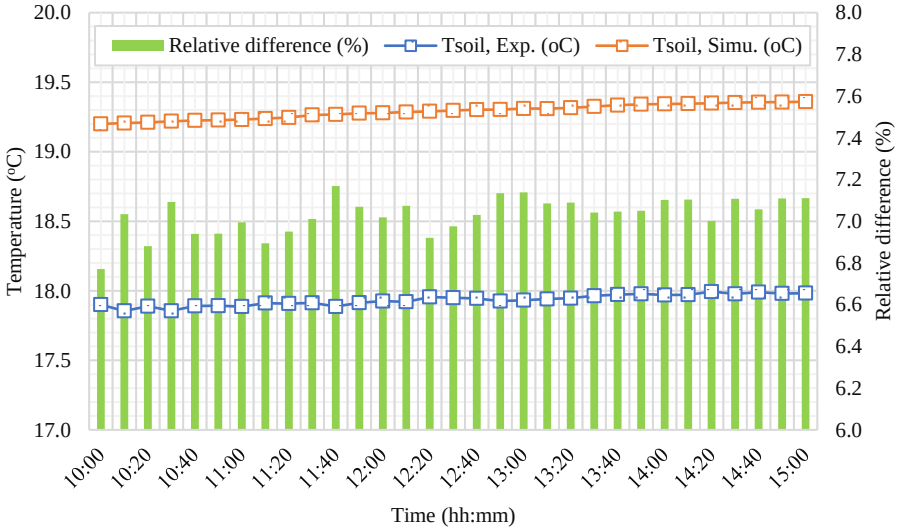

Fig. 4.1. Experimental and simulation soil temperatures over time with their relative difference.

Fig. 4.2 shows measured outlet air temperature data of EAHE ($T_{out,\ EAHE,\ Exp.}$) compared to simulated predictions ($T_{out,\ EAHE,\ Simu.}$) over time, as well as their relative difference. The measured data was slightly lower throughout the examination than MATLAB model predictions. The relative difference between measured data and model predictions ranged between (6.3-6.9)%. There could be several reasons for the difference between the measured outlet air temperature and the simulated predictions. Actual conditions may not be adequately captured within the simulation model, and changing climate conditions may have directly affected outlet temperature. Outlet air temperature may vary over time depending on ambient and climatic factors.

The calculated relative difference expresses the difference between measured data and model predictions in relative terms. For example, sometimes the percentage difference is around 6.30%, while at other times, it is about 6.9%. This indicates variation in the accuracy of model predictions over time. But in general, the percentage of difference was very appropriate. There is excellent agreement between the measured data and the simulated predictions, as the percentage of difference did not exceed 6.6%, which supports the possibility of trusting this new simulation model.

Fig. 4.3 shows the measured and predicted temperatures of the reference PV module over time and their relative difference. When the air temperature and radiation were relatively low at the beginning of the test, the measured data showed temperatures somewhat higher than the reference values. After that, the relative difference between the measured data and the reference values decreased slightly.

It is noted that this relative difference is relatively close between the measured data and the reference values throughout the other period. The measured data reflect temperatures between 5.2% and 6.7% higher than the reference values. This difference may result from several factors, such as the accuracy of temperature measurements and measurement conditions. Temperature changes can be related to ambient conditions, such as pressure, humidity, and ventilation. For example, the measured temperature rise could be due to the influence of solar radiation or hot weather conditions.

In general, the percentage of difference was very appropriate. There is good agreement between the measured data and the simulated predictions, as the percentage of difference did not exceed 6.7%, which supports the possibility of trusting this new simulation model.

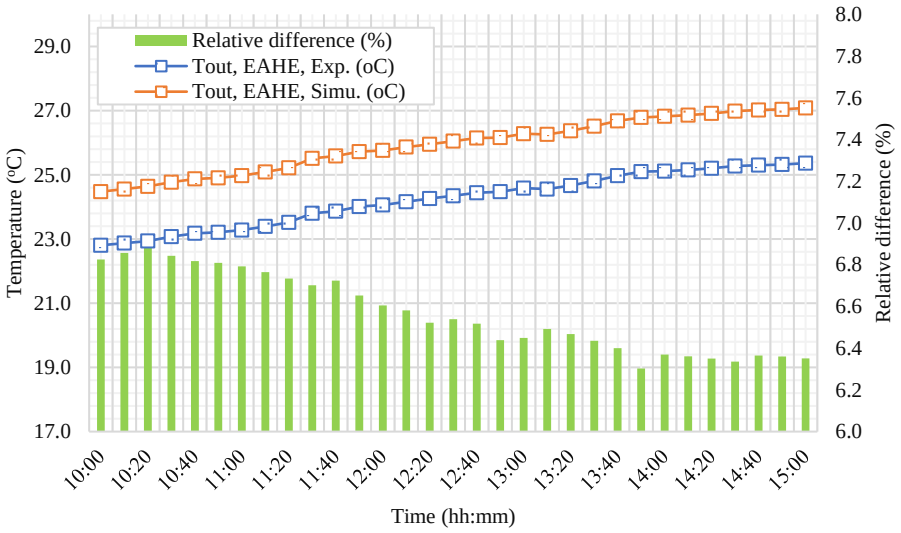

Fig. 4.2. Experimental and simulated outlet temperatures of EAHE over time with their relative difference.

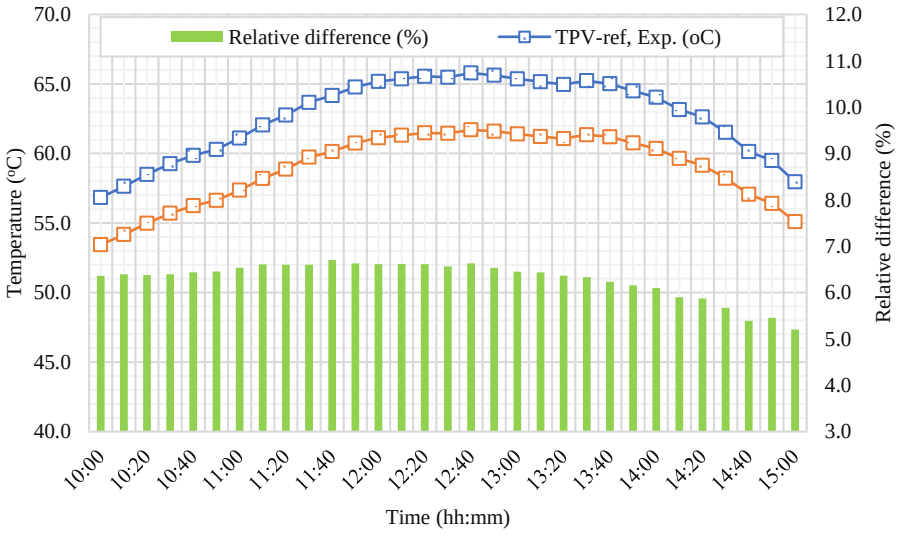

Fig. 4.3. Experimental and simulated PV module temperatures over time with their relative difference.

Fig. 4.4 shows the measured and predicted module temperatures of the PV/T integrated with the hybrid system over time. From the figure, the measured data reflected higher values than the MATLAB model predictions at the beginning of the examination, and the measured data continued to reflect higher values continuously over time.

It is noted that there is a continuous convergence between measured data and simulated predictions throughout the period. However, the values of these relative differences are variable during the test period, as they begin to decrease gradually as the temperature of the PV module rises during noon. Still, the relative difference returns to increase after that until the end of the test during the phase of the decline in the temperature of the PV module. But all these values were within acceptable ranges (5.7-6.6) %. This difference can be due to multiple factors, such as the accuracy of the measurements, the accuracy of the MATLAB model, and the conditions of the surrounding environment. Temperature ratio changes may also relate to ambient conditions, such as

atmospheric pressure, humidity, and airflow. These factors should be taken into account when improving future simulation predictions.

Generally, the percentage of difference was very appropriate. There is excellent agreement between the measured data and the simulated predictions, as the percentage of difference did not exceed 6%, which supports the possibility of trusting this new simulation model.

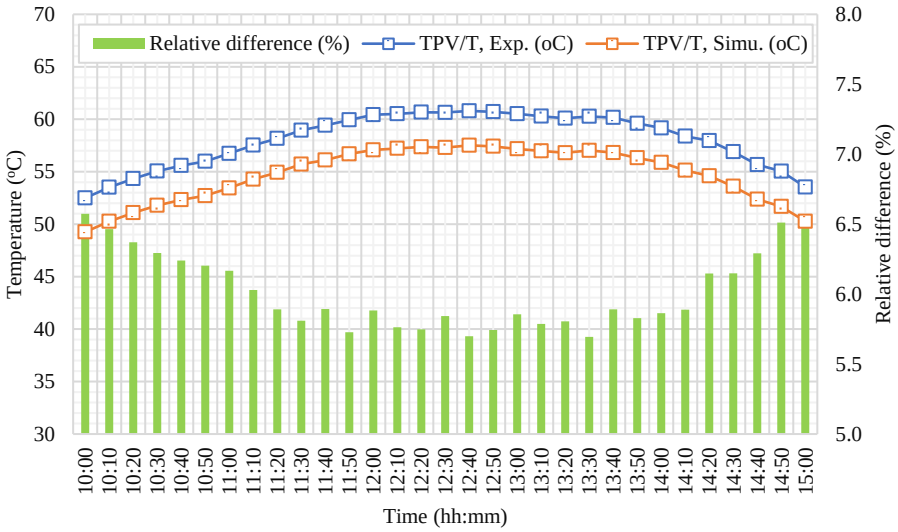

Fig. 4.4. Experimental and simulation temperatures of the PV modules integrated hybrid system over time with their relative difference.

Fig. 4.5 shows data including measured average temperatures of SC compared to model predictions over time. From the figure, the measured data reflected temperatures significantly lower than model predictions. Measured data continued to reflect lower temperatures than model predictions, and the difference gradually increased.

It is observed that there is a persistent discrepancy between the measured data and model predictions throughout the period. Measured data appear to reflect temperatures consistently lower than model predictions. This difference could be due to several possible factors, such as the measurements' accuracy, the simulation model's accuracy, and the surrounding environmental conditions. The devices used for SC temperature measurements must be reviewed and adjusted to ensure their accuracy. SC temperature changes may be related to ambient conditions, such as air temperature, airflow, and weather changes. These factors should be taken into account when improving future simulation predictions.

But in general, the percentage of difference was very appropriate. There is good agreement between the measured data and the simulated predictions, as the percentage of difference did not exceed 8.04%, which supports the possibility of trusting this new simulation model.

Fig. 4.6 shows the measured and predicted of the produced power by the PV modules (reference PV module and combined PV module) over time. Initially, the measured data reflected values significantly lower than model predictions. The measured data kept reflecting values lower than the model predictions, gradually increasing the difference. Until recently, the difference between measured data and model predictions has begun to decrease. It is observed that there is a persistent discrepancy between the measured data and model predictions throughout the period. The measured data consistently reflect electrical power produced less frequently than the simulated predictions.

This difference could be due to several possible factors, such as the measurements' accuracy, the simulation models' accuracy, and the surrounding environment conditions. The devices used in

electrical power measurements must be reviewed and adjusted to ensure their accuracy. Variations in electrical power may be related to ambient conditions, such as temperature, volume, and variations in typical examples. These factors should be taken into account when improving model predictions in the future. Finally, the percentage of difference was very appropriate. There is excellent agreement between the measured data and the simulated forecasts, as the percentage of difference did not exceed 4.08%, which supports the possibility of trusting this new simulation model.

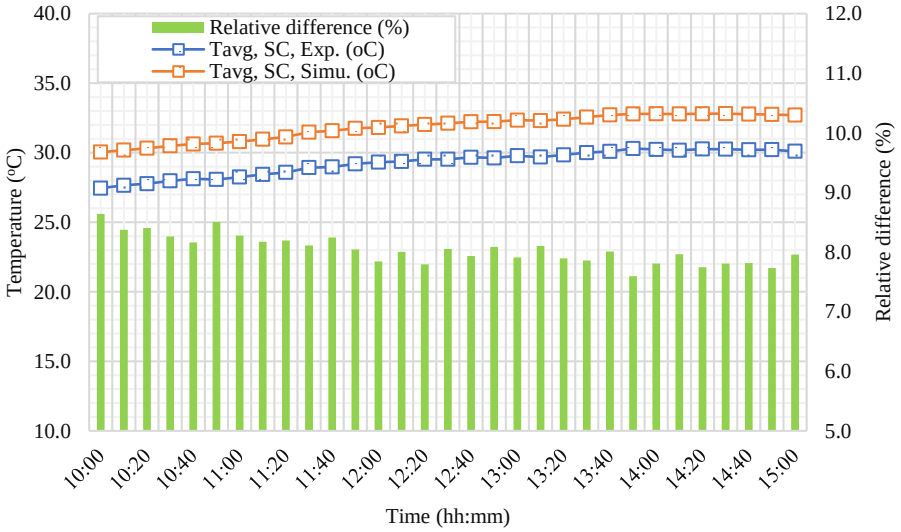

Fig. 4.5. Experimental and simulated average temperatures of SC over time with their relative difference.

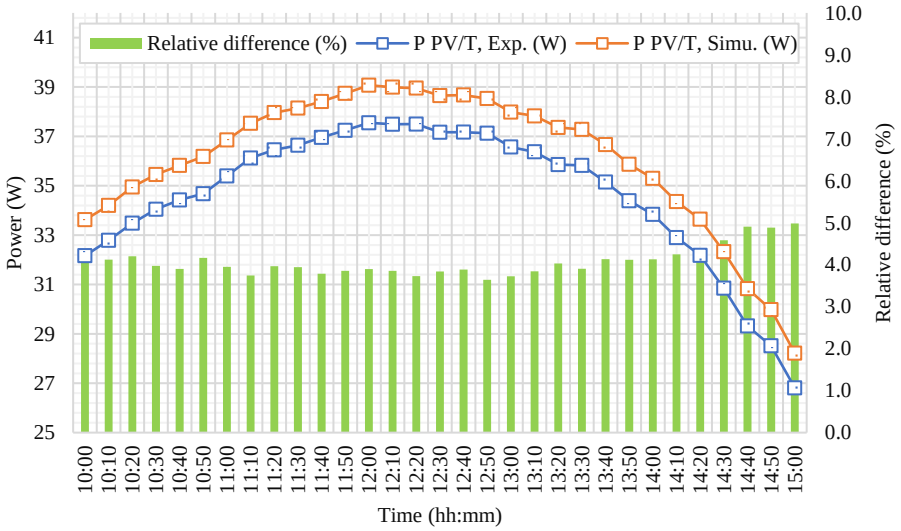

Fig. 4.6. Experimental and simulation power over time with relative differences.

In general, through the measured and predicted results that were presented and discussed, it was found that there were differences between the measured and forecast data, and these differences ranged in percentage between (5.0-6.9)% with an average not exceeding 6.4%. In light of the circumstances surrounding the measurement process and the challenges and instantaneous and continuous weather fluctuations that accompany it, as well as in light of the conditions and assumptions that accompanied the process of building the simulation model using MATLAB, these ratios are considered highly acceptable because of the capabilities and advantages they offer and the saving of efforts and costs. They are considered a reliable tool for providing vision and visualization. It is close to reality for the system that requires its installation in the future, with the possibility of modifying and analyzing its results before commencing its realistic implementation,

as it has been built based on the declared methods and methodologies explained in section (3.5). Therefore, this model is a promising model that can be trusted and relied upon, with the possibility of making modifications and developing it in the future.

4.2. Soil Temperature and Thermo-Physical Properties

4.2.1. Temperature Gradient Analysis

The experimental work described in section 3.3.1 continued for an entire year, during which the soil temperature was measured and recorded at different depths compared to the air temperature. Fig. 4.7 shows the temperature gradient of the soil in Najaf, Iraq, at different depths (1, 2, 3, 4, and 5 m) compared to the ambient air temperature measured simultaneously for reaching these temperatures with the extremely hot climatic conditions prevailing at the study location.

Given the data shown in the figure, the monthly changes in soil temperatures at different depths are influenced by the surface air temperature at different depths, especially the shallow depths. It is also noted that the soil is warmer than the ambient air during January, February, March, November, and December. Meanwhile, the soil is colder than the ambient air during April, May, June, July, August, September, and October. November and March are the months of the solstice. At shallow depths of 1 m and 2 m, the soil temperatures are greater than the surface air temperature in winter and lower in summer. This indicates the influence of soil on heat storage and atmospheric fluctuations. As for temperatures at deeper depths of 3, 4, and 5 m, the soil temperatures show more stability throughout the year than the ambient air temperature, especially at 5 m. This can be useful for systems that rely on heat exchange with the soil.

For comparison, in July, the soil temperature at a depth of 5 m reaches 25.4 °C, while the surface air temperature is 41.6 °C (the highest monthly temperature). That shows how soil is essential in cooling any space or building during summer. On the contrary, in January, the soil temperature at a depth of 5 m reaches 22.9 °C, while the surface air temperature is 11.5 °C. This shows how soil can be used as a heat source during winter. By using these temperature gradients in the engineering design of heating and cooling systems, the energy efficiency of buildings in Al-Najaf can be improved and provide better environmental sustainability.

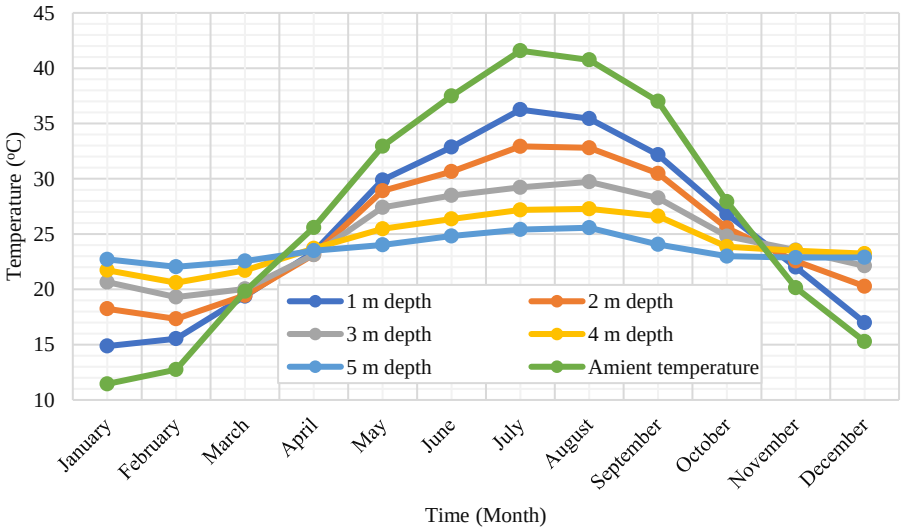

Fig. 4.7. The soil temperature at various depths at Al-Najaf location.

Fig. 4.8 shows the temperature gradient of the soil in Gödöllő, Hungary, at different depths (1 and 2 m) compared to the air temperature measured at the same time. Comparing these temperatures with the extremely cold climatic conditions prevailing at the study location.

Given the data shown in the figure, the monthly changes in soil temperatures at different depths are influenced by the surface air temperature at different depths, especially the shallow depths. It is also noted that the soil is warmer than the ambient air during January, February, March, November, and December. While during April, May, June, July, August, September, and October, the soil is colder than the ambient air. November and March are the months of the solstice. At shallow depths of 1 and 2 m, the soil temperatures are hotter than the surface air temperature in winter and colder in summer. These indicate the influence of soil on heat storage and atmospheric fluctuations.

As for soil temperatures at 2 m depth, the soil temperatures show more stability throughout the year than the ambient air temperature and soil temperature at 1 m depth. That can be useful for systems that rely on heat exchange with the soil.

For comparison, in August, the soil temperature at a depth of 2 m reaches 17.8 °C, while the surface air temperature is 28.1 °C (the highest monthly temperature). This shows how soil plays an important role in cooling any space or building during summer. On the contrary, in January, the soil temperature at a depth of 2 m reaches 10.3 °C, while the surface air temperature is 1 °C. This shows how soil can be used as a heat source during winter.

Soil temperatures at different depths play an essential role in the performance of the EAHE system. In summer, the cold soil at shallow depths can cool the air coming into the building, reducing the load on conventional air-cooling systems. In winter, the warm soil at deeper depths can be used to warm the air coming into the building, reducing the energy consumption needed for heating.

By using these temperature gradients in the engineering design of heating and cooling systems, the energy efficiency of buildings in Gödöllő can be improved, and better environmental sustainability can be provided.

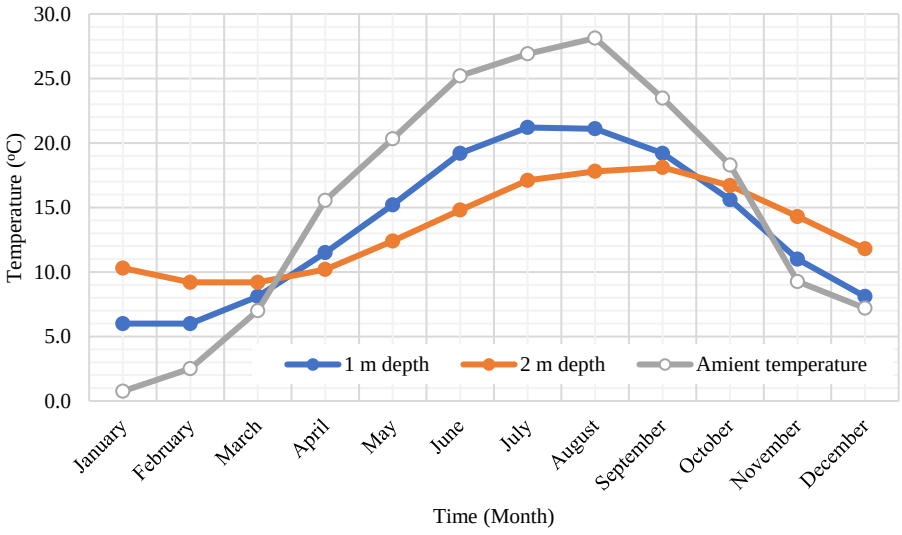

Fig. 4.8. The soil temperature at various depths at Gödöllő location.

By comparing the two locations, Ai-Najaf's soil temperature at a depth of 1 m ranges from 14.9 °C in January to 36.3 °C in July. As for Gödöllő's soil temperature ranges from 6 °C in January to 21.2 °C in July. It is noted that the Al-Najaf location experiences higher summer temperatures than the Gödöllő location. As for soil temperatures at a depth of 2 m, they range from 18.2 °C in January to 32.9 °C in June. As for the Gödöllő location, it goes from 10.3 °C in January to 17.8 °C in August. This indicates that Al-Najaf records higher summer temperatures than Gödöllő due to the harsh weather that Najaf suffers from.

It is also noted from the two figures that the difference between soil temperatures and surface air temperatures in Al-Najaf is higher in summer and lower in winter, which indicates a delayed response of the soil to seasonal changes in air temperature. The difference between soil and ambient air temperatures is greater in winter in Gödöllő, meaning the soil retains heat better in summer. This information can be used to design underfloor heating and cooling systems in both cities to achieve better efficiency.

Using cool soil temperatures in summer as a cooling source for ground cooling systems in Al-Najaf is preferable. In comparison, warm soil temperatures in winter are preferred as a heating source for underfloor heating systems in Gödöllő. This does not mean that this system cannot be installed in both cities to serve the purposes of both cooling and heating. Still, the preference here indicates the system's effectiveness for cooling purposes in the summer in Al-Najaf and for heating purposes in the winter in Gödöllő. This suggests thermal systems can be designed based on local soil properties to increase energy efficiency. This analysis shows the differences and similarities between soil and air temperatures in Al-Najaf and Gödöllő. It helps to identify opportunities to improve the environmental sustainability and efficiency of thermal systems in each.

4.2.2. Thermo-Physical Properties of Soil

The experimental work described in section 3.3.2 was carried out by collecting samples from the study location in Gödöllő. The necessary practical procedures were carried out to measure their thermo-physical properties. Fig. 4.9 shows the physical and thermal properties of all layers of soil as well as the mixed soil. As noticed from the figure, the second and fifth layers had the highest thermal conductivity and were 0.624 W/m K and 0.623 W/m K, respectively. The third layer had the lowest thermal conductivity and was 0.296 W/m K. The mixed soil was of medium conductivity as it was a mixture of soil layer samples.

The specific heat capacity was at its maximum in the fifth layer and lowest in the first layer, while the mixed soil also had an average specific heat capacity. The density of the second layer was relatively the highest compared to the rest of the soil types, while the fourth layer was the least dense, and the mixed soil layer was of medium density, as is apparent in the figure.

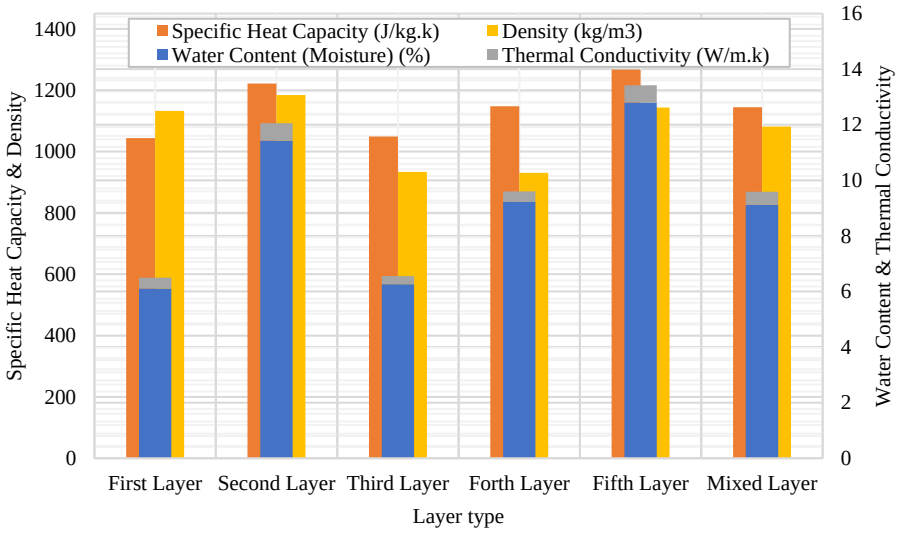

Fig. 4.9. The soil layers' specific heat capacity, density, water content, and thermal conductivity.

As described in this research, the thermo-physical properties analyzed above were measured based on each soil type's water content and the wet and dry densities. It had a significant role in the value of these properties. The amounts of this water content are mentioned in Fig. 4.9. This shows that the highest water content was in the fifth layer, and its lowest was in the first layer.

Thermal diffusivity plays the primary role in getting rid of the heat of the air flowing inside the pipe. The higher its amount, the higher the cooling efficiency of the EAHE, and vice versa. Through this, the thermal diffusivity of all layers as well as the soil mixture, was calculated, as shown in Fig. 4.10. It has been shown that the soil of the second layer is the highest in terms of thermal diffusivity (its amount is equal to 4.32E-07 m^2/s). Therefore, it is the best, followed by the soil of the fifth layer (its amount is equal to 4.30E-07 m^2/s) and then the soil of the second layer. The mixed soil (its amount is equal to 3.83E-07 m^2/s), then the fourth layer of soil (its amount is equal to 3.57E-07 m^2/s), then the first layer's soil (its amount is equal to 3.30E-07 m^2/s), and the third layer's soil was the least thermal diffusivity among the other types of soils (its amount is 3.03 E-07 m^2/s). Based on this, if the heat exchanger system is installed in the soil of the second layer type, it will perform better than if it is installed in the soil of the other layer type.

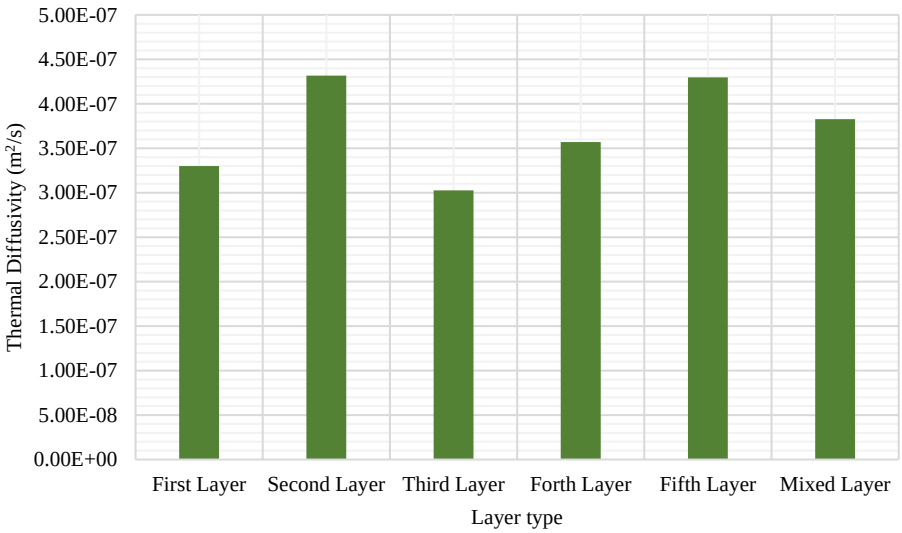

Fig. 4.10. The thermal diffusivity of the soil layers.

4.2.3. Effect of the Soil Thermo-Physical Properties on air temperature inside the EAHE

The simulation study described in Section 3.3.2 was conducted to study the effect of different soil properties on the air temperature inside the EAHE. This research compares the air temperature inside the pipe and at its exit in six cases. These cases are as follows:

- The first case: The EAHE pipe is buried in soil consisting of a mixture of soil types present in the study location, which are five types of soil mentioned in Table 3.2 and Fig. 3.4.
- The second case: The EAHE pipe is buried in soil consisting of the soil of the first layer only, as mentioned in Table 3.2 and Fig. 3.4.
- The third case: The EAHE pipe is buried in soil consisting of the soil of the second layer only, as mentioned in Table 3.2 and Fig. 3.4.
- The fourth case: The EAHE pipe is buried in soil consisting of the soil of the third layer only, as mentioned in Table 3.2 and Fig. 3.4.
- The fifth case: The EAHE pipe is buried in soil consisting of the soil of the fourth layer only, as mentioned in Table 3.2 and Fig. 3.4.
- The sixth case: The EAHE pipe is buried in soil consisting of the soil of the fifth layer only, as mentioned in Table 3.2 and Fig. 3.4.

Fig. 4.11 shows the air temperature along the pipe of the six cases, obtained from simulating the inputs obtained practically: soil and air temperatures. As the figure shows, the air temperatures decrease gradually and are close in value for all cases. The amount of this convergence decreases as the air travels a longer distance inside the tube, reaching the most significant amount of these

differences when the air approaches the exit, where the amount of differences increases to reach its peak at 3.74%, clearly in the same form.

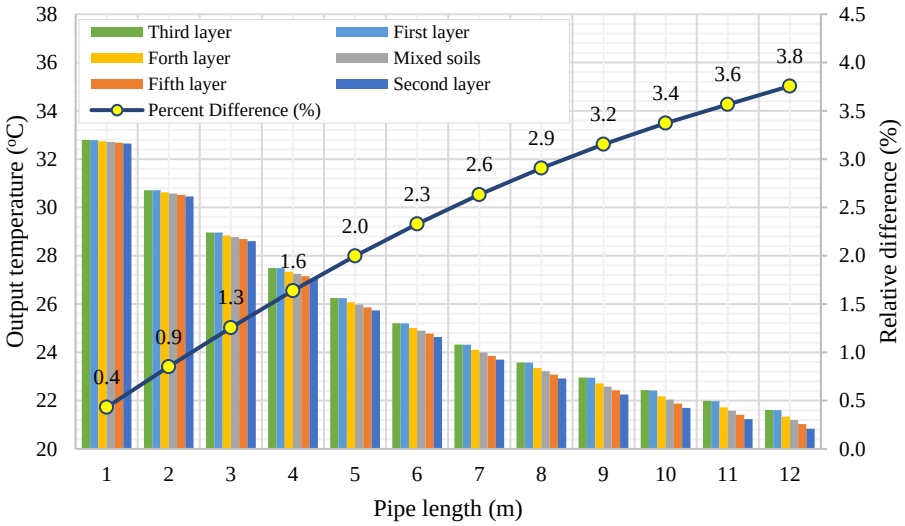

Fig. 4.11. The air temperature along the pipe of the six cases.

As noticed from the figure and from analyzing the results, the air obtained by burying the pipe in the soil of the second layer is the coldest among the other types of soil in the different layers. Likewise, the air produced from the pipe buried in the soil of the fifth layer is hotter than it by 0.9%. The air resulting from the tube buried in the soil of the mixed layer is hotter by 1.74%, the air resulting from the tube buried in the soil of the fourth layer is hotter than it by 2.4%, and the air resulting from the tube buried in the soil of the first layer is hotter than it by 3.7%. The air exiting from the tube buried in the soil of the third layer is 3.74% hotter than it. Therefore, the soil of the third layer is the best for heating purposes. The soil of the second layer is the best when the common purpose of establishing the EAHE system is cooling, and the soil mixture is average in terms of expected efficiency. We may notice that the above percentages are not very large. Still, in relatively large systems, the effect of this difference in layers will certainly be clear, and what this indicates is the increase in the amount of these differences as the distance traveled by air inside the tube increases, as it started at 0.45% at a distance of 1 m until it reaches 3.8% at a length of 12 m, as shown in Fig. 4.11. Therefore, it is necessary to choose the appropriate soil when designing and constructing the ground-to-air heat exchanger to get more EAHE system efficiency.

Accordingly, the relative difference between the outlet temperature of the EAHE system is 3.8% for a system of length 12 m and the thermal diffusivity range between 3.0258E-07 m^2/s and 4.3171E-07 m^2/s. It is subject to the following equation: $RD_{T,out}$ represents the relative difference of the outlet temperature, while L_{pipe} represents the length of the EAHE pipe. The effect of the relative difference in the type of layers was directly proportional to the length of the EAHE. As the length of the EAHE increases, the relative difference increases.

$$RD_{T,out} = 0.0002389 \times L_{pipe}^{3} - 0.01877 \times L_{pipe}^{2} + 0.5089 \times L_{pipe} - 0.09124, R^2 = 0.9999 \quad (4.1)$$

4.3. Earth-Air Heat Exchanger Performance

To analyze the performance of the EAHE in both cooling and heating modes, the main parameters that affect their performance will be considered: ambient temperature, soil temperature, airflow velocity, and outlet temperature. Heat transfer efficiency and system characteristics under different climatic conditions for both scenarios will be evaluated.

4.3.1. Earth-Air Heat Exchanger in Cooling Mode

This experimental work was carried out to determine the performance of EAHE in the hotter month of the study location (Gödöllő), lasted for two days, on a clear day in August of 2022, and was described in subsection 3.3.3. This experiment is necessary to determine the performance of EAHE in generating natural ventilation and the extent of its effect on the temperature of any space, thus, its capacity and efficiency.

Fig. 4.12 shows the temperature variation T_{amb}, $T_{out,\ EAHE}$, and T_{soil} as a function of time for two days. The figure represents using EAHE to cool the air on a hot day. Heat transfer efficiency can be evaluated by analyzing the temperature difference between the ambient air and the EAHE output temperature. A larger temperature difference indicates better heat transfer.

Initially, at 00:00, the temperature difference is two °C. As the day progresses, the temperature difference increases, reaching its highest at 15:00, reaching 11°C. The increase in temperature difference over time indicates that the cooling efficiency of the EAHE decreases with the increase in ambient temperature, but the system efficiency is still high. In hot climates, such as midday, the EAHE can provide cooling, but cooling efficiency decreases as the day progresses and the ambient temperature rises. However, the temperature differences at the inlet and outlet increase. In the evening and at night, when ambient temperatures drop, the cooling performance of the EAHE becomes less critical. By 0:00, the system maintains the air temperature close to the initial soil temperature, indicating that it no longer provides cooling.

The efficiency ratio indicates how effectively the EAHE transfers heat. A higher efficiency ratio indicates better heat transfer. Efficiency starts at around 71% and gradually increases throughout the day, reaching approximately 71.7% in the evening. The slight increases in efficiency indicate that the EAHE maintains reasonably consistent cooling performance throughout the day. The temperature at the EAHE outlet is consistently lower than the ambient temperature, indicating successful cooling. The temperature difference between the ambient air and the EAHE outlet decreases as the day progresses, reflecting a decreasing cooling effect as the day warms.

The EAHE exhibits effective cooling in hot climates, keeping the output temperature lower than the ambient temperature. The system maintains reasonable performance while the cooling efficiency decreases slightly during the day.

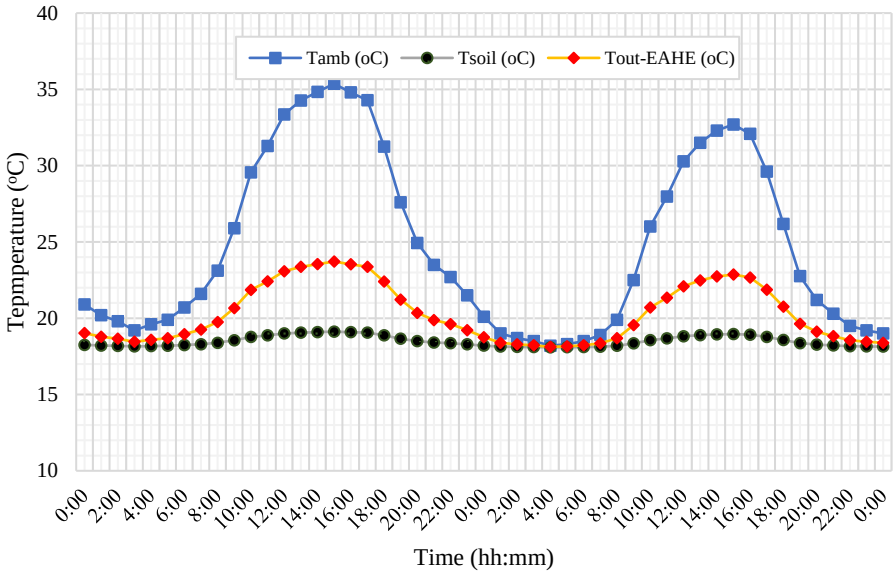

Fig. 4.12. The ambient, soil, and EAHE outlet temperatures in Gödöllő during the cold mode.

4.3.2. Earth-Air Heat Exchanger in Heating Mode

This experimental work was carried out to determine the performance of EAHE in the colder month of study location (Gödöllő), lasted for two days, on the clear day of January of 2023, and described in subsection 3.3.3. This experiment is necessary to determine the performance of EAHE in generating natural ventilation and the extent of its effect on the temperature of any space, thus, its capacity and efficiency.

Fig. 4.13 represents using EAHE to warm the air on a cold day. In this scenario, the heat transfer efficiency is evaluated by the temperature difference between the soil and EAHE outlet temperatures. A more enormous temperature difference indicates better heat transfer.

Initially, at 00:00, the temperature difference is 6.5 °C. As the day progresses, the temperature difference decreases, reaching at 15:00, reaching 3.6 °C. The increasing temperature difference over time indicates that the heating efficiency of the EAHE improves as the ambient temperature decreases. In cold climates, such as during the night and early morning, the EAHE effectively warms the incoming air, increasing the temperature by up to 8.6°C. However, as the ambient temperature rises during the day, the warming effect becomes less significant, but it still provides some thermal comfort.

The efficiency ratio indicates how effectively the EAHE transfer heat. A higher efficiency ratio indicates better heat transfer. The efficiency starts at about 70.1% and increases gradually throughout the day, reaching about 70.9% in the evening.

Increased efficiency means the EAHE provides better heating performance as the day progresses and the ambient temperature decreases. The temperature at the EAHE outlet is consistently higher than the ambient temperature, indicating successful warming. The temperature difference between the ambient air and the EAHE output increases as the day progresses, reflecting an enhanced warming effect as the ambient temperature decreases.

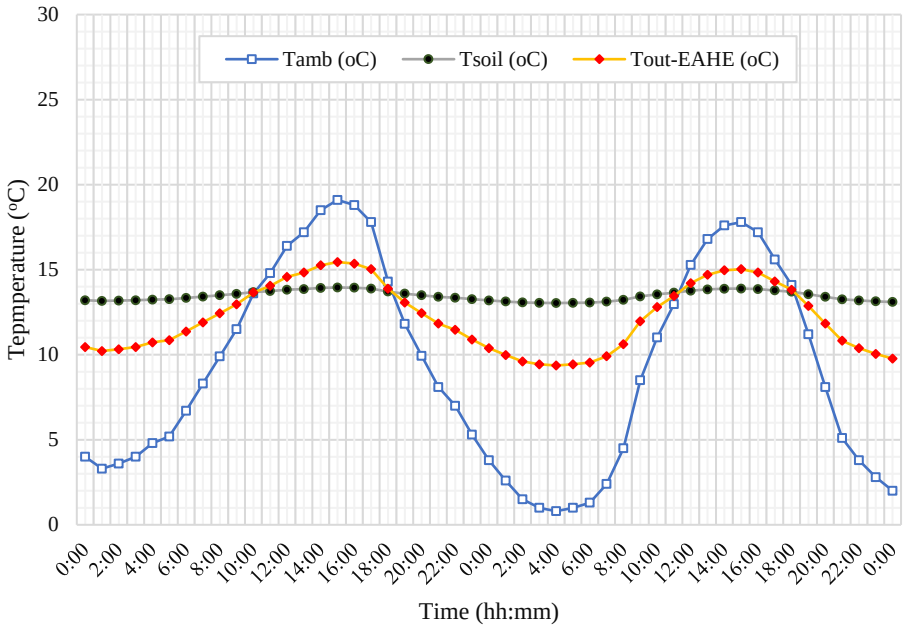

Fig. 4.13. The ambient, soil, and EAHE outlet temperatures in Gödöllő during the hot mode.

The EAHE seems to work well in both cooling and heating modes. However, their effectiveness depends on specific climate conditions and temperature differences between the surrounding air and soil. In hot climates, cooling efficiency increases as the day progresses, also in cold climates, heating efficiency improves as the day progresses.

4.3.3. The effect of configuration on Earth-Air Heat Exchanger's performance

The comparison between four configurations of EAHE using PVC pipes with a total length of 65 m and a diameter of 0.148 m is presented in this section. The first type is a single pipe, the second is a U-shaped multi-pipe, the third is a MS-pipe, and the fourth is a TS-pipe. All types transmit the same airflow of 0.034 m^3/s. The pressure losses and AFP observed in the four types of EAHE tested are illustrated in Fig. 4.14. It can be observed that the MS-pipe EAHE has the lowest pressure losses of all four types, resulting in the least amount of additional AFP required for operation. According to the figure, the MS-pipe EAHE requires an additional AFP of approximately 0.014 W. The multi-pipe EAHE, on the other hand, has slightly higher pressure losses than the MS-pipe EAHE, resulting in a slightly higher amount of additional AFP required at approximately 0.177 W. The single-pipe EAHE has the third-highest pressure losses, requiring around 1.01 W of additional AFP. The TS-pipe EAHE, which has the highest-pressure losses, requires the most additional AFP, at approximately 1.07 W. These findings indicate that the MS-pipe EAHE configuration is not only the most effective in terms of minimizing pressure losses but also in terms of reducing the required additional air fan power for operation.

Accordingly, the MS-EAHE has the lowest pressure loss among other EAHE system types, resulting in the least additional air fan power required to operate the fan needed to circulate the air inside it. M-EAHE had more significant pressure losses compared to MS-EAHE by approximately 1.6 times. The S-EAHE and TS-EAHE types had the highest pressure losses. They required the most significant amount of additional air fan power for operation, as their pressure losses were 13.8 and 14.7 times, respectively, and their additional air fan power was 71.1 and 75.5 times higher than MS-EAHE.

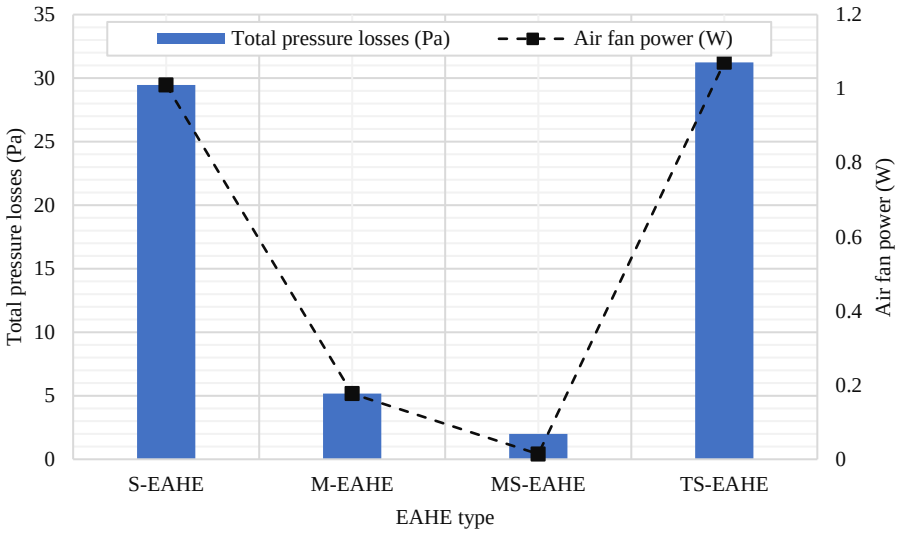

Fig. 4.14. The pressure losses and air fan power as a function of EAHE types; the result of investigation for exchanger model: L_{pipe}= 65 m, d_{pipe}= 0.148 m, V= 0.0343 m^3/s.

Figs. 4.15 and 4.16 provide insights into the thermal performance of four types of EAHE in different months of the year. From March to December, all EAHE are usable for cooling, but their cooling potentials vary depending on the ambient air and soil temperatures. Among the four types, the single-pipe and TS-pipe systems have the highest cooling potential, with 897.91 W each during the hottest month of August, while the MS-pipe type has less cooling potential with a value of 712 W. The multi-pipe type has the least cooling potential with a value of 683.65 W. During January and February, all systems are usable for heating, with the single-pipe and TS-pipe systems being the preferred choice. The air temperatures supplied by the four types of EAHE during these months range from 27.1 to 33.4 ºC.

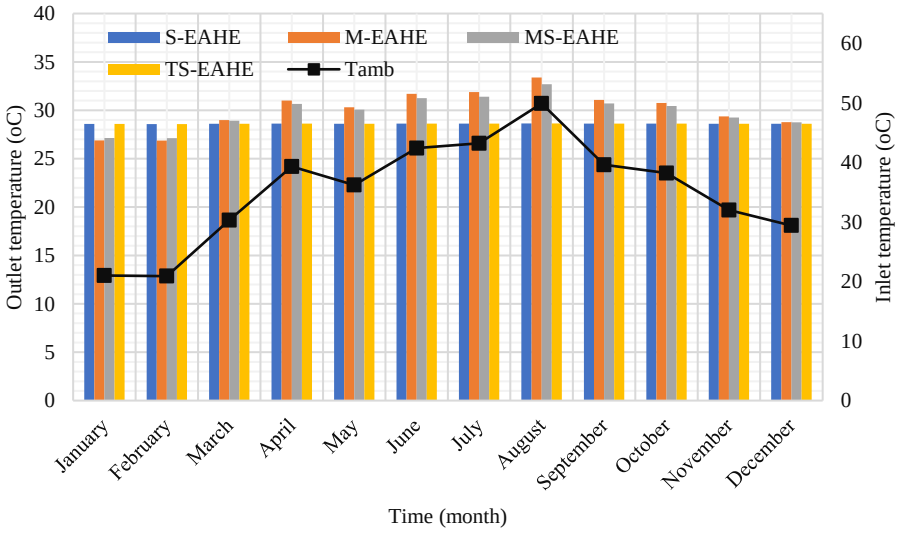

Fig. 4.15. The output and input temperature of EAHE types as a function of time; the result of investigation for exchanger model: L_{pipe}= 65 m, d_{pipe}= 0.148 m, V= 0.0343 m^3/s.

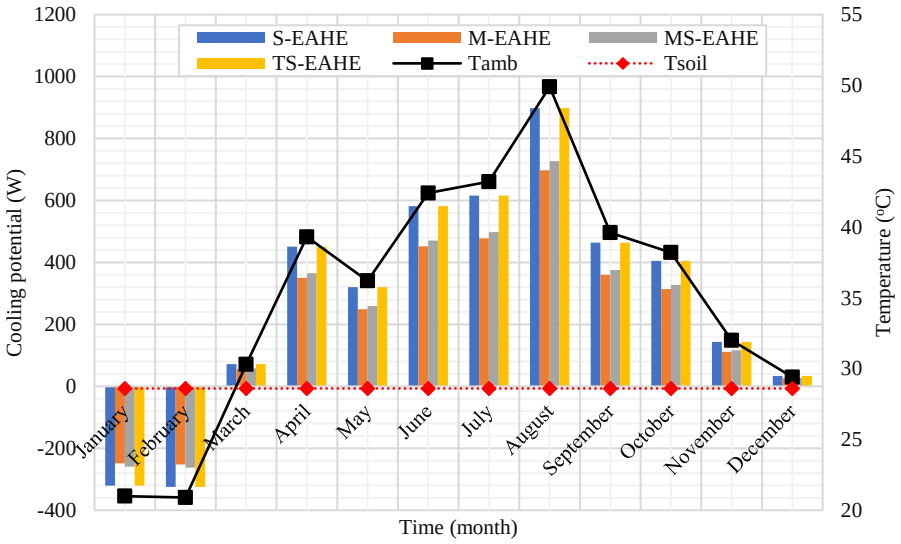

Fig. 4.16. The cooling potential and input temperature of EAHE types as a function of time; the result of investigation for exchanger model: L_{pipe}= 65 m, d_{pipe}= 0.148 m, V= 0.0343 m^3/s.

Accordingly, the S-EAHE and TS-EAHE have the highest cooling potential compared to other EAHE system types, at 278.3 W on average. The MS-EAHE and the M-EAHE have less cooling potential of 19.1% and 22.3%, respectively, compared to the S-EAHE and the TS-EAHE types. The four types are subject to the following equations, where CP represents the cooling potential of the EAHE types and T_{in} represents the inlet temperature of the EAHE.

$$CP = 1.853\times10^4 \sin(0.002276\, T_{in} + 6.218), \quad R^2=1 \quad \text{(For S-EAHE and TS-EAHE)} \tag{4.2}$$

$$CP = 1.295\times10^4 \sin(0.002528\, T_{in} + 6.211), \quad R^2=1 \quad \text{(For M-EAHE)} \tag{4.3}$$

$$CP = 1.383\times10^4 \sin(0.002467\, T_{in} + 6.213), \quad R^2=1 \quad \text{(For MS-EAHE)} \tag{4.4}$$

4.4. The performance of the PV module depends on the natural ventilation

4.4.1. Investigation of the effect of the solar chimney on the PV module efficiency

This experimental work was carried out to determine the effect of solar chimney integration on the efficiency of the PV module, described in subsection 3.3. It lasted on a clear day in August of 2022. This experiment is necessary to determine the effect of integrating the solar chimney on generating natural ventilation and air circulation and the extent of its impact on the operation temperature of the PV module and its capacity and efficiency.

Fig. 4.17 shows the temperature variation T_{amb}, $T_{out,\ EAHE\text{-}a}$, $T_{out,\ EAHE\text{-}b}$, $T_{PV\text{-}ref}$, $T_{PV\text{-}a}$, $T_{PV\text{-}b}$, and $T_{avg,\ SC\text{-}a}$ and air velocity of the PV/T-a and the PV/T-b versus the PV-ref (shown in Fig. 3.14 and Fig. 3.20) as a function of time (10:00 a.m. to 03:00 p.m.).

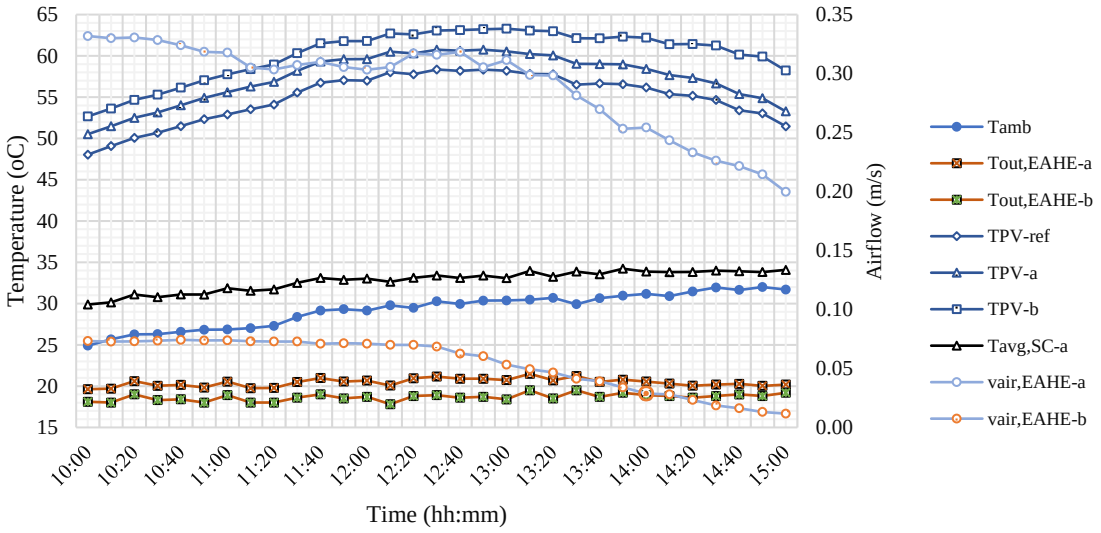

Fig. 4.17. The variation of T_{amb} vs. $T_{out,\ EAHE-a}$, $T_{out,\ EAHE-b}$, T_{PV-ref}, T_{PV-a}, T_{PV-b}, and $T_{avg,\ SC-a}$ and air velocity of the PV/T-a and PV/T- during the test time, 11 August 2022 (Natural airflow - Case 1).

It is clear from the figure that the PV-a module shows a lower temperature compared to the PV-b module, which indicates the cooling effectiveness gained from the EAHE and SC. The average T_{PV-a} and T_{PV-b} achieved were 57.3 °C and 60.2 °C respectively (The average reduction in temperature was approximately 5%) on the day of the experiment, encountered with the highest SR of 926.4 W/m^2 with an average SR of 837.7 W/m^2. Fig. 4.18 shows the SR intensity during the experiment day.

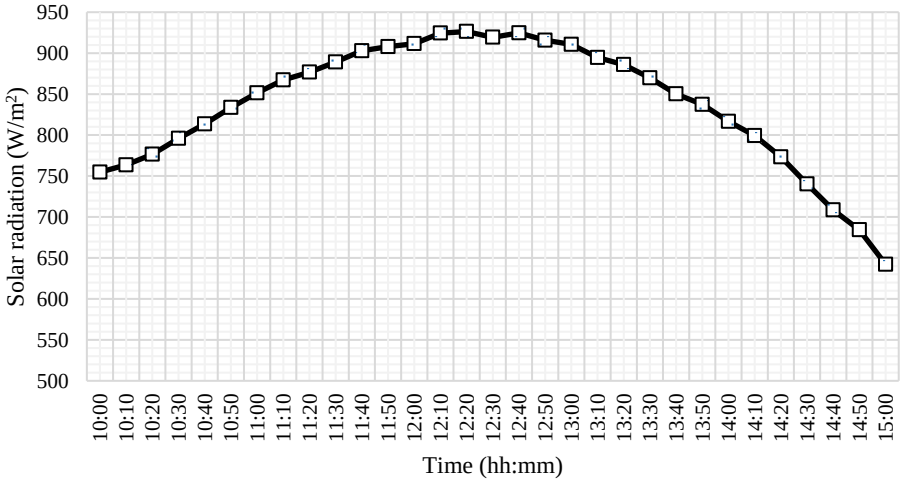

Fig. 4.18. The variation of solar radiation during the test time, 11 August 2022 (Natural airflow - Case 1).

The module PV-b, although connected to the EAHE-b, shows a slightly higher temperature than PV-a, which indicates that the solar chimney plays a vital role in improving cooling. But even though PV-a is connected to the EAHE and SC and PV-b is connected to the EAHE, the temperature of the two modules is still higher than that of the T_{PV-ref}. The average T_{PV-ref} achieved was 54.4 °C. The reason is that the airflow generated in the PV/T-a and PV/T-b is insufficient to cool them as their values were a few, as is apparent in Fig. 4.17.

The air velocity in PV/T-a is much higher than PV/T-b by 5.3 times, confirming the SC's benefit in increasing the airflow velocity and thus cooling the PV module better. However, its value is still less than what is required to cool the PV module.

A decrease in the temperature of the PV module leads to an increase in the power it generates, and this was observed by measuring the power generated for each of the three modules. As a result, the PV-ref may be more effective at converting SR into electrical power than other PV-a and PV-b modules.

Fig. 4.19 shows the average PV power production for the three modules. From the figure, the PV-ref board generated the highest amount of electrical power compared to PV-a and PV-b, and this can be attributed to its lower temperature compared to other modules, even though it is not equipped with any cooling and heat dissipation system. The average $P_{PV\text{-}ref}$ achieved was 35.7 W. The PV-a module generates more power than the PV-b module because it is cooled using an EAHE-a and SC-a, which helps reduce the module's temperature and thus increases its efficiency. The average $P_{PV\text{-}a}$ and $P_{PV\text{-}b}$ achieved were 35.1 W and 34.5 W, respectively. The power increase produced by PV-ref was higher by 1.7 % and 3.5 % than by the PV-a and PV-b modules, respectively.

Although the PV-b module is integrated with an EAHE and relies on heat generated by the PV module itself to move the air, it shows a lower power output than the PV-ref and lower than the PV-a.

Thus, it can be seen from Fig. 4.19 that the PV-ref was the most efficient compared to PV-a and PV-b. The average efficiency achieved by PV-ref, PV-a, and PV-b was 15.9% , 15.6%, and 15.4%, respectively.

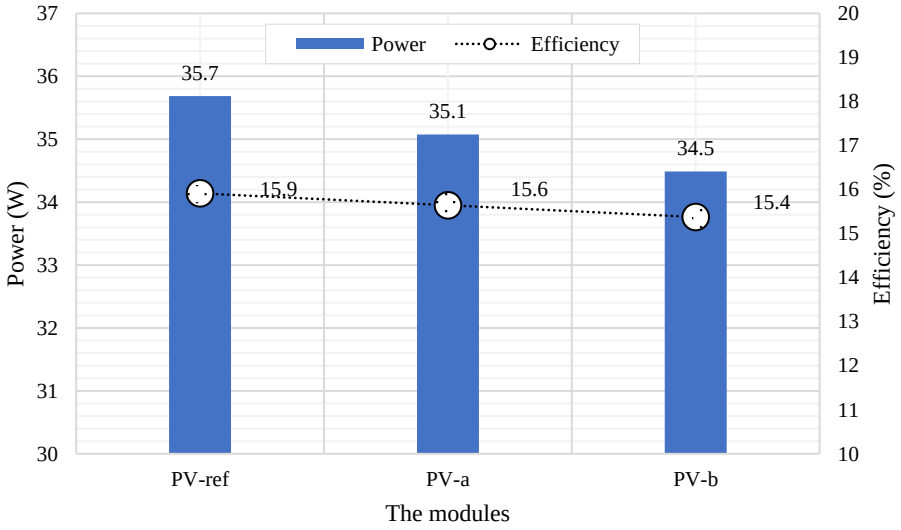

Fig. 4.19. The efficiency and power produced by the PV modules, 11 August 2022 (Natural airflow - Case 1).

Accordingly, the SC, when integrated with PV modules and EAHE, leads to an increase of approximately 5.3 times in the airflow velocity. The airflow velocity is subjected to the following equation because of this integration:

$$v_{air} = 2.807 - 0.003708\, I - 0.06196\, T_{amb} + 1.005\times10^{-6}\, I^2 + 7.783\times10^{-5}\, I\, T_{amb} - 0.0002501\, T_{amb}{}^2, \quad R^2 = 0.9623 \tag{4.5}$$

The solar chimney helps move the air and increase speed, enhancing the cooling process. This property improves the efficiency of the PV module and maintains its performance. The hot air generated by the PV module helps move the air inside the SC, creating a synergistic cycle that enhances the performance of both the SC and the PV module.

4.4.2. Investigation of the effect of solar chimney color on the PV module efficiency

This experimental work was carried out to determine the effect of the color of the integrated solar chimney on the efficiency of the PV module, described in subsection 3.3. It lasted on a clear day in August of 2022. This experiment is necessary to determine the effect of the color of the integrated solar chimney on generating natural ventilation and air circulation and the extent of its impact on the operation temperature of the PV module and its capacity and efficiency.

Fig. 4.20 shows the temperature variation T_{amb}, $T_{out,\ EAHE\text{-}a}$, $T_{out,\ EAHE\text{-}b}$, $T_{PV\text{-}ref}$, $T_{PV\text{-}a}$, $T_{PV\text{-}b}$, $T_{avg,\ SC\text{-}a}$, and $T_{avg,\ SC\text{-}b}$ and air velocity of the PV-a and the PV-b modules versus the PV-ref (shown in Fig. 3.14 and Fig. 3.20) as a function of time (10:00 a.m. to 03:00 p.m.).

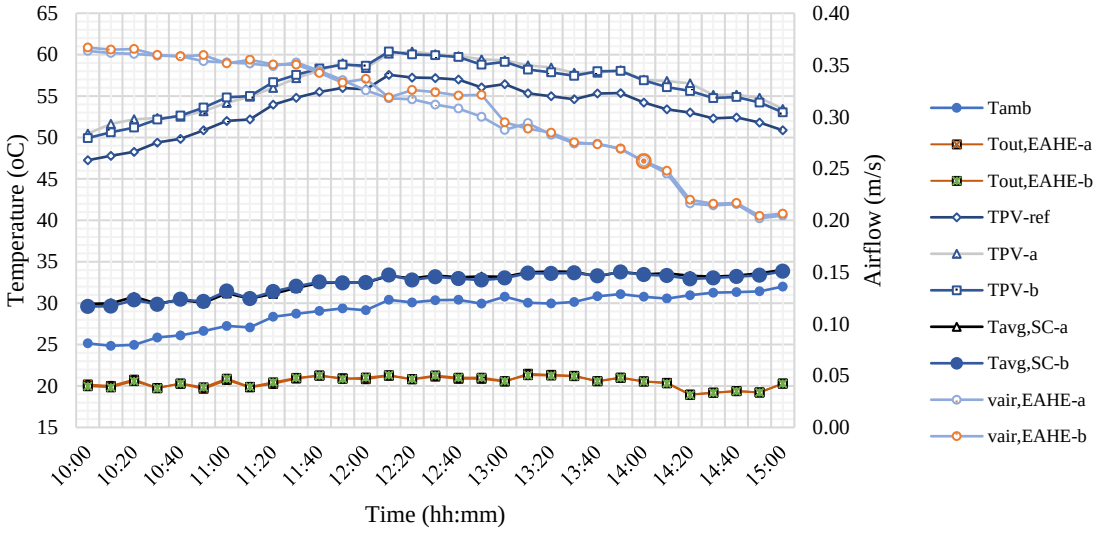

Fig. 4.20. The variation of T_{amb} vs. $T_{out,\ EAHE\text{-}a}$, $T_{out,\ EAHE\text{-}b}$, $T_{PV\text{-}ref}$, $T_{PV\text{-}a}$, $T_{PV\text{-}b}$, $T_{avg,\ SC\text{-}a}$ and $T_{avg,\ SC\text{-}b}$ and air velocity of the PV/T-a and PV/T- during the test time, 12 August 2022 (Natural airflow - Case 2).

It is clear from the figure that the PV-b module shows a slightly lower temperature compared to the PV-a module, which indicates the cooling effectiveness gained from the EAHE and the color of black SC together. The average $T_{PV\text{-}b}$ and $T_{PV\text{-}a}$ achieved were 56.3 °C and 56.4 °C respectively (The average reduction in temperature did not exceed 0.3%), on the day of the experiment encountered with the highest SR of 905.2 W/m^2 with an average SR of 810.6 W/m^2. Fig. 4.21 shows the SR intensity during the experiment time.

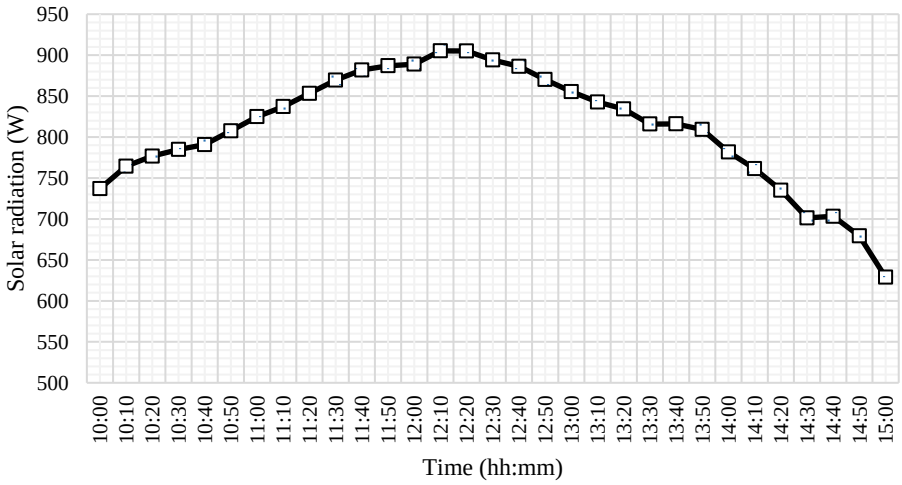

Fig. 4.21. The variation of solar radiation during the test time, 12 August 2022 (Natural airflow - Case 2).

The PV-a and PV-b modules, although connected to the EAHE, but the PV-a module shows a slightly higher temperature than PV-b, which indicates that the color of the solar chimney plays a somewhat role in improving cooling. But even though the two modules are connected to the EAHE and SC, the temperatures of the two modules are still higher than the $T_{PV\text{-}ref}$. The average $T_{PV\text{-}ref}$ achieved was 53.7 °C. The reason is that the airflow generated in the two $T_{PV\text{-}a}$ and $T_{PV\text{-}b}$ modules is insufficient to cool the PV-a and PV-b modules as their values were a few, as is clear in Fig. 4.20.

The air velocity in PV/T-b is higher than in PV/T-a, but not much. It is increasing by 1%, which confirms the benefit of the black SC in increasing the airflow velocity compared to white SC, thus cooling the PV module better. However, its value is still less than what is required to cool the PV module than PV-ref.

A decrease in the temperature of the PV module leads to an increase in the power it generates, and this was observed by measuring the power generated for each of the three modules. As a result, the PV-ref may be more effective at converting SR into electrical power than PV-a and PV-b modules.

Fig. 4.22 shows the average PV power production for the three modules. The PV-ref board generated the highest amount of electrical power compared to PV-a and PV-b, which can be attributed to its lower temperature than other modules, even though it is not equipped with any cooling and heat dissipation system. The average $P_{PV\text{-}ref}$ achieved was 34.7 W. The PV-b module generates more power than the PV-a module because it is cooled using an EAHE-a and black SC-a, which helps reduce the module's temperature and thus increases its efficiency. The average $P_{PV\text{-}b}$ and $P_{PV\text{-}a}$ achieved were 34.2 W and 34.1 W, respectively. The power increase produced by PV-ref was higher by 1.6 % and 1.7 % than by the PV-b and PV-a modules, respectively.

Although the PV-a module is integrated with an EAHE and relies on heat generated by the SC itself to move the air, it shows a lower power output than the PV-ref and slightly lower than the PV-b.

Thus, it can be seen from Fig. 4.22 that the PV-ref was the most efficient compared to PV-a and PV-b. The average efficiency of PV-ref, PV-b, and TPV-a achieved were 16%, 15.74%, and 15.73% respectively.

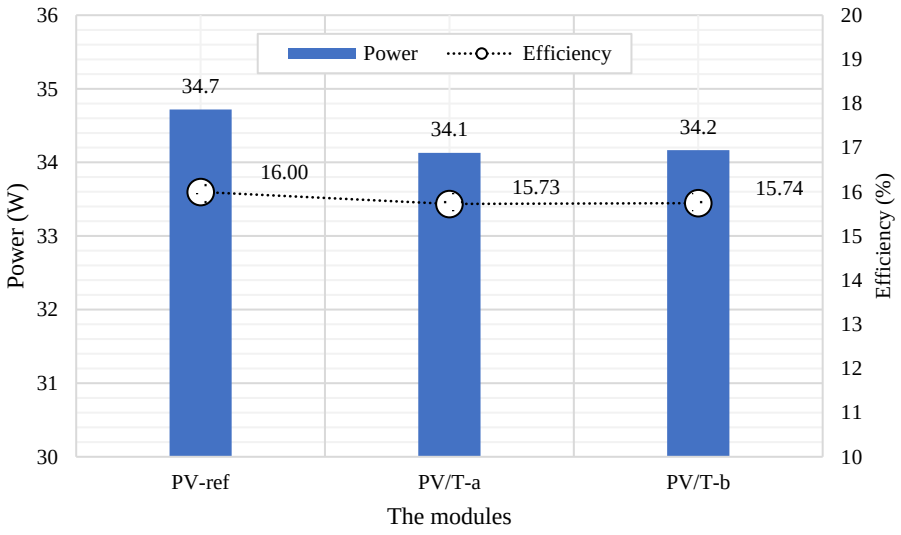

Fig. 4.22. The efficiency and power produced by the PV modules, 12 August 2022 (Natural airflow - Case 2).

The black solar chimney helps move the air and increase speed, enhancing the cooling process. This property improves the efficiency of the PV module and maintains its performance. The hot air generated by the PV module helps move the air inside the SC, creating a synergistic cycle that enhances the performance of both the SC and the PV module.

4.4.3. Investigation of the effect of solar chimney shape on the PV module efficiency

This experimental work was carried out to determine the effect of the shape of the integrated solar chimney on the efficiency of the PV module, described in subsection 3.3. It lasted on a clear day in August of 2022. This experiment is necessary to determine the effect of the shape of the integrated solar chimney on generating natural ventilation and air circulation and the extent of its impact on the operation temperature of the PV module and its capacity and efficiency.

Fig. 4.23 shows the temperature variation T_{amb}, $T_{out,\ EAHE\text{-}a}$, $T_{out,\ EAHE\text{-}b}$, $T_{PV\text{-}ref}$, $T_{PV/T\text{-}a}$, $T_{PV/T\text{-}b}$, $T_{avg,\ SC\text{-}a}$, and $T_{avg,\ SC\text{-}b}$ and air velocity of the PV/T-a and the PV/T-b versus PV-ref (shown in Fig. 3.14 and Fig. 3.20) as a function of time (10:00 a.m. to 03:00 p.m.).

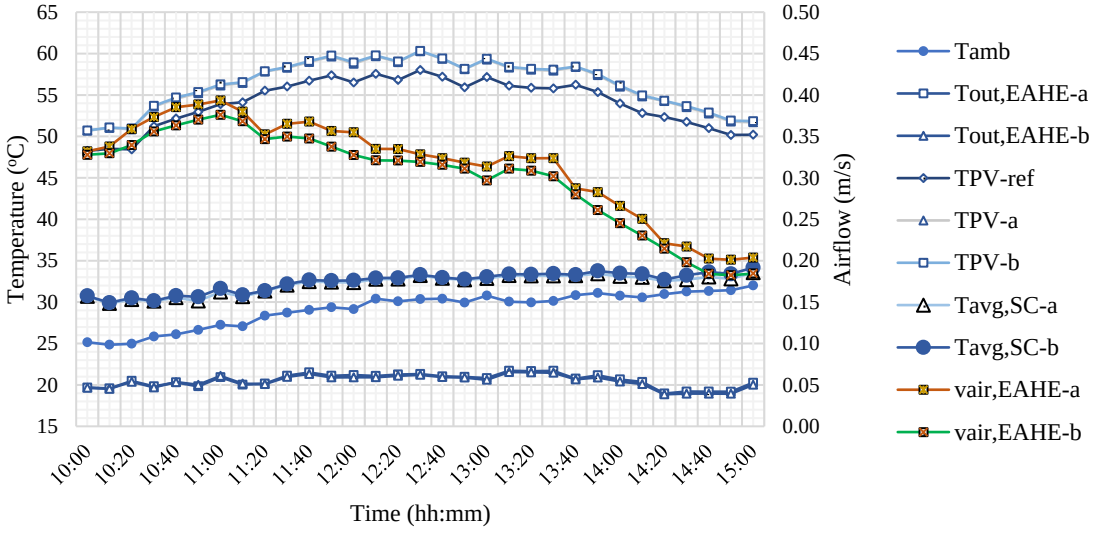

Fig. 4.23. The variation of T_{amb} vs. $T_{out,\ EAHE\text{-}a}$, $T_{out,\ EAHE\text{-}b}$, $T_{PV\text{-}ref}$, $T_{PV\text{-}a}$, $T_{PV\text{-}b}$, $T_{avg,\ SC\text{-}a}$ and $T_{avg,\ SC\text{-}b}$ and air velocity of the PV/T-a and PV/T- during the test time, 13 August 2022 (Natural airflow - Case 3).

It is clear from the figure that the PV-a and PV-b modules show great convergence between their respective temperatures, as the temperature dissipation ratio did not exceed 0.17% in their best performance, which indicates the little cooling efficiency gained from the EAHE and the rectangular shape SC together. The average $T_{PV\text{-}a}$ and $T_{PV\text{-}b}$ were 56.2°C and 56.3°C on the day of the experiment, which experienced the highest SR of 916.6 W/m^2 with an average of 812.5 W/m^2. Fig. 4.24 shows the intensity of SR during the day of the experiment.

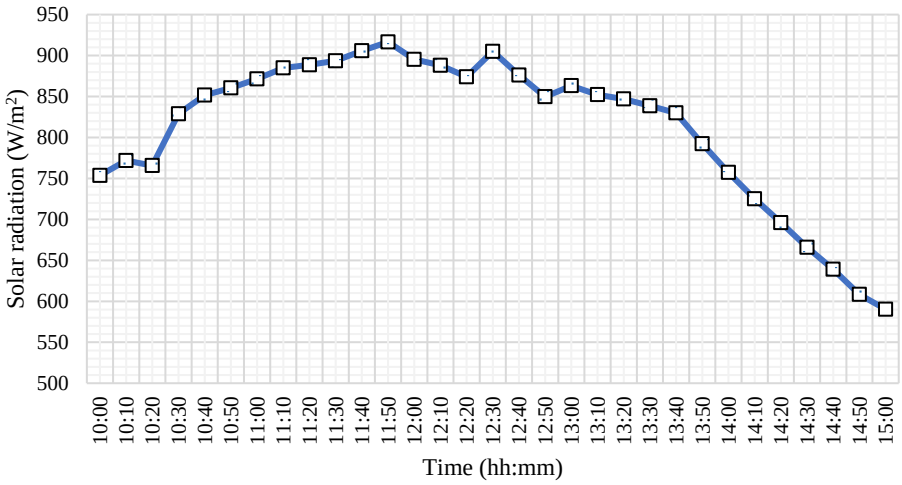

Fig. 4.24. The variation of solar radiation during the test time, 13 August 2022 (Natural airflow - Case 3).

The PV-a and PV-a modules, although connected to the same EAHE with different shapes of SC, show a very similar temperature, indicating that the shape of the solar chimney does play a limited role in improving cooling. It is possible that changing the shape may be more effective in larger sizes, but with regard to the available size in the current research, the amount of improvement in cooling does not exceed 0.2%. But even though the two modules are connected to EAHE and SC, the temperatures of the two modules are still higher than the reference temperature module. The average $T_{PV\text{-}ref}$ achieved was 54.1°C. The reason is that the airflow generated in the PV/T-a and PV/T-b modules is insufficient to cool the modules PV-a and PV-b, as their values were low, as is clear in Fig. 4.23.

The air velocity in PV/T-a is higher than the air velocity in PV/T-b, but it is not much. It is increasing by 5%, confirming the rectangular SC's benefit in increasing the airflow velocity compared to circular SC, thus cooling the PV module better. However, its value is still less than what is required to cool the PV module than PV-ref.

A decrease in the temperature of the PV module leads to an increase in the power it generates, and this was observed by measuring the power generated for each of the three modules. As a result, the PV-ref may be more effective at converting SR into electrical power than PV-a and PV-b modules.

Fig. 4.25 shows the average PV power production for the three modules. From the figure, the PV-ref board generated the highest amount of electrical power compared to PV-a and PV-b, and this can be attributed to its lower temperature compared to other modules, even though it is not equipped with any cooling and heat dissipation system. The average $P_{PV\text{-}ref}$ achieved was 34.8 W. The PV-a module generates slightly more power than the PV-b module since it is cooled slightly with EAHE-a and rectangular SC-a, which helps to slightly reduce the temperature of the module compared to PV-b and thus increases its efficiency. The average $P_{PV\text{-}a}$ and $P_{PV\text{-}b}$ were 34.2 W and 34.2 W, respectively. The increase in energy produced by PV modules was 1.64% and 1.6% higher compared to PV-b and PV-a modules, respectively.

Although the PV-b module is integrated with an EAHE and relies on heat generated by the SC itself to move the air, it shows a lower power output than the PV-ref and slightly lower than the PV-a.

Thus, it can be seen from Fig. 4.25 that the PV-ref was the most efficient compared to PV-a and PV-b. The average efficiency of PV-ref, PV-a, and PV-b achieved were 15.9%, 15.8%, and 15.7% respectively.

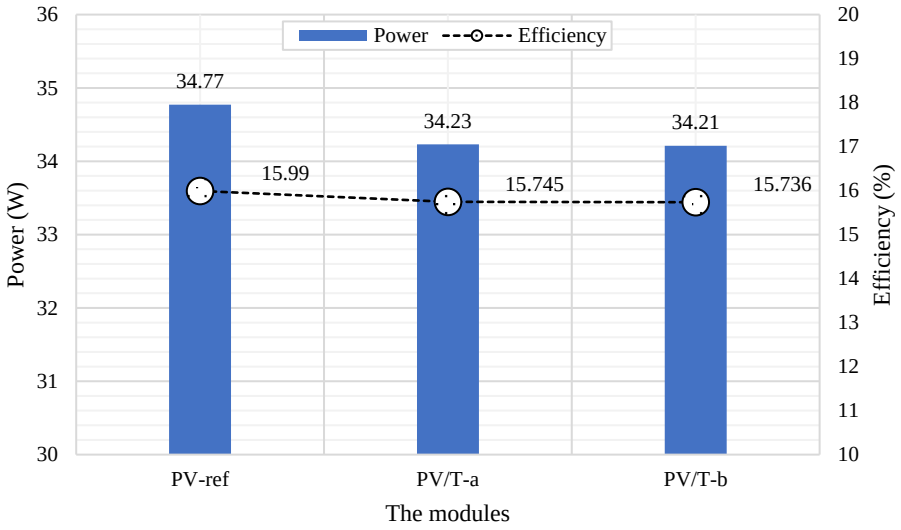

Fig. 4.25. The efficiency and power produced by the PV modules, 13 August 2022 (Natural airflow - Case 3).

Accordingly, the airflow velocity is increased by about 5% when the rectangular SC is utilized, as compared to the cylindrical SC. In order to estimate the velocity of the airflow, the following equation is applied:

$$v_{air} = -0.746 + 0.001783\, I + 0.02385\, T_{amb} + 8.364\times10^{-8}\, I^2 - 4.812\times10^{-5}\, I\, T_{amb}, \quad R^2 = 0.9789 \qquad (4.6)$$

The rectangular solar chimney helps move the air and increase speed, enhancing the cooling process. This property improves the efficiency of the PV module and maintains its performance. The hot air generated by the PV module helps move the air inside the SC, creating a synergistic cycle that enhances the performance of both the SC and the PV module.

4.4.4. Investigation of the effect of EAHE system length on the PV module efficiency

This experimental work was conducted to determine the effect of EAHE length on PV module efficiency, described in subsection 3.3. It lasted on a clear day in August of 2022. This experiment is necessary to determine the effect of the length of the integrated EAHE on the generation of cold air and the extent of its impact on the operating temperature of the PV module and its capacity and efficiency.

Fig. 4.26 shows the temperature variation T_{amb}, $T_{out,\ EAHE\text{-}a}$, $T_{out,\ EAHE\text{-}b}$, $T_{PV\text{-}ref}$, $T_{PV\text{-}a}$, $T_{PV\text{-}b}$, $T_{avg,\ SC\text{-}a}$, and $T_{avg,\ SC\text{-}b}$ and air velocity of the PV/T-a and PV/T-b versus the PV-ref (shown in Fig. 3.14 and Fig. 3.20) as a function of time (10:00 a.m. to 03:00 p.m.).

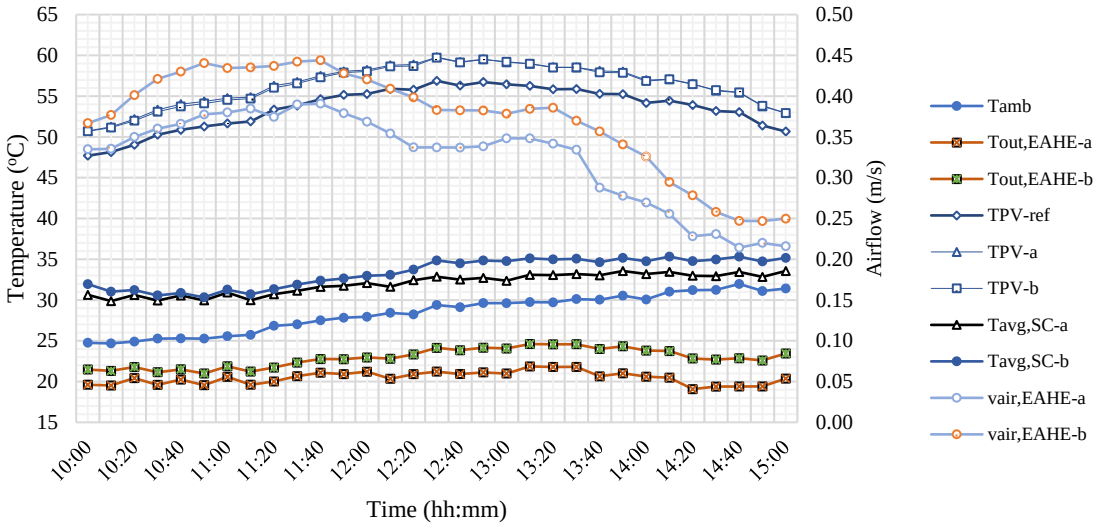

Fig. 4.26. The variation of T_{amb} vs. $T_{out,\ EAHE-a}$, $T_{out,\ EAHE-b}$, T_{PV-ref}, T_{PV-a}, T_{PV-b}, $T_{avg,\ SC-a}$ and $T_{avg,\ SC-b}$ and air velocity of the PV/T-a and PV/T- during the test time, 10 August 2022 (Natural airflow - Case 4).

It is clear from the figure that the PV-a and PV-b modules show great convergence between their respective temperatures, as the temperature dissipation ratio did not exceed 0.2% in their best performance, which indicates the little cooling efficiency gained from the EAHE and the SC together. The average T_{PV-a} and T_{PV-b} were 56.4 °C and 56.3 °C, respectively, on the day of the experiment which experienced the highest SR of 918.1 W/m^2 with an average of 837.9 W/m^2. Fig. 4.27 shows the intensity of SR during the day of the experiment.

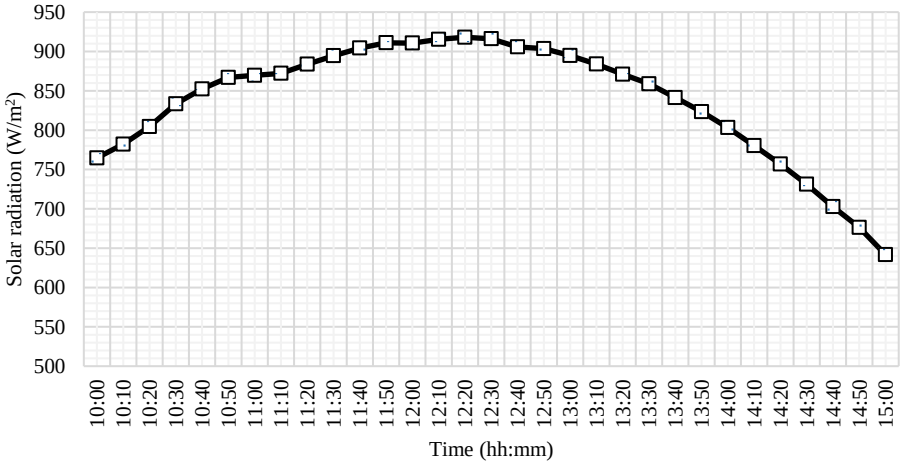

Fig. 4.27. The variation of solar radiation during the test time, 10 August 2022 (Natural airflow - Case 4).

Although the PV-a and PV-b modules are connected to the different EAHE and the same SC, both modules show very similar temperatures, indicating that the EAHE's length does not play an important role in improving overall cooling. It is possible that for larger sizes of hybrid systems, changing the length of the EAHE may have a more influential effect. Still, concerning the size available in the current research, the amount of cooling improvement does not exceed 0.2%, even though the two modules are connected to EAHE and SC. This is not due to a decrease in the EAHE's efficiency. The percentage of difference in cooling between the two EAHE was high (on average 12%), as the PV-a module was equipped with air at a lower temperature from the EAHE-a system, as $T_{out,\ EAHE-a}$ was 20.5 °C, which is lower than the temperature of the air surrounding by 8 °C, while the PV-b module was equipped with relatively higher-temperature air from the EAHE-b system, as $T_{out,\ EAHE-b}$ was 22.9 °C which is lower than the temperature of the air surrounding by

6 ºC which indicates that high efficiency has been achieved from both EAHE systems (EAHE-a and EAHE-b) about 79.3% and 55% respectively.

The reason is that the cooler air supplied to the SC, the lower natural airflow velocity occurs through the SC, as the amount of airflow velocity inside the SC depends on the difference between the average temperature of the air SC and T_{amb}. Therefore, as cooler air is supplied through the EAHE, the $T_{avg,SC}$ will decrease; thus, the difference between the $T_{avg,SC}$ and the T_{amb} will reduce. So this leads to a decrease in airflow velocity. This idea supports the fact that the airflow velocity in the $v_{air,EAHE-a}$ was 0.325 m/s, less than the $v_{air,EAHE-b}$ (it was 0.373 m/s) due to the carefully analyzed reason. Fig. 4.26 shows the airflow velocity in both models.

Therefore, the temperatures in both modules were still higher than the reference module temperature, and the average T_{PV-ref} achieved was 53.6 °C. The reason is that the airflow is generated in the modules. T_{PV-a} and T_{PV-b} are insufficient to cool the modules PV-a and PV-b, as their values were low, as is evident in Fig. 4.26.

A decrease in the temperature of the PV module leads to an increase in the power it generates, and this was observed by measuring the power generated for each of the three modules. As a result, the PV-ref may be more effective at converting SR into electrical power than PV-a and PV-b modules.

Fig. 4.28 shows the average PV power production for the three modules. From the figure, the PV-ref board generated the highest amount of electrical power compared to PV-a and PV-b, and this can be attributed to its lower temperature compared to other modules, even though it is not equipped with any cooling and heat dissipation system. The average P_{PV-ref} achieved was 35.9 W. The PV/-b module generates slightly more power than the PV-a module since it is cooled somewhat with shorter EAHE and higher airflow velocity, which helps to reduce the module's temperature slightly compared to PV-a and thus increases its efficiency. The average P_{PV-b} and P_{PV-a} were 35.31 W and 35.29 W, respectively. The increase in energy produced by PV modules was 1.7% and 1.6% higher than PV-b and PV-a modules, respectively.

Although the PV-a module is integrated with longer EAHE and relies on heat generated by the SC to move the air, it shows a lower power output than the PV-ref and slightly lower than the PV-b.

Thus, it can be seen from Fig. 4.28 that the PV-ref was the most efficient compared to PV-a and PV-b. The average efficiency of PV-ref, PV-a, and PV-b achieved were 16%, 15.73%, and 15.74% respectively.

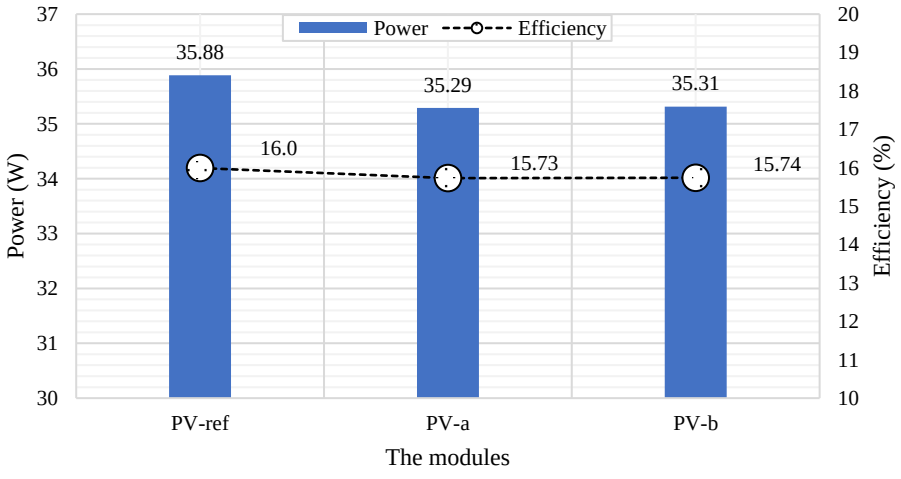

Fig. 4.28. The efficiency and power produced by the PV modules, 10 August 2022 (Natural airflow - Case 4).

Accordingly, the airflow velocity caused by the SC through the EAHE with a length of 5 m is 14.7% more than the airflow velocity through the EAHE with a length of 10 m. The following equation establishes the airflow velocity:

$$v_{air} = -2.173 + 0.001843\, I + 0.1288\, T_{amb} - 4.726\times10^{-5}\, I\, T_{amb} - 0.001891\, T_{amb}^{\,2}\,, \qquad (4.7)$$
$$R^2 = 0.9731$$

The EAHE helps supply the cold air, which enhances the cooling process. This property improves the efficiency of the PV module and maintains its performance. The hot air generated by the PV module helps move the air inside the SC, creating a synergistic cycle that enhances the performance of both the SC and the PV module.

4.4.5. Investigation of the effect of the depth of PV/T ducts on the efficiency of the PV module

This experimental work was carried out to determine the effect of duct depth of PV/T on the efficiency of PV modules integrated with EAHE and SC, described in subsection 3.3. It lasted on a clear day in August of 2022. This experiment is necessary to determine the effect of the depth of the integrated PV/T on removing the heat from the PV modules by generating natural ventilation and air circulation and the extent of its impact on the operation temperature of the PV module and its capacity and efficiency.

Fig. 4.29 shows the temperature variation T_{amb}, $T_{out,\,EAHE\text{-}a}$, $T_{out,\,EAHE\text{-}b}$, $T_{PV\text{-}ref}$, $T_{PV\text{-}a}$, $T_{PV\text{-}b}$, $T_{avg,\,SC\text{-}a}$, and $T_{avg,\,SC\text{-}b}$ and air velocity of the PV/T-a and the PV/T-b versus the reference module (PV-ref) (shown in Fig. 3.14 and Fig. 3.20) as a function of time (10:00 a.m. to 03:00 p.m.).

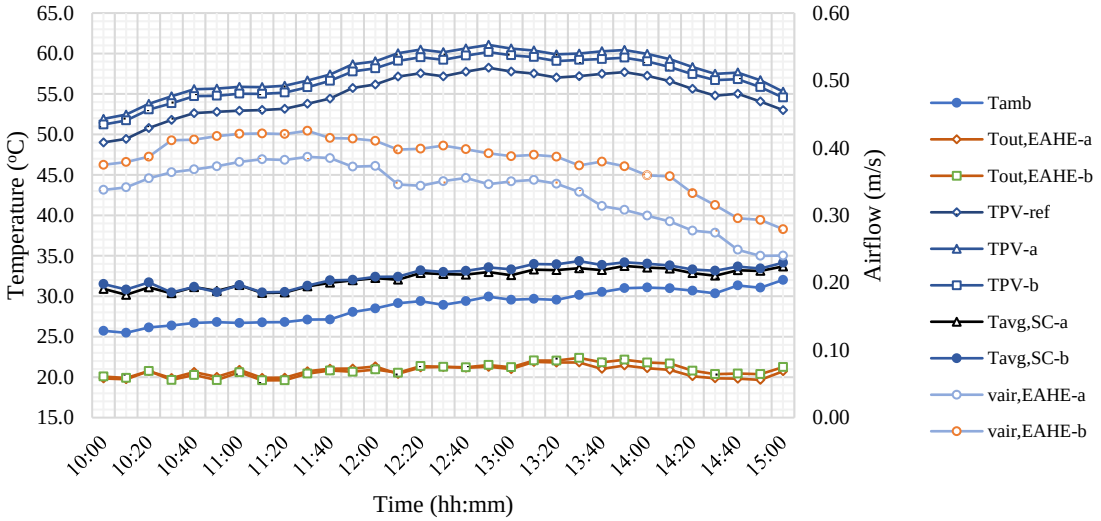

Fig. 4.29. The variation of T_{amb} vs. $T_{out,\,EAHE\text{-}a}$, $T_{out,\,EAHE\text{-}b}$, $T_{PV\text{-}ref}$, $T_{PV\text{-}a}$, $T_{PV\text{-}b}$, and $T_{avg,\,SC\text{-}a}$ and air velocity of the PV/T-a and PV/T- during the test time, 9 August 2022 (Natural airflow - Case 5).

It is clear from the figure that the PV-a and PV-b modules show great convergence between their respective temperatures, as the temperature dissipation ratio did not exceed 1.5%, which indicates the limited cooling efficiency gained from the integration of the EAHE and the SC and reduction the depth of the PV/T. The average $T_{PV\text{-}a}$ and $T_{PV\text{-}b}$ were 57.8 °C and 57 °C on the day of the experiment, which experienced the highest SR of 945.3 W/m^2 with an average of 872.6 W/m^2. Fig. 4.30 shows the intensity of SR during the day of the experiment.

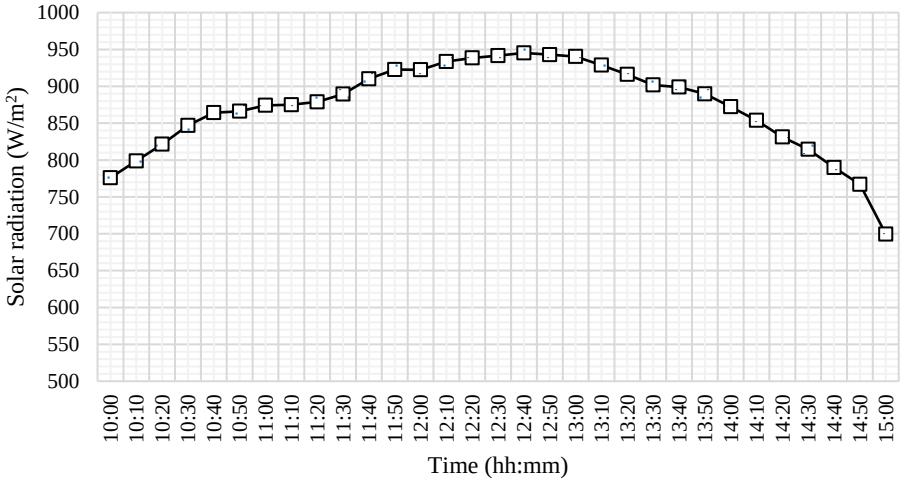

Fig. 4.30. The variation of solar radiation during the test time, 9 August 2022 (Natural airflow - Case 5).

Although the PV-a and PV-b modules are combined with different PV/T depths, they show slightly different temperatures, indicating that the PV/T depth can improve cooling, especially in larger systems that may be affected more by changing the depths. However, for the depth available in the present research, the improvement in cooling amount exceeds 1.5%.

However, the temperatures of the two modules (PV-a and PV-b) are still higher than the reference module temperature. The average $T_{PV\text{-}ref}$ achieved was 55.5 °C. The reason is that the airflow generated in the PV/T-a and PV/T-b ducts is insufficient to cool the PV-a and PV-b modules, as their values were low, as is apparent in Fig. 4.29.

The air velocity in PV/T-b is higher than that in PV/T-a; it is increasing by 13.5%, which confirms the benefit of decreasing the PV/T depth, which leads to an increase in the airflow velocity. However, its value is still less than what is required to cool the PV module compared to PV-ref.

A decrease in the temperature of the PV module leads to an increase in the power it generates, and this was observed by measuring the power generated for each of the three modules. As a result, the PV-ref may be more effective at converting SR into electrical power than other modules (PV-a and PV-b).

Fig. 4.31 shows the average PV power production for the three modules. From the figure, the PV-ref board generated the highest amount of electrical power compared to PV-a and PV-b, and this can be attributed to its lower temperature compared to other modules, even though it is not equipped with any cooling and heat dissipation system. The average $P_{PV\text{-}ref}$ achieved was 37.1 W. The PV-b module generates slightly more power than the PV-a module since it is cooled slightly with the decrease in the depth of PV/T-b, which helps to reduce the module's temperature slightly compared to PV-b and thus increases its efficiency. The average $P_{PV\text{-}a}$ and $P_{PV\text{-}b}$ were 36.4 W and 36.6 W, respectively. The increase in energy produced by the PV-ref module was 1.2% and 1.7% higher than the PV-b and the PV-a modules, respectively.

Although the PV-a module is integrated with an EAHE and relies on heat generated by the SC to move the air, it shows a lower power output than the PV-ref and slightly lower than the PV-b.

Thus, it can be seen from Fig. 4.31 that the PV-ref was the most efficient compared to PV-a and PV-b. The average efficiency achieved by PV-ref, PV-a, and PV-b was 15.9%, 15.6%, and 15.7%, respectively.

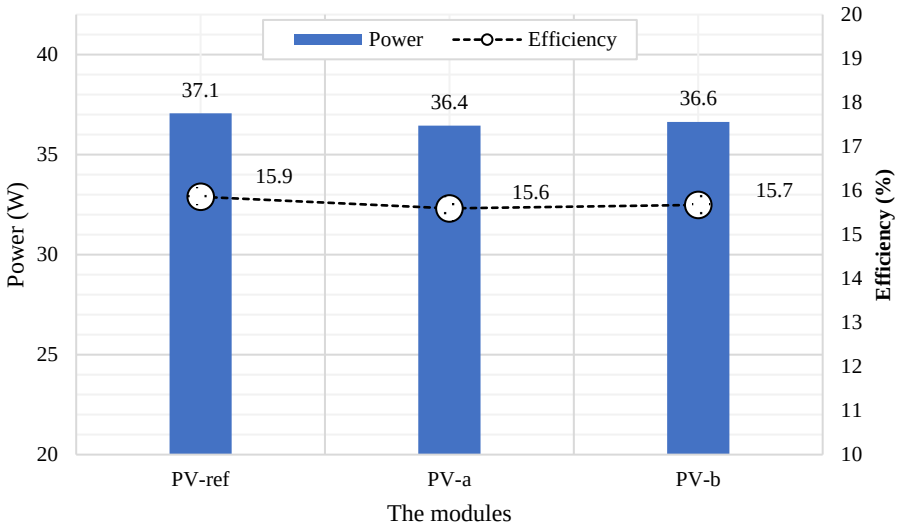

Fig. 4.31. The efficiency and power produced by the PV modules, 9 August 2022 (Natural airflow - Case 5).

Accordingly, the airflow velocity that passes through a narrower PV/T collector is 1.2 times higher than the airflow that passes through a wider PV/T collector. It is necessary to make use of the following equation to determine the velocity of the airflow:

$$v_{air} = 1.696 + 0.003903\,I - 0.2162\,T_{amb} - 7.523\times10^{-7}\,I^2 - 6.719\times10^{-5}\,I\,T_{amb} + 0.004525\,T_{amb}{}^2, \quad R^2 = 0.9617 \tag{4.8}$$

The decrease in PV/T depth helps move the air, increase its speed, and remove the heat from the PV module, enhancing the cooling process. This property improves the efficiency of the PV module and maintains its performance. The hot air generated by the PV module helps move the air inside the SC, creating a synergistic cycle that enhances the performance of both the SC and the PV module.

4.4.6. Investigation of the effect of the Earth-Air Heat Exchanger on the PV module efficiency

This experimental work was conducted to determine the effect of EAHE system integration on PV module efficiency, described in subsection 3.3. It lasted on a clear day in August of 2022. This experiment is necessary to determine the effect of integrating the EAHE system on the generation of cold air and the extent of its impact on the operating temperature of the photovoltaic module and its capacity and efficiency.

Fig. 4.32 shows the temperature variation T_{amb}, $T_{out,\,EAHE\text{-}a}$, $T_{out,\,EAHE\text{-}b}$, $T_{PV\text{-}ref}$, $T_{PV\text{-}a}$, $T_{PV\text{-}b}$, $T_{avg,\,SC\text{-}a}$, and $T_{avg,\,SC\text{-}b}$ and air velocity of the PV/T-a and the PV/T-b versus the reference module (PV-ref) (shown in Fig. 3.14 and Fig. 3.20) as a function of time (10:00 a.m. to 03:00 p.m.).

It is clear from the figure that the PV-a and PV-b modules show variations between their respective temperatures, as the temperature dissipation ratio exceeds 1.8%, which indicates the cooling efficiency gained from the SC and providing the air from the surroundings without using the EAHE. The average $T_{PV\text{-}a}$ and $T_{PV\text{-}b}$ were 59.8 °C and 58.8 °C, respectively, on the day of the experiment, which experienced the highest SR of 898.2 W/m^2 with an average of 812.6 W/m^2. Fig. 4.33 shows the intensity of SR during the day of the experiment.

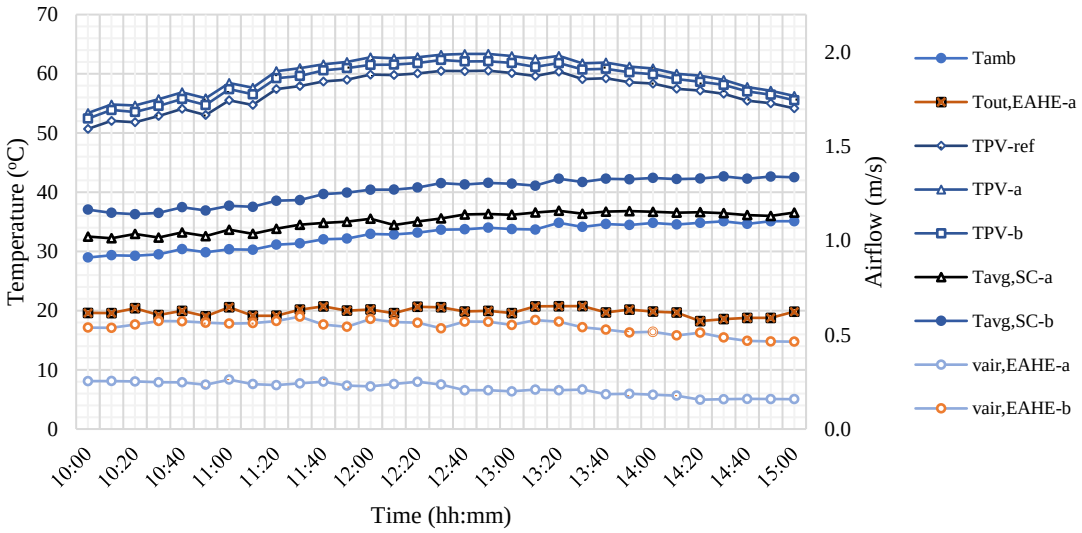

Fig. 4.32. The variation of T_{amb} vs. $T_{out,\ EAHE\text{-}a}$, $T_{PV\text{-}ref}$, $T_{PV\text{-}a}$, $T_{PV\text{-}b}$, and $T_{avg,\ SC\text{-}a}$ and air velocity of the PV/T-a and PV/T- during the test time, 27 August 2022 (Natural airflow - Case 6).

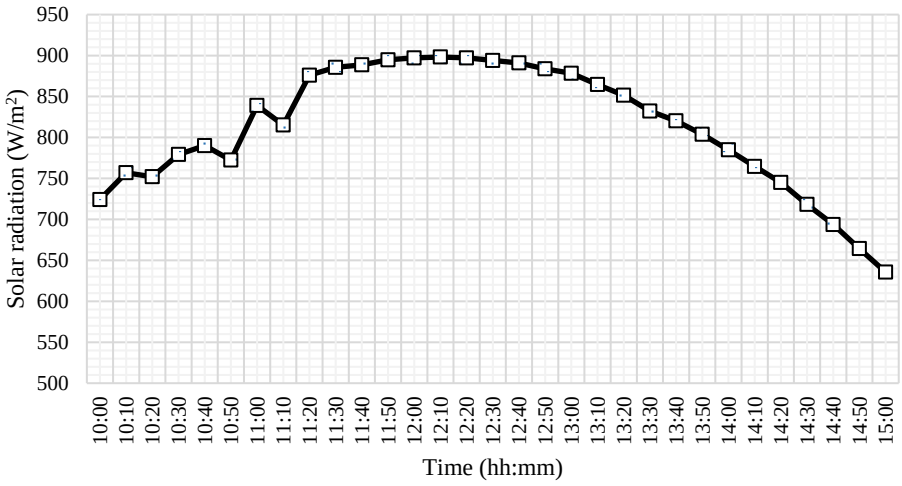

Fig. 4.33. The variation of solar radiation during the test time, 27 August 2022 (Natural airflow - Case 6).

Although the PV-a module is combined with the EAHE and the SC, the module shows higher temperatures than PV-b, which indicates that using the EAHE does not play an essential role in improving overall cooling. Depending on the analysis of the results, this is not due to a decrease in the EAHE's efficiency. The PV-a module was equipped with air at a lower temperature from the EAHE-a system, as $T_{out,\ EAHE\text{-}a}$ was 19.8 °C, lower than the air surrounding by 12.9 °C. While the PV-b module was equipped with hotter air, the air was extracted from the surroundings, as T_{amb} was 32.7 °C. This indicates that high efficiency has been achieved from the EAHE system (its efficiency was about 90.8%).

The reason is that the cooler air supplied to the SC, the lower natural airflow velocity occurs through the SC, as the amount of airflow velocity inside the SC depends on the difference between the average temperature of the air inside the SC ($T_{avg,\ SC}$) and T_{amb}. Therefore, as cooler air is supplied through the EAHE, the $T_{avg,SC}$ will decrease; thus, the difference between the $T_{avg,SC}$ and the T_{amb} will reduce. This leads to a decrease in airflow velocity. This supports this because the airflow velocity in the PV/T-a was 0.2 m/s, less than the PV/T-b (it was 0.54 m/s) due to the carefully analyzed reason. Fig. 4.32 shows the airflow velocity in both PV/T.

Therefore, the T_{PV-a} and T_{PV-b} were higher than T_{PV-ref}, the average T_{PV-ref} achieved was 57.1 °C. The reason is that the airflow is generated in the PV/T. T_{PV-a} and T_{PV-b} are insufficient to cool the modules PV-a and PV-b, as their values were low.

A decrease in the temperature of the PV module leads to an increase in the power it generates, and this was observed by measuring the power generated for each of the three modules. As a result, the PV-ref may be more effective at converting SR into electrical power than other modules (PV-a and PV-b).

Fig. 4.34 shows the average PV power production for the three modules. From the figure, the PV-ref board generated the highest amount of electrical power compared to PV-a and PV-b, and this can be attributed to its lower temperature compared to other modules, even though it is not equipped with any cooling and heat dissipation system. The average P_{PV-ref} achieved was 34.1 W. The PV-b module generates slightly more power than the PV-a module since it is cooled somewhat with higher airflow velocity, which helps to reduce the module's temperature slightly compared to PV-a and thus increases its efficiency. The average P_{PV-a} and P_{PV-b} were 33.5 W and 33.7 W, respectively. The increase in energy produced by PV-ref modules was 1.7% and 1% higher compared to PV-b and PV-a modules.

Although the PV-b module is integrated with SC only and relies on heat generated by the SC itself to move the air, it shows a lower power output than the PV-ref and slightly higher than the PV-a.

Thus, it can be seen from Fig. 4.34 that the PV-ref was the most efficient compared to PV-a and PV-b. The average efficiency achieved by PV-ref, PV-a, and PV-b was 15.7%, 15.4%, and 15.5%, respectively.

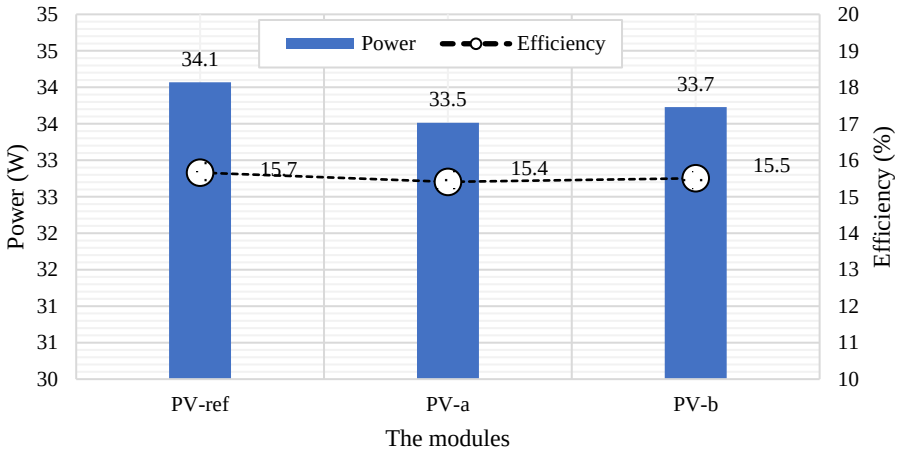

Fig. 4.34. The efficiency and power produced by the PV modules, 27 August 2022 (Natural airflow - Case 6).

Accordingly, the SC integrated with the PV module generates an airflow velocity 252.3% faster than the airflow velocity generated by the SC integrated with the PV module and the EAHE. The airflow velocity is subjected to the following equation:

$$v_{air} = -228.3 + 0.9259\, I + 5.233\, T_{amb} - 0.001332\, I^2 - 0.01941\, I\, T_{amb} + 7.847\times10^{-7}\, I^3 + 2.384\times10^{-5}\, I^2\, T_{amb} - 1.481\times10^{-10}\, I^4 - 9.713\times10^{-9}\, I^3\, T_{amb}, \quad R^2 = 0.8699 \tag{4.9}$$

4.5. The performance of the PV module depends on the forced ventilation

4.5.1. Investigation of the effect of forced air (0.5 m/s) and EAHE on the PV module efficiency

This experimental work was conducted to determine the effect of forced air with velocity 0.5 m/s and EAHE on the PV module efficiency, described in subsection 3.3. It lasted on a clear day in August of 2022. This experiment is necessary to determine the effect of forced air by a fan with a velocity of 0.5 m/s, integration with EAHE, and using the solar chimney on the generation of cold air and the extent of its effect on the operating temperature of the PV module and thus its capacity and efficiency.

Fig. 4.35 shows the temperature variation T_{amb}, $T_{out,\ EAHE\text{-}a}$, $T_{PV\text{-}ref}$, $T_{PV\text{-}a}$, $T_{PV\text{-}b}$, $T_{avg,\ SC\text{-}a}$, and $T_{avg,\ SC\text{-}b}$ and air velocity of the PV/T-a and the PV/T-b versus the reference module (PV-ref) (shown in Fig. 3.14 and Fig. 3.21) as a function of time (10:00 a.m. to 3:00 p.m.).

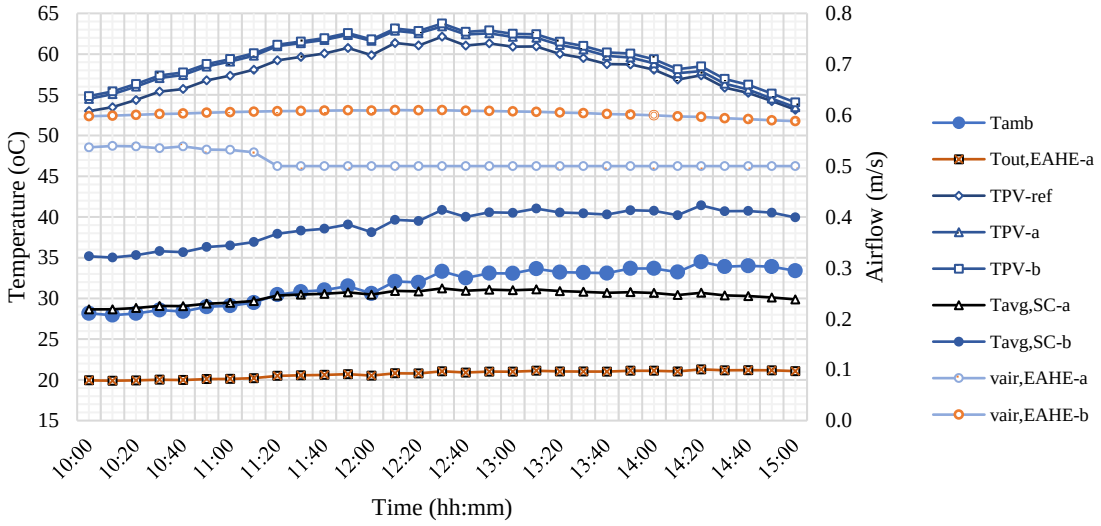

Fig. 4.35. The variation of T_{amb} vs. $T_{out,\ EAHE\text{-}a}$, $T_{PV\text{-}ref}$, $T_{PV\text{-}a}$, $T_{PV\text{-}b}$, and $T_{avg,\ SC\text{-}a}$ and air velocity of the PV/T-a and PV/T- during the test time (Forced airflow - Case 1).

It is clear from the figure that the PV-a and PV-b modules show great convergence between their respective temperatures, as the temperature dissipation ratio did not exceed 0.6%, which indicates the little cooling efficiency gained from the fan, the EAHE, and the SC. The average $T_{PV\text{-}a}$ and $T_{PV\text{-}b}$ were 59.3 °C and 59.7 °C, respectively, on the day of the experiment which experienced the highest SR of 976.2 W/m^2 with an average of 879.3 W/m^2. Fig. 4.36 shows the intensity of SR during the day of the experiment.

Although the PV-a module is connected to the fan, EAHE, and the SC, it shows slightly lower temperatures than the PV-b module, which indicates that the use of the EAHE does not play an essential role in improving cooling overall in this case. Using the EAHE may have a more compelling effect on larger sizes of hybrid systems. This is not due to a decrease in the EAHE's efficiency. The PV-a module was equipped with air at a lower temperature from the EAHE-a system, as $T_{out,\ EAHE\text{-}a}$ was 20.7 ^{o}C, lower than the air surrounding by 11 ^{o}C. While the PV-b module was equipped with hotter air, the air was extracted from the surroundings, as T_{amb} was 31.7 ^{o}C. This indicates that high efficiency has been achieved from the EAHE system (its efficiency was about 82.1%).

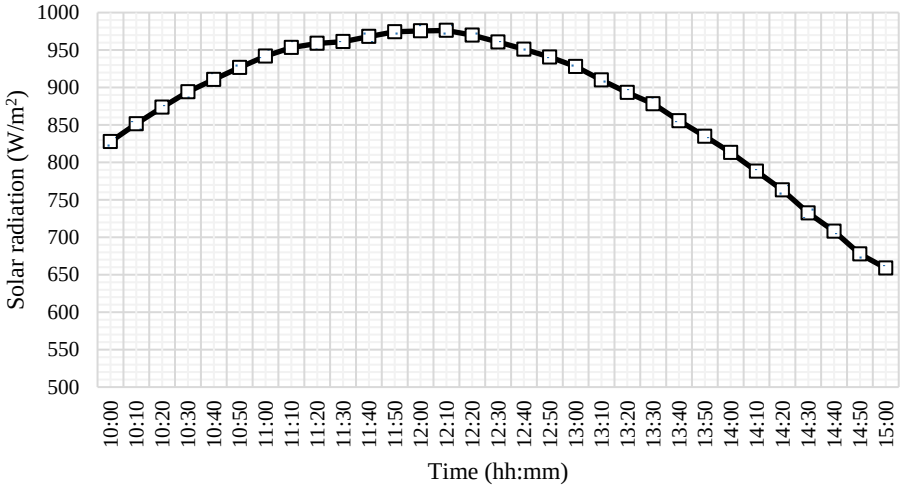

Fig. 4.36. The variation of solar radiation during the test time (Forced airflow - Case 1).

Although the airflow velocity in PV/T-a was 0.51 m/s, which is less than the velocity in PV/T-b (0.6 m/s), what was observed was that the temperature of PV-a was lower than PV-b and the reason is that the cold air supplied from the EAHE compared to air supplied from the ambient. This leads to the conclusion that it is possible to benefit from integrating the EAHE with the PV module to cool it and improve its efficiency if sufficient velocity is available.

What is worth noting here is that the airflow velocity specified by the fan is 0.5 m/s, but what was observed is that airflow velocity is higher than the selected speed in the PV/T-a and the PV/T-b. The reason is that there is an additional velocity that the SC generated because the average temperatures of the SC were higher than the ambient air temperatures during the experiment period, especially the PV/T-b, which is apparent in Fig. 3.35, which led to an increase in airflow velocity inside it. As for the PV/T-a model, an additional airflow was generated for up to 11:15 AM, and after this time, the airflow velocity remained relatively stable until the end of the experiment, which is also evident in the figure.

Therefore, the temperatures in both modules were still higher than the reference module temperature, and the average $T_{PV\text{-}ref}$ achieved was 58.1 °C. The reason is that the airflow is generated in the modules. $T_{PV\text{-}a}$ and $T_{PV\text{-}b}$ are insufficient to cool the PV-a and PV-b modules, as their values were low, as shown in Fig. 4.35.

A decrease in the temperature of the PV module leads to an increase in the power it generates, and this was observed by measuring the power generated for each of the three modules. As a result, the PV-ref may be more effective at converting SR into electrical power than other modules (PV-a and PV-b).

Fig. 4.36 shows the average PV power production for the three modules. From the figure, the PV-ref board generated the highest amount of electrical power compared to PV-a and PV-b, and this can be attributed to its lower temperature compared to other modules, even though it is not equipped with any cooling and heat dissipation system. The average $P_{PV\text{-}ref}$ achieved was 36.6 W. The PV-b module generates slightly more power than the PV-a module since it is cooled somewhat with higher airflow velocity, which helps reduce the module's temperature slightly compared to PV-a and thus increases its efficiency. The average $P_{PV\text{-}a}$ and $P_{PV\text{-}b}$ were 36.4 W and 36.3 W, respectively. The increase in energy produced by PV modules was 0.8% and 1% higher compared to PV-a and PV-b modules, respectively.

Although the PV-a module is integrated with SC and EAHE, it relies on heat generated by the SC itself and the fan to move the air, and it shows a lower power output than the PV-ref and slightly higher than the PV-b.

Thus, it can be seen from Fig. 4.37 that the PV-ref was the most efficient compared to PV-a and PV-b. The average efficiency achieved by PV-ref, PV-a, and PV-b was 15.6%, 15.5%, and 15.4%, respectively.

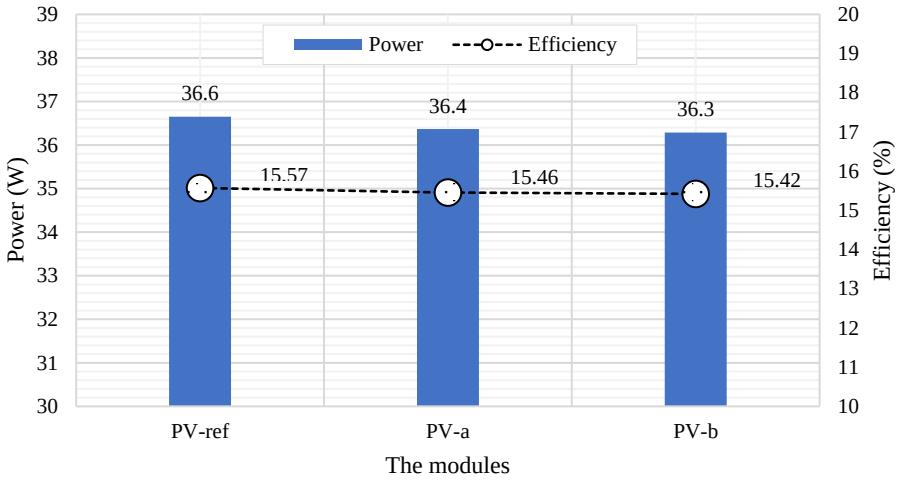

Fig. 4.37. The efficiency and power produced by the PV modules (Forced airflow - Case 1).

4.5.2. Investigation of the effect of forced air (1 m/s) and EAHE on the PV module efficiency

This experimental work was conducted to determine the effect of forced air with a velocity of 1 m/s and EAHE on the PV module efficiency, described in subsection 3.3. It lasted on a clear day in August of 2022. This experiment is necessary to determine the effect of forced air by a fan with a velocity of 1 m/s, integration with EAHE, and using the solar chimney on the generation of cold air and the extent of its effect on the operating temperature of the PV module and thus its capacity and efficiency.

Fig. 4.38 shows the temperature variation T_{amb}, $T_{out,\ EAHE\text{-}a}$, $T_{PV\text{-}ref}$, $T_{PV\text{-}a}$, $T_{PV\text{-}b}$, $T_{avg,\ SC\text{-}a}$, and $T_{avg,\ SC\text{-}b}$ and air velocity of the PV/T-a and PV/T-b versus PV-ref (shown in Fig. 3.14 and Fig. 3.21) as a function of time (10:00 a.m. to 03:00 p.m.).

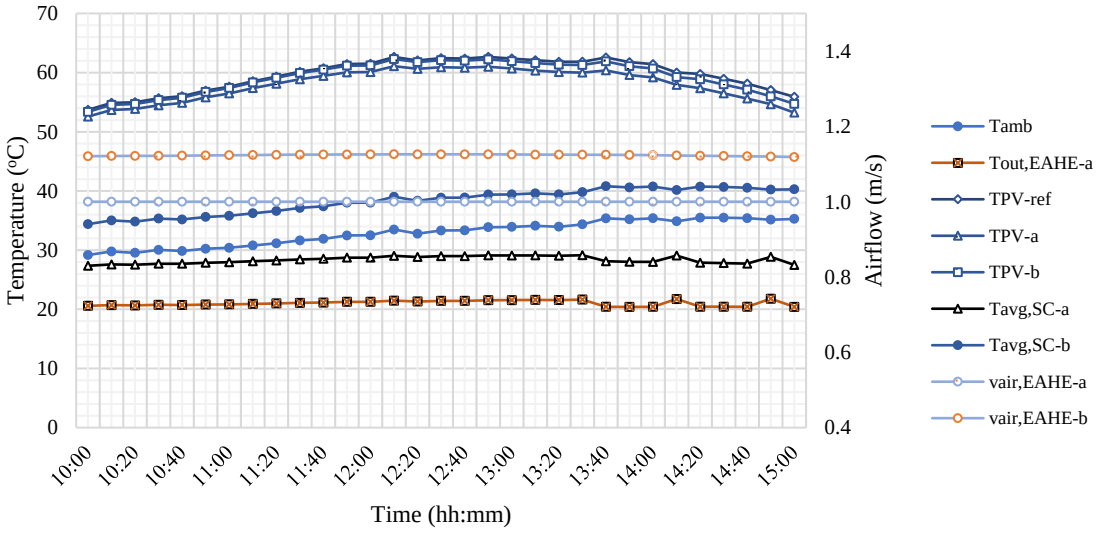

Fig. 4.38. The variation of T_{amb} vs. $T_{out,\ EAHE\text{-}a}$, $T_{PV\text{-}ref}$, $T_{PV\text{-}a}$, $T_{PV\text{-}b}$, and $T_{avg,\ SC\text{-}a}$ and air velocity of the PV/T-a and PV/T- during the test tie (Forced airflow - Case 2).

It is clear from the figure that the PV-a and PV-b modules show convergence between their respective temperatures, as the temperature dissipation ratio did not exceed 2%, which indicates the cooling efficiency gained from the fan, the EAHE, and the SC together. The average $T_{PV\text{-}a}$ and

T_{PV-b} were 57.9 °C and 59.7 °C, respectively, on the day of the experiment which experienced the highest SR of 976.2 W/m^2 with an average of 889.6 W/m^2. Fig. 4.39 shows the intensity of solar radiation during the day of the experiment.

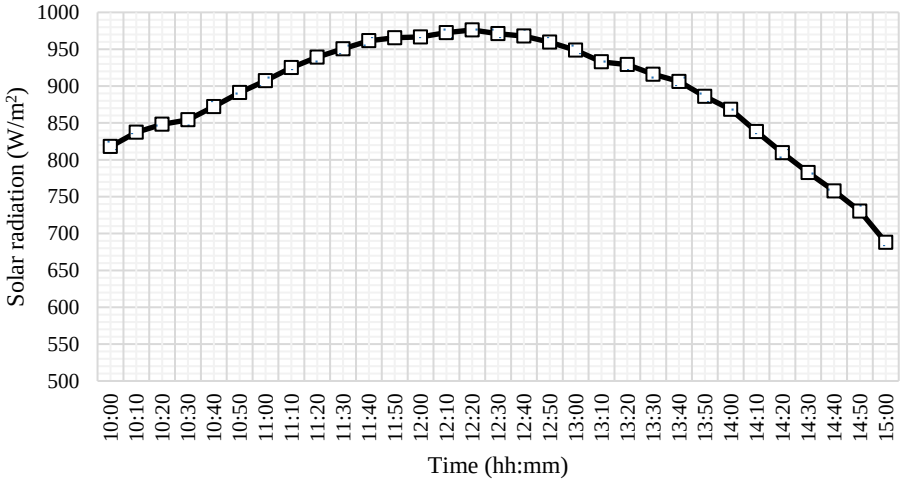

Fig. 4.39. The variation of solar radiation during the test time (Forced airflow - Case 2).

Due to the PV-a module being connected to the fan, EAHE, and the SC, the module shows lower temperatures than PV-b, which indicates that the EAHE play an important role in improving overall cooling. Using the EAHE may have a more practical effect for larger sizes of hybrid systems. The reason for this is due to the efficiency of the EAHE itself. The PV-a module was equipped with air at a lower temperature from the EAHE-a system, as $T_{out, EAHE-a}$ was 21 ^oC, which is lower than the temperature of the air surrounding by 11.9 ^oC. While the PV-b module was equipped with hotter air, the air was extracted from the surroundings, as T_{amb} was 32.9 ^oC. This indicates that high efficiency has been achieved from the EAHE system (its efficiency was about 81%).

What is worth noting here is that the airflow velocity specified by the fan is 1 m/s, but what was observed is that airflow velocity higher than the selected speed was measured in the PV/T-b model. The reason is that there is an additional speed that the SC generated because the average temperatures of the SC were higher than the ambient air temperatures during the experiment period, which is clear in Fig. 4.38, which led to an increase in airflow velocity inside it. As for the PV/T-a model, no additional airflow was generated, and the airflow velocity remained relatively stable during the experiment period, which is also apparent in the figure.

What is also worth noting is that although the airflow velocity in the PV/T-b model was higher than that in the PV/T-a model, the PV-a had a lower temperature than the PV-b and PV-ref, which was more efficient.

Therefore, the temperatures in both modules were lower than T_{PV-ref}, and the average T_{PV-ref} achieved was 59.6 °C. The reason is that the airflow is supplied in the modules. T_{PV-a} and T_{PV-b} were sufficient to cool the PV-a and PV-b modules, as their values were high, as is clear in Fig. 4.38.

A decrease in the temperature of the PV module leads to an increase in the power it generates, and this was observed by measuring the power generated for each of the three modules. As a result, the PV-ref may be less effective at converting SR into electrical power than the PV-a and the PV-b modules.

Fig. 4.40 shows the average PV power production from the three modules. From the figure, the PV-ref board generated the lowest amount of electrical power compared to PV-a and PV-b, and this can be attributed to its higher temperature compared to other modules because it is not

equipped with any cooling and heat dissipation system. The average $P_{PV\text{-}ref}$ achieved was 36.7 W. The PV-a module generates more power than the PV-b and PV-ref modules since it is cooled somewhat with lower airflow velocity and colder air, which helps to reduce the module's temperature compared to PV-b and PV-ref, thus increasing its efficiency. The average $P_{PV\text{-}a}$ and $P_{PV\text{-}b}$ were 37.1 W and 36.8 W, respectively.

Due to the PV-b module being integrated with SC without EAHE, it relies on heat generated by the SC and the fan to move the air, which is cooled by ambient air. It shows a higher power output than the PV-ref and lower than the PV-a.

Thus, it can be seen from Fig. 4.40 that PV-a was the most efficient compared to PV-b and PV-ref. The average efficiency of PV-ref, PV-a, and PV-b achieved were 15.4%, 15.6%, and 15.5% respectively.

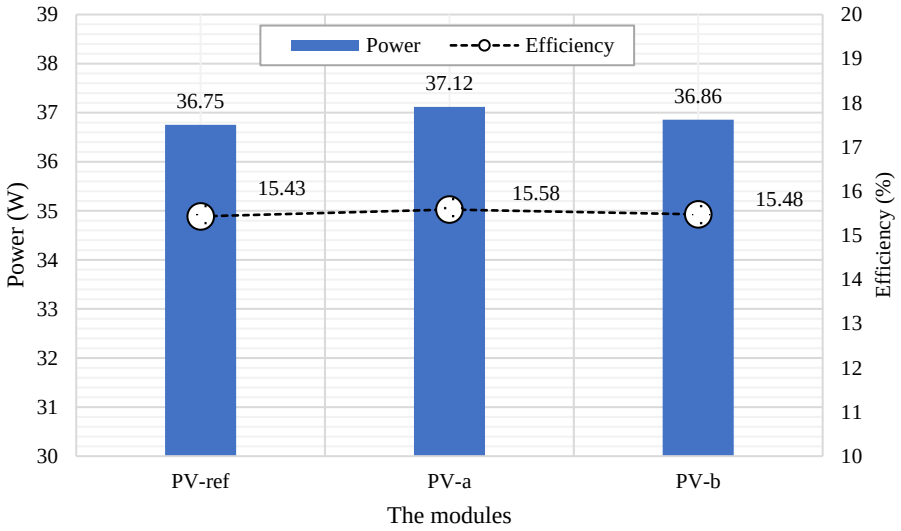

Fig. 4.40. The efficiency and power produced by the PV modules (Forced airflow - Case 2).

4.5.3. Investigation of the effect of forced air (1.5 m/s) and EAHE on the PV module efficiency

This experimental work was conducted to determine the effect of forced air with a velocity of 1.5 m/s and EAHE system on the PV module efficiency, described in subsection 3.3. It lasted on a clear day in August of 2022. This experiment is necessary to determine the effect of forced air by a fan with a velocity of 1.5 m/s, integration with EAHE, and using the solar chimney on the generation of cold air and the extent of its effect on the operating temperature of the PV module and thus its capacity and efficiency.

Fig. 4.41 shows the temperature variation T_{amb}, $T_{out,\ EAHE\text{-}a}$, $T_{PV\text{-}ref}$, $T_{PV\text{-}a}$, $T_{PV\text{-}b}$, $T_{avg,\ SC\text{-}a}$, and $T_{avg,\ SC\text{-}b}$ and air velocity of the PV/T-a and the PV/T-b modules versus PV-ref (shown in Fig. 3.14 and Fig. 3.21) as a function of time (10:00 a.m. to 03:00 p.m.).

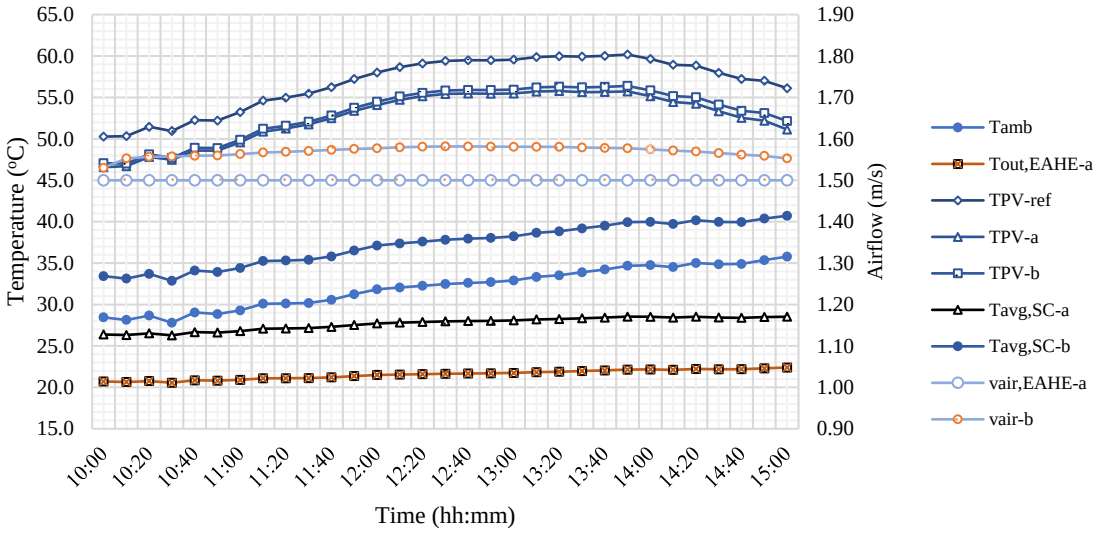

Fig. 4.41. The variation of T_{amb} vs. $T_{out,\ EAHE\text{-}a}$, $T_{PV\text{-}ref}$, $T_{PV\text{-}a}$, $T_{PV\text{-}b}$, and $T_{avg,\ SC\text{-}a}$ and air velocity of the PV/T-a and PV/T- during the test tie (Forced airflow - Case 3).

It is clear from the figure that the PV-a and PV-b modules show great convergence between their respective temperatures, as the temperature dissipation ratio did not exceed 1%, which indicates the little cooling efficiency gained from the fan, the EAHE, and the SC. The average $T_{PV\text{-}a}$ and $T_{PV\text{-}b}$ were 52.7 °C and 53.2 °C, respectively, on the day of the experiment, which experienced the highest SR of 898 W/m^2 with an average of 822.1 W/m^2. Fig. 4.42 shows the intensity of SR during the day of the experiment.

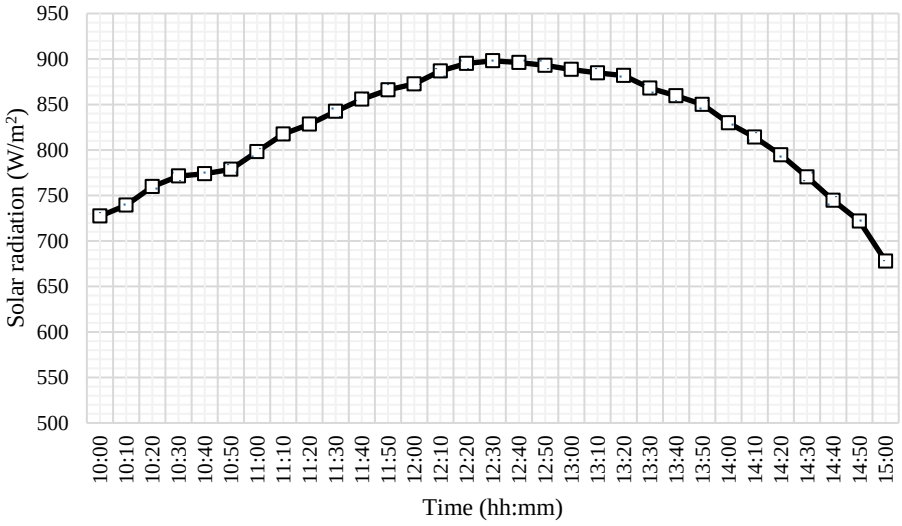

Fig. 4.42. The variation of solar radiation during the test time (Forced airflow - Case 3).

Due to the PV-a module being connected to the fan, the EAHE, and the SC, the module shows lower temperatures than PV-b, which indicates that the EAHE play an important role in improving overall cooling. Using the EAHE may have a more practical effect for larger sizes of hybrid systems. The reason for this is due to the efficiency of the EAHE itself. The PV-a module was equipped with air at a lower temperature from the EAHE-a system, as $T_{out,\ EAHE\text{-}a}$ was 21.5 °C, which is lower than the temperature of the air surrounding by 10.5 °C. While the PV-b module was equipped with hotter air, the air was extracted from the surroundings, as T_{amb} was 32.1 °C. This indicates that high efficiency has been achieved from the EAHE system (its efficiency was about 76.4%).

What is worth noting here is that the airflow velocity specified by the fan is 1.5 m/s, but what was observed is that airflow velocity higher than the selected speed was measured in the PV-b model. The reason is that there is an additional speed that the SC generated because the average temperatures of the SC were higher than the ambient air temperatures during the experiment period, which is clear in Fig. 4.41, which led to an increase in airflow velocity inside it. As for the PV/T-a model, no additional airflow was generated, and the airflow velocity remained relatively stable during the experiment period, which is also apparent in the figure.

What is also worth noting is that although the airflow velocity in the PV/T-b model was higher than that in the PV/T-a model, the PV-a had a lower temperature than the PV-b and PV-ref, which was more efficient.

Therefore, the temperatures in both modules were lower than $T_{PV\text{-}ref}$, and the average $T_{PV\text{-}ref}$ achieved was 56.7 °C. The reason is that the airflow is supplied in the modules. $T_{PV\text{-}a}$ and $T_{PV\text{-}b}$ were sufficient to cool the PV-a and PV-b modules, as their values were high, as is clear in Fig. 4.41.

The decrease in the temperature of the PV module leads to an increase in the power generated by it, and this was observed by measuring the power generated for each of the three modules. As a result, the PV-ref may be less effective at converting SR into electrical power than the PV-a and the PV/b modules.

Fig. 4.43 shows the average PV power production for the three modules. From the figure, the PV-ref board generated the lowest amount of electrical power compared to PV-a and PV-b, and this can be attributed to its higher temperature compared to other modules because it is not equipped with any cooling and heat dissipation system. The average $P_{PV\text{-}ref}$ achieved was 34.6 W. The PV-a module generates more power than the PV-b and PV-ref modules since it is cooled somewhat with lower airflow velocity and colder air, which helps to reduce the module's temperature compared to PV-b and PV-ref, thus increasing its efficiency. The average $P_{PV\text{-}a}$ and $P_{PV\text{-}b}$ were 35.4 W and 35.3 W, respectively.

Due to the PV-b module being integrated with SC without EAHE, it relies on heat generated by the SC and the fan to move the air, which is cooled by ambient air. It shows a higher power output than the PV-ref and lower than the PV-a.

Thus, it can be seen from Fig. 4.43 that PV-a was the most efficient compared to PV-b and PV-ref. The average efficiency of PV-ref, PV-a, and PV-b achieved were 15.7%, 16.1%, and 16%, respectively.

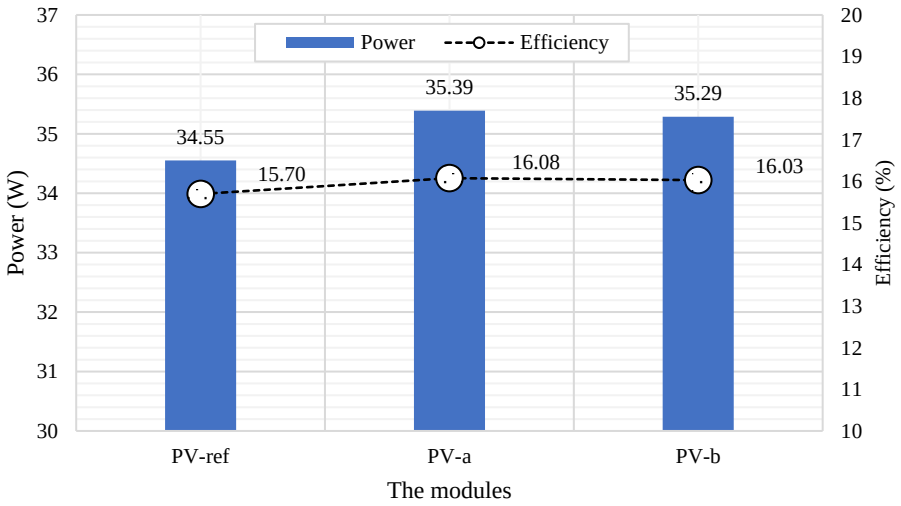

Fig. 4.43. The three modules' average PV power and efficiency (Forced airflow - Case 3).

Accordingly, the forced airflow by using the fans would cause an increase in the electrical energy generated by the integrated PV modules. However, the forced speed must not be less than 1 m/s or 1.5 m/s, as the increase in generated power is not less than 37.1 W and 35.4 W, respectively. The additional power generated by the integrated PV module was subject to the following equation:

$$P_{pv\text{-}add} = P_{pv} - P_{pv\text{-}ref} = -0.7054 + 1.087 \times v_{fan} - 0.02717\, P_{fan}\,, \quad R^2 = 0.9999 \qquad (4.10)$$

In this case, power was generated from the PV module, but at the same time, power was consumed from another source to operate the fans, which is not less than 3 W at a fan speed of 1 m/s and 4.6 W at a fan speed of 1.5 m/s. This requires finding an alternative way to generate sufficient flow without consuming electrical energy while improving the performance of PV modules using a PV-SC-EAHE hybrid system.

4.6. The performance of the PV module depends on the solar air collector

4.6.1. Investigation of the effect of solar collectors on the efficiency of PV module

It has been observed through the results obtained through the practical experiments of this research that the performance of the SC depends greatly on the amount of difference between the average air temperature inside the SC and the ambient air temperature; the greater amount of their difference leads to more extraordinary the SC performance. The performance of the solar chimney was better by increasing the air flow rate through it.

During the experimental cases described in sections (4.4 and 4.5), the temperature of the air entering the SC is usually low because the EAHE has cooled this air before entering PV/T, which leads to its temperature being relatively low before entering the SC, which leads to its efficiency is low, which requires increasing the air temperature before entering the SC and after leaving the PV/T. This can be done by installing a SAC after the PV/T and before the SC. The air will be heated after leaving the PV/T and crossing the PV module and before it reaches the SC, which leads to heating and increasing the efficiency of the SC and thus increasing the air flow rate, which leads to generating sufficient flow to cool the PV module integrated with the new hybrid system (PV-SC-EAHE) Thus, increasing the efficiency of the system as a whole.

The temperature of the heated air before entering the SC depends on the size and efficiency of the SAC itself. Therefore, in this research, the hybrid system will be simulated using the new MATLAB simulation model by simulating the conditions surrounding the study location in Gödöllő.

A SAC will be tested by selecting several sizes as a function of the dimensions of the PV module itself to be cooled, meaning the width of the SAC will be adopted with a width equal to the width of the PV module, which is 0.4 m in this research, and the length of the SAC will be tested as a function of the length of the PV module, i.e., multiples of PV module length itself. These multiples will be (1 to 10) times the length of the PV module. The purpose is to determine which of these SAC sizes is sufficient to heat the air before it enters the SC and through which sufficient airflow is generated to draw the cooled air from the EAHE necessary to cool the PV module and thus increase its efficiency.

The experimental data collected in Gödöllő simulated for this research. The ambient air temperature, solar radiation, and soil temperature (at a depth of 2 m in the Gödöllő), the EAHE length (10 m), and the same specifications of the PV module and the used were chosen. The system was described in subsection 3.3. and Fig. 3.22.

Fig. 4.44 shows the relationship between the length of the SAC and the airflow rate through the SC as a result of using the SAC. It is clear from the figure that the airflow velocity is directly proportional to the length of the SAC, meaning that as the length of the SAC increases, the airflow

rate increases. It is subject to Eq. (4.11). The airflow rate was 0.47 m/s when the length of the collector was equal to the length of the PV module. When the length of the SAC became ten times the length of the PV module, the velocity became equal to 1.03 m/s, which is sufficient at this value to sufficiently cool the PV module and increase the amount of power output compared to the non-integrated PV module.

The length of the SAC, which is equal to six times the length of the PV module, was sufficient to generate sufficient air velocity to cool the integrated PV module. This collector, of this size, generated a speed of 0.84 m/s to draw air from the EAHE at a low temperature of 20.8 °C, while the ambient air temperature was not less than 30 °C.

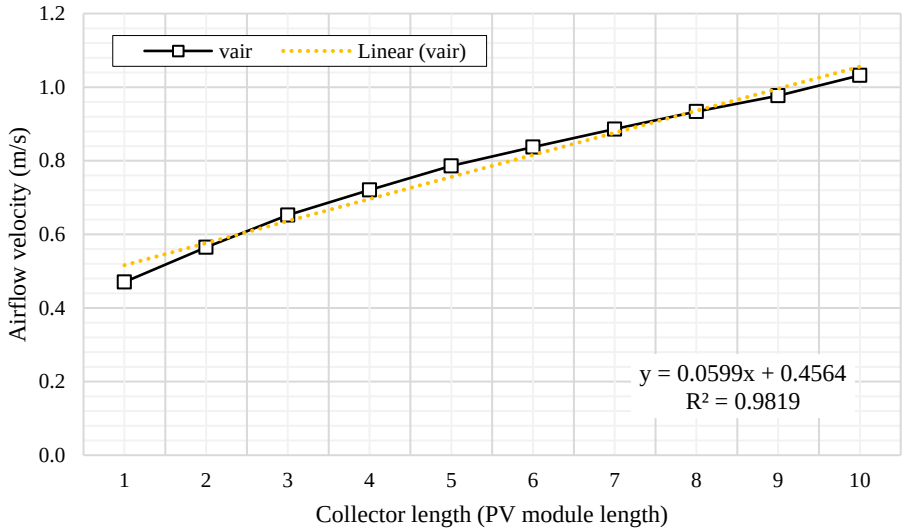

Fig. 4.44. The airflow velocity generated in the combined-assisted solar collector system is a function of the length of the PV module.

$$v_{air} = 0.0599\, L_{coll} + 0.4564 \;, \quad R^2 = 0.9819 \tag{4.11}$$

Fig. 4.45 shows the relationship between the length of the SAC compared to the generated power and the temperature of the PV module. It is clear from the figure that the amount of power output from the PV module increased with the increase in the length of the SAC, as its amount was 37.4 W when the size of the collector was equal to the size of the PV module. Still, when the length of the collector was ten times the length of the PV module, the power increased by 2.2%. This occurred due to increased airflow, which helped reduce the solar panel's temperature from 58.9 °C to 56 °C. The generated power and temperature of the PV module with the SAC and the hybrid system (PV-SC-EAHE) are governed by Eqs. (4.12) and (4.13) respectively.

$$P_{PV} = 37.335\, L_{coll}^{0.0077} \;, \quad R^2 = 0.9822 \tag{4.12}$$

$$T_{PV} = 0.0226\, {L_{coll}}^2 - 0.5569\, L_{coll} + 59.326 \;, \quad R^2 = 0.9983 \tag{4.13}$$

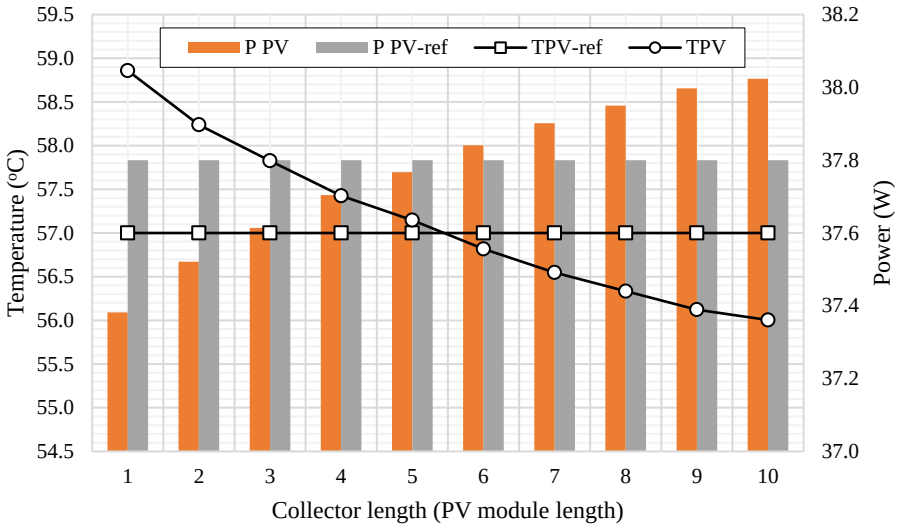

Fig. 4.45. The average PV power production by the PV modules and their temperatures.

4.6.2. The effect of solar air collectors on the efficiency of the photovoltaic module in different climates

SAC is seeing a rapid increase in interest as an effective way to improve the efficiency of PV modules integrated into solar energy systems. This investigation aims to evaluate the effect of SAC in different climates, where the system is tested in a hot climate (Najaf, Iraq) and a colder climate (Gödöllő, Hungary). The effect of SAC on the efficiency of the PV module integrated with the EAHE and the SC was studied in different climates.

Through this study, the change in naturally generated velocities when integrating the hybrid system (PV-SC-EAHE) with (SAC) was studied in the two different climates, as well as analyzing the effect of this on reducing the temperature of the PV module and thus evaluating its impact on the energy produced and efficiency of the PV module.

Fig. 4.46 shows the monthly naturally generated airflow velocity from combining PV-SC-EAHE with SAC at both study locations. SAC in Al-Najaf appears to naturally increase airflow velocity in the hot region, especially in the hot months of the year. As is the case for Gödöllő, SAC also shows an effect of increasing airflow velocity. However, the velocity generated in the hot location was more significant than Gödöllő by 20%, as the generated velocity reached its maximum of 1.1 m/s in Al-Najaf and 0.95 m/s in Gödöllő. The following equation is put into effect to the airflow velocities in order to perform the estimation:

$$v_{air} = 0.2762 + 0.005205\,I - 0.0423\,T_{amb} - 1.158\times10^{-5}\,I^2 + 0.0001367\,I\,V + 8.533\times10^{-9}\,I^3 - 1.166\times10^{-7}\,I^2\,T_{amb}, \quad R^2 = 0.9627 \tag{4.14}$$

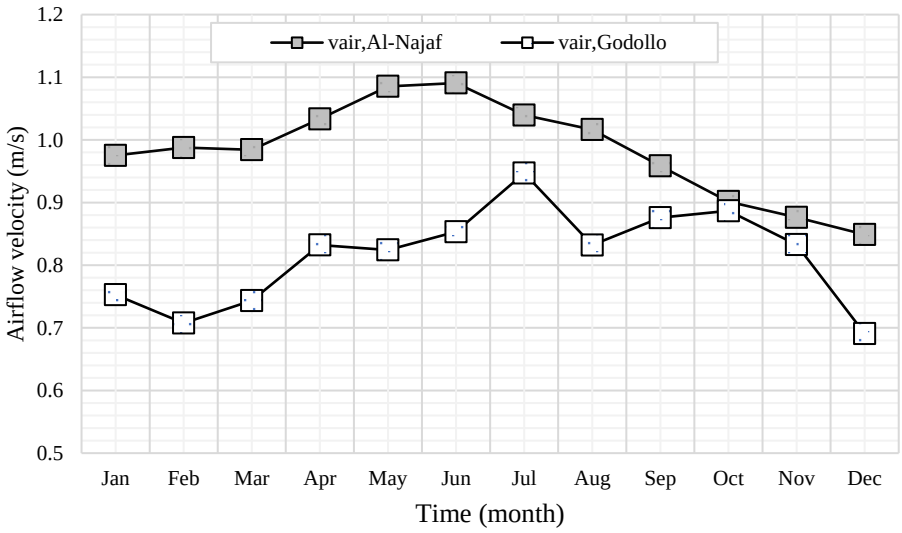

Fig. 4.46. The monthly naturally generated airflow velocity in Al-Najaf and Gödöllő.

Fig. 4.47 shows the temperatures of the integrated PV module compared to the reference PV module for both study locations. It is observed that PV module temperatures in Al-Najaf are generally higher compared to Gödöllő. The integrated PV module shows lower temperatures compared to the reference PV module in Al-Najaf and Gödöllő in all months. But what is noticeable is that the amount of cooling in Al-Najaf was higher and better than in Gödöllő.

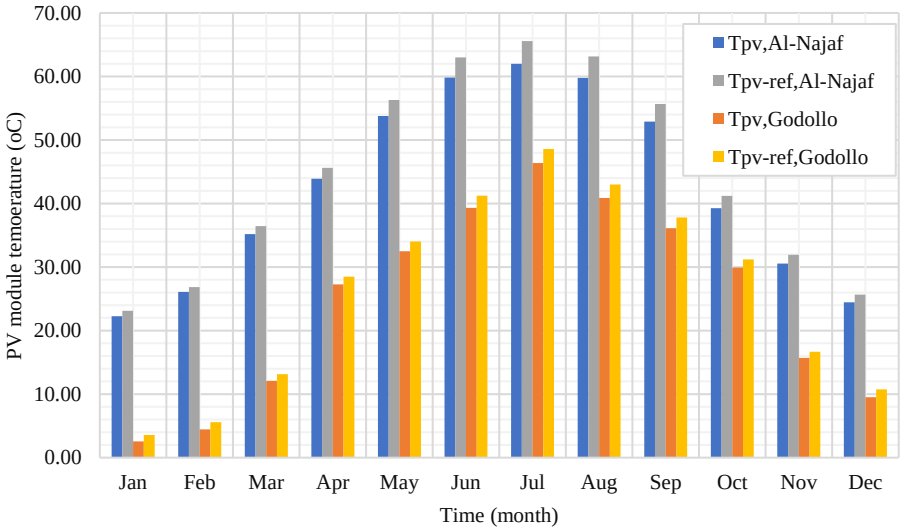

Fig. 4.47. The monthly temperatures of the integrated PV module compared to the reference PV module for Al-Najaf and Gödöllő.

The use of SAC shows an improvement in the power generated by the PV module compared to the reference module in most months. As well as the power produced in the Gödöllő also seems to have a positive effect on the power of the PV module. However, the increase in power in the hot region is greater than in the colder region by 49%, where the average generated power in the hot region reached 24.6 W. In contrast, the highest gain in the colder region was 16.5 W., as shown in Fig. 4.48.

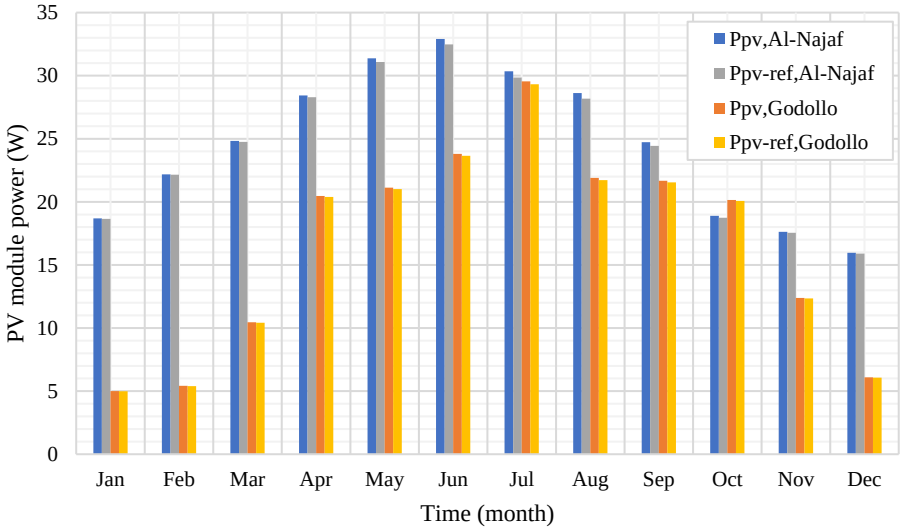

Fig. 4.48. The monthly power of the integrated PV module compared to the reference PV module for Al-Najaf and Gödöllő.

The effect of SAC is shown to improve the efficiency of the PV module compared to the reference PV module, especially in the hotter months.

In the cold region, SAC also shows a positive effect on efficiency, especially in hot months. However, what was observed is that the improvement in efficiency was better in the hot area than in the colder area, especially in the hot months, where the percentage increase in efficiency reached 2%, as shown in Fig. 4.49.

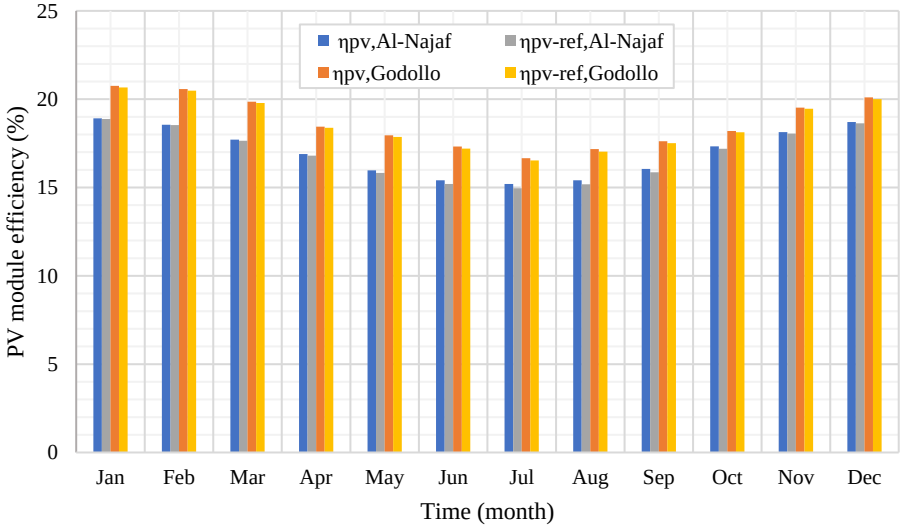

Fig. 4.49. The monthly efficiency of the integrated PV module in Al-Najaf and Gödöllő.

Thus, SAC shows a positive effect in reducing the temperatures of the PV module and improving its performance in hot conditions. SAC can also positively impact Gödöllő by improving the power and efficiency of the PV module. Increased airflow velocity with SAC indicates additional benefits that contribute to improving system performance.

Based on the results, studying the integration of SAC with PV modules in more scenarios and climatic conditions is preferable. Additional studies may be needed to determine the effect of solar air collectors on the extent of energy produced in the long term. The economic and environmental aspects of using solar air collectors in PV systems should be considered.

5. CONCLUSION AND SUGGESTIONS

The efficiency of the photovoltaic (PV) module integrated with the solar chimney (SC) and earth-air heat exchanger (EAHE) has been studied experimentally and in simulation. This research filled the knowledge gap by studying a new system that combines these three systems (SC, PV, and EAHE) to estimate the effect of the integration between SC and EAHE on the efficiency of the PV module. This study was conducted in two locations with different climates, Najaf in Iraq (hot and dry climate) and Gödöllő in Hungary (cold climate). This study presented a new MATLAB/Simulink model to predict soil temperature distribution and design combined or individual EAHE, SC, and PV systems. The soil's thermo-physical properties and temperature gradient were studied, and the EAHE's performance for the two modes (cooling and heating) was also studied. This study provided a comprehensive comparison between four different types of EAHE. The experiments were extended using the developed MATLAB program to demonstrate the role of integrating renewable energy sources. It provides important data for researchers and engineers to choose the best system that suits their needs. It is concluded that the new hybrid system combined with solar air collector (SAC) and SC has the best performance. In light of the results reached, the following conclusions can be drawn:

- New laboratory and theoretical simulation approaches assess multilayer soil thermo-physical characteristics based on moisture content and density.
- The MATLAB simulation approach for planning and predicting PV-SC-EAHE system performance worldwide is dependable and promising. It matches the measured data of 93.6%.
- The MS-pipe EAHE has the lowest pressure losses of the four varieties, requiring the least air fan power (AFP= 0.014 W), while the TS-pipe EAHE requires the most, 1.071 W.
- S-pipe and TS-pipe EAHE have the highest cooling potential (897.9 W) and the multi-pipe has the lowest (683.7 W).
- SC boosts the airflow velocity by 5.2 times when integrated with PV modules and EAHE.
- A rectangular SC enhances the airflow velocity by 5% over a circular SC and the dark SC has 1% higher airflow velocity than the white SC.
- EAHE length affects natural airflow. Airflow velocity is 14.7% higher in 5 m EAHE than in 10 m ones.
- In EAHE with the narrower PV/T depth (0.04 m), the tube airflow velocity was 1.2 times that of the wider PV/T depth (0.06 m).
- The SC with PV module generates 252.3% faster airflow than the SC with PV module and EAHE.
- The PV module cannot be cooled by the SC's natural airflow velocity alone in the PV-SC-EAHE system. Integration of a SAC before the SC and after the PV/T is required.
- Integrating a SAC with a PV-SC-EAHE system ten times the PV module's size increases PV module efficiency by 2.2%.
- The airflow velocity created by the PV-SC-EAHE system in Al-Najaf is 20% faster than the airflow velocity generated by the PV-SC-EAHE system in Gödöllő.
- In summer, the difference between ambient air and soil temperatures at 2 m was 10.3 °C in Gödöllő and 8.7 °C in Al-Najaf. In winter, the difference was 11.5 °C in Gödöllő and 6.7 °C in Al-Najaf.
- Al-Najaf soil temperature is stable year-round at 5 m depth. The soil-air temperature difference is 16.2 ^{o}C in summer and 11.4 ^{o}C in winter.

- EAHE in Gödöllő can achieve 71% and 70.1% cooling and heating efficiency. It lowered summer temperatures by 11 ^{o}C and heated the winter temperatures by 6.5 ^{o}C.

These theses can be expanded by examining more variables and exploring their effects on system performance, such as studying the possibility of integrating the solar dryer with the new hybrid system to dry agricultural products by taking advantage of the hot air generated and flowing naturally. Study the possibility of utilizing the EAHE for cooling and heating at night while the solar systems are not working. Research deeper into maximizing natural flow by introducing developments in the PV/T structure, SAC, SC, and EAHE. There may be opportunities to explore using additional renewable energy sources or integrate the solar system with energy storage. Studying the impact of the system in different locations around the world would be an extension of the research. It would be helpful to conduct an economic analysis to evaluate the long-term cost and benefits of the PV-SC-EAHE system.

6. NEW SCIENTIFIC RESULTS

This section presents the new scientific findings from this research work as follows:

1. *The effect of thermo-physical properties of the multilayer soil on earth-air heat exchanger efficiency*

I discovered that the multi-layer soil affects the efficiency of the EAHE. Based on the experimental results, I found that the amount of the relative difference between the outlet temperature of the EAHE system is 3.8% for a system of length 12 m and the thermal diffusivity range between 3.0258E-07 m^2/s and 4.3171E-07 m^2/s. It is subject to the following equation, $RD_{T,out}$ represents the relative difference of the outlet temperature, while L_{pipe} represents the length of the EAHE pipe. The effect of the relative difference in the type of layers was directly proportional to the length of the EAHE. As the length of the EAHE increases, the relative difference increases.

$$RD_{T,out} = 0.0002389 \times L_{pipe}^{\,3} - 0.01877 \times L_{pipe}^{\,2} + 0.5089 \times L_{pipe} - 0.09124, \quad R^2 = 0.9999$$

For this reason, it was necessary to develop a new methodology to estimate the thermo-physical properties of the multi-layered soil, especially since the method adopted so far by researchers and engineers when estimating the temperature distribution of soil assumes that the soil is one layer, and this is not available in most locations around the world. Soil thermo-physical properties include specific heat capacity, thermal conductivity, density, which depends on moisture content and dry and wet density.

Accordingly, a practical laboratory method and a theoretical simulation method were developed as a general rule; the practical laboratory approach calls for all types of soil to be mixed, the amount of each type being proportional to its presence on the work site, and then subjected to standard procedures to examine their properties and use the following equations:

$$w_{eq} = \left(\frac{(M_T)_{be} - (M_T)_{af}}{(M_T)_{be}} \times 100 \right)$$

$$\rho_{eq,wet} = \left(\frac{(M_T)_{be}}{(V_T)_{be}} \right)$$

$$\rho_{eq,dry} = \left(\frac{(M_T)_{af}}{(V_T)_{af}} \right)$$

The theoretical simulation methodology can also be used by using the following equations to determine the equivalent moisture content if the sample size and mass for each type of soil removed and its moisture content are known:

$$w_{eq} = \left(w_1 \times \frac{t_1}{t_T} + w_2 \times \frac{t_2}{t_T} + w_3 \times \frac{t_3}{t_T} + w_4 \times \frac{t_4}{t_T} + w_5 \times \frac{t_5}{t_T} + \ldots\ldots + w_n \times \frac{t_n}{t_T} \right)$$

$$\rho_{eq,wet} = \left(\frac{(M_1 + M_2 + M_3 + M_4 + M_5 + \ldots\ldots + M_n)_{be}}{(V_1 + V_2 + V_3 + V_4 + V_5 + \ldots\ldots + V_n)_{be}} \right)$$

$$\rho_{eq,dry} = \left(\frac{(M_1 + M_2 + M_3 + M_4 + M_5 + \ldots\ldots + M_n)_{af}}{(V_1 + V_2 + V_3 + V_4 + V_5 + \ldots\ldots + V_n)_{af}} \right)$$

2. *Performance assessment of the integrated solar energy system with earth-air heat exchanger system.*

I have created the mathematical and programming linkage of equations and formulas critical for the design, evaluation, and analysis of an integrated solar energy system with EAHE (PV-SC-EAHE), with the aim of assisting designers and researchers in the task of visualizing and

estimating the performance of a complex system across different global locations. This model is extremely important, as it not only facilitates the determination of the optimal length of the tube and ground area necessary to bury the tube to achieve the required air cooling of the integrated PV module and SC, but also provides valuable explanations about the basic mathematical relationships that manage the system.

The model is implemented using the MATLAB/Simulink environment, this model brings together a comprehensive set of crucial mathematical equations and formulas, which are complexly related both mathematically and programmatically. This allows designers across the world to evaluate soil temperature distribution at a variety of depths, estimate the thermo-physical properties of the soil at a specific location, as well as evaluate the temperature, efficiency, and power of the PV module. The model also provides assistance in determining the SC dimensions needed to ensure adequate airflow, drawing air from the surroundings through the integrated EAHE, PV and SAC system to enhance the use of solar energy. In addition, it provides a means of checking the temperature of the air entering the SC, forcing it out into the surrounding environment.

The provided and discussed measured and anticipated findings showed that the disparities between the two ranged from (6.0-6.9)%, with an average of 6.4%. These ratios are acceptable due to their capabilities, advantages, and cost savings in light of the measurement process, its challenges, and instantaneous and continuous weather fluctuations, as well as the conditions and assumptions that accompany the simulation model-building process using MATLAB. They are dependable vision and visualization tools. Since it was constructed using authorized scientific procedures and processes, the future system can alter and analyze its results before implementing it. Thus, this concept is promising and can be modified and developed in the future.

3. *Effect of geometric configuration on natural airflow generation in the integrated solar energy system with an earth-air heat exchanger system.*

I have explored the effect of the integration of SC and its shape, the integration of the EAHE and its length, PV/T depth, and the effect of climate on natural ventilation and air circulation during a hybrid system (PV-SC-EAHE). Based on the experimental results, the following are the outcomes that I have investigated:

- The SC, when integrated with PV modules and EAHE, leads to an increase of approximately 5.3 times in the airflow velocity. The airflow velocity is subjected to the following equation because of this integration:

$$v_{air} = 2.807 - 0.003708\, I - 0.06196\, T_{amb} + 1.005\times10^{-6}\, I^2 + 7.783\times10^{-5}\, I\, T_{amb} - 0.0002501\, T_{amb}^{\,2},\ R^2 = 0.9623$$

- The airflow velocity is increased by about 5% when the rectangular SC is utilized, as compared to the cylindrical SC. In order to estimate the velocity of the airflow, the following equation is applied:

$$v_{air} = -0.746 + 0.001783\, I + 0.02385\, T_{amb} + 8.364\times10^{-8}\, I^2 - 4.812\times10^{-5}\, I\, T_{amb},\quad R^2 = 0.9789$$

- The velocity of the airflow that passes through a narrower PV/T collector is 1.2 times higher than the velocity of the airflow that passes through a wider PV/T collector. It is necessary to make use of the following equation to determine the velocity of the airflow:

$$v_{air} = 1.696 + 0.003903\, I - 0.2162\, T_{amb} - 7.523\times10^{-7}\, I^2 - 6.719\times10^{-5}\, I\, T_{amb} + 0.004525\, T_{amb}^{\,2},\ R^2 = 0.9617$$

- The SC integrated with the PV module generates an airflow velocity 252.3% faster than the airflow velocity generated by the SC integrated with the PV module and the EAHE. The airflow velocity is subjected to the following equation:

$$v_{air} = -228.3 + 0.9259\,I + 5.233\,T_{amb} - 0.001332\,I^2 - 0.01941\,I\,T_{amb} + 7.847\times10^{-7}\,I^3 + 2.384\times10^{-5}\,I^2\,T_{amb} - 1.481\times10^{-10}\,I^4 - 9.713\times10^{-9}\,I^3\,T_{amb}, \quad R^2 = 0.8699$$

- The airflow velocity caused by the SC through the EAHE with a length of 5 m is 14.7% more than the airflow velocity through the EAHE with a length of 10 m. The following equation establishes the airflow velocity:

$$v_{air} = -2.173 + 0.001843\,I + 0.1288\,T_{amb} - 4.726\times10^{-5}\,I\,T_{amb} - 0.001891\,T_{amb}{}^2, \quad R^2 = 0.9731$$

- The airflow velocity that is created by the PV-SC-EAHE system in Al-Najaf is noticeably 20% faster when compared to the airflow velocity that is generated by the PV-SC-EAHE system in Gödöllő. The following equation is put into effect to the airflow velocities in order to perform the estimation:

$$v_{air} = 0.2762 + 0.005205\,I - 0.0423\,T_{amb} - 1.158\times10^{-5}\,I^2 + 0.0001367\,I\,V + 8.533\times10^{-9}\,I^3 - 1.166\times10^{-7}\,I^2\,T_{amb}, \quad R^2 = 0.9627$$

4. *The effect of the forced air and earth-air heat exchanger on the photovoltaic module efficiency.*

I have found that the speed normally generated by the SC alone (without additional SAC) is insufficient to generate sufficient airflow to cool the integrated PV module. For reasons related to the loss of pressure that occurs along the path through which the air passes through the EAHE and the PV/T collector to reach the SC, which dissipates part of the generated velocity on the one hand, and as a result of the insufficient temperature difference between the inside of the SC and the ambient temperature which reduces of the buoyant force inside the SC on the other hand. Therefore, the flow necessary to cool the PV module is not generated. For this reason, one of the proposed methods is to combine the hybrid system (PV-SC-EAHE) with forced airflow using fans, which would cause an increase in the electrical energy generated by the integrated PV modules. However, the forced speed must not be less than 1 m/s or 1.5 m/s, as the increase in generated power is not less than 37.1 W and 35.4 W, respectively. The additional power generated by the integrated PV module was subject to the following equation:

$$P_{pv\text{-}add} = P_{pv} - P_{pv\text{-}ref} = -0.7054 + 1.087 \times v_{fan} - 0.02717\,P_{fan}, \quad R^2 = 0.9999$$

In this case, power was generated from the PV module, but at the same time, power was consumed from another source to operate the fans, which is not less than 3 W at a fan speed of 1 m/s and 4.6 W at a fan speed of 1.5 m/s.

This necessitates the exploration of an alternative approach to generate sufficient airflow without relying on electrical energy consumption, aiming to enhance the efficiency of PV modules through the utilization of an innovative hybrid system combining PV modules and SC with EAHE (PV-SC-EAHE). The focus of this alternative method should be directed towards elevating the temperature of the air exiting the PV/T collector and entering the SC, ensuring that the average air temperature inside the SC is maximized compared to T_{amb}.

5. *The effect of the solar air collector on the efficiency of photovoltaic modules.*

I have explored that the temperature of the air exiting the PV/T collector and entering the SC is not sufficient to create an adequate flow to draw air from the EAHE, passing through the PV/T, and reaching the SC. This requires raising the temperature of the air before it enters the SC by incorporating a SAC. Therefore, I found that the airflow velocity is directly proportional to the length of the SAC, which means that as the length of the SAC increases, the airflow rate increases and is subject to the equation:

$$v_{air} = 0.0599\,L_{coll} + 0.4564, \quad R^2 = 0.9819$$

The airflow rate was 0.47 m/s when the length of the collector was equal to the length of the PV module (the collector's width is similar to the PV module's width). When the length of the SAC became ten times the length of the PV module, the velocity became equal to 1.03 m/s, which is sufficient at this value to sufficiently cool the PV module and increase the amount of power output compared to the non-integrated PV module.

The length of the SAC, which is equal to six times the length of the PV module, was sufficient to generate sufficient air velocity to cool the integrated PV module. This collector, of this size, caused a speed of 0.84 m/s to draw air from the EAHE at a low temperature of 20.8 °C, while the air temperature was not less than 30 °C.

The amount of power output from the PV module increased with the increase in the length of the SAC, as its amount was 37.4 W when the length of the collector was equal to the length of the PV module. Still, when the length of the collector was ten times the length of the PV module, the power increased by 2.2%. This occurred due to increased airflow, which helped reduce the temperature of the PV module from 58.9 °C to 56 °C. The generated power and temperature of the PV module with the SAC and the hybrid system (PV-SC-EAHE) are governed by the following equations, respectively.

$$P_{PV} = 37.335\, L_{coll}^{0.0077} \quad , \quad R^2 = 0.9822$$

$$T_{PV} = 0.0226\, {L_{coll}}^2 - 0.5569\, L_{coll} + 59.326 \, , \quad R^2 = 0.9983$$

6. The effect of geometric configuration of an earth-air heat exchanger system on its efficiency.

Based on experimental and simulation results, I have discovered that the efficiency of EAHE is affected by its geometric configuration by comparing four types of geometric configurations of EAHE (S-EAHE, M-EAHE, MS-EAHE, and TS-EAHE systems). Accordingly, the MS-EAHE has the lowest pressure loss among other EAHE system types, resulting in the least additional air fan power required to operate the fan needed to circulate the air inside it.

M-EAHE had more significant pressure losses compared to MS-EAHE by approximately 1.6 times. The S-EAHE and TS-EAHE types had the highest pressure losses. They required the most significant amount of additional air fan power for operation, as their pressure losses were 13.8 and 14.7 times, respectively, and their additional air fan power was 71.1 and 75.5 times higher than MS-EAHE.

Furthermore, the S-EAHE and TS-EAHE have the highest cooling potential compared to other EAHE system types, at 278.3 W on average. The MS-EAHE and the M-EAHE have less cooling potential of 19.1% and 22.3%, respectively, compared to the S-EAHE and the TS-EAHE types.

The four types are subject to the following equations, where CP represents the cooling potential of the EAHE types and T_{in} represents the inlet temperature of the EAHE.

$CP = 1.853\times10^4 \sin(0.002276\, T_{in} + 6.218), \quad R^2=1$ (For S-EAHE and TS-EAHE)

$CP = 1.295\times10^4 \sin(0.002528\, T_{in} + 6.211), \quad R^2=1$ (For M-EAHE)

$CP = 1.383\times10^4 \sin(0.002467\, T_{in} + 6.213), \quad R^2=1$ (For MS-EAHE)

7. SUMMARY

THE EFFECT OF INTEGRATING AN EARTH-AIR HEAT EXCHANGER ON PHOTOVOLTAIC MODULE EFFICIENCY IN COMBINATION WITH A SOLAR CHIMNEY

In summary, experimental investigations and software simulations using the MATLAB model developed in this work evaluated the combined Photovoltaic (PV) module Earth-Air Heat Exchanger (EAHE) system and solar chimney (SC) efficiency under extreme cold and hot conditions in Hungary and Iraq. In Gödöllő, Hungary (latitude 47.593434N, longitude 19.364198E), two hybrid systems with PV modules, SC, and EAHE and one without (reference system) were developed and tested to achieve this goal.

All reference and hybrid models have been built thoughtfully to achieve the accuracy required to draw results and conclusions. Experimental results and software simulations indicate that the best case obtained from each experiment was a combination of EAHE, PV/T, SC, and solar air collector (SAC), which was investigated and compared to a reference PV module. The experiments were expanded using the developed MATLAB program to demonstrate the role of integrating renewable energy sources, considering several aspects.

This study created new laboratory and theoretical simulation approaches to evaluate multi-layer soil thermo-physical properties based on moisture content and densities. This study's MATLAB simulation model for PV-SC-EAHE system design and global performance estimation is dependable and promising. With a 6.4% difference, it matches the measured data. MS-tubed EAHE have the lowest pressure losses of the four varieties, requiring the least air fan power (AFP = 0.014 W). TS-tubed EAHE have the biggest pressure losses and need the most AFP power, approximately 1,07 W. The multi-tube type has the lowest cooling potential of 683.7 W, whereas EAHE MS-tubes have the most at 897.9 W. Combining SC, PV module, and EAHE boosts airflow velocity inside the tube by 5.2 times. EAHE's length affects natural airflow, as proven. EAHE-5 m generates 14.7% quicker airflow than EAHE-10 m.

Experimentally, a rectangular SC increases the airflow velocity inside an EAHE tube to 5% compared to using a circular SC. The airflow velocity in the dark SC (black) has a limited increase of 1% compared to the white SC. As a result of experimental tests, the airflow velocity inside the tube of EAHE combined with a narrower PV/T was 1.2 times that of EAHE combined with a wider PV/T. The airflow velocity generated by the SC combined with the PV module is 252.3% faster than the airflow velocity generated by the SC combined with the PV module and EAHE.

It has been shown through experiments that the airflow velocity naturally generated by the SC (without additional SAC) combined with the PV-SC-EAHE system is not sufficient to cool the PV module regardless of the temperature supplied by the EAHE, which requires adding SAC before SC and after PV/T. Accordingly, the SAC was integrated with the PV-SC-EAHE system with an area 10 times the area of the PV module, which led to an improvement in the efficiency of the PV module by 2.2%. Based on the simulation results, the natural airflow was 20% faster in the hot location (Al-Najaf) than in the colder location (Gödöllő). The generated velocity reached a maximum of 1.1 m/s in the hot location and 0.95 m/s in the colder location.

In Gödöllő, the summertime temperature differential between the air and the soil at a depth of 2 m was 10.3 °C, while in Al-Najaf, it was 8.7 °C. Gödöllő, on the other hand, had a wintertime temperature differential of 11.5 °C and Al-Najaf, 6.7 °C. Within Al-Najaf, the soil temperature remained mostly consistent at a depth of 5 m all year round. There is a temperature differential of almost 16.2 °C in the summer and 11.4 °C in the winter between the soil and the surrounding air. According to practical testing, the installation of EAHE in Gödöllő can reach at least 71% efficiency in cooling mode and 70.1% efficiency in heating mode. In summer, it lowered the temperature by 11 °C; in winter, it raised it by 6.5 °C.

8. ÖSSZEFOGLALÁS (SUMMARY IN HUNGARIAN)

A FÖLD-LEVEGŐ HŐCSERÉLŐ BEÉPÍTÉSÉNEK HATÁSA A FOTOVOLTAIKUS MODUL HATÉKONYSÁGÁRA, NAPKÉMÉNNYEL KOMBINÁLVA

Doktori munkában kifejlesztett MATLAB modell segítségével kísérleti vizsgálatokat és szoftveres szimulációkat végeztem a kombinált PV-modul, a levegő-föld hőcserélő (EAHE) rendszer és a napkémény (SC) hatékonyságának értékelésére, Magyarországon extrém hideg körülmények között és Irakban extrém meleg körülmények között. A cél elérése érdekében több hibrid rendszert építettem és teszteltem, ezek közül kettőt integráltan (egy-egy PV-modullal, SC-vel és EAHE-vel, a másikat SC és EAHE nélkül (referencia rendszer)), Magyarországon, Gödöllő éghajlati viszonyai között (47,593434N szélesség, 19,364198E hosszúság).

Valamennyi referencia- és hibrid modell olyan átgondolt módon készült, hogy elérje az eredmények és következtetések levonásához szükséges pontosságot. A kísérleti eredmények és a szoftveres szimulációk azt mutatták, hogy az egyes kísérletekben kapott legjobb eset az EAHE, PV/T, SC és napkollektor (SAC) kombinációja volt, amelyet egy referencia PV-modullal vizsgáltam és hasonlítottam össze. A kísérleteket a kifejlesztett MATLAB programmal bővítettem, hogy bemutassam a megújuló energiaforrások együttes integrálásának szerepét, több szempontot is figyelembe véve.

A tanulmány révén új laboratóriumi és elméleti szimulációs módszereket dolgoztam ki a többrétegű talajok termofizikai tulajdonságainak becslésére a nedvességtartalom és a sűrűség alapján. Az e tanulmány keretében kifejlesztett MATLAB szimulációs modell a PV-SC-EAHE rendszer teljesítményének megtervezésére és becslésére világszerte megbízhatónak és nagyon ígéretesnek tekinthető. Jól egyezik a mért adatokkal, az eltérések átlagosan körülbelül 6,41%-osak. Az MS-csöves EAHE-kről kimutattam, hogy a négy típus közül a legkisebb nyomásveszteséggel rendelkeznek, ami a működéshez szükséges legkisebb kiegészítő ventilátorteljesítményt eredményezi (kb. AFP=0,014 W). A TS-csöves EAHE-knél a legnagyobb a nyomásveszteség, így a legnagyobb AFP-teljesítményre van szükség. Ráadásul körülbelül 1,1 W-tal. Az MS csöves EAHE-k rendelkeznek a legnagyobb hűtési potenciállal, 897,9 W-tal, a többcsöves típus pedig a legalacsonyabb hűtési potenciállal, 683,7 W-tal. Az SC kombinálása a PV-modullal és az EAHE-kkel akár 5,2-szeresére növeli a légáramlási sebességet az EAHE-k csövén belül, mintha nem kombinálnánk őket. Bebizonyosodott, hogy az EAHE-n belüli természetes légáramlást befolyásolja annak hossza. A rövidebb EAHE-kben (EAHE-5 m) keletkező légáramlási sebesség 14,7%-kal nagyobb, mint a hosszabb EAHE-kben (EAHE-10 m).

Kísérleti úton bizonyítást nyert, hogy a téglalap alakú SC 5%-kal növeli a légáramlási sebességet az EAHE-s csőben, szemben a kör alakú SC használatával. A légáramlási sebesség a sötét SC-ben (fekete) korlátozottan, 1%-kal nőtt a fehér SC-hez képest. A kísérleti vizsgálatok eredményeként a szűkebb PV/T-vel kombinált EAHE-k csövében a légáramlási sebesség 1,2-szöröse volt a szélesebb PV/T-vel kombinált EAHE-kénak. A PV-modullal kombinált SC által generált légáramlási sebesség 252,3%-kal nagyobb, mint a PV-modullal és EAHE-kkel kombinált SC által generált légáramlási sebesség.

Kísérletek során bebizonyosodott, hogy a PV-SC-EAHE rendszerrel kombinált SC által természetesen generált légáramlási sebesség nem elegendő a PV-modul hűtéséhez, függetlenül az EAHE által biztosított hőmérséklettől. Ez a tény szükségessé teszi a SAC hozzáadását az SC előtt és a PV/T után. Ennek megfelelően a SAC-ot a PV-SC-EAHE rendszerbe integráltam a PV-modul területének 10-szeresével, ami a PV-modul hatékonyságának 2,2%-os javulását eredményezte. A szimulációs eredmények alapján a természetes légáramlás 20%-kal gyorsabb volt a meleg helyen (Al-Najaf), mint a hideg helyen (Gödöllő). A generált maximális sebesség a meleg helyen 1,1 m/s, a hideg helyen pedig 0,95 m/s volt.

A talaj hőmérsékleti gradiensének mérésére végzett kísérletek alapján a környezeti levegő és a talaj hőmérséklete közötti különbség 2 m mélységben nyáron elérte Gödöllőn a 10,3 °C-ot és Al-Najaf-ban a 8,7 °C-ot. Ezzel szemben télen Gödöllőn 11,5 °C-os, Al-Najaf-ban pedig 6,7 °C-os különbséget mértem. Al-Najaf-ban a talaj hőmérséklete 5 m mélységben az év minden hónapjában gyakorlatilag állandó volt. A talaj és a környezeti levegő közötti hőmérséklet-különbség nyáron több mint 16,2 °C, télen pedig 11,4 °C volt. A gyakorlati kísérletek eredményeként az EAHE-k telepítése Gödöllőn nem kevesebb, mint 71%-os, illetve 70,1%-os hatékonyságot érhet el hűtési és fűtési üzemmódban. Nyáron 11 °C-os hőmérsékletcsökkenést, télen pedig 6,5 °C-os hőmérsékletnövekedést ért el.

9. APPENDICES

A1: Bibliography

1. Abbas, R. R., and Al-Naseri, S. K. (2008): Natural transport of volatile organic compounds due to annual variation of soil temperature, Jordan J. Civ. Eng., 2, 355–362
2. Abd Malek, N. A. A., Chew, J. M., Naamandadin, N. A., Zainol, N. Z., and Muhammad, K. (2018): A study on association between tilt angle, solar insolation exposure and output of solar PV panel using BIM 3D modelling, in MATEC Web of Conferences. EDP Sciences, 6009
3. Abdulmouti, H., and EMIRATES, U. A. (2022): Passive Cooling Module to Improve the Solar Photovoltaic (PV) Performance, in The 4th Int. Conf. on Environment, Chemical Engineering & Materials. Athens, Greece, 11–17
4. Abu-Hamdeh, N. H. (2003): Thermal properties of soils as affected by density and water content, Biosystems engineering, 86(1), 97–102
5. Abu-Hamdeh, N. H., and Reeder, R. C. (2000): Soil thermal conductivity effects of density, moisture, salt concentration, and organic matter, Soil science society of America Journal, 64(4), 1285–1290
6. Abuel-Naga, H., Raouf, M. I. N., Raouf, A. M. I., and Nasser, A. G. (2015): Energy piles: current state of knowledge and design challenges, Environmental Geotechnics, 2(4), 195–210
7. Agrawal, K. K., Agrawal, G. Das, Misra, R., Bhardwaj, M., and Jamuwa, D. K. (2018): A review on effect of geometrical, flow and soil properties on the performance of Earth air tunnel heat exchanger, Energy and Buildings, 176, 120–138
8. Agrawal, K. K., Misra, R., and Agrawal, G. Das (2020): Improving the thermal performance of ground air heat exchanger system using sand-bentonite (in dry and wet condition) as backfilling material, Renewable Energy, 146, 2008–2023
9. Agrawal, K. K., Misra, R., and Agrawal, G. Das (2021): CFD simulation study to evaluate the economic feasibility of backfilling materials for ground-air heat exchanger system, Geothermics, 90, 102002
10. Agrawal, K. K., Misra, R., Yadav, T., Agrawal, G. Das, and Jamuwa, D. K. (2018): Experimental study to investigate the effect of water impregnation on thermal performance of earth air tunnel heat exchanger for summer cooling in hot and arid climate, Renewable energy, 120, 255–265
11. Agrawal, K. K., Yadav, T., Misra, R., and Agrawal, G. Das (2019): Effect of soil moisture contents on thermal performance of earth-air-pipe heat exchanger for winter heating in arid climate: In situ measurement, Geothermics, 77, 12–23
12. Agrawal, S., Varshney, T., and Kumar, J. (2023): Comparative Analysis of Hybrid Photovoltaic Thermal (PV/T) Solar Dryer, Asian Journal of Water, Environment and Pollution, 20(1), 57–66
13. Aguilar, O. F. S., Arredondo, J. A. A., Trujillo, B. A. E., and Fundora, A. J. B. (2018): Determining the in situ apparent thermal diffusivity of a sandy soil, Revista Brasileira de Ciência do Solo, 42, e0180025
14. Ahmed, M. H., Al-Salihi, A. M., and Hussain, H. H. (2021): Testing the performance of a solar energy cooling system in Baghdad city, Przegląd Naukowy. Inżynieria i Kształtowanie Środowiska, 30(2 [92])
15. Ahmed, O. K., Algburi, S., Ali, Z. H., Ahmed, A. K., and Shubat, H. N. (2022): Hybrid solar chimneys: A comprehensive review, Energy Reports, 8, 438–460
16. Ahmed, O. K., and Hussein, A. S. (2018): New design of solar chimney (case study), Case studies in thermal engineering, 11, 105–112
17. Ahmed, S. F., Amanullah, M. T. O., Khan, M. M. K., Rasul, M. G., and Hassan, N. M. S. (2016): Parametric study on thermal performance of horizontal earth pipe cooling system in

summer, Energy Conversion and Management, 114, 324–337
18. Akpinar, E. K., and Koçyiğit, F. (2010): Experimental investigation of thermal performance of solar air heater having different obstacles on absorber plates, International Communications in Heat and Mass Transfer, 37(4), 416–421
19. Al-Dabbas, A. M. (2011): A performance analysis of solar chimney thermal power systems, Thermal Science, 15(3), 619–642
20. Al-Maliky, S. J. B. (2011): Investigation of the readiness of ground soils for the installation of ground heat exchange systems in Baghdad city, Journal of Geography and Geology, 3(1), 200
21. Alagöz, M., and Beyhan, F. (2020): Methods to discover the optimum building envelope in the context of solar data, Gazi University Journal of Science, 33(2), 318–340
22. Ali, M. H., Kurjak, Z., and Beke, J. (2023): Investigation of earth air heat exchangers functioning in arid locations using Matlab/Simulink, Renewable Energy, 209, 632–643
23. Ali, M. H., Kurják, Z., and Beke, J. (2021): The Readiness Investigation of The Ground Soil Temperature for Underground Heat Exchange Systems Installation in Hot Climates, European Journal of Energy Research, 1(2), 1–6
24. Alkaragoly, M., Maerefat, M., Targhi, M. Z., and Abdljalel, A. (2022): An innovative hybrid system consists of a photovoltaic solar chimney and an earth-air heat exchanger for thermal comfort in buildings, Case Studies in Thermal Engineering, 40, 102546
25. Alomar, O. R., Abd, H. M., and Salih, M. M. M. (2022): Efficiency enhancement of solar air heater collector by modifying jet impingement with v-corrugated absorber plate, Journal of Energy Storage, 55, 105535
26. Alwesabi, F. A. A., Aziz, A. S., Rahim, M. S. A., Tajuddin, M. F. N., Mohammed, M. F., Azmi, A., Satterlee, C., Ayob, S. M., and Sutikno, T. (2022): Fundamental study on the impacts of water-cooling and accumulated dust on photovoltaic module performance, International Journal of Power Electronics and Drive Systems, 13(4), 2421
27. Amanowicz, Ł. (2018): Influence of geometrical parameters on the flow characteristics of multi-pipe earth-to-air heat exchangers–experimental and CFD investigations, Applied energy, 226, 849–861
28. Amanowicz, Ł., and Wojtkowiak, J. (2018): Validation of CFD model for simulation of multi-pipe earth-to-air heat exchangers (EAHEs) flow performance, Thermal Science and Engineering Progress, 5, 44–49
29. Amanowicz, Ł., and Wojtkowiak, J. (2020a): Approximated flow characteristics of multi-pipe earth-to-air heat exchangers for thermal analysis under variable airflow conditions, Renewable Energy, 158, 585–597
30. Amanowicz, Ł., and Wojtkowiak, J. (2020b): Thermal performance of multi-pipe earth-to-air heat exchangers considering the non-uniform distribution of air between parallel pipes, Geothermics, 88, 101896
31. Amanowicz, Ł., and Wojtkowiak, J. (2021): Comparison of single-and multipipe earth-to-air heat exchangers in terms of energy gains and electricity consumption: A case study for the temperate climate of central europe, Energies, 14(24), 8217
32. Amori, K. E., and Hmood, K. N. (2013): Numerical study of solar chimney with absorber at different locations, Journal of Engineering, 19(4), 485–499
33. Amran, N. M. H. N., Hassan, S. L. M., Halim, I. S. A., Sulaiman, N., and Abdullah, N. E. (2023): Effect of Water Cooling and Dust Removal on Solar Photovoltaic Module Efficiency, Journal of Advanced Research in Fluid Mechanics and Thermal Sciences, 105(1), 184–193
34. Anderson, W. G., Dussinger, P. M., Sarraf, D. B., and Tamanna, S. (2008): Heat pipe cooling of concentrating photovoltaic cells, in 2008 33rd IEEE Photovoltaic Specialists Conference. IEEE, 1–6
35. Ascione, F., D'Agostino, D., Marino, C., and Minichiello, F. (2016): Earth-to-air heat exchanger for NZEB in Mediterranean climate, Renewable Energy, 99, 553–563

36. ASHRAE, F. (2009): ASHRAE handbook, ASHRAE, Atlanta
37. Asokan, K., Park, J. Y., Choi, S.-W., and Kim, S. S. (2010): Nanocomposite ZnO–SnO 2 nanofibers synthesized by electrospinning method, Nanoscale research letters, 5, 747–752
38. ASTM, D. (2008): Standard test method for determination of thermal conductivity of soil and soft rock by thermal needle probe procedure, ASTM Data Ser. Publ., 5334, 1–8
39. Badescu, V. (2007): Simple and accurate model for the ground heat exchanger of a passive house, Renewable energy, 32(5), 845–855
40. Badescu, V., and Isvoranu, D. (2011): Pneumatic and thermal design procedure and analysis of earth-to-air heat exchangers of registry type, Applied Energy, 88(4), 1266–1280
41. Balghouthi, M., Kooli, S., Farhat, A., Daghari, H., and Belghith, A. (2005): Experimental investigation of thermal and moisture behaviors of wet and dry soils with buried capillary heating system, Solar energy, 79(6), 669–681
42. Bansal, V., Misra, R., Agarwal, G. Das, and Mathur, J. (2013a): 'Derating Factor'new concept for evaluating thermal performance of earth air tunnel heat exchanger: A transient CFD analysis, Applied Energy, 102, 418–426
43. Bansal, V., Misra, R., Agarwal, G. Das, and Mathur, J. (2013b): Transient effect of soil thermal conductivity and duration of operation on performance of Earth Air Tunnel Heat Exchanger, Applied Energy, 103, 1–11
44. Bansal, V., Misra, R., Agrawal, G. Das, and Mathur, J. (2009): Performance analysis of earth–pipe–air heat exchanger for winter heating, Energy and Buildings, 41(11), 1151–1154
45. Barakat, S., Ramzy, A., Hamed, A. M., and El-Emam, S. H. (2019): Augmentation of gas turbine performance using integrated EAHE and Fogging Inlet Air Cooling System, Energy, 189, 116133
46. Bart Römgens (2021): *The variation in temperatures and solar radiation around the world*, IPCC climate grid data. Available at: https://climatemaps.romgens.com/
47. Belhadj, O., Benzenine, H., and Saim, R. (2021): Experimental analysis of height to base length effect in trapezoidal prism inclined solar chimney, Periodica Polytechnica Mechanical Engineering, 65(1), 47–55
48. Benato, A., Stoppato, A., De Vanna, F., and Schiro, F. (2021): Spraying cooling system for PV modules: experimental measurements for temperature trends assessment and system design feasibility, Designs, 5(2), 25
49. Benhammou, M., and Draoui, B. (2015): Parametric study on thermal performance of earth-to-air heat exchanger used for cooling of buildings, Renewable and Sustainable Energy Reviews, 44, 348–355
50. Besler, M., Cepiński, W., and Kęskiewicz, P. (2022): Direct-contact air, gravel, ground heat exchanger in air treatment systems for cowshed air conditioning, Energies, 15(1), 234
51. Bevington, P. R., Robinson, D. K., Blair, J. M., Mallinckrodt, A. J., and McKay, S. (1993): Data reduction and error analysis for the physical sciences, Computers in Physics, 7(4), 415–416
52. Bezbaruah, P. J., Das, R. S., and Sarkar, B. K. (2020): Solar air heater with finned absorber plate and helical flow path: a CFD analysis, Applied solar energy, 56, 35–41
53. Bihari, S. P., and Sadhu, P. K. (2022): Techno-economic analysis for fertilizer house using hybrid power stations, Soft Computing, 26(18), 9515–9525
54. Bisoniya, T. S. (2015): Design of earth–air heat exchanger system, Geothermal Energy, 3(1), 1–10
55. Bisoniya, T. S., Kumar, A., and Baredar, P. (2013): Experimental and analytical studies of earth–air heat exchanger (EAHE) systems in India: a review, Renewable and Sustainable Energy Reviews, 19, 238–246
56. Bordoloi, N., Sharma, A., Nautiyal, H., and Goel, V. (2018): An intense review on the latest advancements of Earth Air Heat Exchangers, Renewable and Sustainable Energy Reviews, 89, 261–280
57. Brum, R. S., Ramalho, J. V. A., Rodrigues, M. K., Rocha, L. A. O., Isoldi, L. A., and Dos

Santos, E. D. (2019): Design evaluation of Earth-Air Heat Exchangers with multiple ducts, Renewable Energy, 135, 1371–1385
58. Chabane, F., Moummi, N., and Benramache, S. (2014): Experimental study of heat transfer and thermal performance with longitudinal fins of solar air heater, Journal of Advanced Research, 5(2), 183–192. https://doi.org/https://doi.org/10.1016/j.jare.2013.03.001
59. Chen, K.-J., Hung, F.-Y., Lui, T.-S., and Hsu, L. (2019): Low Conductivity Decay of Sn–0.7 Cu–0.2 Zn Photovoltaic Ribbons for Solar Cell Application, Micromachines, 10(8), 550
60. Chen, S., Dewancker, B. J., Yang, S., Mao, J., and Chen, J. (2021): Study on the Roof Solar Heating Storage System of Traditional Residences in Southern Shaanxi, China, International Journal of Environmental Research and Public Health, 18(23), 12600
61. Chen, S. X. (2008): Thermal conductivity of sands, Heat and mass transfer, 44(10), 1241–1246
62. Chmielewski, K. (2017): Bezprzeponowe powietrzne gruntowe wymienniki ciepła w układach wentylacji mechanicznej, Rynek instalacyjny, (5), 76–80
63. Chowdhury, S., Chowdhury, S. P., Taylor, G. A., and Song, Y. H. (2008): Mathematical modelling and performance evaluation of a stand-alone polycrystalline PV plant with MPPT facility, in 2008 IEEE Power and Energy Society General Meeting-Conversion and Delivery of Electrical Energy in the 21st Century. IEEE, 1–7
64. Cuny, M., Lapertot, A., Lin, J., Kadoch, B., and Le Metayer, O. (2020): Multi-criteria optimization of an earth-air heat exchanger for different French climates, Renewable Energy, 157, 342–352
65. Cuny, M., Lin, J., Siroux, M., and Fond, C. (2020): Influence of rainfall events on the energy performance of an earth-air heat exchanger embedded in a multilayered soil, Renewable Energy, 147, 2664–2675
66. Cuny, M., Lin, J., Siroux, M., Magnenet, V., and Fond, C. (2018): Influence of coating soil types on the energy of earth-air heat exchanger, Energy and Buildings, 158, 1000–1012
67. Davidsson, H., Bernardo, R., and Hellström, B. (2013): Hybrid ventilation with innovative heat recovery—a system analysis, Buildings, 3(1), 245–257
68. Debnath, S., Das, B., Randive, P. R., and Pandey, K. M. (2018): Performance analysis of solar air collector in the climatic condition of North Eastern India, Energy, 165, 281–298
69. Dhaundiyal, A. (2023): Thermo-Statistical Investigation of the Solar Air Collector Using Least Angle Regression, Energies, 16(5), 2461
70. Dhinesh, V., Vijayakumar, D. G., and Saravanan, D. S. (2020): A photovoltaic modeling module with different converters for grid operations, International Journal of Innovative Research in Technology, 6(8), 89–95
71. Dubey, S., Sandhu, G. S., and Tiwari, G. N. (2009): Analytical expression for electrical efficiency of PV/T hybrid air collector, Applied Energy, 86(5), 697–705
72. Dubey, S., and Tiwari, G. N. (2008): Thermal modeling of a combined system of photovoltaic thermal (PV/T) solar water heater, Solar energy, 82(7), 602–612
73. Dutkowski, K., Kruzel, M., Fiuk, J., Rokosz, K., Michalska-Pożoga, I., and Szczepanek, M. (2023): Experimental Studies on the Influence of Spatial Orientation of a Passive Air Solar Collector on Its Efficiency, Energies, 16(10), 4125
74. Ekechukwu, O. V, and Norton, B. (1997): Design and measured performance of a solar chimney for natural-circulation solar-energy dryers, Renewable energy, 10(1), 81–90
75. Elghamry, R., and Hassan, H. (2020): An experimental work on the impact of new combinations of solar chimney, photovoltaic and geothermal air tube on building cooling and ventilation, Solar Energy, 205, 142–153
76. Elminshawy, N. A. S., Siddiqui, F. R., Farooq, Q. U., and Addas, M. F. (2017): Experimental investigation on the performance of earth-air pipe heat exchanger for different soil compaction levels, Applied Thermal Engineering, 124, 1319–1327
77. Eslamnezhad, H., and Rahimi, A. B. (2017): Enhance heat transfer for phase-change materials in triplex tube heat exchanger with selected arrangements of fins, Applied Thermal

Engineering, 113, 813–821. https://doi.org/https://doi.org/10.1016/j.applthermaleng.2016.11.067
78. Evans, D. L. (1981): Simplified method for predicting photovoltaic array output, Solar energy, 27(6), 555–560
79. Faridi, H., Arabhosseini, A., Zarei, G., and Okos, M. (2019): Utilization of Soil Temperature Modeling to Check the Possibility of Earth-Air Heat Exchanger for Agricultural Building, Iranian (Iranica) Journal of Energy & Environment, 10(4), 260–268
80. Faridi, H., Arabhosseini, A., Zarei, G., and Okos, M. (2021): Degree-Day Index for Estimating the Thermal Requirements of a Greenhouse Equipped with an Air-Earth Heat Exchanger System, Journal of Agricultural Machinery, 11(1), 83–95
81. Farooq, A. A., Afram, A., Schulz, N., and Janabi-Sharifi, F. (2015): Grey-box modeling of a low pressure electric boiler for domestic hot water system, Applied Thermal Engineering, 84, 257–267
82. Le Feuvre, P. (2007): An investigation into ground source heat pump technology, its UK market and best practice in system design, Mechanical Engineering, University of Strathclyde. MSc, 180
83. Florides, G., and Kalogirou, S. (2007): Ground heat exchangers—A review of systems, models and applications, Renewable energy, 32(15), 2461–2478
84. Fraunhofer Institute for Solar Energy Systems, I. (2023): *Photovoltaics Report 2023*. https://doi.org/DOI: 10.4228/zenodo.5588389
85. Gandjalikhan Nassab, S. A. (2024): Three-dimensional CFD analysis of solar air heaters for improving thermal performance using converged air ducts, International Journal of Green Energy, 21(1), 43–53
86. Ghaffari, A., and Mehdipour, R. (2015): Modeling and improving the performance of cabinet solar dryer using computational fluid dynamics, International journal of food engineering, 11(2), 157–172
87. Gharzi, M., Arabhosseini, A., Gholami, Z., and Pakchi, M. (2023): A hybrid CPV/T system equipped with compound parabolic concentrator and Nano-Pcmfor optimal electricity generation and hot water, in 2023 8th International Conference on Technology and Energy Management (ICTEM). IEEE, 1–6
88. Górka, A., Szymański, M., and Mróz, T. (2013): Measurements and modeling of an earth-to-air heat exchanger for retail building ventilation, in Proceedings of the 34th AIVC Conference “Energy conservation technologies for mitigation and adaptation in the built environment: the role of ventilation strategies and smart materials”, Athens
89. Gow, A. J., and Langston, D. (1977): *Growth history of lake ice in relation to its stratigraphic, crystalline and mechanical structure*. Department of Defense, Army, Corps of Engineers, Cold Regions Research and …
90. GÜLÇİMEN, F., KARAKAYA, H., and DURMUŞ, A. (2023): Efficiency Analysis in Solar Air Heaters with Attached Internal Fins, European Journal of Technique (EJT), 13(1), 12–17
91. Haghighi, A. P., and Maerefat, M. (2015): Design guideline for application of earth-to-air heat exchanger coupled with solar chimney as a natural heating system, International Journal of Low-Carbon Technologies, 10(3), 294–304
92. Haigh, S. K. (2012): Thermal conductivity of sands, Geotechnique, 62(7), 617–625
93. Han, J., Cui, M., Chen, J., and Lv, W. (2021): Analysis of thermal performance and economy of ground source heat pump system: a case study of the large building, Geothermics, 89, 101929
94. Hishikawa, Y., Dunlop, E. D., Green, M. A., Hohl, J., Anita, E., Baillie, W. Y. H., and Levi, D. H. (2017): Solar cell efficiency tables (version 50), Prog. Photovolt., 25(7), 668–676
95. Höfle, C., Edwards, M. E., Hopkins, D. M., Mann, D. H., and Ping, C.-L. (2000): The full-glacial environment of the northern Seward Peninsula, Alaska, reconstructed from the 21,500-year-old Kitluk paleosol, Quaternary Research, 53(2), 143–153

96. Hollmuller, P. (2003): Analytical characterisation of amplitude-dampening and phase-shifting in air/soil heat-exchangers, International Journal of Heat and Mass Transfer, 46(22), 4303–4317
97. Hussain, A. (2007): Hybrid geothermal/solar energy technology for power generation, Higher Institute of Engineering
98. Hussain, F. M., Rehman, S., and Al-Sulaiman, F. A. (2021): Performance analysis of a solar chimney power plant for different geographical locations of Saudi Arabia, FME Transactions, 49(1), 64–71
99. Huynh, T. N., and Nguyen, Y. Q. (2021): Numerical simulation of a solar chimney for natural ventilation of a building: Comparison of different computational domains, in IOP Conference Series: Materials Science and Engineering. IOP Publishing, 12014
100. Ishaque, K., Salam, Z., and Taheri, H. (2011): Modeling and simulation of photovoltaic (PV) system during partial shading based on a two-diode model, Simulation Modelling Practice and Theory, 19(7), 1613–1626
101. Jakhrani, A. Q., Jatoi, A. R., and Jakhrani, S. H. (2017): Analysis and fabrication of an active cooling system for reducing photovoltaic module temperature, Engineering, Technology & Applied Science Research, 7(5), 1980–1986
102. Johansen, O. (1977): Thermal conductivity of soils. Norwegian Institute of Technology.
103. Joshi, A. S., Tiwari, A., Tiwari, G. N., Dincer, I., and Reddy, B. V (2009): Performance evaluation of a hybrid photovoltaic thermal (PV/T)(glass-to-glass) system, International Journal of Thermal Sciences, 48(1), 154–164
104. Kaushik, S. C., Lal, S., and Bhargava, P. K. (2013): Earth–air tunnel heat exchanger for building space conditioning: a critical review, Nanomaterials and energy, 2(4), 216–227
105. KB, P. (2023): Energy analysis of a novel butterfly serpentine flow-based PV/T and PV/T heat pump system with phase change material–an experimental comparative study, Energy Sources, Part A: Recovery, Utilization, and Environmental Effects, 45(2), 5494–5507
106. Khabbaz, M., Benhamou, B., Limam, K., Hollmuller, P., Hamdi, H., and Bennouna, A. (2016): Experimental and numerical study of an earth-to-air heat exchanger for air cooling in a residential building in hot semi-arid climate, Energy and Buildings, 125, 109–121
107. Khalili, N. N. W., Othman, M., Abu Bakar, M. N., and Abdullah, L. (2020): Modelling of a single passage air PV/T solar collector: experimental and simulation design, Processes, 8(7), 763
108. Khan, B., and Singh, P. (2017): Optimal power flow techniques under characterization of conventional and renewable energy sources: A comprehensive analysis, Journal of Engineering, 2017
109. Kim, D.-J., Kim, D. H., Bhattarai, S., and Oh, J.-H. (2011): Simulation and model validation of the surface cooling system for improving the power of a photovoltaic module
110. *Köppen climate classification* (2022):
111. Kothari, R., Sahu, S. K., Kundalwal, S. I., and Mahalkar, P. (2021): Thermal performance of phase change material–based heat sink for passive cooling of electronic components: An experimental study, International Journal of Energy Research, 45(4), 5939–5963
112. KR, C. L., Thangavel, G., Aadithya, V., and RK, J. D. (2023): A Study of the Effect of Optical Filters on the Performance of Solar Panel, in 2023 Second International Conference on Electronics and Renewable Systems (ICEARS). IEEE, 319–324
113. Krarti, M., and Kreider, J. F. (1996): Analytical model for heat transfer in an underground air tunnel, Energy conversion and management, 37(10), 1561–1574
114. Kukreti, A., Thapliyal, M., Kurmanchali, N., Ramola, G. C., and Singh, R. (2023): Tree species diversity, distribution and population structure of Fraxinus xanthoxyloides in Western Himalayas
115. Kumar Singh, R., and Sharma, R. V (2017): Mathematical Investigation of Soil Temperature Variation for Geothermal Applications, International Journal of Engineering, 30(10), 1609–1614

116. Kwan, T. H., and Wu, X. (2016): Power and mass optimization of the hybrid solar panel and thermoelectric generators, Applied Energy, 165, 297–307. https://doi.org/https://doi.org/10.1016/j.apenergy.2015.12.016
117. Lahcene, A., Benazza, A. Y., and Benguediab, M. (2020): The Effect of Geometric Parameters on the Performance of Solar Chimney: A Numerical and Experimental Study, Engineering, Technology & Applied Science Research, 10(6), 6456–6461
118. Lapertot, A., Cuny, M., Kadoch, B., and Le Métayer, O. (2021): Optimization of an earth-air heat exchanger combined with a heat recovery ventilation for residential building needs, Energy and Buildings, 235, 110702
119. Laurini, E., De Vita, M., De Berardinis, P., and Friedman, A. (2018): Passive ventilation for indoor comfort: A comparison of results from monitoring and simulation for a historical building in a temperate climate, Sustainability, 10(5), 1565
120. Layeni, A. T., Waheed, M. A., Adewumi, B. A., Nwaokocha, C. N., Sharifpur, M., Tongo, S. O., Okeze, R. C., and Mboreha, C. A. (2021): Computational and sensitivity analysis of a dual purpose solar chimney for buildings, Materials Today: Proceedings, 47, 4126–4136
121. Lei, Y., Zhang, Y., Wang, F., and Wang, X. (2016): Enhancement of natural ventilation of a novel roof solar chimney with perforated absorber plate for building energy conservation, Applied Thermal Engineering, 107, 653–661
122. Li, A., Jones, P., Zhao, P., and Wang, L. (2004): Heat transfer and natural ventilation airflow rates from single-sided heated solar chimney for buildings, Journal of Asian Architecture and Building Engineering, 3(2), 233–238
123. Li, H., Ni, L., Liu, G., and Yao, Y. (2019): Performance evaluation of Earth to Air Heat Exchange (EAHE) used for indoor ventilation during winter in severe cold regions, Applied Thermal Engineering, 160, 114111
124. Li, H., Yu, Y., Niu, F., Shafik, M., and Chen, B. (2014): Performance of a coupled cooling system with earth-to-air heat exchanger and solar chimney, Renewable Energy, 62, 468–477
125. Li, W., Liu, J., Zhang, G., Wang, Q., and Shi, L. (2021): Energy assessment methods for solar chimney in buildings: A review, Journal of Renewable and Sustainable Energy, 13(4)
126. Li, Y., Liu, S., and Lu, J. (2017): Effects of various parameters of a PCM on thermal performance of a solar chimney, Applied Thermal Engineering, 127, 1119–1131
127. Li, Y., Long, T., Bai, X., Wang, L., Li, W., Liu, S., Lu, J., Cheng, Y., Ye, K., and Huang, S. (2021): An experimental investigation on the passive ventilation and cooling performance of an integrated solar chimney and earth–air heat exchanger, Renewable Energy, 175, 486–500
128. Lin, C., and Lei, Y. (2022): Study on ventilation performance of inclined solar chimney coupled with indoor heat source, in E3S Web of Conferences. EDP Sciences, 3057
129. Liu, H., Li, P., Yu, B., Zhang, M., Tan, Q., Wang, Y., and Zhang, Y. (2021): Contrastive analysis on the ventilation performance of a combined solar chimney, Applied Sciences, 12(1), 156
130. Liu, Q., Du, Z., and Fan, Y. (2018): Heat and mass transfer behavior prediction and thermal performance analysis of earth-to-air heat exchanger by finite volume method, Energies, 11(6), 1542
131. Liu, S., Bliss, N., Sundquist, E., and Huntington, T. G. (2003): Modeling carbon dynamics in vegetation and soil under the impact of soil erosion and deposition, Global Biogeochemical Cycles, 17(2)
132. Liu, S., and Li, Y. (2015): An experimental study on the thermal performance of a solar chimney without and with PCM, Renewable Energy, 81, 338–346
133. Liu, Zhongbing, Li, W., Chen, Y., Luo, Y., and Zhang, L. (2019): Review of energy conservation technologies for fresh air supply in zero energy buildings, Applied Thermal Engineering, 148, 544–556
134. Liu, Z., Sun, P., Xie, M., Zhou, Y., He, Y., Zhang, G., Chen, D., Li, S., Yan, Z., and Qin, D. (2021): Multivariant optimization and sensitivity analysis of an experimental vertical earth-to-air heat exchanger system integrating phase change material with Taguchi method,

Renewable Energy, 173, 401–414
135. Liu, Zhengxuan, Yu, Z. J., Yang, T., El Mankibi, M., Roccamena, L., Sun, Y., Sun, P., Li, S., and Zhang, G. (2019): Experimental and numerical study of a vertical earth-to-air heat exchanger system integrated with annular phase change material, Energy Conversion and Management, 186, 433–449
136. Maerefat, M., and Haghighi, A. P. (2010): Passive cooling of buildings by using integrated earth to air heat exchanger and solar chimney, Renewable energy, 35(10), 2316–2324
137. Magraner, T., Montero, A., Quilis, S., and Urchueguía, J. F. (2010): Comparison between design and actual energy performance of a HVAC-ground coupled heat pump system in cooling and heating operation, Energy and buildings, 42(9), 1394–1401
138. Mahdavi, S., Sarhaddi, F., and Hedayatizadeh, M. (2019): Energy/exergy based-evaluation of heating/cooling potential of PV/T and earth-air heat exchanger integration into a solar greenhouse, Applied Thermal Engineering, 149, 996–1007
139. Mandel, J. (2012): *The statistical analysis of experimental data*. Courier Corporation
140. Mathur, A., Srivastava, A., Agrawal, G. D., Mathur, S., and Mathur, J. (2015): CFD analysis of EATHE system under transient conditions for intermittent operation, Energy and Buildings, 87, 37–44
141. Mathur, A., Srivastava, A., Mathur, J., Mathur, S., and Agrawal, G. D. (2015): Transient effect of soil thermal diffusivity on performance of EATHE system, Energy Reports, 1, 17–21
142. Mathur, A., Surana, A. K., and Mathur, S. (2016): Numerical investigation of the performance and soil temperature recovery of an EATHE system under intermittent operations, Renewable energy, 95, 510–521
143. Mathur, A., Surana, A. K., Verma, P., Mathur, S., Agrawal, G. D., and Mathur, J. (2015): Investigation of soil thermal saturation and recovery under intermittent and continuous operation of EATHE, Energy and Buildings, 109, 291–303
144. Maytorena, V. M., Moreno, S., and Hinojosa, J. F. (2021): Effect of operation modes on the thermal performance of EAHE systems with and without PCM in summer weather conditions, Energy and Buildings, 250, 111278
145. Mehdid, C.-E., Benchabane, A., Rouag, A., Moummi, N., Melhegueg, M.-A., Moummi, A., Benabdi, M.-L., and Brima, A. (2018): Thermal design of Earth-to-air heat exchanger. Part II a new transient semi-analytical model and experimental validation for estimating air temperature, Journal of Cleaner Production, 198, 1536–1544
146. Mehranfar, S., Gharehghani, A., Azizi, A., Andwari, A. M., Pesyridis, A., and Jouhara, H. (2022): Comparative assessment of innovative methods to improve solar chimney power plant efficiency, Sustainable Energy Technologies and Assessments, 49, 101807
147. Mehta, P., Kumar, S., Patel, V., and Joshi, A. (2020): Mathematical modeling and performance assessment of solar air collector, Indian J Sci Technol, 13(18), 1803–1810
148. Mei, V. C. (1987): Effect of backfilling material on ground coil performance, ASHRAE Trans.;(United States), 93(CONF-870620-)
149. Mengistu, A. G., van Rensburg, L. D., and Mavimbela, S. S. W. (2017): The effect of soil water and temperature on thermal properties of two soils developed from aeolian sands in South Africa, Catena, 158, 184–193
150. Mihalakakou, G. (2002): On estimating soil surface temperature profiles, Energy and Buildings, 34(3), 251–259
151. Mihalakakou, G., Santamouris, M., and Asimakopoulos, D. (1994): Use of the ground for heat dissipation, Energy, 19(1), 17–25
152. Mihalakakou, G., Santamouris, M., Lewis, J. O., and Asimakopoulos, D. N. (1997): On the application of the energy balance equation to predict ground temperature profiles, Solar Energy, 60(3–4), 181–190
153. Minaei, A., and Safikhani, H. (2021): A new transient analytical model for heat transfer of earth-to-air heat exchangers, Journal of Building Engineering, 33, 101560

154. Minaei, A., Talee, Z., Safikhani, H., and Ghaebi, H. (2021): Thermal resistance capacity model for transient simulation of Earth-Air Heat Exchangers, Renewable Energy, 167, 558–567
155. Misra, A., Becker, B. R., and Fricke, B. A. (1995): A theoretical model of the thermal conductivity of idealized soil, HVAC&R Research, 1(1), 81–96
156. Misra, R., Bansal, V., Agrawal, G. Das, Mathur, J., and Aseri, T. (2013a): Transient analysis based determination of derating factor for earth air tunnel heat exchanger in summer, Energy and buildings, 58, 103–110
157. Misra, R., Bansal, V., Agrawal, G. Das, Mathur, J., and Aseri, T. (2013b): Transient analysis based determination of derating factor for Earth Air Tunnel Heat Exchanger in winter, Energy and Buildings, 58, 76–85
158. Misra, R., Bansal, V., Agrawal, G. Das, Mathur, J., and Aseri, T. K. (2013): CFD analysis based parametric study of derating factor for Earth Air Tunnel Heat Exchanger, Applied Energy, 103, 266–277
159. Mohamed, S. A., Al-Sulaiman, F. A., Ibrahim, N. I., Zahir, M. H., Al-Ahmed, A., Saidur, R., Yılbaş, B. S., and Sahin, A. Z. (2017): A review on current status and challenges of inorganic phase change materials for thermal energy storage systems, Renewable and Sustainable Energy Reviews, 70, 1072–1089. https://doi.org/https://doi.org/10.1016/j.rser.2016.12.012
160. Mortaza, Y., Nader, J., Alireza, A., and Hasan, M. (2005): Design and Installation of the First Geothermal Heat Pump in Iran, in Proceeding World Geothermal Congress, Antalya, Turkey
161. Muehleisen, R. T. (2012): Simple design tools for earth-air heat exchangers, in Fifth National Conference of IBPSA-USA, SimBuild, 723
162. Mund, C., Rathore, S. K., and Sahoo, R. K. (2021): A review of solar air collectors about various modifications for performance enhancement, Solar Energy, 228, 140–167
163. Nema, S., Nema, R. K., and Agnihotri, G. (2010): Matlab/simulink based study of photovoltaic cells/modules/array and their experimental verification, International journal of Energy and Environment, 1(3), 487–500
164. Nguyen, Y. Q., Huynh, T. N., and Pham, M.-A. H. (2021): Modifications of heat transfer and induced flow rate of a solar chimney by an obstacle in the air channel, Int. J. Adv. Sci. Eng. Inf. Technol, 11, 482–488
165. Nguyen, Y. Q., and Nguyen, V. T. (2021): Effects of heated cavities below and above the air channel on the performance of a solar chimney for natural heating, in AIP Conference Proceedings. AIP Publishing
166. Niu, F., Yu, Y., Yu, D., and Li, H. (2015): Investigation on soil thermal saturation and recovery of an earth to air heat exchanger under different operation strategies, Applied Thermal Engineering, 77, 90–100
167. Nnamchi, S. N., Nnamchi, O. A., Sangotayo, E. O., Ismael, S. A., Nkurunziza, O. K., and Gabriel, V. (2020): Design and simulation of air-solar preheating unit: An improved design of a flat plate solar collector, Iranian (Iranica) Journal of Energy & Environment, 11(2), 97–108
168. Ogoulola, C. E. G., Rezek, A. J. J., Gonzatti, R. B., Silva, V. Z., Ramos, M. L., Alfonso, E. C., and Santos, R. D. (2020): A New Bidirectional Three-phase Neutral Point Clamped (NPC) Grid-Connected Converter: Analysis and Simulation, Simpósio Brasileiro de Sistemas Elétricos-SBSE, 1(1)
169. Okada, S., Uchida, T., Karasudani, T., and Ohya, Y. (2015): Improvement in solar chimney power generation by using a diffuser tower, Journal of Solar Energy Engineering, 137(3), 31009
170. Ozgener, L. (2011): A review on the experimental and analytical analysis of earth to air heat exchanger (EAHE) systems in Turkey, Renewable and sustainable energy reviews, 15(9), 4483–4490

171. Ozgener, O., Ozgener, L., and Tester, J. W. (2013): A practical approach to predict soil temperature variations for geothermal (ground) heat exchangers applications, International Journal of Heat and Mass Transfer, 62, 473–480
172. De Paepe, M., and Janssens, A. (2003): Thermo-hydraulic design of earth-air heat exchangers, Energy and buildings, 35(4), 389–397
173. Palomba, V., Bonanno, A., Brunaccini, G., Aloisio, D., Sergi, F., Dino, G. E., Varvaggiannis, E., Karellas, S., Nitsch, B., and Strehlow, A. (2021): Hybrid cascade heat pump and thermal-electric energy storage system for residential buildings: Experimental testing and performance analysis, Energies, 14(9), 2580
174. Pandiarajan, N., and Muthu, R. (2011): Mathematical modeling of photovoltaic module with Simulink, in 2011 1st International Conference on Electrical Energy Systems. IEEE, 258–263
175. Peretti, C., Zarrella, A., De Carli, M., and Zecchin, R. (2013): The design and environmental evaluation of earth-to-air heat exchangers (EAHE). A literature review, Renewable and Sustainable Energy Reviews, 28, 107–116
176. Qi, J., and Li, X. (2022): Soil Organic Carbon Stock in Hindu Kush Himalayn's Grasslands, Academic Journal of Environment & Earth Science, 4(1), 32–37
177. Qin, D., Liu, J., and Zhang, G. (2021): A novel solar-geothermal system integrated with earth–to–air heat exchanger and solar air heater with phase change material—numerical modelling, experimental calibration and parametrical analysis, Journal of Building Engineering, 35, 101971
178. Qin, D., Liu, Z., Zhou, Y., Yan, Z., Chen, D., and Zhang, G. (2021): Dynamic performance of a novel air-soil heat exchanger coupling with diversified energy storage components—modelling development, experimental verification, parametrical design and robust operation, Renewable Energy, 167, 542–557
179. Rahl, S. R. (2015): Solar thermal air conditioning unit. Google Patents
180. Rahman, M. M., Hasanuzzaman, M., and Abd Rahim, N. (2017): Effects of operational conditions on the energy efficiency of photovoltaic modules operating in Malaysia, Journal of cleaner production, 143, 912–924
181. Ravanfar, A. (2013): Simulation study of solar chimney assisted solarium. Ryerson University
182. Razak, A. A., Majid, Z. A. A., Azmi, W. H., Ruslan, M. H., Choobchian, S., Najafi, G., and Sopian, K. (2016): Review on matrix thermal absorber designs for solar air collector, Renewable and Sustainable Energy Reviews, 64, 682–693
183. Ren, Y., Suganthan, P. N., and Srikanth, N. (2014): A comparative study of empirical mode decomposition-based short-term wind speed forecasting methods, IEEE Transactions on Sustainable Energy, 6(1), 236–244
184. Rezaei, L., Saeidi, S., Sápi, A., Senoukesh, M. R. A., Gróf, G., Chen, W.-H., Kónya, Z., and Klemeš, J. J. (2023): Efficiency improvement of the solar chimneys by insertion of hanging metallic tubes in the collector: Experiment and computational fluid dynamics simulation, Journal of Cleaner Production, 415, 137692
185. Rodrigues, M. K., da Silva Brum, R., Vaz, J., Rocha, L. A. O., dos Santos, E. D., and Isoldi, L. A. (2015): Numerical investigation about the improvement of the thermal potential of an Earth-Air Heat Exchanger (EAHE) employing the Constructal Design method, Renewable Energy, 80, 538–551
186. Romanska-Zapala, A., Bomberg, M., Dechnik, M., Fedorczak-Cisak, M., and Furtak, M. (2019): On preheating of the outdoor ventilation air, Energies, 13(1), 15
187. Rosa, N., Soares, N., Costa, J. J., Santos, P., and Gervásio, H. (2020): Assessment of an earth-air heat exchanger (EAHE) system for residential buildings in warm-summer Mediterranean climate, Sustainable Energy Technologies and Assessments, 38, 100649
188. Rouag, A., Benchabane, A., and Mehdid, C.-E. (2018): Thermal design of Earth-to-Air Heat Exchanger. Part I a new transient semi-analytical model for determining soil temperature,

Journal of cleaner production, 182, 538–544
189. Rubio, C. M. (2013): A laboratory procedure to determine the thermal properties of silt loam soils based on ASTM D 5334, Applied Ecology and Environmental Sciences, 1(4), 45–48
190. Sakhri, N., Moussaoui, A., Menni, Y., Sadeghzadeh, M., and Ahmadi, M. H. (2021): New passive thermal comfort system using three renewable energies: Wind catcher, solar chimney and earth to air heat exchanger integrated to real-scale test room in arid region (Experimental study), International Journal of Energy Research, 45(2), 2177–2194
191. Salih, M. M. M., Alomar, O. R., Ali, F. A., and Abd, H. M. (2019): An experimental investigation of a double pass solar air heater performance: A comparison between natural and forced air circulation processes, Solar Energy, 193, 184–194
192. Samuel, D. G. L., Nagendra, S. M. S., and Maiya, M. P. (2013): Passive alternatives to mechanical air conditioning of building: A review, Building and Environment, 66, 54–64
193. Sarhaddi, F., Farahat, S., Ajam, H., Behzadmehr, A., and Adeli, M. M. (2010): An improved thermal and electrical model for a solar photovoltaic thermal (PV/T) air collector, Applied energy, 87(7), 2328–2339
194. Schott, T. (1985): Operation temperatures of pv modules: a theoretical and experimental approach, in EC Photovoltaic solar energy conference. 6, 392–396
195. Serageldin, A. A., Abdeen, A., Ahmed, M. M. S., Radwan, A., Shmroukh, A. N., and Ookawara, S. (2020): Solar chimney combined with earth to-air heat exchanger for passive cooling of residential buildings in hot areas, Solar Energy, 206, 145–162
196. Serageldin, A. A., Abdelrahman, A. K., and Ookawara, S. (2018): Parametric study and optimization of a solar chimney passive ventilation system coupled with an earth-to-air heat exchanger, Sustainable Energy Technologies and Assessments, 30, 263–278
197. Sharma, A., and Chauhan, R. (2023): Effective Efficiency Distribution Characteristics for Different Configurations of Arc and V-Shape Ribs in Solar Air Channels: A Comparative Study, in Enabling Methodologies for Renewable and Sustainable Energy. CRC Press, 45–71
198. Shojaee, S. M. N., and Malek, K. (2017): Earth-to-air heat exchangers cooling evaluation for different climates of Iran, Sustainable Energy technologies and Assessments, 23, 111–120
199. Siecker, J., Kusakana, K., and Numbi, B. P. (2017): A review of solar photovoltaic systems cooling technologies, Renewable and Sustainable Energy Reviews, 79, 192–203. https://doi.org/https://doi.org/10.1016/j.rser.2017.05.053
200. Sinacka, J., and Szczechowiak, E. (2017): Analiza eksploatacyjna budynku pasywnego w aspekcie komfortu klimatycznego i zużycia energii, Ciepłownictwo, Ogrzewnictwo, Wentylacja, 48
201. Singh, P., Khanna, S., Becerra, V., Newar, S., Sharma, V., Mallick, T. K., Hutchinson, D., Radulovic, J., and Khusainov, R. (2020): Power improvement of finned solar photovoltaic phase change material system, Energy, 193, 116735. https://doi.org/https://doi.org/10.1016/j.energy.2019.116735
202. Smith, S. L., Maxfield, L., and Hunter, E. J. (2019): Sensitivity analysis of muscle mechanics-based voice simulator to determine gender-specific speech characteristics, Biomechanics and modeling in mechanobiology, 18, 453–462
203. Smits, K. M., Sakaki, T., Howington, S. E., Peters, J. F., and Illangasekare, T. H. (2013): Temperature dependence of thermal properties of sands across a wide range of temperatures (30–70 C), Vadose Zone Journal, 12(1)
204. Soares, N., Rosa, N., Monteiro, H., and Costa, J. J. (2021): Advances in standalone and hybrid earth-air heat exchanger (EAHE) systems for buildings: A review, Energy and Buildings, 253, 111532
205. Sodha, M. S., Sawhney, R. L., Jayashankar, B. C., and Sharma, A. K. (1990): Effect of different earth surface treatments on the thermal performance of a room coupled to an earth-air tunnel, International journal of energy research, 14(3), 337–354
206. Som, T., Sharma, A., and Thakur, D. (2020): Effect of solar tilt angles on photovoltaic

module performance: a behavioral optimization approach, Artificial Intelligence Evolution, 90–101
207. Song, Y., Wu, D., Wagdy Mohamed, A., Zhou, X., Zhang, B., and Deng, W. (2021): Enhanced success history adaptive DE for parameter optimization of photovoltaic models, Complexity, 2021, 1–22
208. Song, Y., Yao, Y., and Na, W. (2006): Impacts of soil and pipe thermal conductivity on performance of horizontal pipe in a ground-source heat pump
209. Soni, S. K., Pandey, M., and Bartaria, V. N. (2015): Ground coupled heat exchangers: A review and applications, Renewable and Sustainable Energy Reviews, 47, 83–92
210. Soytürk, G., KIZILKAN, Ö., and Ezan, M. A. (2022): Mathematical modeling of a photovoltaic thermal (PV/T) collector, Uluslararası Teknolojik Bilimler Dergisi, 14(3), 144–152
211. Starace, G., Ayr, U., Conte, E., Fato, I., Stefanizzi, P., and Cirillo, E. (1998): Termodinamica e trasmissione del calore
212. Sultan, T. N., Farhan, M., and ALRkabi, H. (2022): Study the effect of Environmental Factors on the performance of Photovoltaic Module, Wasit Journal of Engineering Sciences, 10(2), 83–91
213. Tan, A. Y. K., and Wong, N. H. (2013): Parameterization studies of solar chimneys in the tropics, Energies, 6(1), 145–163
214. Tang, L., Liu, Z., Zhou, Y., Qin, D., and Zhang, G. (2020): Study on a dynamic numerical model of an underground air tunnel system for cooling applications—experimental validation and multidimensional parametrical analysis, Energies, 13(5), 1236
215. Thulasiyammal, C., and Sutha, S. (2014): Design and comparative analysis of DC-DC boost and single-ended primary-inductance converter converters using solar powered maximum power point tracking algorithms, American Journal of Applied Sciences, 7(11), 1113–1122
216. Tiendrebeogo, S. E., Christian, T. G., Jean, K. G., Bernard, N., Moumini, K., Oumar, D. A., Jean, K., and Antoine, B. (2022): Design and Thermal Behavior Analysis of a Plan Air Solar Collector, Science, 10(1), 1–7
217. Tiwari, A., Sodha, M. S., Chandra, A., and Joshi, J. C. (2006): Performance evaluation of photovoltaic thermal solar air collector for composite climate of India, Solar Energy Materials and Solar Cells, 90(2), 175–189
218. Tiwari, G. N., Akhtar, M. A., Shukla, A., and Khan, M. E. (2006): Annual thermal performance of greenhouse with an earth–air heat exchanger: An experimental validation, Renewable Energy, 31(15), 2432–2446
219. Tlatelpa-Becerro, A., Rico-Martínez, R., Cárdenas-Manríquez, M., Urquiza, G., Alarcón-Hernández, F. B., and Fuentes-Albarran, M. C. (2022): Prediction of the dynamic behavior of a solar chimney by means of artificial neural networks, Revista Mexicana de Ingeniería Química, 21(1), IE2495–IE2495
220. Tong, F., Jing, L., and Zimmerman, R. W. (2009): An effective thermal conductivity model of geological porous media for coupled thermo-hydro-mechanical systems with multiphase flow, International Journal of Rock Mechanics and Mining Sciences, 46(8), 1358–1369
221. TOSSA, A., Cossi, T., Aza-Gnandji, R., and Semassou, G. C. (2023): Performance Analysis of PV/T Modules in West African Climate Zones, Current Journal of Applied Science and Technology
222. Tzaferis, A., Liparakis, D., Santamouris, M., and Argiriou, A. (1992): Analysis of the accuracy and sensitivity of eight models to predict the performance of earth-to-air heat exchangers, Energy and buildings, 18(1), 35–43
223. Valley, K., Sheikh, A. A., Shameem, S. A., and Ahmad, N. (2020): Impact of Biotic Stress on Edaphic Features under two Important Medicinal Plants (Podophyllum hexandrum and Rumex acetosa L .), 9(6), 859–873
224. Vélez-Sánchez, J., Bastidas-Rodríguez, J. D., Ramos-Paja, C. A., González Montoya, D., and Trejos-Grisales, L. A. (2019): A non-invasive procedure for estimating the exponential

model parameters of bypass diodes in photovoltaic modules, Energies, 12(2), 303
225. Vieira, A., Alberdi-Pagola, M., Christodoulides, P., Javed, S., Loveridge, F., Nguyen, F., Cecinato, F., Maranha, J., Florides, G., and Prodan, I. (2017): Characterisation of ground thermal and thermo-mechanical behaviour for shallow geothermal energy applications, Energies, 10(12), 2044
226. Wang, D., Qiao, J., Zhang, Y., Liao, M., Wang, Dong, Zhao, X., and Qiao, Y. (2023): Micro-topographies formed by erosion can drive seedling emergence by rebuilding micro-habitats on weathered waste dumps in northeastern China, Frontiers in Earth Science, 10, 1040814
227. Wang, H., Zhang, J., Hu, N., and Cheng, Z. (2023): Comprehensive performance of pv/t-gchps under heating conditions, Energy Conversion and Management: X, 100406
228. Wang, J., He, H., Dyck, M., and Lv, J. (2020): A review and evaluation of predictive models for thermal conductivity of sands at full water content range, Energies, 13(5), 1083
229. Wei, H., and Yang, D. (2019): Performance evaluation of flat rectangular earth-to-air heat exchangers in harmonically fluctuating thermal environments, Applied Thermal Engineering, 162, 114262
230. Widhiyanuriyawan, D., Hamidi, N., Hatib, R., and Arifin, Z. (2022): Nickel Oxide/Graphene Oxide (NiO/GO) as Double Hole Transport Layer in Perovskite Solar Cell, Tehnički vjesnik, 29(6), 1861–1867
231. Williams, D. E. (1991): Thermal properties of soils, Power Engineering Journal, 5(1), 37
232. Wojtkowiak, J. (2012): Experimental flow characteristics of multi-pipe earth-to-air heat exchangers, Foundations of Civil and Environmental Engineering, (15), 5–18
233. Yildiz, A., Ozgener, O., and Ozgener, L. (2011): Exergetic performance assessment of solar photovoltaic cell (PV) assisted earth to air heat exchanger (EAHE) system for solar greenhouse cooling, Energy and Buildings, 43(11), 3154–3160
234. Yoomak, S., and Ngaopitakkul, A. (2020): Investigation and feasibility evaluation of using nanogrid technology integrated into road lighting system, IEEE Access, 8, 56739–56754
235. Yu, W., Chen, X., Ma, Q., Gao, W., and Wei, X. (2022): Modeling and assessing earth-air heat exchanger using the parametric performance design method, Energy Sources, Part A: Recovery, Utilization, and Environmental Effects, 44(3), 7873–7894
236. Yu, Y., Li, H., Niu, F., and Yu, D. (2014): Investigation of a coupled geothermal cooling system with earth tube and solar chimney, Applied energy, 114, 209–217
237. Yue, S., Ge, Z., Xu, J., Xie, J., Xie, Z., Zhang, S., and Li, J. (2023): Analysis of the Ventilation Performance of a Solar Chimney Coupled to an Outdoor Wind and Indoor Heat Source, Applied Sciences, 13(4), 2585
238. Zarezade, M., and Mostafaeipour, A. (2016): Identifying the effective factors on implementing the solar dryers for Yazd province, Iran, Renewable and Sustainable Energy Reviews, 57, 765–775
239. Zeng, C., Yuan, Y., Xiang, B., Cao, X., Zhang, Z., and Sun, L. (2019): Thermal and infrared camouflage performance of earth-air heat exchanger for cooling an underground diesel generator room for protective engineering, Sustainable Cities and Society, 47, 101437
240. Zhang, H., Wang, H., and Xuan, J. (2020): Rational design of photoelectrochemical cells towards bias-free water splitting: Thermodynamic and kinetic insights, Journal of Power Sources, 462, 228113
241. Zhang, L., Huang, G., Zhang, Q., and Wang, J. (2018): An hourly simulation method for the energy performance of an office building served by a ground-coupled heat pump system, Renewable Energy, 126, 495–508
242. Zhang, L., Luo, X., Huang, G., and Zhang, Q. (2019): Comparative analysis of U-pipe location on the sizing of borehole heat exchangers, Applied Thermal Engineering, 150, 666–673
243. Zhang, N., and Wang, Z. (2017): Review of soil thermal conductivity and predictive models, International Journal of Thermal Sciences, 117, 172–183
244. Zhao, Y., Li, R., Ji, C., Huan, C., and Zhang, B. (2019): Parametric study and design of an

earth-air heat exchanger using model experiment for memorial heating and cooling, Applied Thermal Engineering, 148, 838–845
245. Zhou, T., Xiao, Y., Huang, H., and Lin, J. (2020): Numerical study on the cooling performance of a novel passive system: Cylindrical phase change material-assisted earth-air heat exchanger, Journal of Cleaner Production, 245, 118907
246. Zhu, J., Koehl, M., Hoffmann, S., Berger, K. A., Zamini, S., Bennett, I., Gerritsen, E., Malbranche, P., Pugliatti, P., and Di Stefano, A. (2016): Changes of solar cell parameters during damp-heat exposure, Progress in Photovoltaics: Research and Applications, 24(10), 1346–1358
247. Zsiboracs, H., Zentko, L., Pinter, G., Vincze, A., and Baranyai, N. H. (2021): Assessing shading losses of photovoltaic power plants based on string data, Energy Reports, 7, 3400–3409
248. Zukowski, M., and Topolanska, J. (2018): Comparison of thermal performance between tube and plate ground-air heat exchangers, Renewable Energy, 115, 697–710
249. Zuo, L., Yuan, Y., Li, Z., and Liu, W. (2012): Numerical analysis of flow heat transfer characteristics in solar chimneys integrated with seawater desalination, in International Conference on Sustainable Power Generation and Supply (SUPERGEN 2012). IET, 1–7

A2: Publications related to the dissertation

Refereed papers in foreign languages:

1. **Ali, M. H.**, Kurjak, Z., & Beke, J. (2020): Evaluation of the temperature effect on the outputs and efficiency of photovoltaic (PV) cell by using Simulink/MATLAB, Mechanical Engineering Letters, Gödöllő, Hungary, Vol. 20, pp. 59-66, HU ISSN 2060-3789
2. **Ali, M. H.,** Kurjak, Z., & Beke, J. (2021): Experimental evaluation of the underground soil temperature readiness for heating and cooling systems installation, European Journal of Energy Research, Vol. 1, pp. 1-6, ISSN 2506-8016. https://doi.org/10.24018/ejenergy.2021.1.2.8

3. **Ali, M. H.**, Kurjak, Z., & Beke, J. (2022): Simulation Modeling for Earth to Air Heat Exchanger System by Using MATLAB, European Journal of Engineering Science and Technology, Vol. 5, pp. 1-19, ISSN 2538-9181. https://doi.org/10.33422/ejest.v5i1.843
4. **Ali, M. H.**, Kurjak, Z., & Beke, J. (2023): Investigation of earth air heat exchangers functioning in arid locations using Matlab/Simulink, Renewable Energy, Vol. 209, pp. 632-643, ISSN 2506-8016. https://doi.org/10.1016/j.renene.2023.04.042 (Scopus: Q1/D1, IF: 8.7)
5. **Ali, M. H.**, Kurjak, Z., & Beke, J. (2023): Modelling and simulation of solar chimney power plants in hot and arid regions using experimental weather conditions, International Journal of Thermofluids, Vol. 20, pp.100434, ISSN 2666-2027. (Scopus: Q1/D1) https://doi.org/10.1016/j.ijft.2023.100434
6. **Ali, M. H.,** Kurjak, Z., & Beke, J. (2023): Developing an Experimental Method to Estimate Multilayer Soil Equivalent Characteristics and Their Impact on Earth-Air Heat Exchanger Performance, Renewable Energy, Vol., pp., ISSN 2506-8016 (Scopus: Q1/D1, IF: 8.7). (Under review)
7. **Ali, M. H.,** Kurjak, Z., & Beke, J. (2023): Enhancing the Efficiency of Photovoltaic Modules by Combining Solar Chimneys and Earth-Air Heat Exchangers: A Thorough Study and Simulation in Diverse Climates, Energy & Buildings, Vol., pp., ISSN 0378-7788 (Scopus: Q1/D1, IF: 6.7). (Under review)
8. **Ali, M. H.,** Kurjak, Z., & Beke, J. (2023): The Effect of Integrating an Earth-Air Heat Exchanger on Photovoltaic Module Efficiency in Combination with a Solar Chimney, Applied Energy, Vol., pp., ISSN 0306-2619 (Scopus: Q1/D1, IF: 11.2). (Under review)
9. **Ali, M. H.,** Kurjak, Z., & Beke, J. (2023): Integrating Photovoltaic Modules with a Solar Chimney and Earth-Air Heat Exchanger to Boost Efficiency: Fundamentals, Components, and Working Principles, Energy Reports, Vol., pp., ISSN 2352-4847 (Scopus: Q2, IF: 5.2). (Under review)
10. **Ali, M. H.,** Kurjak, Z., & Beke, J. (2024): Evaluation of the monthly impact of ambient temperature and solar radiation on the power produced by photovoltaic panels in two different climates, Results in Engineering, Vol., pp., ISSN 2590-1230 (Scopus: Q1, IF: 5). (In progress)
11. **Ali, M. H.,** Kurjak, Z., & Beke, J. (2024): Evaluation of the performance of Photovoltaic system integrated with an air-ground heat exchanger system in a hot climate, Journal of Electrical Engineering & Technology, Vol., pp., ISSN 1975-0102 (IF: 1.9). (In progress)
12. **Ali, M. H.,** Kurjak, Z., & Beke, J. (2024): Evaluation of the performance of the solar chimney integrated with the Photovoltaic/Thermal collector in different climates, International Journal of Thermofluids, Vol., pp., ISSN 2666-2027 (Scopus: Q1/D1). (In progress)
13. **Ali, M. H.,** Kurjak, Z., & Beke, J. (2024): Numerical comparison between the effect of regular soil and multi-layer soil on the performance of the hybrid system consisting of the ground-to-air heat exchanger and the solar system, Journal of Engineering and Sustainable Development, Vol., pp., ISSN 2520-0925. (In progress)
14. **Ali, M. H.,** Kurjak, Z., & Beke, J. (2024): The effect of the depth of the ground-air heat exchanger on its performance in hot climates, European Journal of Energy Research, Vol., pp., ISSN 2506-8016. (In progress)

Refereed papers in Hungarian language:

15. **Ali, M. H.,** Kurjak, Z., & Beke, J. (2024): Napkémény légáramának növelése kényszeráramlás akalmazásával, Mezőgazdasági Technika, Vol., pp, ISSN 0026-1890 (submitted)

International conference proceedings:

16. **Ali, M. H.**, Kurjak, Z., & Beke, J. (2020): Experimental evaluation of the groundwater temperature readiness for heating and cooling systems installation in subtropical region, 12th International Symposium on Exploitation of Renewable Energy Sources and Efficiency, Subotica, Serbia, April 16-18, 2020, P. 18, ISBN: 978-86-919769-7-2.
17. **Ali, M. H.**, Kurjak, Z., & Beke, J. (2024): Investigating the effect of the depth of the ground-to-air heat exchanger on the performance of the solar chimney integrated with it in different climates, 4th International Conference on Innovative Academic Studies ICIAS 2024, Konya, Turkey, March 12-13, 2024, P., ISBN: xxx-xx-xxxxxx-x-x. (under preparation)
18. **Ali, M. H.**, Kurjak, Z., & Beke, J. (2024): Investigating the effect of the depth of the ground-to-air heat exchanger on the performance of the solar chimney integrated with it in different climates, International Conference on Power and Energy Engineering (EnergyEng-2024), Paris, France, September 23-25, 2024, P., ISBN: xxx-xx-xxxxxx-x-x. (under preparation)
19. **Ali, M. H.**, Kurjak, Z., & Beke, J. (2024): Solar chimney performance across climates: Exploring the influence of size, International Conference on Power and Energy Engineering (EnergyEng-2024), Paris, France, September 23-25, 2024, P., ISBN: xxx-xx-xxxxxx-x-x. (under preparation)

International conference abstracts:

20. **Ali, M. H.**, Kurjak, Z., & Beke, J. (2020): Enhancement the efficiency of photovoltaic solar cell by using combination earth-air heat exchanger with assist solar chimney, Book of Abstracts, 26th Workshop on Energy and Environment, Gödöllő, Hungary, December 10-11, 2020, p. 18., ISBN 978-963-269-928-8.
21. **Ali, M. H.,** Kurjak, Z., & Beke, J. (2021): Impact a Combination of Solar Energy and Geothermal Systems on PV Output Power, Book of Abstracts, 20th International Workshop for Young Scientists, BioPhys Spring 2021, Prague, Czech Republic, May 18, 2021, p. 56, ISBN 978-83-89969-68-2.
22. **Ali, M. H.**, Kurjak, Z., & Beke, J. (2023): The effect of forced airflow inside the solar chimney on the photovoltaic module power generation, Book of Abstracts, 29th Workshop on Energy and Environment, Gödöllő, Hungary, December 7-8, 2023, p. 13., ISBN 978-963-623-079-1.
23. **Ali, M. H.**, Kurjak, Z., & Beke, J. (2023): The effect of integrated solar air collector on the photovoltaic module power generation, Book of Abstracts, 29th Workshop on Energy and Environment, Gödöllő, Hungary, December 7-8, 2023, p. 15., ISBN 978-963-623-079-1.
24. **Ali, M. H.**, Kurjak, Z., & Beke, J. (2023): The effect of the geometric configuration of earth-air heat exchangers on their performance, Book of Abstracts, 29th Workshop on Energy and Environment, Gödöllő, Hungary, December 7-8, 2023, p. 17., ISBN 978-963-623-079-1.

A3: The mathematical procedures used to formulate the parameters of the PV/T model

In this appendix, we detail the mathematical procedures used to formulate all of the parameters of the PV/T model explicitly.

Here is the formula for the temperature of solar cells:

$$T_{CELL} = \frac{(\alpha\tau)_{EFF} \cdot I + U_t \cdot T_{AMB} + U_T \cdot T_{BS}}{U_t + U_T} \tag{9.1}$$

Where:

$$(\alpha\tau)_{EFF} = \tau_G \cdot (\alpha_{CEL} \cdot p + (1-p) \cdot \alpha_T + p \cdot \eta_{CEL}). \tag{9.2}$$

Suppose we plug the values into Eqs. (9.1) and (9.2), we get the following expression for the Tedlar back surface temperature:

$$T_{BS} = \frac{h_{P1} \cdot (\alpha\tau)_{EFF} \cdot I + U_A \cdot T_{AMB} + h_f \cdot T_{AIR} + \hbar_{RUD\_DUCT} \cdot T_f}{U_{aT} + h_f + h_{RAD\_DUCT}} \tag{9.3}$$

Where:

$$h_{p1} = \frac{U_T}{U_t + U_T}\ , U_{tT} = \frac{U_t \cdot U_T}{U_t + U_T}$$

The subsequent linear differential equation is found by combining Eqs (9.1), (9.2), and (9.3):

$$\frac{dT_{AR}}{dx} + T_{AIR} \cdot \vartheta = \zeta \tag{9.4}$$

Where:

$$\vartheta = \frac{(h_{p3})}{\dot{m_{AIR}} \cdot C_{AIR}} \cdot b$$

$$\varsigma = \left[T_{AIR} \cdot (U_{tf} + U_{b0}) + h_{P1} \cdot h_{P2} \cdot (\alpha\tau)_{EFF} \cdot I - T_l \cdot (h_{P4} + U_{b0})\right] \cdot \frac{b}{\dot{m}_{AIR} \cdot C_{AIR}}$$

$$h_{P2} = \frac{(h_f + h_{ARD\_DUCT})}{(h_f + h_{RAD\_DUCT} + U_{tT})}$$

$$h_{P3} = \frac{U_{tT} \cdot h_f}{(h_f + h_{RAD\_DUCT} + U_{tT})}$$

$$h_{P4} = \frac{U_{tT} \cdot h_{RUD\_DUCT}}{(h_f + h_{RAD\_DUCT} + U_{tT})}$$

$$U_{tf} = \frac{U_{tT} \cdot (h_f + h_{RAD\_DUCT})}{(h_f + h_{RAD\_DUCT} + U_{tT})}$$

Because of the boundary constraints at x=0, we get: $T_{AIR}(x) = T_{AIR\_IN}=T_{AMB}$, the equation as follow:

$$T_{AIR}(x) = \frac{\zeta}{\vartheta} + \left(T_{AR\_IN} - \frac{\zeta}{\vartheta}\right) \cdot e^{-\vartheta x} \tag{9.5}$$

By plugging x=L_{PV}=$L_{PV/T,\,DUCT}$ into Eq. (9.5), we may determine the air temperature as it exits the duct (at a distance L_{PV} from the entrance).

The following is the formula for calculating the average fluid temperature across the length of the PV module that is being considered:

$$\begin{aligned} \bar{T}_{AIR} &= \frac{1}{L_{PV}} \int_0^{L_{PV}} T_{AIR}(x) \cdot dx \\ &= \frac{\varsigma}{\vartheta} + \frac{1}{\vartheta \cdot L_{PV}} \cdot \left(T_{AIR\_IN} - \frac{\varsigma}{\vartheta}\right) \cdot \left(1 - e^{-\vartheta \cdot L_{PV}}\right) \end{aligned} \tag{9.6}$$

The value of T_I (temperature of the insulation upper surface) is used in the formulas for air temperature obtained in Eqs. (9.5) and (9.6).

A4: The heat transfer coefficients that are defined for use in the model equations

This is how the heat transfer coefficients that are defined for use in the model equations are defined:

$$h_{CONV,UPP} = 2.8 + 3 \cdot Vw \tag{9.1}$$

$$h_{CONY,UND} = 2.8 + 3 \cdot V_{AIR\_UNDER\_I} \tag{9.2}$$

$$h_{RAD} = \varepsilon_G \cdot \sigma \cdot (T_{SKY} + T_{CELL}) \cdot (T_{SKY}^2 + T_{CELL}^2) \tag{9.3}$$

One method for determining the radiative heat transfer coefficient within the PV/T duct is to use the formula for two infinitely long, grey, opaque, parallel plates with the same finite width opposite each other (Starace et al., 1998). The emissivity of the aluminum sheet insulation on top was determined to be 0.1, whereas that of the PV module's rear surface was fixed at 0.87.

$$h_{RAD\_DUCT} = \left(\frac{1}{\frac{1}{\varepsilon_{BS}} + \frac{1}{\varepsilon_l} - 1}\right) \cdot \sigma \cdot (T_{BS} + T_I) \cdot \ (T_{BS}^2 + T_I^2) \tag{9.4}$$

$$T_{SXY} = T_{AMB} - 6 \tag{9.5}$$

$$U_{b0} = \frac{1}{\left(\frac{L_I}{K_I} + \frac{1}{h_{CONV,UND}}\right)} \tag{9.6}$$

$$U_t = \frac{1}{\left(\frac{L_G}{K_G} + \frac{1}{h_{CONV,UPP} + h_{RAD}}\right)} \tag{9.7}$$

$$U_T = \frac{1}{\left(\frac{L_{CEIL}}{K_{CEIL}} + \frac{L_T}{K_T}\right)} \tag{9.8}$$

The relative difference is a special case of the percentage form of relative change calculated from the absolute change between the experimental (measured) and theoretical (accepted) values and divided by the theoretical (accepted) value (Bevington et al., 1993)(Mandel, 2012).

$$RD = \frac{|Experimental - Theoretical|}{|Theoretical|} \times 100\% \tag{9.9}$$

A5: Practical steps for digging the trench and laying the PVC pipes for installing the EAHE

Fig. 9.1. Practical steps for digging the trench and laying the PVC pipes for installing the EAHE.

9. ACKNOWLEDGEMENT

I extend my deepest gratitude to the Stipendium Hungaricum Scholarship Programme for the financial support that made this doctoral journey possible. This research was carried out under the auspices of the Doctoral School of Mechanical Engineering at MATE (Szent István University formerly), Gödöllő, Hungary.

Embarking on this arduous path toward my PhD in September 2019 and reaching its culmination in mid-2023, it has been a transformative journey marked by the invaluable support of numerous individuals. I owe a debt of gratitude to a diverse array of people, including professors, staff members, classmates, senior and junior colleagues, technical and support staff at the university, local Hungarians, international friends, and my cherished family members and relatives.

Foremost among those to whom I am indebted are my supervisors, **Prof. Dr. János Beke, DSc**, and **Associate Prof. Dr. Zoltán Kurják, PhD**. Their unwavering guidance, insightful advice, constant encouragement, and remarkable patience were instrumental in shaping this dissertation. Their vast knowledge and experience served as a beacon, inspiring me throughout my academic pursuits.

My heartfelt appreciation extends to my parents, **my dear father** and **mother**, who have been my foremost blessings in life. I express profound gratitude to my beloved wife, **Worood**, and my children, **Eileen**, **Thulfiqar**, and **Yazen**. They stood by me through every stage of this academic endeavor, sharing both the challenging and triumphant moments sacrificing their time for the sake of my studies.

I am also indebted to my **extended family** and **friends,** whose love and sacrifices played a pivotal role in making this achievement possible. I would like to express my deep appreciation and gratitude to my dear friends **Qudama**, **Ahssan**, **Mansoor**, **Maytham**, **Alaa**, and **Mohsin**, who have been dedicated study companions and supportive allies throughout my academic journey, contributing significantly to my success.

Special thanks go to **Prof. Dr. Gábor Kalácska**, the current head of the Doctoral School of Mechanical Engineering, and **Prof. Dr. István Farkas**, the former head, for their steadfast managerial support from the commencement of my studies until the fulfillment of all requirements for obtaining the PhD.

I sincerely appreciate the Doctoral School of Mechanical Engineering staff and the University administration for their kindness and cooperation throughout my academic journey. Particularly, I want to express gratitude to **Ms. Csilla Kánai**, the coordinator of the Stipendium Scholarship Program, and **Ms. Zsuzsanna Tassy**, the coordinator for international relations and administrative PhD studies, for their unwavering support during my tenure in Hungary.

Lastly, I acknowledge the Ministry of Higher Education of Iraq and my home institution, the University of Kufa - Faculty of Engineering, for their nomination and steadfast support, which were crucial in achieving this significant milestone.

Mohammed H. Ali

Gödöllő, February 2024